UAB
Universitat Autònoma de Barcelona

Design and Rapid Prototyping of Graphene-based Electrodes Fabricated by Direct Writing for Electrochemical Biosensing towards Point-of-Care Testing

Lei Zhao

Universitat Autònoma de Barcelona

Design and Rapid Prototyping of Graphene-based Electrodes Fabricated by Direct Writing for Electrochemical Biosensing towards Point-of-Care Testing

Lei Zhao

PhD Thesis

PhD in Biotechnology

Directors:

Prof. Arben Merkoçi, Dr. Giulio Rosati & Dr. Andrew Piper

Department of Chemical, Biological and Environmental Engineering

Chemical Engineering Faculty

2023

The present work entitled “Design and rapid prototyping of graphene-based electrodes fabricated by direct writing for electrochemical biosensing towards point-of-care testing”, presented by Lei Zhao to obtain the degree of doctor by the Universitat Autònoma de Barcelona, was performed at the Nanobioelectronics and Biosensors Group at the Institut Català de Nanociencia i Nanotecnología (ICN2), under the supervision of Prof. Arben Merkoçi, Dr. Giulio Rosati and Dr. Andrew Piper.

Bellaterra, March 7, 2023

The supervisors

Prof. Arben Merkoçi

Dr. Giulio Rosati

Dr. Andrew Piper

The present thesis was performed also under the doctoral program studies “Doctorado en Biotecnología” at the Faculty of Chemical Engineering, Universitat Autònoma de Barcelona, under the tutorship of Professor Francesc Godia.

The University tutor

Prof. Francesc Godia Casablancas

This PhD thesis aims to develop reliable, affordable, robust biosensors with graphene electrodes fabricated by direct writing (inkjet printing and direct laser writing).

The state-of-the-art studies carried out will be published as a review:

Design and rapid prototyping of graphene-based electrodes fabricated by direct writing for electrochemical biosensing towards point-of-care testing.

The experimental work performed conducted to three publications:

Kudr, J.; **Zhao, L**.; Nguyen, E. P.; Arola, H.; Nevanen, T. K.; Adam, V.; Zitka, O.; Merkoçi, A. Inkjet-printed electrochemically reduced graphene oxide microelectrode as a platform for HT-2 mycotoxin immunoenzymatic biosensing. Biosens. Bioelectron. 2020, 156, 112109

Zhao, L.; Rosati, G.; Piper, A; de Carvalho Castro, E. S. C.; Hu,L; Yang, Q.; Pelle; Álvarez, R, Merkoçi, A. Laser Reduced Graphene Oxide Electrode for Pathogenic Escherichia Coli Detection. ACS Appl. Mater. Interfaces, 2023, 15, 7, 9024–9033.

Rosati, G.; Urban, M.; **Zhao, L.**; Yang, Q.; de Carvalho Castro, E. S. C.; Bonaldo, S.; Parolo, C.; Nguyen, E. P.; Ortega, G.; Fornasiero, P.; Merkoçi, A. A plug, print & play inkjet printing and impedance-based biosensing technology operating through a smartphone for clinical diagnostics. Biosens. Bioelectron. 2022, 196, 113737

Besides, the author participated in several conferences, presenting his work:

TNT2021 International Conference (Tirana-Albania, 04-08 October, 2021) – oral contribution

31st Anniversary World Congress on Biosensors (online, 26-29 July 2021) – oral contribution

Acknowledgements

I would like to express my heartful thanks to prof. Arben Merkoci for allowing me to pursue a doctoral career in his group. His profound knowledge, keen insight and personal charisma have guided and encouraged me to tackle the difficulties in my academic and personal life. Giulio and Andrew, I have learned a lot from you about the attitude of research, planning of projects and time management. Thank you so much for the professional guidance and support you have given me in my work. Ruslan and Anna Puig, thank you so much for your kind help during my stay in the group.

Qiuyue, Daniel, Jose, Amadeo, Enric, Celia, Liming, Xin Yi, Massimo, Marc, Emily, Jose from Columbia, Vernalyn and Gabriel, it is a pleasure to know you guys. The staying and the music in the lab, the lunch table, the bars, the clubs and the wild disco and the travels, all these moments flash through my mind now and then. Thank you sooo much for the accompany, especially the take-caring in my super difficult period. Big hugs to all of you!

Jiri and Cecilia, my honor to work with you and learn from you. Anna Gratacos, Eleonora, Anna Testolin, Caterina, Laura, Nerea, Flavio, Bernardo, Niloufar, Riham, Chiara, Mayla, Emilia, Winnie, Andrea, Claudio, Lourdes, Leyla, Alfred, Annalisa, Claudia, Gregoire, Jose from Brazil, Eva, David, Duy, Miguel, Mohga, Bhawna, Stefano, Marta, Lorenzo, Carmen, Karla, Aleksandra, Hassan, Carla, Ain Bukhari, it is super nice to meet you and thank you for offering me the chance to know different cultures and to taste plenty of delicious meals.

I want to also thank all the colleagues from ICN_2 and the financial support from China Scholarship Council, graphene flagship and MICROB-PREDICT.

At last, thank you so much, my beloved mom, dad and brothers, you've been supporting me all the time, and no matter what happens you are always there. Thank you, thank you so so much!!!

List of terms, acronyms and abbreviations

3,3’,5,5’-tetramethylbenzidine	TMB
Antibody	Ab
Area specific double layer capacitance	C_S
Atomic force microscope	AFM
Boron-doped diamond electrode	BDD
Bovine serum albumin	BSA
Capacitance	C
Capacitance of helmholtz plane	C_h
Charge transfer resistance	R_{ct}
Chemical vaper deposition	CVD
Chronoamperometry	CA
Computer aided design	CAD
Constant phase element	CPE
Continuous inkjet printing	CIP
Counter electrode	CE
Critical micelle concentration	CMC
Current	I
Current density	j
Cyclic voltammetry	CV
Deoxyribonucleic acid	DNA
Differential-pulse voltammetry	DPV
Diffusion coefficient	D
Dimethyl sulfoxide	DMSO
Direct laser writing	DLW
Direct writing	DW
Direct-laser-written graphene	DLWG
Dodecyl benzenesulfonic acid	SDBS
Dots per inch	DPI
Double layer	DL
Double layer capacitance	C_{dl}
Drop-on-demand	DOD

Escherichia coli	*E. coli*
Electrochemical impedance spectroscopy	EIS
Electrochemical impedance spectroscopy	SWV
Electrochemical surface area	ECSA
Enzyme linked immunosorbent assay	ELISA
Ethylene glycol	EG
Field effect transistors	FET
Flash graphene	FG
Fluorine doped tin oxide	FTO
Formal potential	E°
Fragment antigen-binding	F(ab)
Fragment crystallizable region	Fc
Frequency	f
Glassy carbon electrode	GCE
Graphene oxide	GO
Graphene quantum dot	GQD
Hanging mercury drop electrode	HMDE
Heterogeneous electron transfer rate	k◦
High resolution transmission electron microscope	HRTEM
Highest occupied molecular orbital	HOMO
Highly oriented pyrolytic graphite	HOPG
Horseradish peroxidase	HRP
Imaginary part of impedance	Z″
Impedance module	Z or |Z|
Indium tin oxide	ITO
Inner helmholtz plane	IHP
Inter-defect distances	La
Interdigitated electrode	IDE
International union of Pure Appl. Chem.	IUPAC
Ion-selective electrode	ISE
Isopropanol	IPA
Laplace number	Z
Laser induced graphene	LIG
Laser scribed graphene	LSG

Limit of detection	LOD
Limit of quantification	LOQ
Linear sweep voltammetry	LSV
Lithium dodecyl sulfate	LDS
Lowest unoccupied molecular orbital	LUMO
Mercury film electrode	MFE
Micro super capacitor	MSC
Microelectrode	ME
Molecular imprinted polymer	MIP
Multilayered graphene	MLG
Niobium doped anatase tio_2	NTO
N-methyl-2-pyrrolidone	NMP
Normal hydrogen electrode	NHE
Ohnesorge number	Oh
Open circuit potential	OCP
Organic electrochemical transistor	OECT
Outer helmholtz plane	OHP
Peak current	I_p
Peak current	I_p
Peak-to-peak potential separation	ΔE_p
Phase angle	ϕ
Point-of-care	POC
Poly (ethylene terephthalate)	PET
Poly pyrrole	PPy
Poly (3,4-ethylenedioxythiophene) polystyrene sulfonate	PEDOT: PSS
Polyaniline	PANI
Polydimethylsiloxane	PDMS
Polyimide	PI
Polyvinylpyrrolidone	PVP
Potential scan rate	ν
Real part of impedance	Z'
Reduced graphene oxide	rGO
Reference electrode	RE
Reynolds number	Re

R-square	R^2
Saturated calomel electrode	SCE
Scanning electron microscope	SEM
Scanning transmission electron microscopy	STEM
Screen-printed carbon electrode	SPCE
Single-strand DNA	ss-DNA
Single-walled carbon nanotubes	SWNT
Sodium cholate	SC
Sodium deoxycholate	SDC
Sodium dodecyl benzenesulfonate	SDBS
Sodium dodecyl sulfate	SDC
Spatially shaped femtosecond laser	SSFL
Standard deviation	SD
Standard hydrogen electrode	SHE
Surface plasmon resonance	SPR
Systematic evolution of ligands by exponential enrichment	SELEX
Tetra-butyl ammonium	TBA
Three-dimensional	3D
Transmission electron microscopy	TEM
Warburg impedance	Z_w
Weber number	We
Working electrode	WE
World health organization	WHO
X-ray photoelectron spectroscopy	XPS
X-ray diffraction	XRD

Abstract

Environmental pollution, food contamination and pandemics (e.g., COVID-19), require reliable strategies for the early detection of analytes. The rapid diagnostic of diseases and contaminants, and the accurate and precise monitoring of their changes over time are of great importance. In this sense, electrochemical biosensors are of particular interest due to their low cost, high sensitivity, and ease of miniaturization. Graphene-based materials, with their unique properties such as high surface area and biocompatibility, have great potential for biosensing applications. However, the production of graphene electrodes is typically slow, expensive and inefficient. There is therefore a drive within the research community to develop low-cost, large-scale graphene fabrication methods. Moreover, the development of reliable, affordable, sensitive devices for real-world applications has yet to find broad success. This thesis addresses the aforementioned issues about graphene electrodes, proposing a maskless, non-contact, low-cost graphene electrode fabrication method, i.e., the direct writing (inkjet printing and direct laser scribing), allowing for the miniaturization of the electrode and sensing platform.

Initially, the researcher approached the limits of inkjet printing by fabricating reduced graphene oxide microelectrodes after a comparative study between commercial and research-grade inkjet printers. Using the research-grade inkjet printer, 78 μm wide graphene

microwires were printed and functionalized for the detection of HT-2 mycotoxin. A low LOD of 1.6 ng/mL and a linear dynamic range of 6.3-100 ng/mL were achieved with the sensing system.

Then, reduced graphene oxide electrodes were fabricated on large scale and at low cost by direct laser scribing combined with inkjet printing and a stamp transfer process. Based on such electrodes, biosensors were developed for the detection of Escherichia coli with a wide dynamic range (917 - 2.1×10^7 CFU/mL) and a low LOD (283 CFU/mL). The assay was validated in spiked artificial urine, and the sensor was integrated into a portable wireless system driven and measured by a smartphone.

These works demonstrated the potential of biosensors based on the direct-written graphene electrodes for real-world, point-of-care applications and could be modified for other bacteria or biomarker detection by replacing appropriate bioreceptors.

Keywords *graphene, electrode fabrication, electrochemical biosensor, inkjet printing, direct laser writing, point-of-care testing*

Thesis overview

This thesis is divided into four chapters. A brief explanation of each chapter is given below:

Chapter 1. Introduction. This chapter provides an introduction to the main topics of the thesis and covers the basic theories and state-of-the-art related to them. It begins with the motivation and objectives of the thesis and then moves on to introduce biosensors, with a specific emphasis on electrochemical biosensors. The discussion covers electrochemical cells and techniques, as well as point-of-care testing. Following this, the chapter describes graphene-based materials, including their properties, production, characterization, and advantages for electrochemical biosensing. Rapid prototyping of graphene electrodes is also discussed, with a focus on simple, efficient, and maskless direct writing methods e.g., inkjet printing and laser scribing strategies, along with their working mechanisms and critical parameters. Finally, the chapter concludes with a discussion of biosensing applications of graphene electrodes and the challenges associated with them. (**Figure 1**)

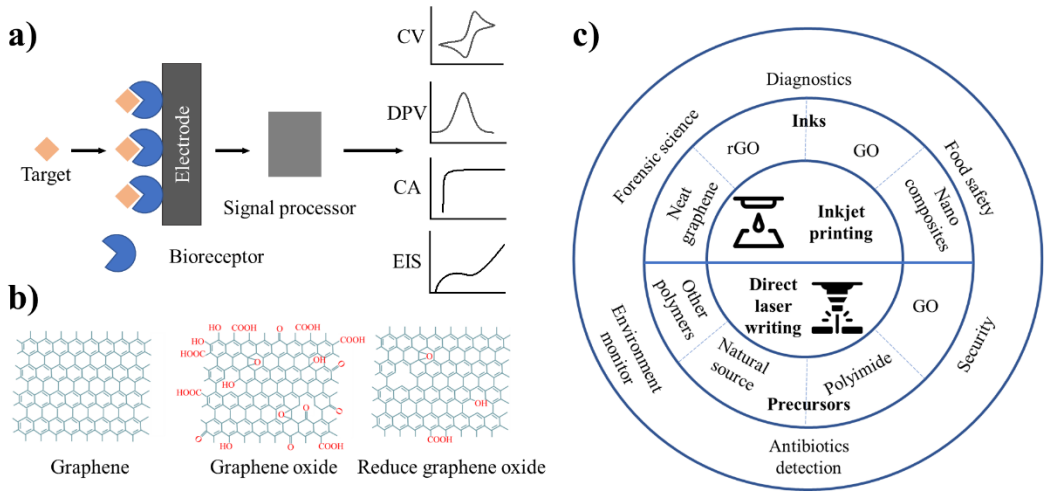

Figure 1 *(a) Illustration of the working mechanism of electrochemical biosensors. (b) Representative chemical structures of typical graphene-based materials. (c) Direct writing of graphene electrode and its biosensing applications.*

Chapter 2. Inkjet-printed electrochemically reduced graphene oxide microelectrode for HT-2 detection. In this section, a water-based graphene oxide ink was formulated to fabricate rGO microelectrodes and demonstrate their biosensing ability. The performance of both consumer and research-grade inkjet printers was evaluated to choose the appropriate printer for this purpose. A three-electrode system was constructed with a GO micropattern printed with the research grade printer on plastic as the working electrode, screen-printed carbon and Ag/AgCl as the counter and reference electrodes, respectively. After optimizing the GO reduction parameters, electrochemically reduced graphene oxide (ERGO) microelectrodes

were produced. An enzymatic immunosensor was constructed based on the as-prepared electrode for the detection of HT-2 mycotoxin, with detailed optimization of the biosensor. The LOD of the biosensor was 1.6 ng/mL, and a linear dynamic range between 6.3 and 100 ng/mL was obtained. The proposed biosensor achieved biologically relevant analytical parameters and satisfactory recovery in a biological matrix, indicating its potential for real-life applications. (**Figure 2**)

Figure 2 *(a) Scheme of ERGO microelectrode fabrication process. (b) Optical microscope image of the printed GO microelectrode. (c) Illustration of the sensing platform for HT-2 toxin detection and (d) the obtained calibration curve.*

Chapter 3 Laser reduced graphene oxide electrode for *E. coli* detection. This chapter presents a novel approach for the large-scale, low-cost fabrication of reduced graphene oxide electrodes using direct writing techniques (laser scribing and inkjet printing) combined with a stamp-transferring method. In this process, graphene oxide is reduced and patterned simultaneously with a laser before being press-stamped onto polyester sheets. The transferred electrodes were characterized using SEM, XPS, Raman, and electrochemical methods. The functionalized electrodes were used to develop an electrochemical biosensor for the detection of *Escherichia coli*, which exhibited a wide dynamic range (917-2.1×10^7 CFU/mL) and a low limit of detection (283 CFU/mL) using only 5 µL of the sample. The biosensor was also

validated in spiked artificial urine and integrated into a portable smartphone-based wireless system. Such biosensors have the potential to be used for real-world, point-of-care applications, and can potentially detect other pathogenic bacteria by changing the bioreceptors. (**Figure 3**)

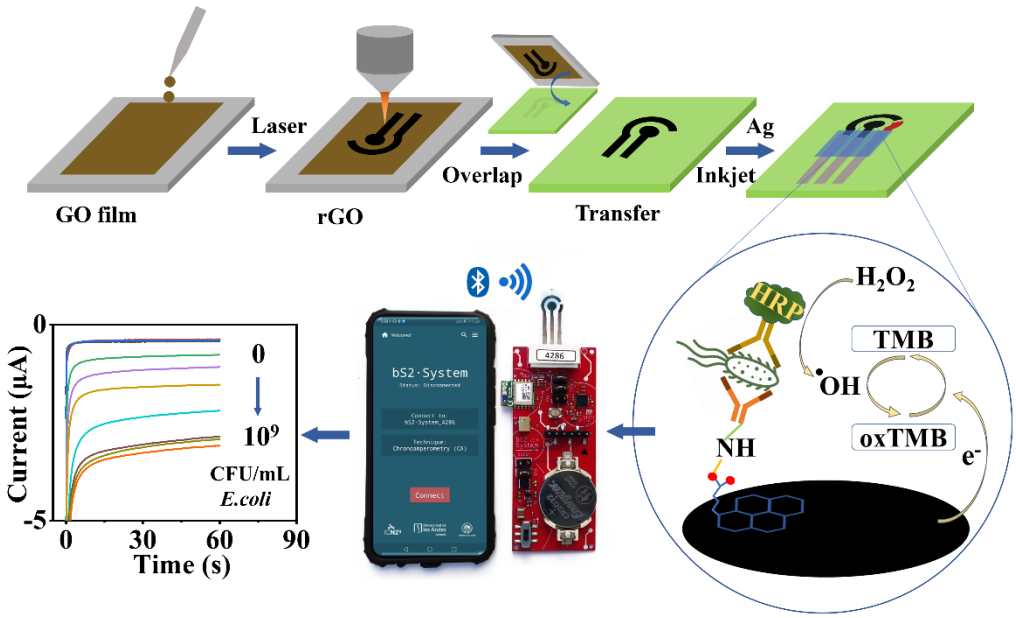

Figure 3 *Illustration of the sensor fabrication procedure and the E. coli detection process.*

Chapter 4. Conclusions and perspectives. Based on the motivation of the thesis and the results obtained in Chapters 2 and 3, this chapter summarizes the achievements of the thesis and identifies possible areas for improvement. The study shows that the consumer inkjet printer is an affordable and fast option for printing, but it is not as accurate and reliable as the research-grade printer, which is qualified for ink patterning with precision and resolution in the tens of micrometer scale. Direct writing has proven to be a powerful tool for producing simple, scalable, and low-cost graphene electrodes, and biosensors based on these electrodes show great promise for sensing towards point-of-care applications.

To further improve the fabrication of sensors, multichannel printing with consumer printers could be explored as an area of interest. The development of graphene microelectrode arrays by direct writing on various substrates would be promising for multiplex sensing and could help address the challenges faced in different sensing scenarios. Overall, the thesis presents a significant contribution to the development of low-cost and efficient graphene-based biosensors for point-of-care applications, with potential for further advancements in the field.

Contents

1 Introduction

1.1 Motivation and objectives

Global issues, such as mycotoxin contamination and bacterial infections, pose serious threats to human health. Therefore, reliable strategies for timely and accurate hazard monitoring are necessary. Chromatography, mass spectrometry, spectroscopy, polymerase chain reaction, enzyme linked immunosorbent assay, and sample culture are well-established techniques for this purpose, but they have limitations such as long operational times, laborious procedures, and the need for highly trained personnel and sophisticated instruments, hindering their utility for rapid, low-cost, and on-field detection[1-3].

Electrochemical biosensors have proven to be an excellent alternative due to their low cost, high sensitivity, and ease of miniaturization[4]. The tunable electrical conductivity, high surface area, versatile functionality, and biocompatibility make graphene-based materials show great potential for developing sensitive electrochemical sensors[5]. However, the fabrication of graphene electrodes remains slow, expensive, and inefficient. It is still a challenge to develop affordable, user-friendly, rapid, and robust devices that can be delivered to end-users for real-world applications.

Maskless, non-contact direct writing methods, such as inkjet printing and direct laser writing, offer a promising solution for rapid prototyping of devices and could lead to the development of smaller, faster, and more efficient sensors[5-7]. To address the aforementioned issue, this thesis will employ direct writing methods for the simple, low-cost, large-scale fabrication of graphene electrodes and further development of electrochemical sensors that can be applied for practical use towards the point-of-care level.

The research will begin with an investigation of state-of-the-art graphene-based electrochemical biosensing platforms, focusing on electrode development and optimization, as well as advancements in applications. To address the need for portable, wearable, or point-of-care electrochemical sensing platforms where miniaturized electrodes/devices are essential, graphene microelectrodes will be fabricated by inkjet printing. The research will first explore and compare the performances of research- and consumer-grade inkjet printers for electrode production. Then, a stable, well-printable, and easy-to-cure ink suitable will be formulated for printing graphene microelectrodes with the proper printer. The microelectrodes will be used for the sensitive monitoring of mycotoxin by creating an enzymatic electrochemical immunosensor. Finally, the research will optimize and validate the sensor in buffer and biological matrix for HT2 mycotoxin detection.

The challenges will also be addressed by direct laser writing of graphene electrodes to develop a complete electrochemical biosensing platform for the detection of bacteria. The research will fabricate graphene electrodes by direct laser writing and a stamp-transferring process, characterize the electrodes in detail using different techniques, and verify the electrodes' efficacy in bacterial detection in buffer and artificial urine. Finally, the sensor will be integrated with a wireless system controlled by a smartphone for sensing towards the point-of-care.

Overall, the proposed research will have the potential to make a significant contribution to the field of graphene electrode production and its biosensing applications, and could have a positive impact on global health by enabling rapid and accurate detection of hazardous contaminants.

1.2 Theoretical backgrounds

1.2.1 Biosensors

1.2.1.1 Definition & application & market

"Biosensor" was defined by the International Union of Pure Appl. Chem. (IUPAC) [8], as “a device that uses specific biochemical reactions mediated by isolated enzymes, immunosystems, tissues, organelles or whole cells to detect chemical compounds usually by electrical, thermal or optical signals”. In the detection process, biosensors utilize a bioreceptor to recognize and bind to the analyte, leading to physiological changes or the presence of chemicals/biological materials. These changes are then recorded by a transducer and converted into measurable signals, providing qualitative and/or quantitative information about the analyte.

Biosensors have numerous applications in fields such as disease diagnostics, environmental monitoring, food control, forensics, and medical research. They are recognized as a rising trend in the scientific and technical communities, as evidenced by the projected market growth from approximately $25.5 billion in 2021 to $36.7 billion by 2026 [9]. This growth is driven by the impressive developments of cutting-edge technologies and paradigms, such as nanotechnology, artificial intelligence, and the internet of things, as well as the pressing need for diagnostic tools that can be used at the bedside or near the patient [9]. The recent COVID-19 pandemic has further emphasized this need and the urgency to expand access to biosensors around the world.

1.2.1.2 Biosensor evaluation

There are several criteria used to evaluate the performance of biosensors, including selectivity,

reproducibility, stability, detection range, and limit of detection [10-14]. These parameters are primarily related to the mechanism of detection of the sensor, the stability and affinity of the bioreceptor to the target molecule, i.e., the analyte, and the efficiency of the transducer.

Selectivity refers to the ability of the biosensor to distinguish the target analyte from other similar substances, and it is determined by the specificity of the bioreceptors (e.g., enzyme towards the substrate, antibody towards the antigen and aptamer towards the respective target). Practically the selectivity is evaluated by testing the sensor in complex media, with a known concentration of the target molecule.

Reproducibility reflects the consistency of the data obtained from the biosensor under the same protocol and tested under the same conditions (such as the same analyte, reagents, equipment, and instruments), and it can be evaluated by the standard deviations (SDs) of at least triplicate tests of multiple concentrations (at least three) of the analyte from the calibration curve [15]. The reproducibility can be also evaluated based on both the intra-batch variations, i.e. the variability of sensors produced in the same batch, and the inter-batch variations, i.e., the signal variations between sensors from different batches. Ideally, both these variations should be as small as possible, but in practice, they depend on many factors.

Stability is important to estimate, especially for the sensors involved in multiple incubating steps and continuous measurements, and it is related to the structure of the biosensor, biorecognition element, and transducer. The operational (using) stability reflects the sensor's susceptibility to ambient disturbances in and around the biosensing system[11, 15]. It is related to the structure of the biosensor, biorecognition element, transducer and the operational atmosphere; analyte concentration, temperature, pH, buffer solution, sample matrix composition, etc. need to be evaluated to obtain a stable sensing response [16]. The storage (shelf) stability shows the usability of a sensor after a period of storage. It is determined by the response deviations of the sensor tested under identical conditions after being stored in a specific atmosphere (usually 4 °C or ambient conditions) for different periods[16].

A very important tool to evaluate the characteristics of a biosensor is the calibration curve, presenting the relationship between the biosensor's signal output and the target analyte concentration. The curve is typically fitted with a linear equation but more complicated equations can be considered [17-20]; a fit is considered "good" if the corresponding R-square (R^2) value is higher than 0.99. The detection range (dynamic range) of the biosensor is defined as the range of analyte concentrations giving the 10% ~90% of the maximum signal response

in the calibration curve [21, 22]. Ideally, the biosensor should show a linear range in its calibration curve, where the output signal is proportional to the analyte concentration. In that case, the sensitivity of the biosensor is defined as the slope of its linear fit in the detection range.

Besides, qualified biosensors should have a limit of detection (LOD) in (or below) the clinical range of the interested analyte. The LOD is the lowest concentration which can be detected by the sensor. A standard method is to measure the signal response of the biosensor to a series of decreasing analyte concentrations until the signal falls below the noise level, and then the LOD is calculated as the analyte concentration corresponding to the SNR threshold, which is typically 3:1. It can also be obtained generally, by substituting, the sum of the mean value of the blank (at least twenty) and its three-time SD (blank+3SD), into the calibration curve[20, 21]. It is important to note that the LOD is not always equivalent to the biosensor's lowest detectable concentration, as the LOD is influenced by various factors such as the signal stability and reproducibility, which can affect the biosensor's sensitivity and accuracy [20, 23-25].

1.2.1.3 Clarification based on the bioreceptors

Based on the bioreceptor types, biosensors can be categorized into three groups: (i) biocatalytic biosensors, typically employing enzymes (enzymatic biosensors); (ii) affinity biosensors using antibodies (immunosensors), nucleic acids (DNA, RNA), or aptamers; (iii) whole-cell biosensors, employing microorganisms as bioreceptors.

1.2.1.3.1 Enzymatic sensor

An enzymatic sensor uses an enzyme that specifically catalyzes the reaction of a relative substrate as a receptor to identify and quantify targets. Enzymes serve as both recognition and amplification elements, so the sensor's performance depends highly on the activity, sensitivity, and affinity of the enzyme towards the target analyte. The concentration of the analyte can be determined by the amount of product(s) from the biocatalytic reaction or by the inhibition/promotion of the enzyme's catalytic activity if the analyte affects the performance of the enzyme.

The immobilization of enzymes plays an important role in biosensor fabrication as it may change the enzyme's behaviors, such as stability and catalytic properties. Various approaches have been applied, including physical encapsulation, chemical encapsulation (embedding the enzyme in the polymer matrix during the polymerization process), electrostatic absorption, covalent anchoring, and bio-specific interaction (e.g., biotin–avidin complex) [26]. Numerous

enzymes, including glutamate oxidase, tyrosinase, nitrate reductase, polyphenol oxidase, sulphite oxidase, glutamate dehydrogenase, and alkaline phosphatase, have been used for the detection of many analytes [19]. Note that some elements may reduce enzyme activity, such as immobilization strategies, working solvents, and toxic compounds present in the sample. Furthermore, components in the sample may interfere with the enzyme, generating false positives. Additionally, enzyme sensitivity is highly related to its structure, which puts a heavy burden on improving sensitivity, stability, and adaptability[27].

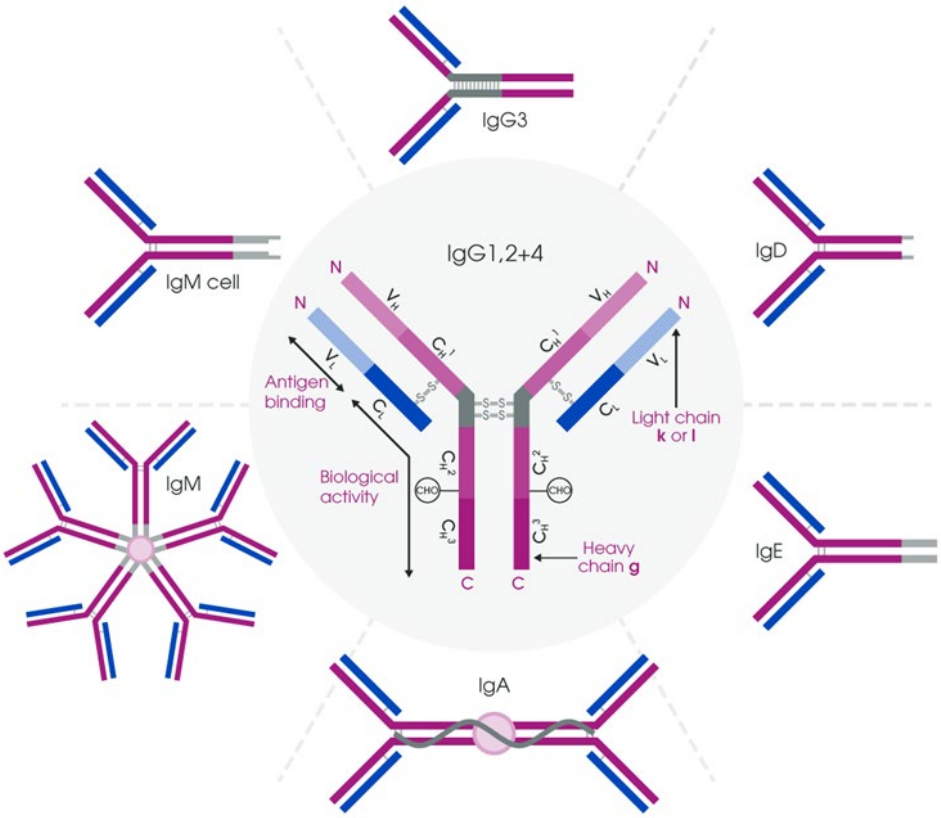

Figure 1.1 Antibody structure. The basic structure of an antibody (shaded area) and different isotypes of antibodies (surrounding area). VH –heavy chain variable domain, VL- light chain variable domain, CH – heavy chain constant domain, CL – light chain constant domain. Adapted from [28].

1.2.1.3.2 Immunosensor

Immunosensors rely on the specific molecular recognition between antigens and antibodies. During the sensing process, the immune recognition is recorded and converted to a measurable signal (optical, electrochemical, or mass change) by a transducer.

Antibodies, also known as immunoglobulins (Ig), are produced by B-cells as the primary

immune defense against antigens, which are anything that the immune system identifies as foreign. Antibodies consist of one or more copies of Y-shaped units formed by four polypeptide chains, with a molecular weight of approximately 150 kDa (Figure 1.1) [29, 30]. The four chains consist of two identical heavy chains (H) and two identical light chains (L), with different sequences and lengths (heavy chain contains more amino acids). The variable part (V), known as the fragment antigen-binding region, F(ab), can bond specifically to an antigen through noncovalent interactions, such as Van Der Waals forces, hydrogen bonds, and electrostatic forces, based on its shape and size. A constant region (C) forms the "legs" of an antibody, called the fragment crystallizable region (Fc). In biosensor fabrication, the Fc is frequently functionalized, for example, with a thiol group to form a self-assembling layer or with enzymes for signal transformation and/or amplification. In mammals, based on the Y unit number and arrangement order, antibodies are divided into five isotypes: IgG, IgM, IgA, IgD, and IgE (Figure 1.1)[30]; the Fc region is identical in all antibodies of the same isotype but varies in different isotypes. Note that antibody fragments (Fab) often show reduced nonspecific binding and steric hindrance compared to full-sized antibodies and have demonstrated success in electrochemical sensing [31].

Antibodies can be classified, based on the species number of the producing B cell, as polyclonal and monoclonal antibodies [30, 32, 33]. A monoclonal antibody is produced by a single clone of B cells via hybridoma technology and binds with an exclusive epitope (a specific part of an antigen recognizable by the antibody), while polyclonal antibodies are a pool of antibodies from different clones of B cells, and can bind to several epitopes from the same antigen. Thus, a kind of polyclonal antibody could be considered a mixture of monoclonal antibodies against the same antigen. The properties of monoclonal and polyclonal antibodies are listed in Table 1.1 (it is a general comparison, and depends on each case).

In general, polyclonal antibodies have multiple epitope-binding sites that enable robust, quick, and highly sensitive target detection. However, their affinity towards the antigen can vary when produced in different animals or even in the same animals at different times. Affinity purification of the serum is essential to reduce cross-reactivity between different antibodies. By contrast, monoclonal antibodies display identical production and much less cross-reactivity, resulting in highly reproducible and selective sensing results. However, they may lose their binding capability against antigens when encountering even minor changes, such as denaturation, polymorphism, or conformational changes.

Table 1.1 Characteristic comparison of monoclonal and polyclonal antibodies.

Property	**Monoclonal Antibodies**	**Polyclonal Antibodies**
Source	Single clone of B cells	Multiple clones of B cells
Specificity	Recognize a single epitope	Recognize multiple epitopes
Homogeneity	Homogeneous	Heterogeneous
Reproducibility	Highly reproducible	Less reproducible
Cost	High	Low
Production time	Longer	Shorter
Storage condition	Restrict	Tolerant to ph or buff changes
Tolerance to the antigen variation	Low	High
Cross-reactivity	Low	High

1.2.1.3.3 Aptasensor

Aptasensor applies aptamer as the bio-recognizing element which may bind to nearly any type of target specifically by complementary shape [34], and are becoming a strong competitor against immunosensor. Aptamers are short oligonucleotides (RNA or single-stranded DNA) with 30–40 nucleobases and can be synthesized in vitro without animal or cell cultures [35]. The structural and functional stability endow aptamers' tolerance over a wide range of temperatures and storage conditions. They can be mass-produced from oligonucleotide libraries, by SELEX (Systematic Evolution of Ligands by Exponential enrichment) [36], and exhibit much low cost than antibodies.

Aptamer has high batch-to-batch reproducibility, and shows high affinity, comparable with antibody-antigen interaction, to its target, but the binding activity is easily influenced by the operation atmospheres (e.g., ionic strength, interfering molecules)[34].

1.2.1.3.4 DNA biosensors

DNA biosensors employ DNA hybridization events to detect a wide range of targets. Hydrogen bonds between DNA base pairs[37] play a crucial role in the recognition of target DNA by the probe (single-stranded DNA with 20–40 base pairs), which is complementary to the target. To ensure high reactivity and prevent non-specific binding/adsorption events, careful control of probe immobilization is essential. Similar to aptamer sensors, the hybridization conditions, such as ionic strength, temperature, and time, can significantly affect the sensitivity and selectivity of DNA biosensors.

1.2.1.3.5 Whole-cell-based biosensors

Whole-cell-based biosensors use microorganisms (such as bacteria, fungi, algae, protozoa, and viruses) as biorecognition elements to monitor target species. These targets induce variations in the metabolic processes of the cells, which can be recorded by the transducer and result in signal changes proportional to the concentration of the analytes. For further details, please refer to the references [38-40].

1.2.1.4 Clarification based on the transducing methods

Biosensors can be categorized based on their transducer as (will be discussed in detail in section 1.2.2), thermal, and gravimetric biosensors [41]. Optical biosensors measure optical signals correlated with the concentrations of the analytes. Paper-based lateral flow assays, e.g., a pregnancy test strip or Covid-19 antigen test strip, are examples of colorimetric-based optical biosensors that have been widely used in our daily life. Enzyme linked immunosorbent assay (ELISA), fluorescent biosensors, chemiluminescence biosensors and surface plasmon resonance (SPR) biosensors are among the most used optical sensors. Fluorescent biosensors [42] display the quantity of the analyte by measurement of the fluorescence signal generated by the transducer (fluorophores). Chemiluminescence biosensors [43] detect the emitting light induced by chemical reactions. Surface plasmon resonance biosensors [44] record the change in the refractive index of a polarized light caused by the binding of an analyte to the bioreceptor immobilized onto a metal surface (usually gold).

ELISA is a plate-based technique used to detect a target using an enzyme-labelled antibody as the bioreceptor in which the enzyme works as a signal amplifier. The typical model has a sandwich structure, as shown in Figure 1.2: capture antibody binds to the ELISA plate by physical absorbing; it selectively captures the target via immune recognition; an enzyme

conjugated with the detection antibody (the same or different from the capture antibody) catalases a colorless substrate into a colored product; the concentration of the target is determined based the color intensity of the resulting product[45]. ELISA has been widely used as a 'gold standard' method for quantifying analysis in disease diagnostics, drug screening, food safety, and environmental monitoring, due to its high specificity, sensitivity and reproducibility [46]. However, it suffers from long operational time (from hours to even days), large sample volumes requirement (100–200 µL), laborious procedures, highly trained personnel and sophisticated instruments, thus limiting its utility in rapid and low-cost detection[47].

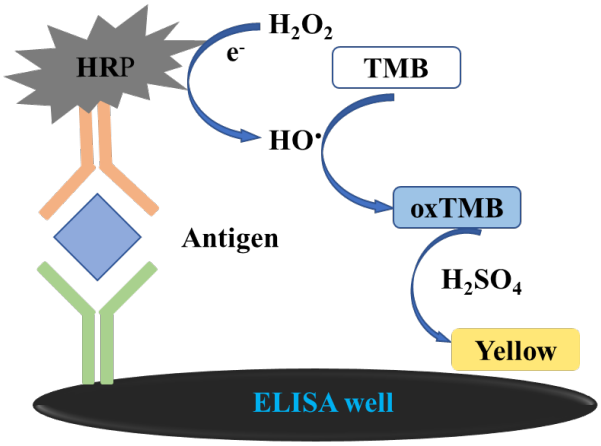

Figure 1.2 Illustration of typical ELISA with 3,3',5,5'-tetramethylbenzidine (TMB) as substrate. Horseradish Peroxidase (HRP) catalyzes the generation of OH radicals from H_2O_2, and these radicals oxidize colorless TMB to blue-colored oxidized TMB (oxTMB). The reaction then is stopped by adding H_2SO_4, and the resulting mixture displays a yellow color, which can be quantified by a spectrophotometer.

Gravimetric biosensors detect targets by the mass changes after material binding (usually with a quartz crystal microbalance). Thermal biosensors detect targets by recording the thermal phenomenon during biological reactions.

1.2.2 Electrochemical biosensors

Electrochemical biosensors use electrochemical cells as transducers to convert biological interaction events such as enzyme catalytic reactions, antibody-antigen binding, aptamer/DNA recognition, and microbe metabolism into electrochemical signals (current, voltage, and impedance). These signals can then be linked to qualitative and quantitative information about the target analytes (Figure 1.3).

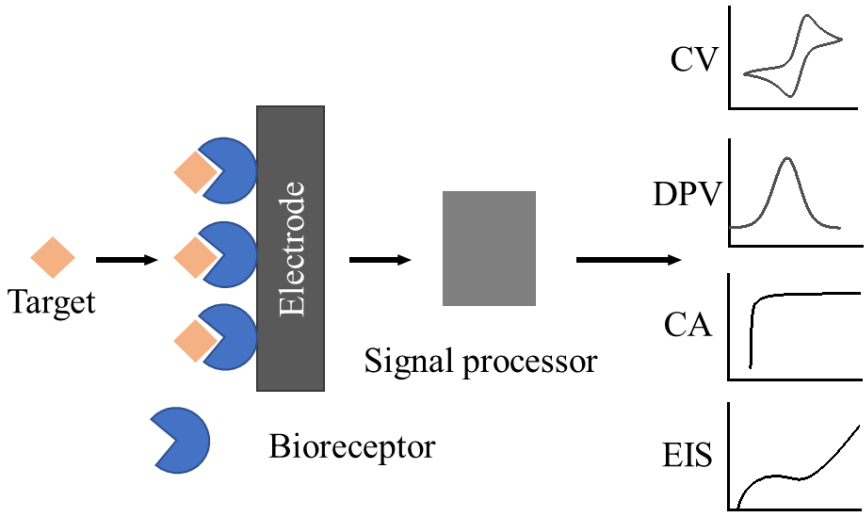

Figure 1.3 Scheme of electrochemical biosensors.

In 1962, Clark developed the first electrochemical biosensor for glucose monitoring in blood, in which the enzyme was immobilized on the electrode as a bioreceptor [48]. Since then, advancements in material science and manufacturing techniques such as printing technologies have provided numerous opportunities for the fabrication of robust, inexpensive, sensitive, and user-friendly electrochemical devices. These devices are leading among currently available sensors due to their low cost, high selectivity and sensitivity, ability to be miniaturize (hence analytical multiplexing), and availability of various measuring techniques. Electrochemical methods are surface techniques that do not rely on the detection solution volume significantly, so small sample volumes in microliters can be applied for measurements [49]. As a result, electrochemical biosensors have demonstrated great promise in healthcare, industrial analyses, environmental sensing, and agricultural monitoring.

1.2.2.1 Electrochemical cell

An electrochemical cell consists of typically three electrodes immersed inside the electrolyte solution, namely working, counter (or auxiliary) and reference electrodes (Figure 1.4).

In an electrochemical sensor, electrochemical processes triggered by the target analytes take place at the electrode-solution interface and are monitored. The working electrode (WE) is the most important element in an electrochemical cell as it monitors the interfacial/reaction phenomenon of interest. The reference electrode (RE) provides a constant, reproducible, and stable half-cell potential in a wide variety of sample solutions and situations, and the potential of the working electrode can be observed or controlled with respect to the reference[50]. The counter electrode (CE) is responsible for establishing a closed loop of the electric circuit

between the WE and CE.

For a reference electrode to work properly, it should be non-polarizable (no current passing through it), but when the current is negligible, it can be used as the CE at the same time[50]. Two-electrode systems[4, 51, 52] have been used in conductometry, capacitive measurements, and electrochemical impedance spectroscopy, especially in non-faradaic impedance cases. Additionally, a variety of commercially available glucose sensors usually have two electrodes, where the RE and CE are combined in one electrode made up of Ag/AgCl or an inert metal conductor[53].

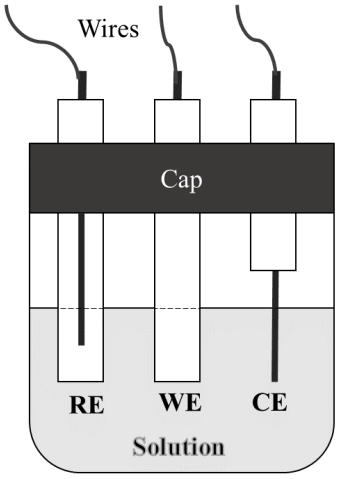

Figure 1.4 Illustration of a typical three-electrode cell.

To obtain reliable sensing results, proper design of the electrochemical cell, especially the electrodes, is crucial. The current between the WE and CE, which is related to the amount of analyte, is typically recorded after applying a potential perturbation between the WE and RE. while applying a potential also results in an ohmic potential drop (potential error) from the cell resistance, mainly the solution resistance, which can affect the accuracy of the target detection. To reduce this error, various strategies can be used, such as placing the RE as close as possible to the WE without creating a short circuit, or increasing the ionic strength of the solution to decrease its resistance. In a flow cell, the RE and CE should be positioned downstream of the WE to avoid disturbance from reaction products or leakage from the RE (e.g., silver and chloride ions from Ag/AgCl reference electrode). Current density is another crucial aspect to consider, as it shows the highest current density at the points closest to the CE, and a homogeneous electrode surface is preferable for obtaining reliable and reproducible responses. Additionally, to ensure consistency, the placement of all three electrodes with respect to each other and the cell must remain constant.

1.2.2.2 Working electrode

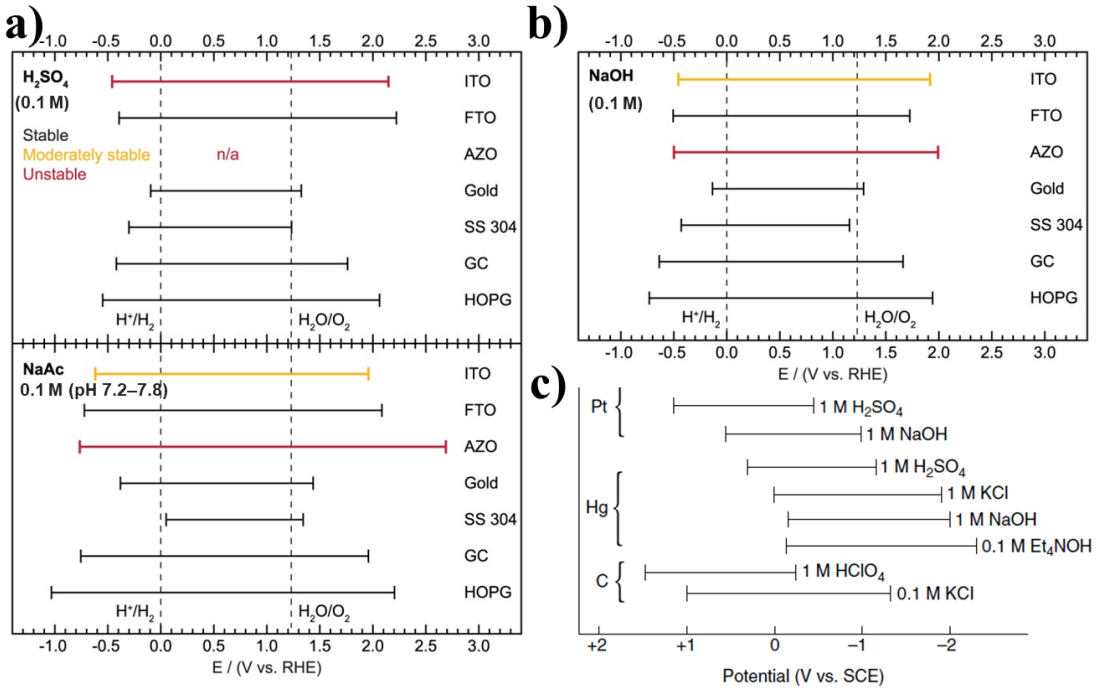

Figure 1.5 Potential windows of different materials in various electrolyte solutions. ITO, indium tin oxide; FTO, fluorine-doped tin oxide; AZO, aluminum-doped zinc oxide; SS 304, stainless steel 304, GC, glassy carbon; HOPG, highly oriented pyrolytic graphite; Et4NOH, tetraethylammonium hydroxide; NaAc, sodium acetate; E(RHE) = 0.059pH. Adapted from ref (a, b) [54], (c) [26].

The choice of material for the electrode, especially the WE, should be based on the application requirements, taking into consideration whether the electrode can provide a reproducible response with a high signal-to-noise (S/N) ratio. To achieve reproducible results, the WE always requires pretreatment and/or polishing to clean or activate it [19]. This can involve mechanical polishing (such as for glassy carbon and gold rod electrodes), chemical, electrochemical (e.g., cyclic voltammetry scanning in H_2SO_4), or thermal treatments. Other factors to consider include cost, availability, toxicity, conductivity, configuration, surface morphology, mechanical stability, and potential window. The potential window, or electrochemical window, is the potential range where no faradic reactions occur, meaning that the electrode and electrolyte are stable in that range [55, 56]. Lai et al. described the background signals and potential window of Au, Pt, and glassy carbon electrodes in several biological buffers [56]. Figure 1.5 shows the potential window of commonly used electrodes in analytical electrochemistry.

1.2.2.2.1 Metal electrode

Mercury electrodes, including the hanging mercury drop electrode (HMDE) and the mercury film electrode (MFE), are some of the earliest and most extensively investigated and applied standard electrodes. Gold (Au) and platinum (Pt) electrodes are the most commonly used due to their chemical inertness, wide anodic potential window, and satisfactory electron transfer kinetics. Au electrodes are more popular since they are more inert and can facilitate the self-assembly of various ligands via strong thiol-Au interaction, which is essential for the development of some biosensors. However, Au and Pt electrodes have cathodic potential windows as high as -0.2 to -0.5 V due to low hydrogen overpotential, which is influenced by pH. Other metals, such as silver, copper, nickel, and alloys, have found applications in specific situations, such as ion detection.

Metal electrodes are fabricated using various methods, including cutting from bulk blocks, physical vapor deposition coupled with lithography techniques, printing techniques such as screen printing and inkjet printing, and selective layer melting. The electrodes are embedded in or deposited on electrochemically insulating substrates such as Teflon, plastics, glass, and ceramics.

1.2.2.2.2 Carbon electrode

Carbon-based electrodes have become increasingly popular in the past two decades due to their low cost, low background signal, wide potential window, and chemical inertness[57]. Their lower conductivity compared to metals results in slower electron transfer rates. The defects and edge planes from the aromatic ring, which is the basic structure of almost all the carbon electrodes, hold the highest electrochemical activity (change transfer rate) [58]. Therefore, the electrochemical activity of carbon electrodes depends heavily on their production strategies and surface treatments, such as polishing or functionalization.

The most commonly used carbon electrodes include the glassy carbon electrode and the carbon paste electrode. The glassy carbon electrode is made of thin, tangled ribbons of cross-linked graphite-like sheets obtained by thermal treatment of polymeric resin in an inert atmosphere[26]. This electrode displays excellent mechanical and electrical properties and reproducible electrochemical performance. The carbon paste electrode is obtained from thermal heating of a mixture of graphite powder and organic liquid binders. The electrode can be factionalized by simply mixing the desired materials (such as protein, enzyme and nanoparticle) with carbon paste under optimized conditions; such electrode can be very cheap

with excellent response, coupling with printing methods (e.g., screen printing, inkjet printing and flexography).

Boron-doped diamond electrode (BDD) is usually produced by chemical vapor deposition. It exhibits high hardness, electronic features from semiconductive to semi-metallic, antifouling property, a wide potential window (approaching 3V, due to the high overpotential for oxygen, hydrogen and chlorine evolution), and very low and stable background currents (ca. 1/10 of that of a glassy carbon electrode with the same working area) [26]. Additionally, BDD electrodes can operate under extreme situations, e.g., surfactant enriched solution with high anodic potentials.

Graphene-based electrodes have found intensive applications in electrochemical biosensing, which will be introduced in section 1.3 and section 1.4.

1.2.2.2.3 Transparent ceramic electrode

These electrodes include indium tin oxide (ITO), fluorine-doped tin oxide (FTO), niobium-doped anatase TiO_2 (NTO), and doped zinc oxide. They are highly transparent to some light, making them of great interest for electrochemiluminescence in electroanalysis [59]. Transparent electrodes also allow for in-situ inspection of target binding using optical microscopy and enable hybridization with optical-based analytical methods.

1.2.2.2.4 Conductive polymer electrode

The charge transfer properties and biocompatibility of conducting polymers, such as polypyrrole, polythiophene, polyaniline, and poly(3,4-ethylene dioxythiophene) polystyrene sulfonate (PEDOT: PSS), have made them widely used in electrochemical biosensing. By reducing or oxidizing the polymer, the conductivity of the electrode can be reversibly switched between a neutral (insulating) state and a positively charged conductive state, which can attract or expel negatively charged entities from and to the electrolyte solution[26]. This controllable electrical conductivity and the fast transfer of the doping ions, along with the benefits of molecularly imprinted polymers (MIP), make conductive polymer electrodes a promising platform for biosensing [60].Additionally, incorporating other nanomaterials, such as metal/oxide particles, carbon nanotubes, and graphene, can improve performance of the sensors based on conductive polymer electrodes (sensitivity, stability, and reproducibility).

1.2.2.2.5 Porous electrode

The surface morphology of the electrode has a great influence on its electrochemical

performance[61]. A porous electrode possesses a higher surface-to-volume ratio compared with a flat electrode, so it offers the possibility to immobilize more bioreceptors[62], and enables the mass transport of electroactive species within the electrode, increasing the rates of electron transfer reactions[63]. The crucial role that electrode porosity plays in the data explanation of cyclic voltammetry (CV) has been theoretically predicted [64]. It was verified by Punckt et al. and the authors also proposed an equation for the evaluation of porosity by electrode porosity factor *P* [65]

$$P = k\frac{I_{max}}{I_{min}} \text{ with } k = \frac{\sqrt{\nu_{min}}}{\sqrt{\nu_{max}}} \qquad \text{(eq.1.1)}$$

where ν_{max} and ν_{min} are the maximum and minimum scan rates applied in the CVs, respectively; I_{max} and I_{min} are the corresponding peak currents.

The same group further verified that even a small degree of porosity affects the apparent reaction kinetics [63]: compared with a flat electrode, porous electrode shows decreased peak-to-peak separation and enhanced peak current in CV for quasi-reversible systems; it shows large peak shifts for irreversible redox reactions; these phenomena are due to the synergism of semi-infinity diffusion (like on a flat electrode) and a superposition of thin-film diffusion. Moreover, it has been proved that mass transport can increase with the optimization of electrode porosity [66]. In addition, the surface morphology can also affect the surface wettability of the electrode[67].

1.2.2.2.6 Microelectrodes

As the demand for point-of-care and wearable electrochemical sensors continues to increase, there is a growing need for miniaturized analytical platforms that can perform accurate and reliable measurements in a portable and convenient format. Microelectrodes, hold great promise for this purpose. Ultramicroelectrodes (UMEs) are of particular interest, which have at least one dimension smaller than 25 μm [26, 68]; they can probe the local concentration on a microscale (e.g., secretions from a single cell [69]) and display the capability of sensing in microfluidic systems with microliter samples. Their merits come from several factors led by the small size effects: the small total current at an UME can result in a low ohmic potential drop, making them able to work in highly resistive solutions, such as milk. UMEs show radial diffusion processes in contrast to the semi-infinity-diffusion of normal macro-electrodes, resulting in much faster mass transport rates. The superfast mass transport can bring a steady-state current swiftly after the potential step, which means a fast sensor response. For instance,

a stable current can be obtained within ~10 ms for a 1-μm-diameter disk electrode, while it takes 1.3 s for a 10-μm-diameter counterpart in chronoamperometry [26]. Moreover, electrodes with dimensions comparable to the target species have shown enhanced sensitivity [70, 71].

1.2.2.3 Counter electrode

Often, the area of the CE is made much larger than that of the WE to ensure that the half-reaction happening at the CE electrode can occur fast enough, thus having negligible interference with the reaction at the WE. The CE usually consists of electrochemically inert conducting materials, including Pt wire or plate, gold, carbon, and polymers. It could also be the same materials as that of the WE, which was already discussed above, thus not requiring further description here.

1.2.2.4 Reference electrode

The constant composition of a redox couple (e.g. Ag/AgCl) endows a reference electrode (RE) with a stable potential with minor temperature dependence. The half-cell potential of the RE should have a small drift of a few microvolts in the operational environment and time period [72]. In practice, it is difficult to build a perfect RE due to potential drift caused by varying liquid junction potential (phase boundary potential) and/or diffusion potential [26].

Preferably, a RE should be cheap, robust and easy to fabricate and use. Standard hydrogen electrode (SHE or normal hydrogen electrode, NHE, Pt/H_2 (activity, a = l)/H^+ (a = 1, aqueous)) have been utilized for potential calibration for other electrodes, since hydrogen's standard electrode potential is defined to be zero volts at any temperature [73]. While this reference electrode is rarely used in practical sensing scenarios due to its large size and operational difficulty. Another common RE is the saturated calomel electrode (SCE, $Hg/Hg_2Cl_2/KCl$ (saturated in water)) with the potential of 0.242 V vs. NHE. Whilst such electrode is nearly discarded owing to the toxicity of the mercury. The silver-silver chloride electrode, Ag/AgCl/KCl (saturated in water) with a potential of 0.197 V vs. NHE, is currently the most commonly used RE owing to its low toxicity, high stability, and small temperature dependence.

A well-conditioned Ag/AgCl reference usually consists of Ag wire coated with AgCl placed in a tube (typically glass), and the tube is filled with concentrated KCl solution (in several M scales). At the end of the tube presents micro/nanoporous frits made of glass, polymer (e.g., Teflon) or ceramic as a salt bridge to separate the reference solution from the sample solution. The AgCl layer can be obtained by (electro)chemical converting of Ag in HCl, $FeCl_3$ or NaClO

solution [74]. However, such electrode is not suitable for measurement in small-volume samples due to the size limitation and possibility of sample contamination. To solve this problem and to meet the requirement of electrode miniaturization for point-of-care sensing, solid-state Ag/AgCl electrodes have emerged, also called pseudoreference electrodes. Inkjet printing [75] and screen printing [76] have been applied for this purpose, using silver salts (needs sequent reduction) or nanoparticle solution (a following chlorination process is needed to produce the AgCl layer) or Ag/AgCl composite as ink. Such references are highly useful for disposable devices owing to the low-cost, scalable production, and capability of dry storage. However, they suffer from the potential draft in the presence of trace bromide and sulfide, and from the possible damage of the AgCl layer [77]. This issue can be solved by solid contact RE, where the porous frits and inner solution for the traditional Ag/AgCl electrode are replaced with a polymer membrane containing KCl, as the "reference solution" and electrode protecting layer. The electrode can be produced by simple drop casting, screen printing and inkjet printing. Polymers including polyvinyl acetate and polyvinyl chloride and polyurethane and urea-formaldehyde resin [72], polypropylene [78], photoresist [79] and polyvinyl butyral [80] have been reported for the electrode production. In the last example [80], the fully inkjet-printed RE showed great stability irrespective of pH and Cl^- concentration. Ag/AgCl reference was demonstrated in which porous frit was replaced with a conductive wire to prevent ion leakage [81]. Note that although numerous efforts have been devoted to it, the electrochemical mechanism of all-solid-state REs is not fully understood, which requires trial-error methods to fabricate new REs [72, 82]. Besides, Ag/AgBr protected by PVC heterogeneous membranes [82], graphene oxide coated PEDOT: PSS [83], Ag [84], Pt [85], carbon [86, 87], and ionic liquid [74] have been applied as REs for certain applications.

1.2.2.5 Electrochemical techniques

Most electrochemical techniques are highly adaptable for biosensing and can be categorized into four main types: potentiometry, voltammetry, conductometry, and electrochemical impedance spectroscopy. In the following text, we will concentrate on the most commonly used techniques and those utilized in the research conducted within this thesis.

1.2.2.5.1 Fundamentals

1.2.2.5.1.1 Electrical Double Layer

An electrical double layer (DL) generates when a solid surface (electrode) exposes to an electrolyte solution, where two layers of unlike charges (ions, particles and/or dipoles) appear

on the interface. In electrochemistry, at a given potential, the electrode is negatively (or positively) charged (q_e), thus attracting a layer of cations (anions) by Coulomb force in the nearby solution (q_s); to reach a neutral state, the sum of q_e and q_s has to be zero. As depicted in Figure 1.6 (take a negatively charged electrode as an example), the accumulation of electrons results in a negative charge on the electrode surface, in a thin layer (<0.1 A [50]), while the solution side is composed of multiple layers. The first layer consists solvent molecules and some cations specifically absorbed on the electrode surface, called the inner Helmholtz plane (IHP), defined by the locus of the absorbed ions; the second layer, called the outer Helmholtz plane (OHP), is defined by the locus of the solvated cations in the proximity to the IHP; the IHP and OHP form a compact layer strongly attached to the electrode surface; the third layer, is a three-dimensional area contains freely moving cations influenced by electric attraction and random thermal motion, named as diffusion layer; this layer ranges from the OHP to the bulk solution and is loosely associated with the compact layer.

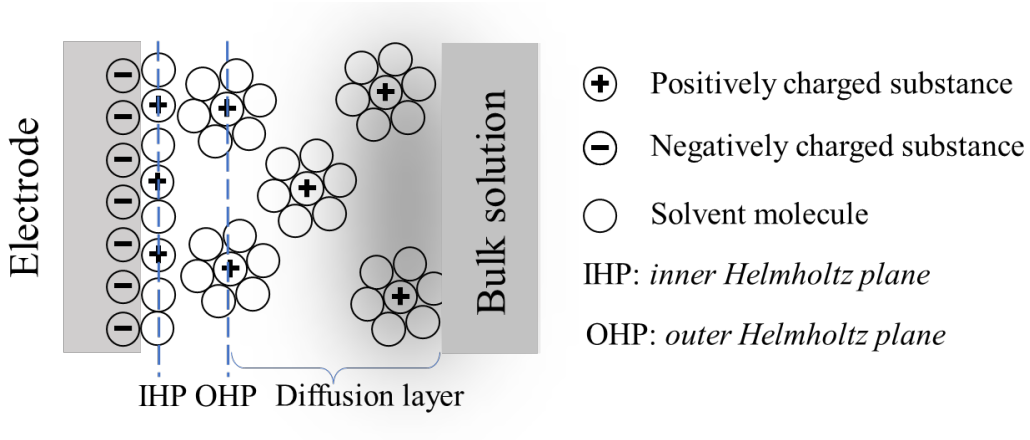

Figure 1.6 Illustration of the electrical double layer.

The electrical DL has been experimentally modelled as a capacitor with capacitance in the range of 10 to 40 μF/cm^2 [50]. It can be considered as a combination of two parallel-plate capacitors in series; one contains two "plates", namely the electrode surface and the compact layer (with the capacitance of C_h); the other is formed by the electrode surface and the diffusion layer (with the capacitance of C_d). Conversely, the total DL capacitance (C_{dl}) can be expressed by

$$\frac{1}{C_{dl}} = \frac{1}{C_h} + \frac{1}{C_d} \qquad \text{(eq.1.2)}$$

in which the concentration of electrolytes (ionic strength) influences C_d dramatically, while C_h is independent of that strongly. The ions arrange a confined charge layer in the diffusion layer

close to the electrode surface with highly concentrated electrolytes, leading to a thin diffusion layer, thus appears a large C_d value (based on the capacitance of a plate capacitor, $C = -\varepsilon /4\pi d$), so $C_{dl} \approx C_h$; in contrast, the diffusion layer is quite thick with dilute solutions (it may be more than 10 nm in extreme case [26]), resulting in small C_d value, and thus $C_{dl} \approx C_d$. When the potential applied on the electrode changes, the charging of the double layer takes place, generating a charging current, which causes background signals for potential scanning techniques.

1.2.2.5.1.2 Mass transfer process

The mass transfer process in a cell consists of convection, migration, and diffusion [50]. Convection arises from external mechanical forces, such as stirring of the solution, which can disrupt the concentration gradient and lead to inaccurate results. Migration is caused by the movement of charged particles (e.g., ions) along an electrical field. Diffusion results from the concentration gradient, moving from a high concentration area to a low one. When a redox process occurs, a concentration gradient appears near the electrode surface, and diffusion occurs. An increasing concentration gradient increases the diffusion rate, and it reaches a maximum when the reaction occurs so rapidly that the concentration of the reactant is almost zero on the electrode surface. Most electrochemical methods are based on the hypothesis that only diffusion is present for the mass transfer; thus, it is crucial to hinder or eliminate convection and migration[50]. In practice, the migration of interested electroactive species can be suppressed by increasing the solution conductivity via adding supporting electrolytes of much higher concentrations than the analyte species. To minimize convection, measurements can be performed in a static solution or with a rotating electrode to create a controlled and uniform flow. Additionally, the use of microelectrodes can also reduce the effects of convection by minimizing the volume of the solution being studied.

1.2.2.5.1.3 Charge transfer process

The interfacial potential of an electrode immersed in a solution remains constant under a static state, known as open circuit potential (OCP). OCP is the potential that reflects the thermodynamic equilibrium of a redox couple, such as $O + ne^- \rightleftharpoons R$, where O represents the oxidized state, and R represents the reduced form. When an external potential is applied, which is high enough to drive the electrode towards a positive direction, the energy of the electrons decreases, leading to the generation of positive holes on the electrode surface. This, in turn, causes the electrons in the highest occupied molecular orbital (HOMO) of R to transfer into

the electrode, resulting in an oxidation current (also called anodic current, as shown in Figure 1.7a). Similarly, a negative-driven potential increases the energy of the electrons within the electrode, leading to an electron transfer from the electrode to the lowest unoccupied molecular orbital (LUMO) of O, causing a reaction shift in the forward direction, generating a reduction current (also called cathodic current, as shown in Figure 1.7b). The electron transfer process between the species in the solution and the electrode is called a faradic process, and the anodic and cathodic currents are faradic currents. Plotting the current against the applied potential results in a current–potential plot, named a voltammogram.

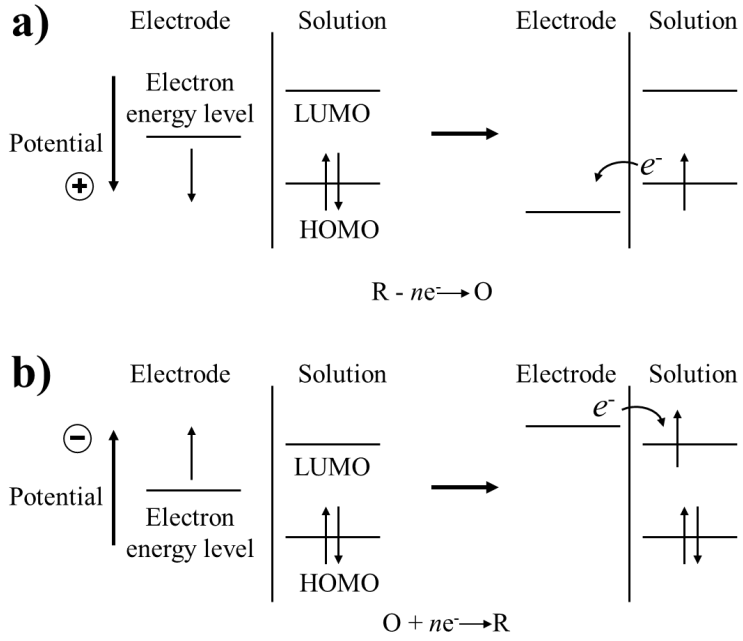

Figure 1.7 Representation of (a) oxidation and (b) reduction processes for O + ne- ⇌R. HOMO, highest occupied molecular orbital of R; LUMO, lowest unoccupied molecular orbital of O. Reproduced from reference [50].

1.2.2.5.2 Potentiometry

Potentiometry is a technique that measures the potential between the working and reference electrodes under zero-current conditions (at an open circuit) or with a fixed current. In the former case, a two-electrode system can be used with an ion-selective electrode (ISE) as the working electrode, taking advantage of the fact that a specific ion can cause a potential change in the ISE [26]. In other words, the potential change can reflect the concentration of the ion. ISEs are capable of detecting ions directly and the substances that produce corresponding ions.

1.2.2.5.3 Voltammetry

Voltammetry, also known as controlled-potential methods, measures the currents generated when a perturbing potential is applied to the electrochemical cell. Different techniques, including cyclic voltammetry, pulse voltammetry (such as differential pulse voltammetry, square wave voltammetry, and staircase voltammetry), and chronoamperometry, have been widely used in biosensing.

1.2.2.5.3.1 Cyclic voltammetry

Cyclic voltammetry (CV) is the most widely used technique for gaining quantitative and qualitative information about an electrochemical process [50]. It is usually the first measurement executed to investigate the adsorption, thermodynamics, and kinetics of charge transfer, from a redox process taking place at the electrode surface.

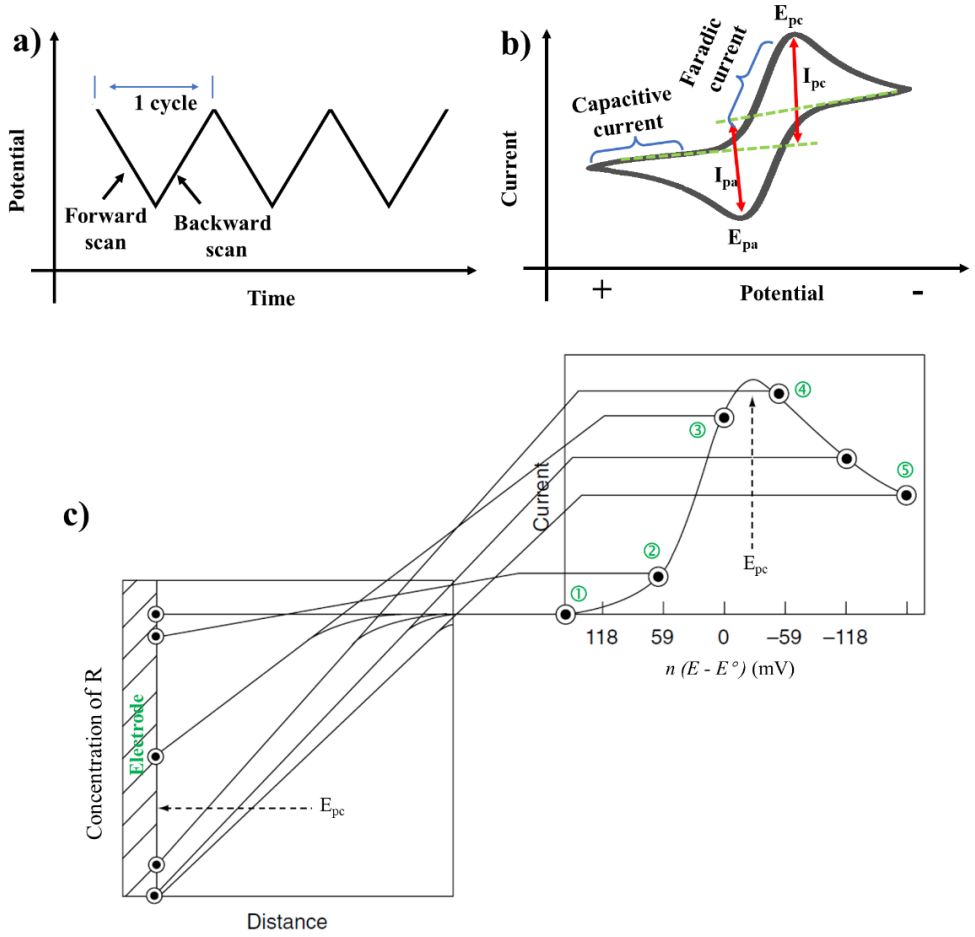

Figure 1.8. Cyclic voltammetry (CV). (a) The applied potential. (b) A typical CV curve. (c) Illustration of the corresponding concentrations of the reductant (O) near the electrode at different stages of the CV curve; n means the electron transfer number in the half-cell; adapted from Ref[88]).

In CV, a linear potential scanning is imposed between the working and the reference electrode in both forward and backward directions (Figure 1.8a), and the current flowing through the working electrode (and the counter electrode) is recorded as a function of the applied potential, resulting in a CV curve (known as cyclic voltammogram, Figure 1.8b). Still taking $O + ne^- \rightleftharpoons R$ as an example, for the reducing process: when the starting potential is much higher than the formal potential (E^0, measured potential of the half-cell when the concentrations of oxidized and reduced species are equal in the unit of mol/L [50]) there is only non-faradaic current (the charging current of the double layer, stage ①→② Figure 1.8c) flowing until the potential reaches a "threshold" (stage ②), where O starts being reduced, generating faradic (cathodic) current. The current keeps increasing along with the potential going more negative (stage ②→③). When the potential passes $E°$, the diffusion approaches its maximum, but the concentration of O keeps decreasing (depletion) and that of R keeps increasing, resulting in a current peak (I_{pc}, stage ③→④). Then the reaction is dominated and limited by diffusion, and the current starts to decline due to the depletion effect (stage ④→⑤). When the potential is well negative of the $E°$ (at least $90/n$ mV beyond the oxidation peak [26], n means the electron transfer number in the half-cell), the potential is reversely scanned, resulting in a reduction peak. Note that the method applying a linear potential scan in one direction is named linear sweep voltammetry (LSV), meaning, CV is a combination of two LSVs in opposite directions.

If the concentrations of the redox probe near the electrode reach thermodynamic equilibrium immediately after a potential change, in other words, the process has a super-fast electron transfer kinetics and it is only affected by the mass-transport, it is said to be a Nernst process (the charge transfer can be described by Nernst equation) or a reversible process. For a reversible process, the anodic and cathodic currents should be equal in absolute value. The peak-to-peak separation (ΔE_p) reflects the electrochemical reversibility of a redox couple on a given electrode; ideally, a reversible process possesses a ΔE_p of $59/n$ mV (n, means electron transfer number in the half-reaction), and in practice, ΔE_p is always larger than $59/n$; small ΔE_p means high reversibility (quasi-reversible process) and large ΔE_p represents an irreversible process. It is worth pointing out that the average of the peak potential indicates the formal potential of a half-reaction ($(E_{pa}+E_{pc})/2 = E^0$). Besides, the electrochemical reversibility can also be evaluated by heterogeneous electron transfer rate ($k°$, for the same redox couple upon different electrodes, higher $k°$ indicates a more reversible process) [89, 90].

In CV, the peak current can be calculated from the Randles-Sevcik equation for a reversible process [50]:

$I_p = 2.69 \cdot 10^5 \cdot A \cdot D^{1/2} \cdot n^{3/2} \cdot \nu^{1/2} \cdot C$ (eq.1.3)

where I_p is anodic (or cathodic) peak current in amp, A is the electrochemical surface area (ECSA, in cm^2), D is the diffusion coefficient of reductant (or oxidant) in solution (cm^2/s), n is the number of electrons transferred in the half-reaction, v is potential scan rate (V/s) and C is the concentration of reductant (or, oxidant, mol/cm^3). The diffusion coefficient of some commonly used redox spices have been listed in literature [91, 92], such as $[Ru(NH_3)_6]^{3+/2+}$, $D_0 = D_R = 6.5\times10^{-6}$ cm^2/s ; $[Fe(CN)_6]^{4-/3-}$, $D_0 = 7.63 \times 10^{-6}$ cm^2/s, $D_R = 6.32 \times 10^{-6}$ cm^2/s; $Fe^{2+/3+}$ $D_0 = D_R = 7.9 \times 10^{-6}$ cm^2/s; dopamine $D_0 = 6.0 \times 10^{-6}$ cm^2/s, where D_0 and D_R are the diffusion coefficients of oxidized and reduced forms of the redox couple.

In reality, the peak current is measurable with a potentiostat by subtraction of the baseline (charging current for electric double layer caused by potential-scanning). Plot the peak current against the square root of the scan rates, for quasi-reversible process, it displays a linear relationship, indicating a semi-infinite linear diffusion (diffusion-controlled) process. On the contrary, a non-linear plot indicates an adsorption-controlled process. Based on the Randles-Sevcik equation, the mass transport limited ECSA of an electrode can be obtained. Note that this value is just an estimation, since the equation is strictly applicable to smooth electrode surfaces with planar semi-infinite diffusion of the redox couple [89].

Another effective strategy to calculate the ECSA, especially for porous electrodes, has been reported [93], in which non-faradic CV is performed at different scan rates, and the following equations are involved:

$$j = \frac{I}{S} \quad \text{(eq.1.4)}$$

$$\mathrm{Cs} = j/v \quad \text{(eq.1.5)}$$

$$\mathrm{ECSA} = S \cdot C_S / C_{Ref} \quad \text{(eq.1.6)}$$

where S is the geometric surface area of the electrode (cm^2); v is scan rate (V/s); I is current (μA); j is current density ($\mu A/cm^2$); C_{Ref} is the area specific double layer capacitance of a flat surface made of the same material as the working electrode ($\mu F/cm^2$). Plotting j with υ, a linear relationship was obtained, in which the slope is equal to the area-specific double layer capacitance (C_S) of the electrode, and then ECSA is derived from eq.1.6. Besides, methodology to assess the porosity of thin nanoporous metal films have been demonstrated by Stanislaw et al[94].

When using CV as a sensing strategy, the peak current and peak potential are related to a specific electrochemical mediator or target analyte for quantitative and qualitative detection, respectively.

1.2.2.5.3.2 Pulse voltammetry

Pulse voltammetry superimposes pulse potentials on the base scanning potential, to dimmish the influence of background signals (charging current).

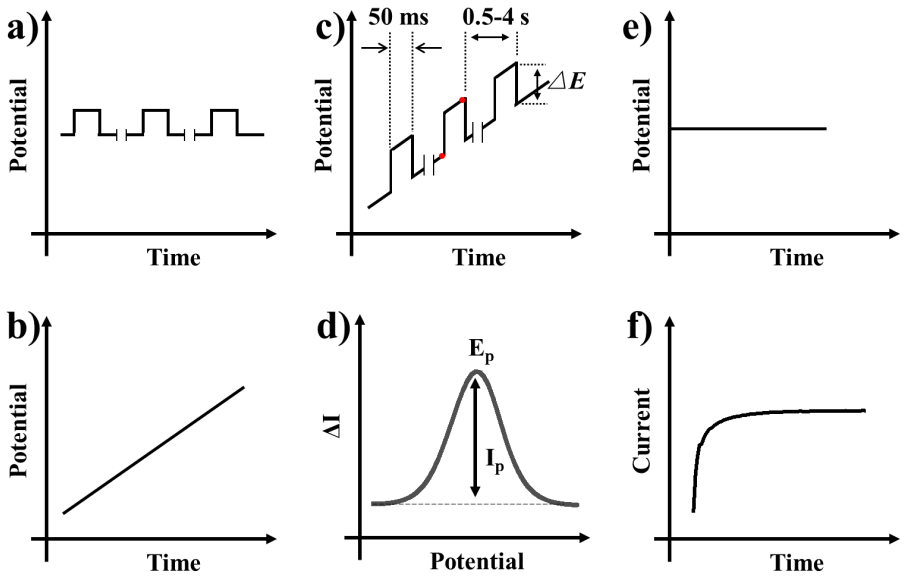

Figure 1.9 Differential pulse voltammetry (DPV); the applied potential scanning (c) is a combination of fixed amplitude pulses (a) and linear potential scanning (b); (d) a typical DPV curve. Chronoamperometry (CA); (e) the stepped potential input signal; (e) a typical CA curve.

Differential-pulse voltammetry (DPV) is a much more sensitive technique than CV, can be applied for trace-level analyte detection, and the limit of detection reaches 10^{-8} M (approximately 1μg/L) [26]. In DPV, the potential is scanned with fixed amplitude pulses (Figure 1.9a) at a specific frequency (indicated by interval time) and superimposed on a linear scanned base potential (Figure 1.9b). Often the interval time, pulse amplitude (modulation amplitude) and pulse width (modulation time), are in the range of 0.5 to 4 s, 10 to 100 mV and ~50 ms (Figure 1.9c)[50]. The current is sampled just before the pulse application and again at the end of the pulse, during which period the non-faradic current (charging current) decays rapidly (exponentially) to nearly zero, while the faradaic current decays much more slowly. Then the former current is subtracted from the latter, and thus the contribution of the charging current is effectively reduced, obtaining a differential-pulse voltammogram by plotting the

current difference (ΔI) against the applied potential. It displays a current peak (Figure 1.9d), the peak position (potential) identifies the analyte and the peak height is directly proportional to the concentration.

1.2.2.5.3.3 Chronoamperometry

In chronoamperometry (CA), the potential is stepped on a (or several) constant value to trigger a redox reaction, and the current is recorded and plotted against time. Experimentally the later part of the transient is focused on, when the redox current reaches a relatively stable state, and meanwhile, the charging current decays to a negligible value. The current is proportional to the concentration of corresponding electroactive specie. (Figure 1.9 e, f). CA is intensively applied within biosensing, especially for enzymatic sensors, due to its simplicity and high signal-to-noise ratio (originated from the diminishment of background signal).

1.2.2.5.4 Electrochemical impedance spectroscopy

Electrochemical impedance spectroscopy (EIS) is a powerful sensing technique due to the capability of monitoring the faradic process and the mass transfer process on the electrode surface at high and low frequency potential sweeping, respectively. This is achieved by applying a sinusoidal potential perturbation with an amplitude typically of 2 - 10 mV [50] to the cell and measuring the current response. The applied potential and resulting current response are considered as two separated phasors rotated with the same speed ω ($\omega=2\pi f$, f is the frequency in Hz), and often they are not in phase, with an angle, ϕ (Figure 1.10a). Impedance is generalized resistance obeying Ohm's law, in the format of complex number, with value expressed as Z (or |Z|), real part as Z′ and imaginary part as Z″, in which $|Z'| = Z\cdot\cos\phi$, $|Z''| = Z\cdot\sin\phi$. A pure resistor holds ϕ as zero, while a pure capacitor is $\pi/2$.

Bode plot (Figure 1.10b) where the Z and ϕ are plotted against frequency (f), and Nyquist plot (Figure 1.10c) where Z″ is plotted against Z′ at varied frequencies can visualize the characteristics of impedance. In EIS, the electrochemical process can be modelled to an Electronic Equivalent Circuit with electronic components (Figure 1.10d and e). Note that practically there are few cases the double-layer can be presented as a perfect plate capacitor, thus a constant phase element (CPE) is used for the equivalent circuit instead of a capacitor.

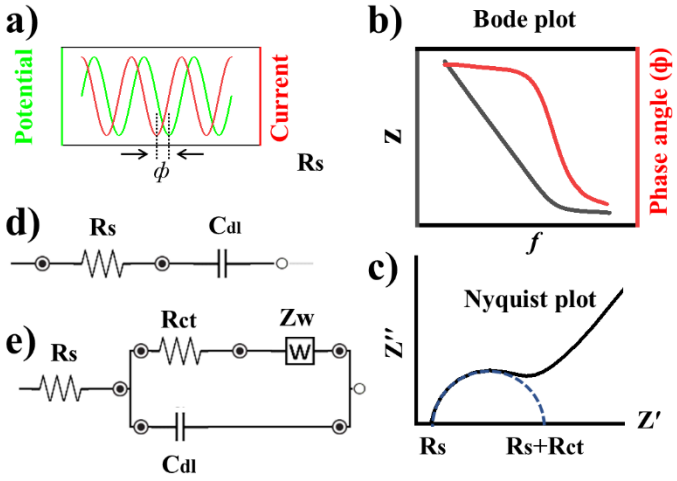

Figure 1.10 Electrochemical impedance spectroscopy (EIS). (a) The input sinusoidal potential scanning and output current response. (b) Bode plot. (c) Nyquist plot. Typical equivalent circuits of non-faradic (d) and faradic (e) impedance response.

Impedimetric sensors can be classified as non-faradic (capacitive), and faradic impedance sensors. In non-faradic impedance mode, the measurement is done in absence of redox probes. The working electrode surface is fully covered by a dielectric layer (usually bioreceptors, e.g., a self-assemble-layer of thiol-ended aptamer on a gold electrode)[95], and the specific-binding event decreases the double-layer capacitance at the electrode-solution interface. The response can be visualized by a bode plot (Figure 1.10b), and the equivalent circuit (Figure 1.10d) is modeled often by a resistor in serial with a capacitor (more likely a constant phase element). Fixed-frequency measurements can be applied for non-faradic impedance, which are operated based on the identification of single or several frequencies in the most sensitive frequency range to the specific-binding event. The changes in impedance are associated with the concentrations of the target. In faradic impedance mode (with the presence of a redox prob), the impedance is monitored in a range of frequencies (typically 0.1-100 kHz). Nyquist plots are usually used to display the measured responses (Figure 1.10c). Randles-Ershler electronic equivalent circuit is particularly useful to model the electrochemical interface and the electron transfer reaction. As shown in Figure 1.10e, the circuit includes the resistance of the electrolyte solution, R_s, the double layer capacitance at the interface, C_{dl} (more likely a constant phase element), the charge transfer resistance, R_{ct}, and the Warburg impedance, which indicates the diffusion-limited process of the redox prob, Z_w. Usually, the change of R_{ct} is proportional to the concentration of the analyte. If the electron transfer is super-fast, the diffusion contributes to the impedance mainly, thus the spectrum displays only the linear part. While it shows only a large semicircle in a slow charge transfer process, such as when large amounts of biomaterials

cover the electrode. Other electronic equivalent circuits can be found in references [52, 95, 96].

In EIS, not only square or disc-shaped, but also interdigitated electrodes (IDEs) have been applied [97]. IDEs are made of two comb-likes planar electrodes consisting of alternated "fingers" with close spacing. The dimensional geometry is a crucial factor since it highly affects the electronic field distribution and mass transfer between the fingers. It has been reported that when the size of the analyte matches the features (mainly width and spacing) of IDEs, the sensor showed better responses [71]. The fingers often are 1-10 mm in length and 1-20 μm both in width and spacing. Micro-IDEs allow the miniaturization of the electrode, hence multiplex sensing; their advantages of microelectrode (call back section 1.2.2.2.6 Microelectrodes) and the narrow electrode distance, endow low ohmic drop, high signal-to-noise ratio, low response time and thus increased sensitivity.

1.2.3 Electrochemical sensor towards point-of-care testing

In 2022, the global point-of-care (POC) diagnostics market was estimated to be USD 43.2 billion, and was predicted to be USD 72.0 billion by 2027 [98]. The huge increase of the market is due to the epidemics such as flu and COVID-19, and the strong demand for POC devices, especially the non-invasive ones. POC test [99-101] refers to rapid, inexpensive testing at the beside or near the patient with a variety of criteria set by the World Health Organization (WHO) with the acronym ASSURED [102] (affordable, sensitive, specific, user-friendly, rapid and robust, equipment-free and deliverable to the end-users). Those criteria were future extended and perfected with two extra criteria, namely R (real-time connectivity) and E (ease of specimen collection and environmental friendliness), with the acronym REASSURED [103].

Electrochemical sensors express great promise for effective diagnostics, particularly in vitro diagnostics, towards laboratory-free POC testing, as guidance for disease and infection treatment, especially in developing areas, where access to traditional laboratory-based testing may be limited. [70, 104]. Smartphones have also emerged as an attractive option for POC testing due to their low cost, portability, and ease of use [105], and an important component for wireless diagnostic platforms integrated with mini-electrochemical workstations. It could work as a power supply, signal collector, data processor for the sensor through wired accessories (USB or audio-port-based connectors), or wireless peripherals (Bluetooth and near-field communication). Moreover, further integration with cloud computing, artificial intelligence, and machine learning, could provide dramatic convenience for POC detection. Microfluidics are microscale laminar fluid flows facilitating the heat and mass transport, and hold the merits

of stability (flow in an isolated space) portability, transparency and easy controllability for sample transmission, mixing or separation of a small volume (in microliter). Thus, the combination of electrochemical devices with microfluidics has shown promise for POC tests [106, 107]. Overall, the combination of electrochemical sensors, microfluidics, and smartphones has the potential to revolutionize POC testing and improve healthcare outcomes.

1.3 Graphene-based materials

Graphene is ideally a single carbon atom-thick sheet consisting of a hexagonal network with no defect sites. It was first reported in 1968[108], and then the term "graphene" was officially defined as "a single carbon layer of graphite structure, describing its nature by analogy to a polycyclic aromatic hydrocarbon of quasi-infinite size" by IUPAC in 1995[109]. It has been catching tremendous attention since the "rediscovering" by Novoselov et al[110, 111] in 2004, who received the Nobel Prize in Physics together with Andre Geim in 2010 for their groundbreaking experiments on graphene. Intensive efforts have been devoted to efficient, low-cost, high-quality graphene production, and the extension of graphene's application in physical, chemical, and biological fields. The graphene market was predicted to increase from <$100 million in 2020 to exceed $1 billion by 2032 [112]. Nowadays, graphene is usually defined as the following categories[113-116]: neat graphene, namely a-few-layered graphene (including single-layer graphene) with minimal defects; functionalized graphene represented by graphene oxide (GO) and reduced graphene oxide (rGO); modified graphene (through the dimension and structure) such as graphene quantum dots, graphene ribbons, graphene nanosheets, doped graphene, fluoridated graphene and its derivatives *etc*.

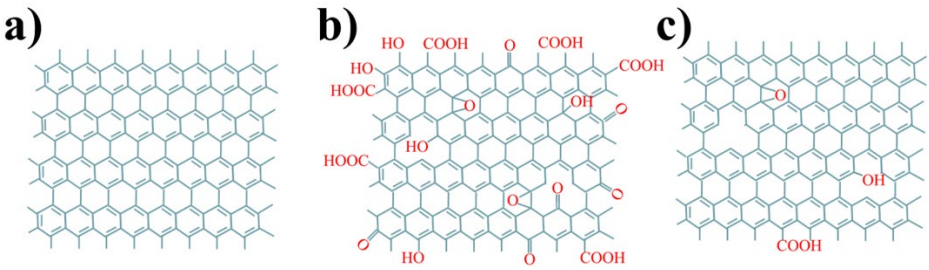

Figure 1.11 Representative structures of (a) graphene, (b) graphene oxide and (c) reduced graphene oxide. Adapted from ref [115].

1.3.1 Properties: what makes graphene good for biosensing?

1.3.1.1 Neat graphene

The sp^2-hybridized carbon atoms in neat graphene are connected with three rigid σ bonds, forming a basal plane, which endows graphene sheets great thermal conductivity (~5000 $W \cdot m^{-1} \cdot K^{-1}$) and mechanical properties (Young's modulus, 0. 1 TPa, fracture strength of 130 GPa) [115]; the perpendicular p_z orbitals towards the basal plane, enable the total delocalization of the electrons alongside the whole sheet, forming a fully π conjugated 2D structure, giving graphene remarkable conductivity (200000 $cm^2 \cdot V^{-1} \cdot s^{-1}$) (Figure 1.11a) [117]. The thickness of ~0.35 nm, gives graphene a theoretical specific surface area as high as 2630 $cm^2 \cdot g^{-1}$ [118]. Besides, graphene has extraordinary optical properties with visible light absorption of approximately 2.3%[115]. These fantastic features award graphene advantages over other nanomaterials in the field of electronics, energy storage and sensors.

Being a nanomaterial, graphene has a natural ability to absorb proteins. Additionally, the highly delocalized π orbital electrons make graphene negatively charged, which enables further binding of bioreceptors through electrostatic adsorption, π-π stacking, or electrophilic addition reactions. The high surface-to-volume ratio of graphene also facilitates a greater number of bonded bioreceptors. However, graphene's lack of dispersibility in most solvents except those with surface energy of~40 mJ/m^2[119], showing aggregation tendency caused by π-π stacking and van der Waals interactions; this makes it difficult to manipulate. Besides, the low defect density is a disadvantage of graphene from an electrochemical point of view, since electron transfer events happen much faster (~10^6 times in the case of catalytic process) at the defects or edge-like parts compared to basal planes[58].

1.3.1.2 Graphene oxide

Graphene oxide (GO)[120-122] is functionalized graphene with numerous oxygen-containing groups including hydroxyl, carbonyl, carboxyl and epoxy groups. The commonly accepted structure model is the Lerf-Klinowski model[123], as depicted in Figure 1.11b, the hydroxyl and epoxy groups are more likely present in the basal plane, while carboxyl and carbonyl groups tend to stay at the edge. GO retains the high surface area and flexibility of graphene, while the hydrophilic functional groups make it easy to manipulate and functionalize in aqueous solutions. However, the introduction of functional groups changes the carbon atoms from sp^2 to sp^3 hybridization, which disrupts the graphene lattice, making GO thermally insulating and electrically resistive. This poor conductivity leads to a suboptimal electrochemical interface for biosensing. Additionally, the functionalization changes the bandgap of graphene from zero to non-zero, resulting in an excellent fluorescence quenching

effect of GO.

1.3.1.3 Reduced graphene oxide

Reduced graphene oxide (rGO) is produced by removing some of the oxygen-containing groups from GO **(**Figure 1.11c**)**, resulting in improved conductivity and stability with defect sites[124, 125]. This makes rGO suitable for use as transducer materials in electrochemical devices. Despite the removal of some oxygen functionalities, rGO still has a high surface area and the graphene basal plane can be used for the immobilization of biomaterials. Various interactions can be used for immobilization, such as covalent bonding, electrostatic bonding, hydrophilic/hydrophobic bonding, hydrogen bonding, π-π stacking, and van der Waals forces.

1.3.1.4 Other graphene-based materials

Graphene quantum dots (GQDs) [126] are layered (less than 10) graphene strips or dots with a lateral dimension of less than 30 nm, which possess fluorescent properties due to the edge effects and significant quantum confinement. The fascinating fluorescent properties and good biocompatibility enable promising applications in biological systems. 3D graphene in the format of aerogel, foam and hydrogel have been applied in the fields such as sensing, water decontamination and energy conversing/storing, due to its high porosity, low density and unique electrochemical performance[127].

1.3.1.5 About bio- and environmental-friendliness

It is important to note that the toxicity and biocompatibility of graphene-based materials are still under investigation, While some studies have reported excellent biocompatibility towards different bioreceptors, others have suggested that graphene-based nanomaterials may be cytotoxic and capable of penetrating cell membranes and interacting with cellular components, exhibiting antibacterial activity. The toxicological effects of graphene are dependent on various factors, including concentration, size, shape, dispersants, and surface functionalities. Moreover, the quantity of graphene nanomaterials being released into the ecosystem is currently unknown, and their accumulation in the aquatic environment may pose a potential threat to both the environment and human health.

Whilst graphene-based materials have been reported to possess excellent biocompatibility toward different bioreceptors[128-130], the toxicity and biocompatibility towards different living organisms are still under debate, and more data is needed to fully understand their potential side effects[131-133]. Graphene-based nanomaterials are cytotoxic and can penetrate

the cell membranes and interact with cellular components, showing antibacterial activity[133, 134]. The concentration, size, shape, dispersants and surface functionalities of graphene play a significant role in their toxicological effects [135, 136]. Moreover, the quantity of graphene nanomaterials being released into the ecosystem is currently unknown [137], and their accumulation in the aquatic environment may pose a potential threat to both the environment and human health.

1.3.2 Graphene production and the influence towards its properties

Various methods have been established to produce graphene with diverse properties. In general, the preparation strategies could be classified into two groups, namely top-down and bottom-up. Top-down methods produce graphene from graphite, by overcoming the van de Waals forces between the graphitic layers through physical, chemical or electrochemical methods. While for bottom-up methods, small molecules are used as "blocks" to build graphene through catalytic, thermal or chemical ways. In the following text, the most used procedures will be introduced.

1.3.2.1 Mechanical exfoliation

The first work of graphene production through mechanical exfoliation of graphite is reported by Novoselov et el. in 2004[138]. The famous 'adhesive tape method' produces nearly defect-free and smooth graphene, by continuously peeling off the highly oriented pyrolytic graphite (HOPG) layers attached to SiO_2-coated Si, until a single layer of carbon network was obtained. The resulting graphene is of the highest quality and is sized up to 1 mm. The method is extremely simple and cost-effective; thus, it is still being used nowadays. However, the low reproducibility of the sheet size and edge properties, and the impossibility of scalable production, limit this mothed to fundamental lab research.

1.3.2.2 Liquid phase exfoliation

This method[114] obtains graphene sheets under ultrasonication with the presence of aiding regents, which can intercalate into and separate the graphite layers. The aiding regents are typically organic solvents with surface tensions of ~40 mJ/m^2[119] such as N-methyl-2-pyrrolidone (NMP) [139] and N, N-dimethylformamide (DMF)[140]; or surfactants, e.g., hydroxide tetra-butyl ammonium (TBA)[141], sodium dodecyl benzenesulfonate (SDBS)[142], sodium cholate (SC)[143], and 1-pyrenecarboxylic acid (PCA)[144]. The mass-scale production of the method is quite appealing, but besides the poor reproducibility similar to

mechanical exfoliation, the residual aiding regents could affect the obtained graphene's properties.

1.3.2.3 Electrochemical exfoliation

The strategy[116] forces negatively/positively charged ions from the solution entering into the graphitic layers by applying a potential between the graphite working electrode and typically a platinum counter electrode, thus gaining separated graphene sheets. This method can alter the exfoliation speed and layer numbers of graphene by changing the potential or current. The applied anodic potential may oxidize the graphene, introducing sp^2 hybridized carbon into the graphene lattice. Since it is performed under ambient conditions, this method is environment-friendly, but still suffers from uncontrollable sheets size and layer number distribution.

1.3.2.4 Chemical vapour deposition

Chemical vapor deposition (CVD), decomposes carbon-containing small organic gases/liquids under H_2 or an inert atmosphere at ~1000 °C, forming graphene lattice onto transitional metals or their alloys along the crystal phase[116, 145]. Methane, ethylene, acetylene, hexane and 1-butanol have been reported as precursors to produce single or few-layer graphene[114]. The metals such as Cu, Ni, Pt, and Pd were used not only as hosting substrates but also as catalysts for the deposition of graphene. The method is scalable for industrial fabrication, but holds the disadvantage of high-temperature requirements and the necessity of graphene transferring to a different surface, which usually needs multiple tedious steps.

1.3.2.5 Chemical exfoliation

Interestingly, GO has a much longer history than graphene. Lord Brodie discovered GO in 1859 during the process of determining the atomic weight of carbon where nitric acid and potassium chlorate mixture was used to oxidize graphite[146]. In 1898[147], Staudenmaier improved the method by adding sulphuric acid to the mixture. In 1958, Hummers and Offeman [148] used potassium permanganate as the oxidant in the presence of sulphuric acid and sodium nitrate solution to avoid the formation of dangerous ClO_2. The formed oxygen functionalities increase the graphitic layer distance, weaken the layer cohesion strength, and thus enable easy layer separation by ultrasonication or high-shear-force stirring [149]. Following this, Tour *et al.* (2010)[150] made the production more efficient by discarding sodium nitrate and increasing the amount of potassium permanganate.

1.3.2.6 Reduction of GO

The reduction of GO to rGO can be realized in thermal, chemical, electrochemical and optical ways.

Chemical reduction is the most widely applied method. A variety of reagents have been used, including hydrazine, $FeCl_2$, sodium borohydride, lithium aluminum hydride, hydroquinone, hydroxylamine, and more eco-friendly L-ascorbic acid, saccharides, tea extract, wild carrot root, and even bacteria[151]. **Thermal reduction** treats GO at about 1000 °C, leading to the decomposition of oxygen groups into molecules such as CO_2, CO, and H_2O[152]. This strategy can lead to structural damage and more defects than GO. **Electrochemical reduction** produces rGO by applying a negative potential to GO solution or thin films[153]. It can be performed under ambient conditions without toxic or dangerous chemical agents and is easily controlled with simple instruments. Thermal, chemical, and electrochemical method is simple and easily scalable. **Optical reduction** eliminates oxygen functionalities on GO by light exposure with photothermal or photochemical effects[154]. Various light sources have been used [155-159] for reducing and patterning GO simultaneously, to obtain rGO with different properties and functionalities[160-163], via masks or direct laser writing setups.

1.3.2.7 Epitaxial growth

Epitaxial growth deposits mono or multilayer defect-free graphene along the crystal phase of the host substrates (Ni[164], BN[165]) with carbon-containing gases as precursors, or form graphene layer by the sublimation of silicon from SiC at high temperature under vacuum atmosphere[166, 167]. The extreme conditions and the high cost of substrates limit these methods to high-end applications. Besides, organic molecules have been used to synthesise graphene ribbons, nanosheets, and quantum dots[154, 168, 169].

1.3.2.8 Laser-assisted production

Laser CVD growth. A laser can be used to replace the thermal heating source in the CVD process to synthesize graphene sheets[170], nanoribbons[170] or nano-matrix heterostructure[171].

Laser-assisted exfoliation. In this procedure, a high-energy laser beam illuminates highly oriented pyrolytic graphite (HOPG) continuously under a vacuum or inert gas atmosphere to produce monolayer or few-layer graphene flakes or films[172, 173]. Temperature control of the substrate can adjust the size and thickness of the graphene. When the laser irradiation of graphite happens in an aqueous medium, such as in nitrogen and water, graphene [174]or

graphene quantum dots[175] can be obtained. Laser ablation of graphite does not need stabilizers as in the liquid exfoliation process. It can produce graphene that can be suspended stably in water, since the thermal decomposition of water during the irradiation can introduce hydrophilic oxygen-containing groups onto the graphite flakes [176].

Flash graphene was proposed in 2020 by Tour's group as an eco-friendly, low-cost, mass-scale graphene production method [177]. Various precursors, including coal, petroleum coke, biochar, carbon black, discarded food, rubber tires and mixed plastic waste were converted to the so-called flash graphene (FG) with both turbostratic and wrinkled flacks via a flash Joule heating process[178]. The carbon-enriched materials were placed in a ceramic tube with two refractory electrodes on both sides; a high electrical discharge was generated from a capacitor bank, leading to a high temperature of 2700 °C, thus transforming the precursors into gram-scale graphene in less than one second. This approach produces graphene without using any solvents or reactive gases so it may be applicable for industrial purposes. For instance, FG was synthesized from plastic waste and only costs ~$125 in electricity per ton of plastic, proving a very affordable way to recycle and transform plastic into a more valuable material [179].

1.3.2.9 Production method introduced property changes

The production methods affect graphene's properties significantly. In electrochemical exfoliation and surfactant-aided liquid exfoliation strategies, the ions migrating from the solvent into the graphite layers can prevent the flakes aggregation. Ionic intercalants and (electro)chemical oxidation, could introduce additional defects to the graphene crystals or lead to oxidation and lattice distortions; the oxidation sides could promote the dispersing of graphene and subsequent functionalization of the electrode; the defects and lattice distortion can improve electron transfer process, which is important for faradic electrochemical sensing. The surface compositions and density of defects of rGO depend highly on the type of GO precursor and the reduction process. For example, the heating speed, final temperature and treatment time in the thermal reduction process; the types of reductants and reaction conditions in the chemical reduction process; the applied potential and electrolyte solutions in the electrochemical reduction process; the light wavelength and intensity in the optical reduction process.

1.3.3 Characterization techniques

1.3.3.1 Scanning electron microscopy

Scanning electron microscope (SEM) is a versatile advanced instrument widely used for non-destructive surface phenomena observation within the sample depth of hundreds of nanometers[180]. A focused accelerated electron beam is projected over the specimen scanning it in a raster pattern, and the high energy electrons (primary electrons) hit the sample surface and interact with its nucleus and electrons, emitting a variety of signals which are collected and processed to form an image. The secondary electrons and backscattered electrons reflect the morphology and topography of the specimen in the resolution of several nanometers, while the X-ray (photons) generated could be gathered for elemental analysis. It is worth mentioning that electron accumulation (overcharging) on the sample can lead to poor SEM image in case the sample is not conductive; to avoid this, the non-conductive samples need to be coated with a thin carbon, gold, or platinum layer.

1.3.3.2 Atomic force microscopy

Atomic force microscope (AFM) measures sample topography, based on the detection of the van der Waals interactions between a sharp tip (<10 nm) and sample surface at a narrow distance[181, 182]. It is used for the topographic characterization of various samples such as polymers, magnetic films, metals, glasses, semiconductors and even biomaterials since it does not require a conductive surface.

Mechanical, frictional, electrical, magnetic, and elastic properties of graphene-based materials can be investigated with different modes of AFM. For instance, it is possible to evaluate the layer number of the sheets, since graphene-based sheets have thicknesses from 0.34 to 1.2 nm.

1.3.3.3 X-ray photoelectron spectroscopy

X-ray photoelectron spectroscopy (XPS) is a surface qualitative /semi-quantitative analysis tool that can disclose materials' internal structural information in the depth of several nanometers (top 20 atomic layers of a material) [183, 184]. When X-rays with certain energies reach the sample, the electrons are excited and ejected from the sample surface at certain kinetic energies, which are detected and analyzed sequentially to obtain elemental composition, nature of bonding and even interactions such as spin-orbit splitting of the sample.

XPS is widely used for the determination of the oxidation grade of graphene by analyzing the C 1s and O 1s spectra [185]. The peak areas of C and O from the survey spectrum reflect the C/O atom ratio, which is in the range of 2-3 for GO, and could reach 40 for rGO[186-188]. The C 1s spectrum can be fitted with different components (C-C sp^2, C-C sp^3, C-OH, O-C-O, C=O,

COOH and π-π*, etc.), displaying the covalent bond percentages of the materials by integral areas. Besides, the π-π peak at ~ 290.5 eV can distinguish GO and rGO since it presents obviously in rGO while negligible in GO.

1.3.3.4 Raman spectroscopy

Raman spectroscopy is a fast, non-destructive, and high-resolution tool to identify mainly the vibrational modes of a molecular system (rotational and other low-frequency modes could be distinguished as well)[189-191]. Photons from the incident light (visible, near-infrared, or near-ultraviolet) interact with the molecular vibrations quantitatively, resulting in scattered light with red or blue shifts. The wavelength shifts are collected in a perpendicular direction to the incident light, giving information about the vibrational modes of the sample.

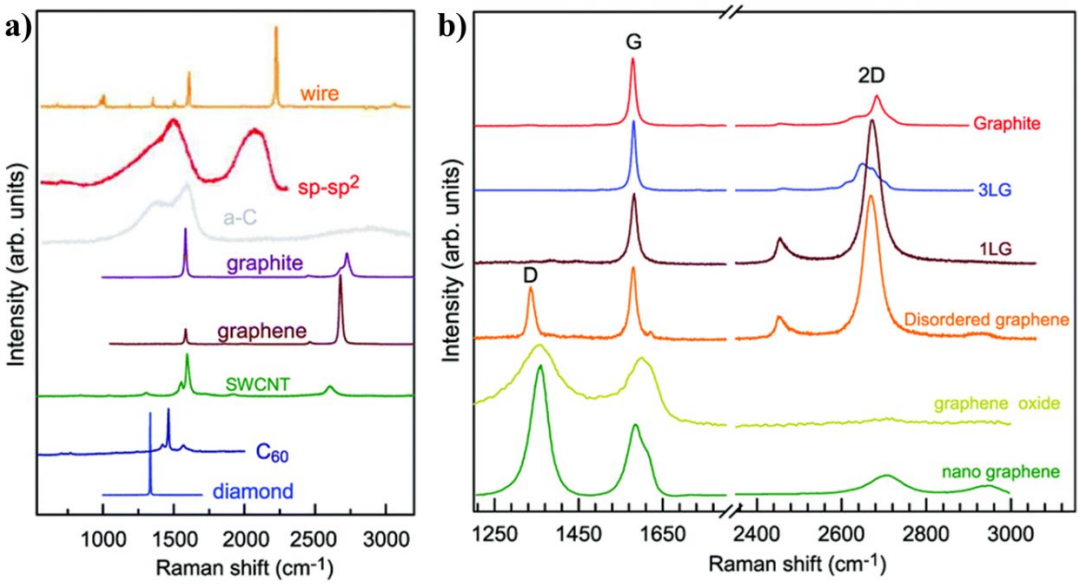

Figure 1.12 Raman spectrum of graphene-related materials. (a) 1D carbon wire, sp-sp2 carbon, amorphous carbon (a-C), graphite, graphene, single-walled carbon nanotubes (SWNT), C60, and diamond. (b) Graphite, 1-layer graphene (1LG), 3-layer graphene (3LG), disordered graphene, graphene oxide and nano graphene. Adapted from ref: (a)[192], (b)[193].

Raman spectroscopy has been used as one of the most fundamental techniques to investigate the properties of graphene-based materials, such as layer number, functional groups, orientation, quality of edges, doping and structure disorder, and to distinguish them from other carbon materials (Figure 1.12). Graphene-based materials typically consist of distinct bands at ~1350 cm^{-1} (D band), ~1580 cm^{-1}(G band) and ~2700 cm^{-1} (2D band). The G band appears due to the in-plane vibration of C atoms in the graphene lattice (stretching and bending of C-C bonds).

The defects and structural disorder generate collective in-plane vibration of atoms towards and away from the center of the hexagonal lattice, thus leading to the presence of the D band. Noticeable that there must be a D' band at ~ 1610 cm^{-1} when a strong D band presents. The peak intensity of both the D band and D' band is proportional to the quantity of defects present. A high concentration of defects will give a broad D' band; since close to the G band, it merges into the G band often. The peak intensity ratio between the D and G bands (I_D/I_G) is usually applied for graphene quality verification, and a lower value means fewer defects in the sp^2 hybridizing hexagonal network and vice versa.

2D, D+G (also refers to D+D'), and 2D' bands are weak Raman active bands at high wavenumber region (2500 cm^{-1}<2D<D+G<2D'), related to the structural organization of graphene[194]. The 2D and 2D' bands are the second order of D and D' bands respectively, and the intensity of both 2D and 2D' bands is contrariwise proportional to the number of defects since they are activated by two-phonon (with opposite momentums) assisted double resonant processes. The D+G band is only distinguishable when the concentration of defects is high. The intensity ratio between 2D and D + G (I_{2D}/I_{D+G}) bands, is a valuable parameter to determine the graphene's quality as well, for example, high I_{2D}/I_{D+G} indicates less defective graphene[195]. Besides, I_{2D}/I_G[196-198] can determine the doping states, and it equals 2 when referred to defect-free single-layer graphene. Moreover, the 2D band displays the layer number and states of graphene (Figure 1.12b). Single-layer graphene shows a single Lorentzian peak with a full width at half maximum (FWHM) of ~30 cm^{-1}. Adding successive layers of graphene causes the 2D band to split into several overlapping modes. Additionally, the mean domain size or inter-defect distance (La) of graphene could be evaluated by an empirical equation La (nm)= $2.4 \cdot 10^{-10}\lambda^4(I_D/I_G)^{-1}$[199-201], λ is the excitation laser wavelength (nm).

1.4 Rapid prototyping of graphene electrode by direct writing for electrochemical biosensing

In recent years the market of sensors and point-of-care tests showed remarkable growth, making cost-effective, large-area, and high-yield biosensor production in intensive demand. In this sense, rapid prototyping of devices is empirically required before commercialization. Rapid prototyping refers to various techniques for medium-throughput fabrication of a physical part or for patterning advanced architectures using two-or three-dimensional computer-aided design (CAD) designs[202-205]. It enables quick final product modification within minutes by

direct adjustment of the CAD design, without changing the fabrication process.

Direct writing (DW), also known as digital writing or digital printing, is one of the star techniques for device rapid prototyping and offered transformational changes towards the fabrication of smaller, faster and more efficient devices for daily use[6, 7, 206-208]. It is a group of maskless material deposition techniques for conformal patterning from nanometer to centimeter scale. A variety of materials could be processed, including metals, ceramics, dielectrics, polymers and even biomaterials. The resulting patterns have thicknesses ranging from less than one nanometer (single-layer 2D materials) to hundreds of micrometers. Due to its flexibility, scalability, dimension and material compatibility, DW has been exceptionally applied in numerous directions, expanding the boundaries of both materials and patterning fields.

There are various DW systems for precise, digital deposition of materials from 1D to 3D, such as inkjet printing[6, 7, 209], aerosol jet printing [142, 210, 211], 3D printing [210, 212], laser writing[91, 213], flow-based writing [206, 214], tip-based writing[206, 215, 216], and energy beam (ions and electrons)-based writing[217-219]. Based on the scope of the thesis, this section discusses the usage of the most matured or widely used DW technologies, namely inkjet printing and direct laser writing, for graphene electrode production.

1.4.1 Inkjet printing

Inkjet printing has attracted enormous attention in the past decades. It allows the direct, controlled, maskless and contactless deposition of materials onto rigid, flexible, and even deformable substrates [222-225]. The procedure is easy, and fast, and does not need a clean room or any particular conditions, with less material waste compared with any other printing technique. The flexibility, scalability, and variability enable its wide applications for the development of printed electronics [7, 226, 227], sensors [228-230], miniaturized power sources [231], tissue engineering [232, 233], and drug delivery[234].

1.4.1.1 History

Lord Rayleigh built a fundamental theoretical base for inkjet printing during his study of the formation of water drops from a continuous jet at the end of the 19th century[235, 236]. Following this, continuous inkjet printers were invented for high-speed, volume-controllable drop deposition[237-239], and soon drop-on-demand inkjet devices appeared [240, 241]. Until now, inkjet printing has been employed as a feasible solution for the deposition of various

materials on different substrates, which was reflected by the incremental trend of publications and market; in 2022 inkjet printing holds a market of $ 86.8 billion globally, and is expected to reach $ 128.9 billion in 2027[242].

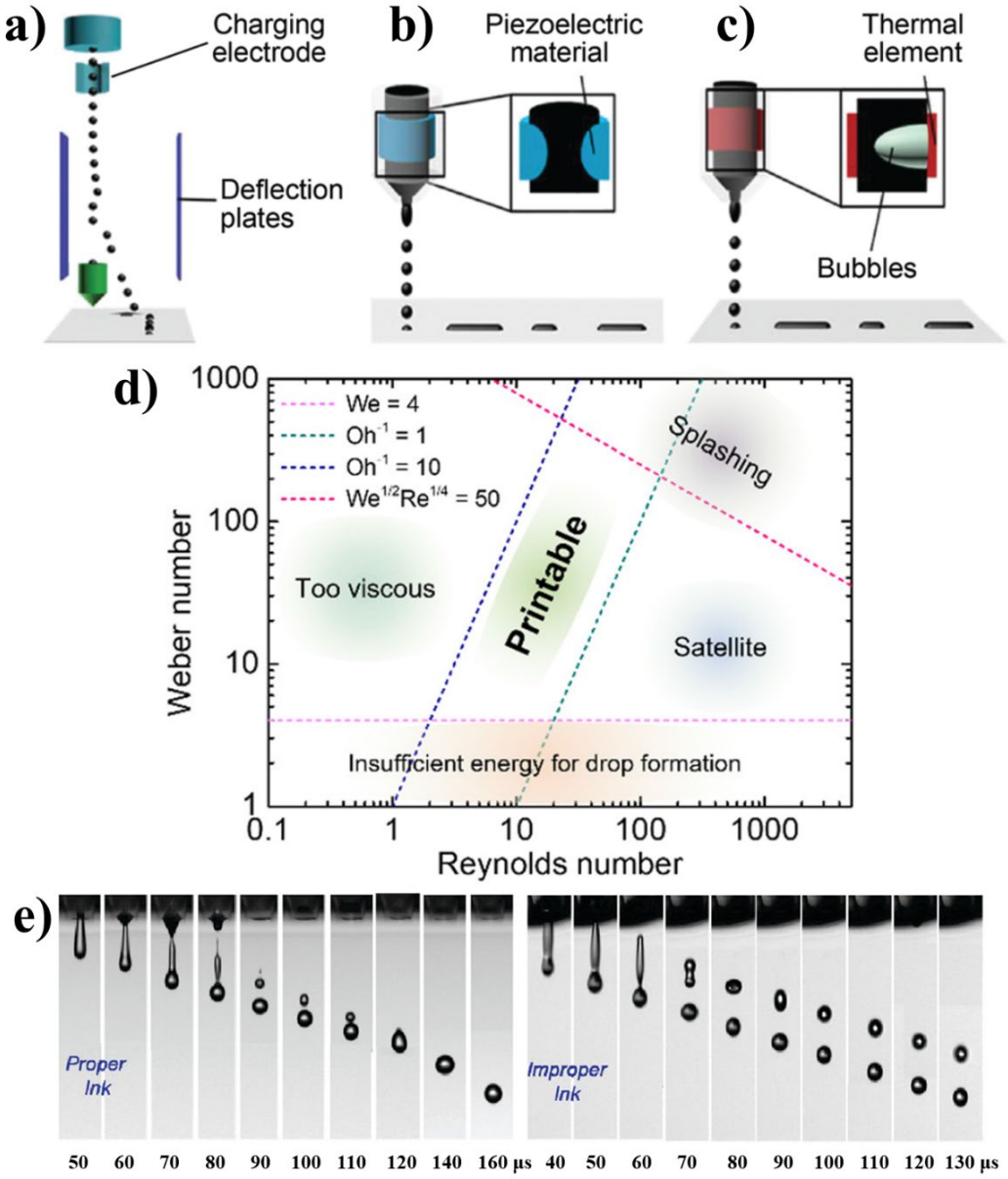

Figure 1.13 Schematic illustration of inkjet printing. (a) Continuous mode and drop-on-demand mode with (b) piezoelectric and (c) thermal printhead. (d) Rheological parameters and expected printability of inkjet inks. (e) The drop formation process with a perfectly round drop and a poor printing process with satellite drop formation. Adapted from ref: (a-c)[220], (d) [209], (e) [221].

1.4.1.2 Working mechanism

Inkjet printing can be classified generally into two groups, namely continuous inkjet printing (CIP) and drop-on-demand printing (DOD) (Figure 1.13a, b and c). CIP usually deposits droplets with a diameter of ~100 μm, which meets the resolution requirement of coding and marking applications in the industry; DOD printers jet fluids with drop diameter of 20-50 μm and are preliminarily applied in graphics and text printing [243]. In CIP[224, 244, 245], pressurized continuous ink flows are ejected through nozzles and break down into charged drops; then the drops go through an electric field and are deflected to intended places, generating a pattern on the substrates. The continuous mode leads to unnecessary drops being collected by a waste tank. Conversely, DOD printers [222-225] only jet droplets when/where needed, and is prominent for the small drop size and excellent placement accuracy. DOD printers contain a transducer for each nozzle, which applies pressure to the ink chamber and forces the ink droplets out of the nozzle. The transducer can be a piezoelectric crystal, which undergoes physical deformation, or a thermal heater, which generates air bubbles by Joule heating of the ink solvent [227, 243, 246], after receiving electrical signals. The ink solvents for thermal inkjet printers are usually water or short-chain alcohols since it has to be volatile to create proper air bubbles, while piezoelectric printers are compatible with a wider range of solvents. Note that, thermal heating may degrade the inks, especially if containing biomaterials. Therefore, piezoelectric DOD printers have been far more applied for custom material deposition[247-249].

1.4.1.3 Ink formulation requirements

Traditionally metallic nanoparticle/ metal precursor inks are printed for conductive traces[250, 251]; recently inks containing carbons, two-dimensional materials and polymers have been developing for the fabrication of various seniors[252-255].To pursue good printing quality, the inks need to be well-designed[256] based on the properties of the substrates, nozzle restrictions, and fluid rheological properties, such as density, surface tension and viscosity. Firstly, the average size of the dispersed pigments should be less than 1/50 (better 1/100) of the nozzle diameter, to avoid nozzle clogging; secondly, a low viscosity in the range of 4-30 cP is necessary to avoid a difficult ejection process; thirdly, the surface tension is suggested to be within 20-50 mN/m to keep a stream of droplets. Thanks to prolonged efforts by research communities, three-dimensional numbers have been defined to describe the relationship between nozzle diameter and rheological parameters of the ink, aiding a stable printing process.

These numbers include the Reynolds (**Re**), Weber (**We**) and Ohnesorge (**Oh**) numbers[257-260]. **Re** number is the ratio of inertial and viscous forces, which predicts the ink flow patterns; smooth, constant laminar flow occurs when viscous forces are dominant (Re < 2100); while turbulent flows, such as chaotic eddies and vortices appear when inertial forces are greater (Re > 3000). **We** number relates the inertia forces to the forces deriving from surface tension, which is used to analyze fluid flows, e.g., whether the droplet will be ejected or breakup. These were further elaborated to the **Oh** number, which doesn't take into consideration the drop speed, and is defined as the ratio between the Re number and the square root of the We number; but due to historical reasons, the Laplace number (**Z**) is used more frequently:

$$Re = \frac{\rho v d}{\eta} \qquad \text{(eq.1.7)}$$

$$We = \frac{\rho v^2 d}{\gamma} \qquad \text{(eq.1.8)}$$

$$Z = \frac{1}{Oh} = \frac{Re}{\sqrt{We}} = \frac{\sqrt{\rho d \gamma}}{\eta} \qquad \text{(eq.1.9)}$$

Where ρ is the density of the ink, v is the average drop velocity, d is the nozzle diameter, η is the viscosity and γ is the surface tension of the fluid.

For stable printing without satellite drop, Z should be between 1 and 10. Very high energy is needed to overcome the surface tension, to form a droplet for a highly viscous ink; low viscosity ink can lead to random drop sizes and satellite droplets; high surface tension increases the jetting energy and hinders the drop spreading on the substrate; ink leakage from the printhead, air-ingestion and blurry pattern may occur in case of low surface tension [261]. The formation, spreading and drying of drops have been studied in detail with different colloidal suspensions[262]. The printable range predicted by the fluid rheological properties is shown in Figure 1.13d. Figure 1.13e displays the drop formation process with a perfectly round drop and poor printing with drop separation[221]. Noticeably, these parameters for the ink formulation are recommended, but there has not been a well-established theory for perfect printing, and thus it relies on a try-and-error process based on the printers, inks and substrates.

1.4.1.4 Printers

Based on their usage fields and cost, inkjet printers can be broadly categorized as consumer-grade printers (CGPs) and high-end research-grade printers (RGPs). Generally, RGPs offer a

resolution of ~10s μm, while CGPs of ~50s μm. Many works related to RGPs have been reported due to their high accuracy and flexibility in custom material deposition, as evidenced by numerous studies [252-255, 263-267]. While the low cost and easy accessibility of CGPs, which cost hundreds of dollars compared to the 0.1 to 3 million US dollars of RGPs, make them an attractive alternative for cost-effective device fabrication. As a result, CGPs with different inks have been widely adopted for this purpose in various studies [204, 266, 268-273].

CGP prints much faster than RGP, resulting from the overwhelming nozzle number (more than~10s times of that for RGP); most RGP only can print one ink each time, and CGP could deposit 4-6 inks, giving the opportunity of depositing multiple materials simultaneously by replacing the original inks. However, consumer printers are customized for the inks the manufacturers supplied, and how the parameter settings affect the behaviors of ink deposition is unknown, hence it is quite challenging to fabricate inks that work for consumer inkjet printers. While RGP offers the choice of printheads with different jetting volumes[253], adjustable printing parameters (e.g., applied electrical signal and temperature), and visualization of ink droplet formation and drying process through the inbuilt cameras, thus far more appliable for custom material deposition. Since the office printer is determined for printing on paper and in some cases on discs of CD/DVD, it limits the substrate height in millimeter scale. While for RGP this can be tens of centimeter. Meanwhile, RCP is highly resistant to a variety of chemicals, including organic solvents of high dissolving power.

Abundant reviews have focused on printing with RGPs, while few of them talked about CGPs[252-255, 263-267]. Until now, a range of inks, containing AgNPs[274], Ti_3C_2/Ag hybrid [275], PEDOT: PSS[273], graphene [274, 276, 277], carbon nanotube [278], and biomaterials [279], have been deposited by CGPs on diverse substrates including paper, glass, silicon, plastics and bio-edible papers. For example, carbon nanotubes were printed on paper with CGP in 2006 (Figure 1.14a)[278]; AgNP and PEDOT: PSS films were printed on poly (ethylene terephthalate) (PET) substrate with a printer cost only 60 $[280]; Blom et al. demonstrated data-enriched (QR code) edible pharmaceuticals on potato starch substrate (Figure 1.14b)[270].

Except for the simple replacement of the genuine inks, as most works done with CGPs, only a few examples made modifications to the hardware and/or software. Mechanical modifications were introduced and showed multiple prints without smearing[268]. The results displayed improved printing accuracy up to 50 folds on different substrates (rigid, elastic, liquid, granular, and sticky). Microelectrodes were printed with carbon nanotubes by a customized inkjet printer

with a spatial resolution of ~12 µm, but lowest line width of 120 µm [281]. Figure 1.14c shows different patterns with various drop spacing, and even droplet overlapping can be observed. Waasdorp et al. reported a remarkable work in which single nozzle control of a CGP was realized by programming the command language of the printing driver[282]. The smallest drop has an average diameter of 62±6.9 µm with a volume of ~4 pL. The position precision reached 5.4 µm and 8.4 µm in the vertical and horizontal directions, respectively. Figure 1.14d shows the droplets with uniform size distribution.

The aforementioned works show the possibility that non-professionals could use a simple CGP to easily fabricate devices in their own homes.

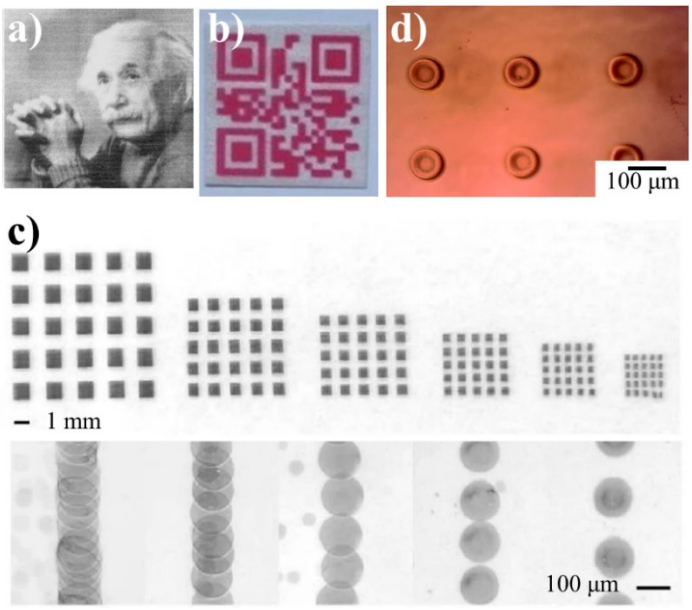

Figure 1.14 Patterns/devices printed with consumer-grade printers. (a) Scanned image of a photograph printed with carbon nanotube on paper. (b) Photo of a QR code printed on potato starch substrate. (c) Carbon nanotube patterns printed on a PET film and single-drop lines of carbon nanotubes with different spacing between drops. (d) Microscopy image of printed single droplets. Adapted from ref: (a) [278], (b) [270], (c) [281], (d) [282].

1.4.1.5 Coffee ring effect

The coffee ring effect (CRE, Figure 1.15a) is generally considered as a drawback for inkjet printing since it leads to inhomogeneous patterns. It is a phenomenon that happens frequently during the drop drying process; the solvent evaporates and induces a capillary flow which will carry the pigments from the interior toward the drop edge, resulting in a ring-like structure on the drop surface perimeter (Figure 1.15b)[283, 284]. CRE can be avoided in several ways: 1)

Enhancing the Marangoni flow induced by surface tension gradient. It replenishes fluid from the edge to the center [285, 286]. Water drop has a weak Marangoni flow [287], and can be promoted by mixing or replacing water with other solvents (usually organic solvents) [288]. Based on this, Hu et al. proposed a universal ink formula (Isopropanol:2-butanol, 1:9 in volume) to print various 2D materials with uniform drops (Figure 1.15c) [284]. 2) Adjusting the evaporation temperature [289, 290]. 3) Surface treatments of the substrates with ultraviolet light, plasma or chemical reagents. E.g., hexamethyldisilane was used to decrease the surface energy of the SiO_2 plate to obtain homogeneous graphene deposition (Figure 1.15d) [276]. Park. et al. revealed that O_2 or Ar plasma can change the diameter of printed silver dots (Figure 1.15e) [291]. 4) Adding surfactants. They can modify liquids' surface tension, and aid the dispersing of materials [245, 292, 293]. The evaluation of how the concentration of surfactant can affect the solution's surface tension is helpful, as the work done with SDC by Richard et al [294].

In addition, waveform, drop spacing, distance between the substrate and the print head, surface energy and topology of the substrate, and the affinity between the ink and substrate are important factors to obtain good printing and final patterns as well[252-255].

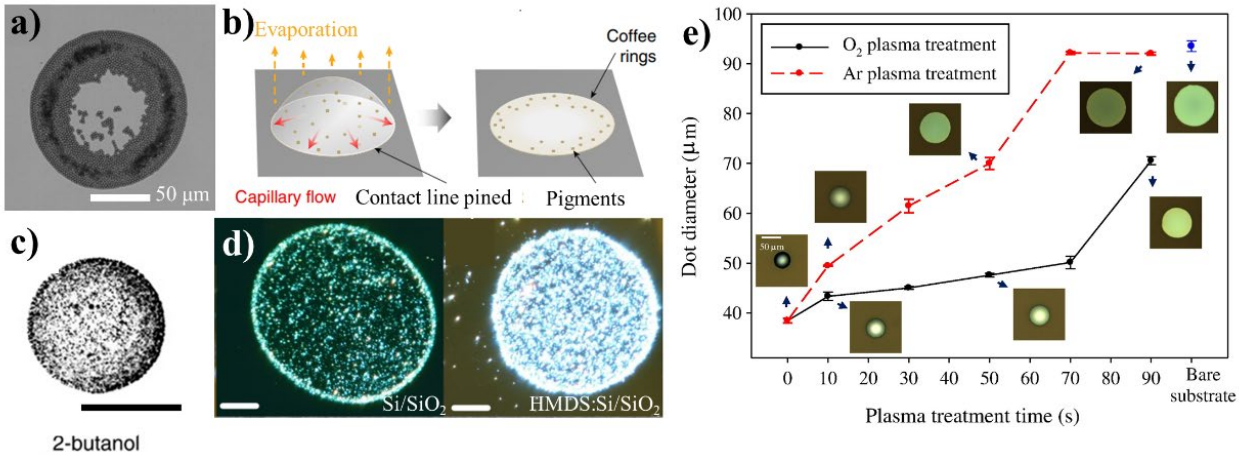

Figure 1.15 (a) Coffee-ring effect displayed by a dried particle-containing colloidal drop. (b) Coffee ring formation process. (c) A dried inkjet-printed droplet on clean glass with MoS2 suspended in isopropanol and 2-butanol mixture; scale bar 50 µm. (d) Microscope pictures reflecting much more uniform graphene distribution within a dried drop on hexamethyldisilane modified silicon. (e) Inkjet-printed silver with diameters as a function of O2 or Ar plasma treatment time. Adapted from ref: (a) [262], (b and c) [284], (d) [276] and (e) [291].

1.4.1.6 Substrates

Inkjet printing can be performed on various substrates including rigid, flexible, or stretchable materials, depending on the requirements of the specific application. Mechanical properties, thermal stability, chemical resistance, and biocompatibility/biodegradability should be taken into account when selecting a suitable substrate. To achieve good wettability and adhesion, the substrate's surface energy should be 7-10 dynes/cm higher than the surface tension of the ink[295]. Substrates such as Si/SiO_2 and glass are commonly used when high-temperature post-printing treatments are required. Plastics such as polyethylene terephthalate (PET), polyethylene naphthalate (PEN), polyimide (PI), polyurethane (PU), polycarbonate (PC), polypropylene (PP) and polyvinyl alcohol (PVA) are still the most commonly used substrates for printed electronics due to their low cost, flexibility, and transparency[258]. However, their low glass transition temperature and poor thermal expansion coefficient limit their use in high-temperature applications. Note that PI could withstand temperatures above 350 ºC, but not suitable for optical based applications due to its low optical transparency[296]. Papers are an eco-friendly and biodegradable option for substrate materials, but they suffer from poor heat and chemical resistance. Treatment of paper with certain chemicals or coating with polymers and ceramic nanoparticles can improve its surface properties, enhancing the functionality of the final devices [251]. Textiles hold the merit of comfort and compatibility with human skin, hence suitable substrates for wearable electronics, showing promise in the fields of energy production/storage, tactile sensors and health monitoring kits [256]. The excellent biocompatibility and stretchability of PDMS films have facilitated their usage for flexible electronics and biosensors[297]. Porous substrates can absorb the solvent of inks, control the drop spreading and hinder or even eliminate the coffee ring effect. The inks display higher affinity towards the porous substrate, are less prone to form cracks under substate deformation, and often show improve conductive compared to that deposited on flat surfaces[251, 298]. Recently, starch, hydrogels, tattoo paper, parchment paper, and bacterial cellulose have emerged as novel substrate materials for smart device fabrication [251, 279, 299].

1.4.1.7 Sintering

Sintering (or curing) is a necessary post-printing process that typically involves evaporating the ink solvents, removing additives, and binding the material together to achieve good conductivity of the printed patterns. Thermal sintering, which usually involves temperatures of 200-350°C for 10-20 minutes [258], is a simple, inexpensive method that can be applied for

large-area and batch processing, making it the most common and widely used strategy, particularly for metallic nanoparticle inks. However, this method is generally not suitable for flexible substrates (such as paper, plastic, and fabrics) due to their low thermal resistance. To overcome this limitation, efforts have been made to develop inks that can be cured at low temperatures, such as AuNP ink sintered at 100°C [300]. Additionally, some low-temperature curable inks are now available on the market, including DryCure Au-J (AuNP ink, curable at 100-250°C, C-INK Co., Ltd), JS-A102A (AgNP ink, curable at ~120°C, Novacentrix Co., Ltd), and Sicrys I40DM-106 (AgNP ink, curable at ~120°C, PV Nano Cell Co., Ltd). Photonic sintering has been demonstrated to be an excellent alternative to thermal sintering, as it can achieve spatial photochemical and/or photothermal effects with lamps, lasers, and flash/pulse light, thereby minimizing thermal damage to the substrate [251]. Chemical sintering involves removing the protective or insulating layer of the nanomaterials by chemical agents and can be applied to heat- and intense light-sensitive substrates, although the chemicals used may be toxic and extra washing steps are needed to remove the residues [251, 301]. Microwave [302], plasma [303], and electrical (Joule heating)[304] sintering have also been used to produce highly conductive traces[253].

1.4.2 Inkjet printing of graphene electrode-inks

The recent advances in graphene printing have facilitated the cost-effective, large-area, and high-yield mass production of electrochemical biosensors for various practical applications[129, 305, 306]. Particularly, inkjet printing endows high design freedom for graphene-based devices and maintains the great electrochemical performance of graphene. The nanosheet-based structure, with its large surface area, ensures higher surface coverage of the ink on the substrate. Additionally, two-dimensional contacts (rather than point contacts, as in the case of nanoparticles and nanowires) with low contact resistance form in a layer-by-layer fashion due to the capillary force between adjacent graphene sheets, resulting in low barrier density and low height of the connections.

Various graphene synthesis methodologies have been introduced in section 1.3.2, from bottom-up growth to top-down reduction/oxidation and exfoliation; this offers plenty of choices for the graphene ink formulation.

1.4.2.1 Graphene inks

The choice of solvent plays an important role to form graphene dispersions and it depends

significantly on the compatibility of the solvents against the substrate and application scenarios of the devices[307]. A number of solvents are used for graphene ink preparation, such as N-methyl-2-pyrrolidone (NMP), N, N-dimethylformamide (DMF) and dimethyl sulfoxide (DMSO), terpineol, ethanol, isopropanol, ethylene glycol, glycerol, ethylene acetate and deionized water[7, 258, 292, 308-310]. General properties of various types of substrates and solvents have been listed in literature [220, 249, 311].

A comparative study was carried out for inkjet-printed flexible electronics with graphene dispersed in ethanol, DMF, and NMP, and transparent conductive film was demonstrated (Figure 1.17a)[312]. After annealing at 350 °C for 150 min, a sheet resistance of 260 Ω/sq was obtained with a thickness of 160 nm. Although DMF, NMP and DMSO are commonly used, as listed in reference[313], the high boiling points (>150 °C) of these solvents require high-temperature post-printing treatments; this hinders the printing on temperature-sensitive substrates. Moreover, the high cost and the toxicity, make them unfeasible for wide, practical use. Thus, researchers are making effort to replace them with more volatile, eco-friendly alternatives such as water, short alcohols and ketones[313, 314].

Parvez et al. inkjet printed water-based graphene inks on glass slides, in which graphene flakes were electrochemically exfoliated [185]. The ink was stabilized with pyrene sulfonic acid sodium salt and annealed at 300°C for 1 h, yielding a high electrical conductivity of 3.91×10^4 S/m. The ink remained stable for one month with a high graphene load of 2. 25 mg / mL, but 5-day sonication was needed to prepare the ink. The dots in Figure 1.16 b and c indicated a uniform graphene distribution after sintering and the minimum features could reach 20 μm (Figure 1.16d**)**. In another work a universal ink formula was proposed, consisting of propylene glycol and water (by mass, 1:10), ≥0.06 mg/mL Triton x-100 and ≥0.1 mg/mL xanthan gum[315]. Water-soluble single-layered graphene oxide (GO) and few-layered graphene oxide (FGO) inks (Figure 1.16e) have been demonstrated with high-quality patterns on diverse flexible substrates, including paper, PET and PI [277]. Figure 1.16f displays a portrait printed on normal office paper with FGO ink. To avoid the high-temperature annealing process, a water-based graphene ink was developed and it reached low sheet resistance of 30 Ω/sq without long-time high-temperature treatment (5 min annealing at 100 °C**)** and the transparency of different layers of printing was investigated (Figure 1.16g) [316]. Although water is the most preferred solvent due to its non-toxic nature and low boiling point, the high surface tension (72.8 mJ/m^2) is not favorable for stable inkjet printing without additives.

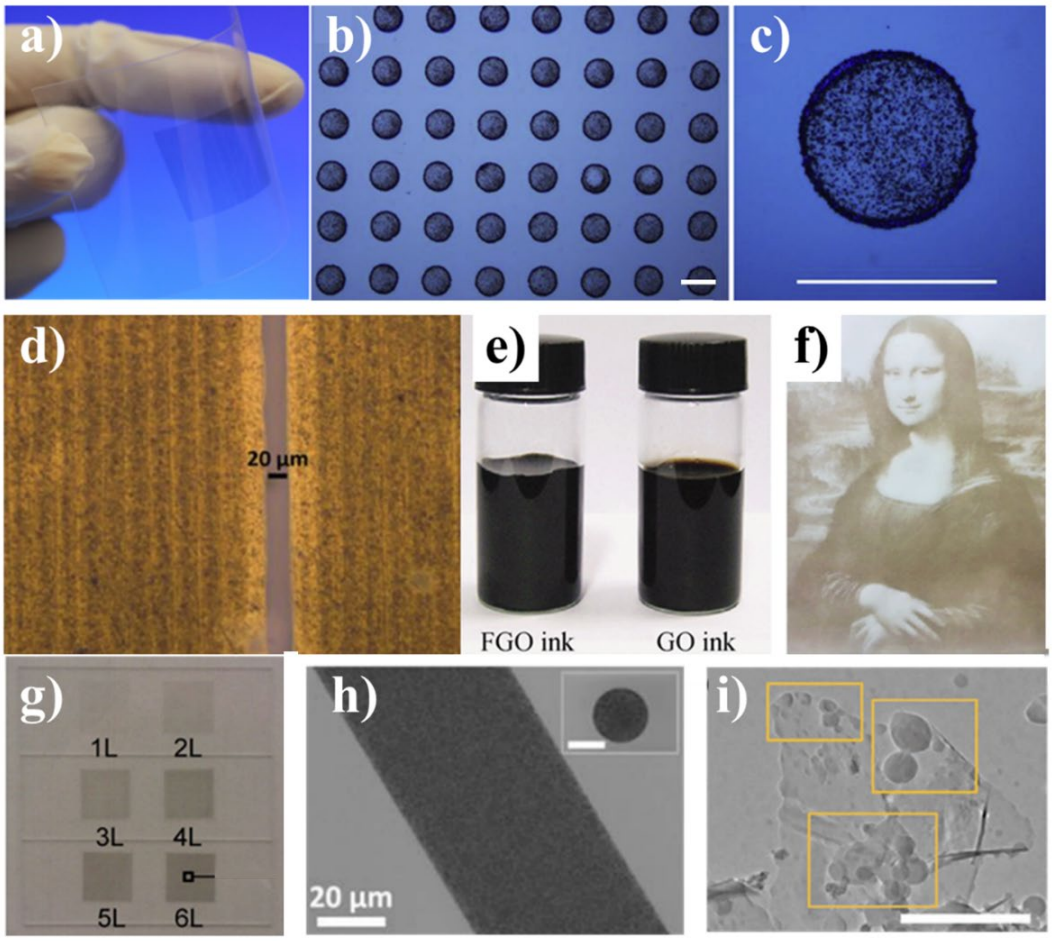

Figure 1.16 (a) Graphene transparent conducting films printed on a plastic substrate. (b) Microscopy picture of an array of graphene dots printed on Si/SiO_2 substrate. (c) Magnified image of a single dot; scale bars in both (b) and (c) are 50 µm. (d) Two printed graphene contacts with a gap of ~20 µm on PEL P60 paper. (e) Stable inks made of single-layered graphene oxide (GO ink) and few-layered graphene oxide (FGO ink). (f) A portrait printed on normal office paper with FGO ink. (g) Photograph of printed graphene films with various printing layers (from 1 to 6). (h) A single-drop line and a drop (inset, scale bar, 40 µm) illustrate the uniformity of the printed features. (i) TEM image of graphene-quantum-dot stabilized graphene nanosheets. The scale bar is 500 nm. Adapted from ref: (a) [312], (b-d) [185], (e and f) [277], (g) [316], (h)[317], (i) [318].

Solvent mixtures, such as terpineol /cyclohexanone [317, 319, 320], isopropanol /polyvinylpyrrolidone [321] and glycol/water [276], are promising alternatives to overcome the problem of unsuitable surface tension from small molecule liquid**.** Figure 1.16h shows highly uniform tracks printed with graphene suspended in terpineol /cyclohexanone [317]. Torrisi et al. produced a stable ink by liquid exfoliation of graphene in NMP in 2012, which was

suspended in a mixture of ethylene glycol and water, and the ink was applied for the fabrication of graphene-based transistor for the first time with good conductivity and transmittance[276]. The work also probed inkjet printing under inappropriate jet parameters (graphene in water with Z = 24). In another case, GO dispersed in water/ethanol / ethylene glycol (1: 1: 1) mixture was inkjet-printed onto PET, followed by intense pulsed light reduction with a xenon lamp to gain patterns with low resistance and good flexibility [322]. A comparative study was performed to inspect the effects of solvent mixtures, including DMF: xylene, DMF: toluene, DMF: ethanol, and DMF: acetone [311]. The graphene ink suspended in mixture of DMF: ethanol showed a higher degree of stability and wettability, and 5% enhanced conductivity. A similar study was demonstrated with mixtures of water (DI): ethylene glycol (EG): glycol (G), isopropyl alcohol (IPA): EG: G, and DMF: EG: G [274]. It revealed the ink prepared in DMF: EG: G solutions had better wettability, electrical conductivity, and higher stability.

Additives are frequently used to stabilize graphene inks through π-π stacking, van der Waals forces, hydrogen bonding or electrostatic activity [209, 323], to overcome the dispersing difficulties of graphene into water, resulting from the hydrophobic nature of graphene. Ethyl cellulose is one of the starting and commonly used materials to improve the stability of graphene inks [143, 319, 324]**.** Surfactants are widely applied to adjust the surface tension of the ink and to stabilize the dispersing of graphene. A comparison of the influence of a range of surfactants was conducted for the preparation of graphene inks, including 8 ionic surfactants, and 4 non-ionic surfactants[142]. The results showed all the surfactants can stabilize the graphene inks, while the best ones were sodium dodecyl sulfate (SDS) (0. 011 mg/mL) and sodium cholate (SC), (0. 026 mg/mL). In this work, UV–vis absorption spectroscopy was proposed for the concentration estimation of the inks. A detailed investigation displayed that graphene ink with 0.3 wt.% of SDS showed the best performance for printed electronic applications [325]. Natural-based surfactants such as gum arabic, cellulose nanocrystals and alkali lignin have been applied for graphene ink production [326]. Graphene quantum dot (GQD) was investigated by Zeng et al. to improve the stability of graphene inks (Figure 1.16i)[318]. The GQD works as a surface tension modifier and stabilizer by π-π interactions between graphene and GQD. In addition, biomaterials, such as BSA [327], have been used as stabilizers as well.

1.4.2.2 Graphene hybrid inks

Despite the remarkable advantages, pure graphene-based inks suffer from poor conductivity,

which confines their wide-range applications [292]. In this sense, hybridizing graphene with metallic nanoparticles or conductive polymers, such as poly (3,4-ethylenedioxythiophene) poly (styrene sulfonate) (PEDOT: PSS) and polyaniline (PANI), poly pyrrole (PPy), are great choices[328-330].

Silver nanoparticle inks are dominant among metal-particle-based conductive inks for printed electronics due to their excellent electrical conductivity and easy access to the market[331-333]. Wang et al. [334] inkjet printed graphene/Ag nanoparticle (Ag NP) hybrid inks on polyimide sheets and gained a low resistivity of 4.62×10^{-4} Ω/m after annealing at 300 °C for 40 min. Pan et al. [335] formulated graphene/Au NP inks for electrochemical detection of bisphenol A. Ag@Au nanocore-shell nanotriangle platelets decorated GO sheets were also prepared for inkjet printing and displayed stable sheet resistance of ~ 149.5 Ω/sq after reduction with hydrazine at 110 °C for 3 h[301].

PEDOT: PSS possess high conductivity, transparency, stability and good biocompatibility; thus is an attractive material for electrochemical biosensing. Liu et al. compared graphene ink, graphene/Ag NP hybrid ink and graphene/PEDOT: PSS hybrid ink, showing that the last ink presented better stability and surface conductivity [336]. PANI/graphene inks were formed in the presence of SDBS under probe-sonication, and conductive patterns (846 Ω/sq) were realized by annealing at 80 °C for 2 h [337].

In summary, the integration of conductive additives not only could prohibit aggregation of graphene flakes in water, improving the stability of the ink, but also can increase the conductivity of the printed patterns. AgNP/graphene hybrid inks have the advantage of being low-cost, lightweight, and transparency, thus appliable for conductive circuits; on the other hand, the good biocompatibility of graphene, gold and polymers, enables their hybrid inks promising application in biosensing.

1.4.3 Electrochemical (bio)sensing applications of inkjet printed graphene electrodes

The bio-functionalization of graphene with different biomaterials, such as enzymes, aptamers, antibodies, and DNA sequences could facilitate diverse biosensor development for diseases diagnostic[338-340], bacterial detection [3, 341], and cell activity monitoring [341, 342], *etc.* [343-349]. As introduced above, inkjet printing is prone to fabricate analytical platforms based on graphene electrodes, although the research focus is more towards flexible electronics other

than biosensing[256, 258, 292, 336, 350].

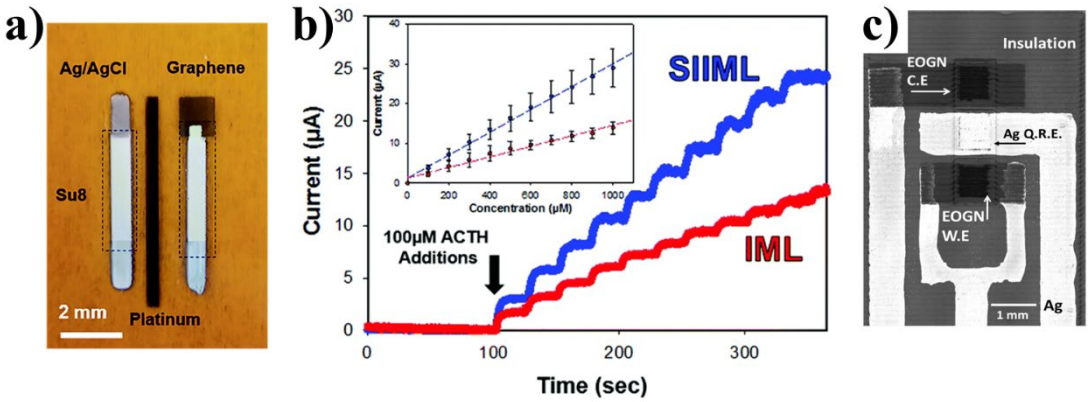

Figure 1.17 (a) A fully inkjet printed three-electrode system, which consists of a multilayered graphene working electrode, a platinum counter, and a Ag/AgCl reference. (b) Sensitivity test of ACTH on graphene electrodes fabricated by salt impregnated inkjet maskless lithography (SIIML, blue, 28.3 μA/nM) and inkjet maskless lithography (IML, red, 13.3 μA/nM); inset, current versus concentration. (c) Microscope image of the fully printed bacteria sensor. Adapted from ref: (a) [351], (b) [352], (c) [353].

Twinkle et al. built a fully inkjet-printed three-electrode system on a PI substrate (Figure 1.17a) for pH and ferric/ferrocyanide sensing[351]. The graphene working electrode displayed repeatable electrochemical performance and sheet resistance even after over 1000 bend cycles.

Graphene nanocomposites can be advantageous to electrochemical sensing. Ti_3C_2/GO nanocomposites were inkjet-printed to fabricate a H_2O_2 sensor, which kept the biological activity of the enzyme and showed a dynamic range of 2 μM-1 mM with a LOD of 1.95 μM [354]. Graphene/polyaniline nanocomposite was inkjet printed to modify screen-printed carbon electrode (SPCE), for detection of polyphenolic antioxidants; compared with the bare SPCE, the modified electrode showed 2-4 times higher electrochemical sensitivity [355].

The post printing treatments can affect the characteristics of the inkjet-printed graphene electrodes and thus their sensing ability. Suprem et al. demonstrated that UV treatment could improve the conductivity of graphene and introduce 3D petal-like nanostructures into the printed planar rGO, which facilitated the electrochemical performance, showing a sensitivity of 3.32 μA/mM and a response time of <5 s towards H_2O_2[358]. John et al., patterned graphene electrode by inkjet printing of a polymer as scarifying layer and formed porous graphene films with salt as scarifying templated[352]. The electrode showed three-ordered improvements in conductivity and enhanced sensitivity to acetylthiocholine (ACTH) compared to the non-

porous graphene electrode (Figure 1.17b).

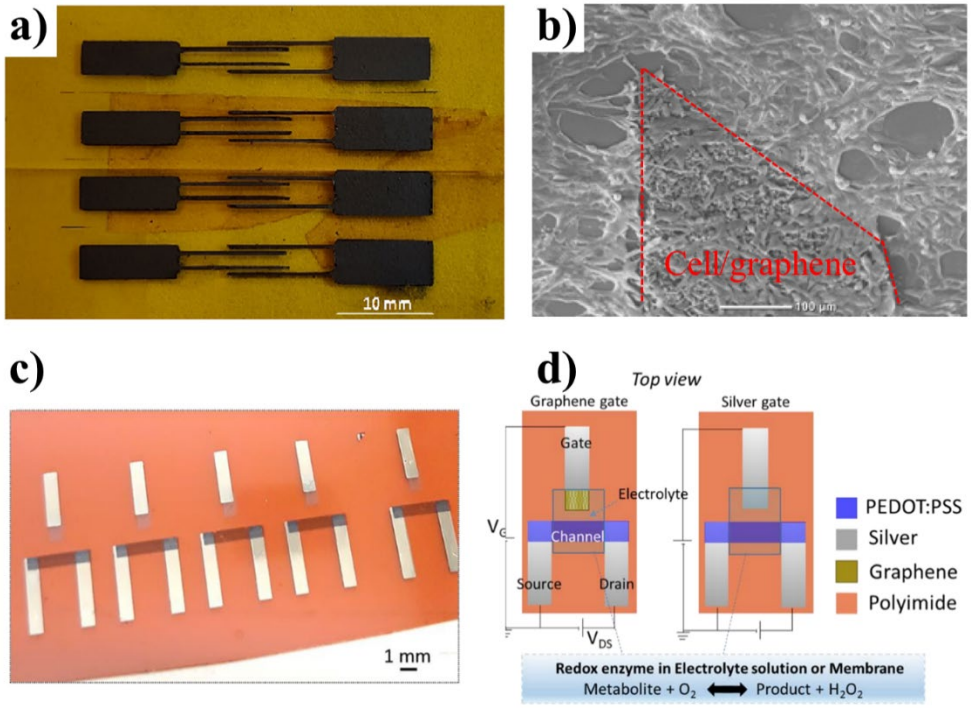

Figure 1.18 (a) Inkjet-printed graphene microelectrodes. (b) Adhesion of N27 cells on a graphene microelectrode tip. (c) Photo of the OECTs with graphene gates. (d) Top-view schematics of a graphene-gated OECT and a silver-gated OECT, showing the materials, the simplified enzymatic reaction, and the bias applied during testing. Adapted from ref: (a, b) [356], (c, d) [357].

Cells can be monitored with inkjet-printed graphene microelectrodes. Bhawna et al. formulated a highly concentrated edge-oxidized graphene nanosheet (EOGN) ink (30 mg/mL) in a solvent mixture of NMP and propylene glycol, with optical annealing a fully inkjet-printed electrochemical sensors was obtained for living bacterial detection (Figure 1.17c)[353]. Amir et al. [356], monitored neural cell activities on time by EIS (Figure 1.18a and b); the graphene microelectrode showed great biocompatibility, offering suitable attachment sites for the cell network; and the microelectrode arrays showed good sensing performance and were capable of multiplexed detection of cellular activities in minutes.

A graphene FET was assembled on flexible PI by inkjet printing for infectious pathogen detection [359]. Fully inkjet-printed graphene-gated organic electrochemical transistors (OECTs) were also demonstrated on polymeric foil for the enzymatic-based biosensing of glucose (Figure 1.18c and d)[357].

1.4.4 Direct laser writing

1.4.4.1 Working mechanism

Direct laser writing (DLW) is an easy, efficient, low-cost, eco-friendly and maskless method to simultaneously produce and pattern electrodes without any catalysts or harmful solvents [154, 157, 158, 207, 349, 360]. DLW is usually performed by a laser machine, which works in a "2D printing mode" with a focused laser beam as a "print nozzle", like a DOD inkjet printer. In the DLW process, a laser beam irradiates the samples, and donates high-energy photons, which interact with the electrons of the material, thus leading to various reactions by photochemical and/or photothermal effects[156, 361, 362]. The samples can be site-selectively heated (>1000 °C), with superfast temperature changing speed (10^6-10^{12} °C/s) [157].

1.4.4.2 Laser processing parameters

The properties of the resulting materials can be fine-tuned by varying the parameters of the laser source. In addition, the pressure, temperature, and surrounding atmosphere during laser exposure also have an impact on the resulting samples.

Wavelength determines how the light interacts with the material, such as the degree of reflection, absorption, transmission, and beam penetrating depth[363-365]. In general, infrared lasers are used for localized heating by photothermal effect with a penetrating depth of 1-100s micrometers. The thermal conductivity and the surrounding atmosphere govern the heat dissipation within the sample, and affect the material near the irradiated region. Although the penetration depth of ultraviolet light is lower (10s to 100s nanometers) [154], the relatively high energy photons enable it a good tool for material ablation. Wavelength also regulates the resolution of the final pattern, and it is confined by the diffraction limit [154], which is half of the wavelength. In fact, the dimension of the final pattern is much larger than that due to the heat dissipation towards the non-irradiated area. For instance, DLW has been shown to produce minimum graphene lines of approximately 12 μm under a 405 nm laser, 50 μm under an ultraviolet laser, and 60–100 μm under infrared lasers[366, 367].

Laser power represents the quantity of energy that the laser generates in the time unit, and it is a time-averaged value. Often a pulse laser works at constant pulse energy with different pulse widths and frequencies. Figure 1.19a displays the relationship between laser power and pulse frequency for a commercial 355 nm diode-pumped solid-state (DPSS) laser [154]. The slope of the curve stands for the value of pulse energy and it remains constant (~200 μJ) up to ~90

kHz. Thus, the laser power can be solely a consequence of different pulse frequencies and does not reflect the instantaneous energy interaction between the laser and the sample.

Pulse width (or duration) is the quantity of time that the laser beam interacts with the sample. There are numerous commercial laser devices with specific pulse widths (milliseconds to femtoseconds), except for continuously emitting lasers, which exit laser with an infinite "pulse width". Figure 1.19a shows average laser powers less than 20 W, but the instant power can reach 5 kW, when the laser pulse was 20 ns (nominal pulse width)[154]. Therefore, pulse width plays an important role in laser scribing applications, especially when using ultrafast lasers, like femtosecond lasers.

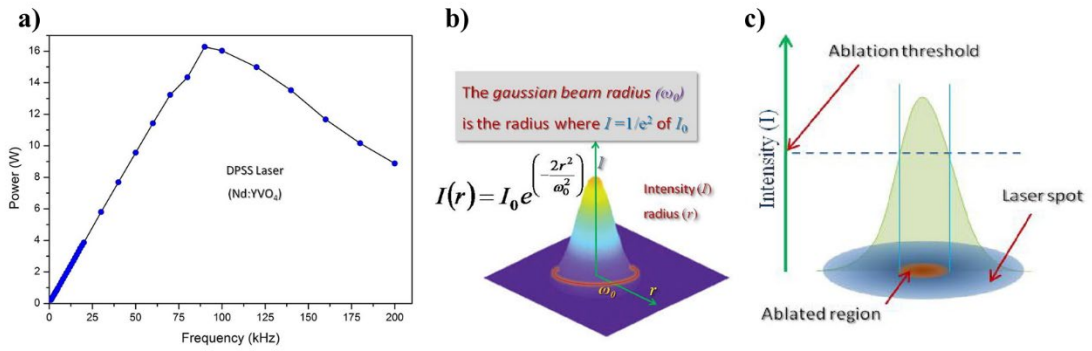

Figure 1.19 (a) Laser power as a function of pulse frequency for a commercial laser. (b) Gaussian beam profile and the equation of beam intensity vs. radial position. (c) An illustration shows that a pattern smaller than the spot size can be obtained when the ablation energy threshold is at a proper place on the Gaussian beam profile. Adapted with permissions from reference[154].

Writing speed of the laser affects the interaction time between the beam and the sample, and thus the resulting product.

Laser fluence is the energy density of the irradiated area [368], which can be adjusted by alternating the pulse energy or beam spot size. Since most commercial lasers have constant pulse energy, changing the beam spot focus is much easier, and could be done with splitters, filters, pinholes, polarizers and wave plates.

Beam energy profile. The majority of lasers possess a circular cross-section and a Gaussian beam energy (Figure 1.19b) profile[154, 369, 370], leading to a much higher intensity at the center than at the edge. Laser fluence is an average of the energy density of the laser spot; thus, it is possible to obtain patterns smaller than the minimum theoretical spot size by taking

advantage of the ununiform energy distribution (Figure 1.19c). Excimer lasers are an exception, since it exhibits rectangular beam cross-section and an almost constant beam energy profile with uniform energy density.

Number of lasering repetitions could influence the properties of the resulting materials. For example, the reduction degree of GO reached a maximum after 5-time lasering steps with an infrared laser (λ = 788 nm, 5 mW, embedded in a standard LightScribe)[371]. Yieu et al. produced graphene from a list of materials through a two-step laser scribing process (CO_2 laser)[158]. The first laser irradiation converted the precursors into amorphous carbon, and the following lasing further transformed the amorphous carbon into graphene.

Cutting/engraving

Laser cutting and engraving are two different processes. Cutting involves the local evaporation of material under laser irradiation, while engraving is controlled cutting to a certain depth[372]. Cutting is typically done using vector files and is faster than the raster printing process used for engraving. Laser engraving can be achieved with lower laser power or using a shorter focal length lens for finer spot size and higher patterning quality. In contrast, a longer focal length lens is more tolerant of focus height variations and produces less taper in the cut edge [373].

1.4.5 Direct laser written graphene

Three-dimensional (3D) graphene-based materials [157, 207, 374] feature interrelated porous networks, good chemical and thermal stability, and a large active surface area, making them excellent electrode materials for biosensing. The high surface area supports the immobilization of bioreceptors, and the highly porous structure with abundant defect sites is advantageous for efficient electrolyte transportation and charge transfer.

Conventional CVD has been extensively used to produce 3D graphene foams, in which graphene is first grown on a porous template at high temperature, and the template is subsequently etched away. However, the high-temperature requirement and high cost limit its mass-scale production[375-377]. Self-assembly of GO with a subsequent reduction process to improve its conductivity is a scalable and cost-effective way to form 3D graphene structures [378-380]. The reduction can be achieved by chemical, thermal, and solvothermal methods [124, 125, 181, 381]. However, these methods suffer from poor control over the shape of the 3D graphene and have long synthesis routes. Moreover, often extra depositing and patterning processes are needed to fabricate graphene electrodes on the substrate.

Recently, many researchers have reported notable results in synthesizing graphene-based materials with dots (in the micro-scale), lines, planar, and hierarchical structures (quasi 0D to 3D structures) by direct laser writing (DLW) [207, 349, 382-388]. The DLW process not only produces graphene but also enables the patterning of the electrode. Under sufficient laser energy, the functional groups on GO can be eliminated to restore the graphene lattices, and carbon-containing precursors can be graphitized into turbostratic arrangement graphene flakes. The layer numbers, reduction degree, and physical, chemical, and electrical properties of the obtained graphene can be adjusted by manipulating laser parameters, modifying the precursor, and changing the laser environment[176, 198, 389-391].

Moreover, heteroatom-doped porous graphene can be formed by adding additives into the precursor, and metal/metal oxide nanoparticles could also be embedded into the graphene complex. These features endow direct laser-written graphene with great potential for practical use in gas sensors[382, 383], micro supercapacitors[384, 385], field effect transistors (FET) [392, 393], transparent circuits[394], and biosensors[207, 349, 386-388].

1.4.5.1 Laser reduced graphene

GO is one of the most commonly used precursors for producing reduced graphene oxide (rGO) electrodes through direct laser writing (DLW). Typically, a free-standing or substrate-supported GO film is first formed through methods such as drop casting, spray coating, spin coating, vacuum filtration, or inkjet printing. Under laser irradiation, oxygen-containing groups are partially eliminated, restoring the graphene hexagonal network while also introducing new defects such as vacancies, resulting in rGO electrodes with varying properties. The physical, (electro)chemical, and electrical properties of the resulting rGO depend strongly on the quality of the GO (e.g., morphology, concentration, and oxidation degree) and the laser parameters.

In 2010, Sokolov et al. reduced graphite oxide through continuous laser irradiation (532 nm) in both air and a nitrogen atmosphere[395]. In the same year, reduced graphite oxide micropatterns with stable conductivities were produced through DLW using a femtosecond laser (790 nm) [396]. Later, the reduction of GO to graphene through picosecond pulsed laser exposure (1064 nm, 10 ps, 100 kHz, 50 mW) was investigated, and dynamic modeling showed the temperature distribution of on the 300 nm thick GO film, up to 1400 °C on the surface and 600 °C inside [397].

In 2011, Wei et al. fabricated microscale supercapacitors through DLW of free-standing hydrated GO films obtained through vacuum filtration [384]. The unreduced GO film not only

separates the rGO electrodes but also serves as the electrolyte since GO is dielectric and its oxygen-containing groups are good ionic conductors. A similar approach was taken by Kumar et al. in 2019 with a nanosecond ultraviolet laser (λ = 355 nm)[385].

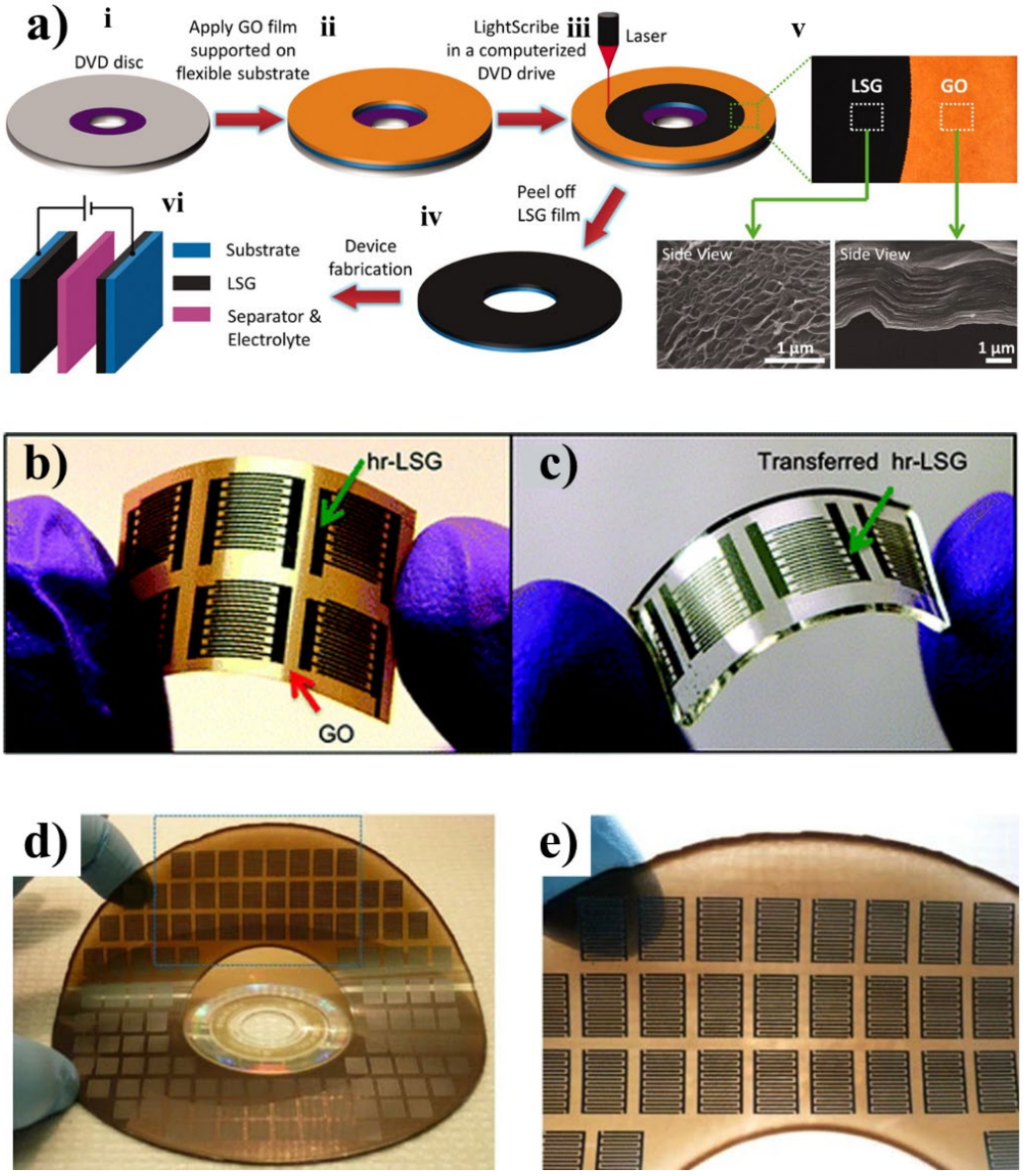

Figure 1.20 (a) Fabrication process of laser scribed graphene (LSG) and an assembled supercapacitor. (b) Interdigitated electrodes made of LSG on PI and (c) electrodes transferred onto polydimethylsiloxane (PDMS). (d, e) LSG micro-device arrays. Adapted from ref: (a) [159], (b-e) [382].

DLW can be used to produce graphene electrodes at a low cost, as demonstrated by Kaner's group [159]. They used an infrared laser (λ = 788 nm, 5 mW) embedded in a standard LightScribe DVD driver to reduce and pattern GO with high resolution (~20 µm), and the total cost of electrode production, including the laser, was less than $20 (Figure 1.20a). The laser-

scribed graphene (LSG) exhibited high conductivity (1738 S/m) and porous structures with a high surface area (1520 m^2/g). The method was further elaborated to produce all-organic, flexible interdigitated graphene electrodes for the detection of NO_2 [382]. Figure 1.20b shows the LSG electrodes on PI substrate, and Figure 1.20c shows the transferred electrodes on polydimethylsiloxane (PDMS) obtained through selective lift-off. The group further expanded the technique for scalable supercapacitor production, with a device being obtained in 18 s, and over 100 devices fabricated on a PI sheet with the size of a DVD disc (Figure 1.20d and e).

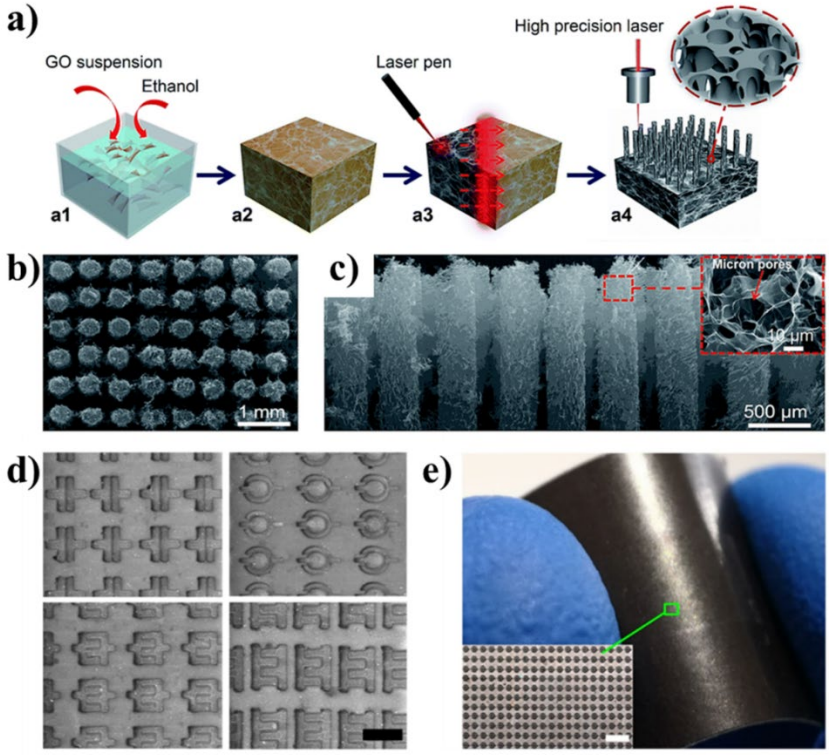

Figure 1.21 (a) Preparation process of highly vertically ordered pillar array of graphene framework (HOPGF). GO suspension (a1) was freeze-dried to obtain a GO aerogel (a2); then (a3) was reduced by a laser pen (1 W); (a4) HOPGF was obtained by etching with a high-precision laser. (b and c) Top and cross-sectional SEM images of HOPGF, showing the highly vertically aligned pillar array structure. The inset in (c) shows the enlarged SEM image of the vertically aligned pillar with macroporous graphene networks. (d) SEM images of LSG micro-devices with different shapes (scale bar, 50 μm). (e) Optical pictures display the overwhelming number of LSG micro-devices in a 1 cm^2 area (scale bar, 150 μm). Adapted from ref : (a-c)[398],(d, e) [399].

DLW has been used to produce graphene nanocomposite electrodes. Li et al. created rGO/Au microelectrodes by using DLW to laser a mixture of GO and $HAuCl_4$ onto commercial photo

paper [400]. Additionally, DLW has been utilized to fabricate sophisticated hierarchical graphene electrodes. Zhang et al. produced a highly vertically ordered pillar array of graphene framework (HOPGF) for water evaporation by using DLW and sequence laser etching. They prepared GO hydrogel, which was then transformed into reduced graphene oxide framework (rGF) by laser irradiation, and shaped into desired structures using a highly precise laser to produce HOPGF with macroporous networks (Figure 1.21 a-c) [398].

In another impressive study, Yuan et al. demonstrated the use of LSG electrodes with a spatially shaped femtosecond laser (SSFL), which enabled the production of over 30,000 devices in 10 minutes (Figure 1.21d and e) [399].The patterns generated were 10 microns in dimension with arrow gaps of 500 nm. Unlike 2D-printing-based conversational DLW, the SSFL technique uses a set of phase modulations to alternate the initial Gaussian beam into various beam shapes, producing a laser beam in a framework style, similar to a variable 3D "photonic stamp." This technique can directly process samples in batches without requiring the cooperation of any other method or the assistance of conversational DLW. It is especially promising for advanced miniaturized electronics, providing a pathway for high-throughput graphene electrode production on an industrial scale.

1.4.5.2 Laser induced graphene

1.4.5.2.1 Polyimide based LIG

Polyimide (PI) is a thermally stable plastic that undergoes oxygen and nitrogen outgassing at 550 °C, carbonization at 700 °C, and graphitization at 3000 °C [296, 401]. In 2014, Lin et al. accidentally obtained 3D porous carbon by DLW on PI sheets with a CO_2 laser (3.6 W), which they termed "laser-induced graphene" (LIG) [402]. Detailed characterization revealed that the carbon possessed properties of layered, highly crystallized graphene, and different LIG patterns could be obtained with a porous structure consisting of abundant five- and seven-membered rings instead of the conventional hexagonal lattice of graphene (Figure 1.22a-d). Since then, LIG has been extended to the graphitization of numerous materials [5, 154, 157, 158, 349, 403], including polymers [157], carbons[403] and even food[158]. LIGs exhibit high surface area, thermal stability, and excellent conductivity, making them promising materials in different fields[404], including batteries[405], oxygen electrocatalysis[406], triboelectric nanogenerators[407], CO_2 capture[408], gas sensors[409], wastewater treatment[410], and bacterial capture and killing (by Joule-heating) [411]. In particular, the fast electron transfer rates and excellent electrocatalytic properties of LIGs make them ideal for electrochemical

sensing [412, 413].

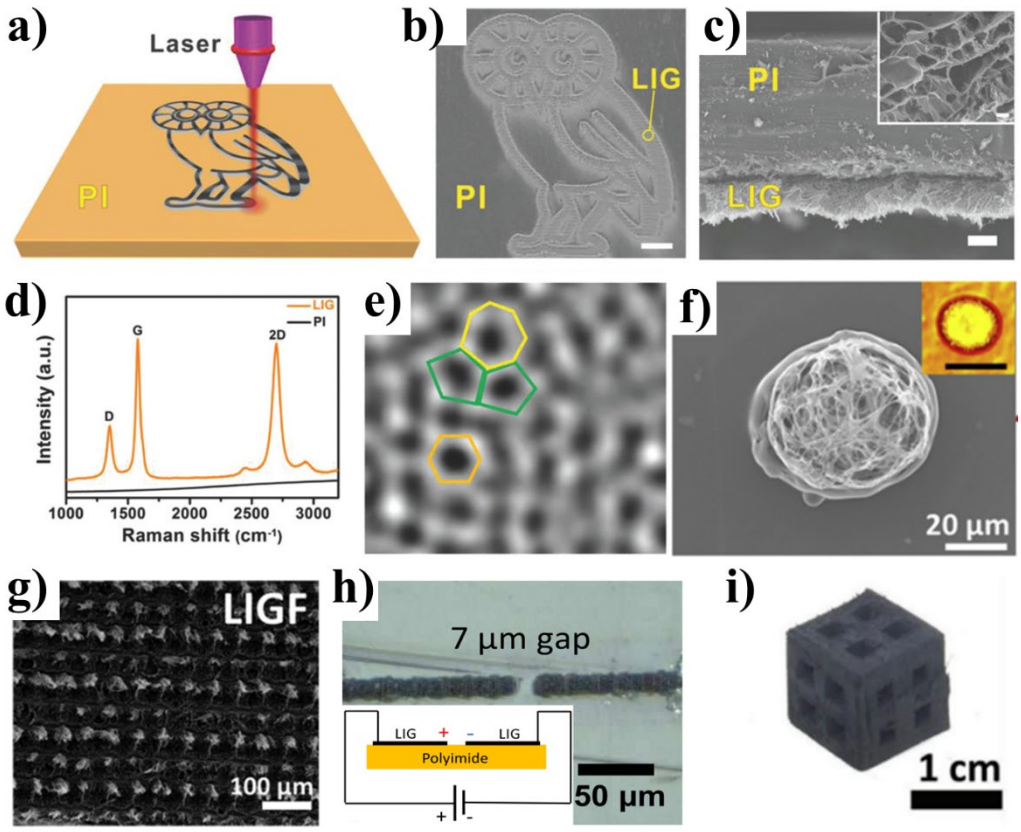

Figure 1.22 LIGs formed from commercial PI films. (a) Schematic of LIG production from PI. (b) SEM image of LIG with an owl shape, scale bar, 1 mm. (c) Cross-sectional SEM image of the LIG film, scale bar, 20 µm, inset is a higher magnification, scale bar, 1 µm. (d) Representative Raman spectra of the LIG film and the pristine PI film. (e) TEM image shows a heptagon with two pentagons and a hexagon. (f) SEM image of single LIG dot; inset is an optical picture with a scale bar of 50 µm. (g) SEM top view of laser induced graphene fiber (LIGF) surface. (h) SEM image of LIG line pattern with one-pixel width (~13 µm); the inset shows the schematic of a LIG humidity sensor with a micro gap channel. (i) Photo of a 3D LIG foam. Reprinted from ref: (a-e) [402], (f, g) [414], (h) [367], (i) [415].

Intensive studies have been conducted with different laser sources ranging from UV-visible, IR, to ultra-short pulse laser, and the characteristics of the LIGs have been investigated in detail during those processes [5, 155, 157-159, 198, 371, 416-421].It has been demonstrated that long-wavelength lasers generate LIGs via a photothermal effect [417], while photochemical reactions play the leading role in the case of UV lasers [418-420]. CO_2 laser treatment of PI results in micron-sized pores and a sheet structure with fewer pores, whereas UV treatment

yields micron-sized and nanometer-sized pores[421].

The resulting electrodes were demonstrated in shapes of quasi-0D dots (one pixel of the input digital pattern, from a printing point of view), quasi-1D lines, 2D planar patterns, and sophisticated 3D structures.

Duy et al. showed that the graphitization of the PI process could occur only when the laser (10.6 μm) fluence was over 5 J/cm^2, irrespective of the laser power [414]**.** LIG dots and LIG fiber arrays (Figure 1.22f and g) were created, and further inspection displayed that the morphology of LIG gradually changed from sheets to fibers and finally to droplets, along with the increasing radiation energy.

Stanford et al. produced dot and line LIG patterns by DLW of PI with a visible 405 nm laser in a SEM chamber [367]. The LIG has a spatial resolution of ~12 μm and a thickness of <5 μm and could be monitored in real-time by SEM. A humidity sensor was fabricated with two electrodes distanced 7 μm, which responded to human breath in 250 ms (Figure 1.22h).

3D LIG foam can be formed by DLW with two laser devices [415]. CO_2 laser (10.6 μm) irradiation led to LIGs; then 3D structures with higher resolution (Figure 1.22i) were obtained by a 1.06 μm fiber laser, since it can be absorbed by LIG while not by PI.

Li et al. presented that the surface morphology and chemical composition of LIG can be tuned by changing the surrounding gas during the laser scribing process, leading to porous graphene with different wetting properties ranging from super hydrophilic (O_2 or air) to super hydrophobic (Ar or H_2)[422].

1.4.5.2.2 Natural material based LIG

A green electrode for biosensing requires several features, including i) the use of vastly abundant and low-cost green resources; ii) a high-throughput, low-cost electrode production process that does not require or generate toxic materials; and iii) a biocompatible electrode that can be used for bio-interface construction with bio-degradability after its usage. In this context, natural materials such as wood, leaves, cellulose, and their derivatives are cheap, renewable, and thus great precursors for LIG. The advantages of DLW meet the aforementioned requirements for green LIG production.

Free-standing 3D graphene foams were fabricated by DLW of sucrose with Ni powders as a sacrificial framework. The foams displayed high porosity (~99.3%), low density (~0.015g/cm), and good electrical conductivity (~8.7 S/cm) [377]. Ye et al. converted wood into hierarchical

porous graphene [423] and hybridized graphene with inorganic nanostructures (Cu, Co, Ni, Fe) [424] by DLW. Romualdas et al. transformed pine wood into LIG and revealed that wood was heated to ~2020 K by a pulsed nanosecond laser[425]. Le et al. patterned LIG on woods and leaves using a UV femtosecond laser in ambient air (UV FS laser, 343 nm, 220 fs, 500 kHz) [426]. Cellulose, hemicellulose, and lignin present in wood were turned into graphene. This work demonstrated a breakthrough toward the eco-friendly manufacture of green electronics by the construction of electrical interconnects, flexible temperature sensors, and a supercapacitor (Figure 1.23a).

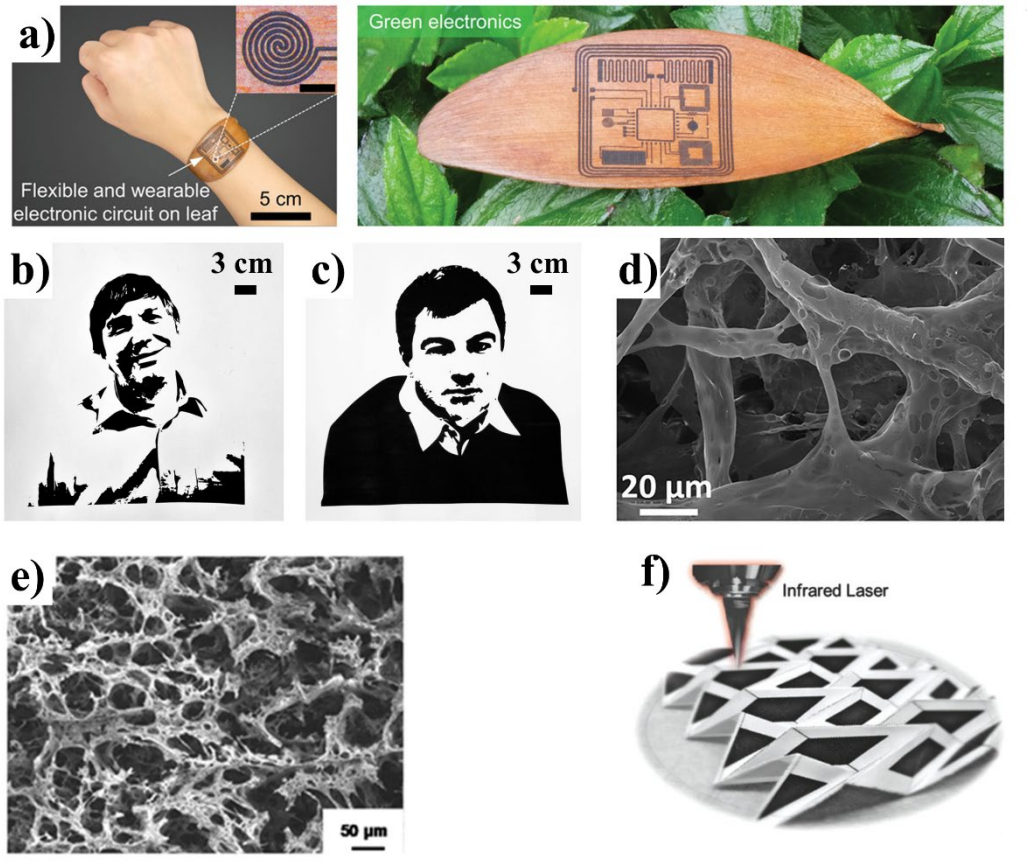

Figure 1.23 (a) Left, Photo of a LIG temperature sensor on a thin leaf; the inset displays an enlarged optical image of the electronic circuit (scale bar: 1 mm); right, photo of LIG electronics on a leaf for green electronics. Portraits of (b) Andre Geim and (c) Konstantin Novoselov on boric acid-treated paper constructed by LIG (dark area). (d) SEM picture of the LIG from filter paper. (e) SEM image of the MCG composites with porous structure and coral-shaped flakes. (f) Illustration of MCG (dark areas) with origami structures on paper (light areas). Adapted from ref: (a) [426], (b, c) [429], (d) [430], (e)[431], (f) [432].

Plastics are still the prominent substrates used in electronics and electrochemical sensors, which are largely available in the market. However, they pose great environmental risks since they can go into the final stage of the product cycle in the form of micro/nano-particles[427].. On the other hand, paper is biodegradable, with flexible and mechanically stable features, and could be a suitable precursor/substrate for LIG[428]. Tour et al. demonstrated graphene production by DLW of paper, presenting graphene artworks with photographs of A. Geim and K. Novoselov (Figure 1.23b and c) [429]. The process was achieved by two times laser irradiation: the first one turned the boric acid-treated paper into amorphous char, and the second one converted the char into porous LIG. The boric acid worked as a fire retardant to prevent the paper from volatilization, since DLW of paper would form levoglucosan and then various volatile products. Kulyk et al. explored the transformation from filter paper (cellulose) to graphene under CO_2 laser in detail (Figure 1.23d) and showed that the laser focal plane position is empirical [430]. A conductive porous hybrid with coral-shaped flakes (Figure 1.23e), made of molybdenum/carbide/graphene (MCG) composite on paper, was demonstrated as a strain sensor[431]. Then, 3D origami folded MCG structures were fabricated (Figure 1.23f), taking advantage of the physical behaviors of paper and enhancing the design possibility for paper-based electronics[432]. The electrode showed good structural stability, indicated by the conductivity maintenance (less than 5% degradation) after 750 cycles of 180-degree mechanical deformation.

1.4.5.2.3 Other LIGs

The characteristics of LIG have been extensively investigated, but little attention has been paid to the intrinsic properties of the carriers (precursors/substrates). The stability of the carriers under exposure to acid/base or organic solvent is of great importance for the application of LIG, particularly for devices that may operate under harsh conditions. For example, PI and polyetherimide are commonly used in printed electronics, but they are sensitive to alkali and can collapse under long-term incubation[433], leading to damage to the hosted LIG. Additionally, renewable resources such as wood and paper have complex and variable components, which can make it difficult to ensure the reproducibility and stability of the resulting LIG.

These issues can be addressed by exploring other precursors or substrates. Yu et al. produced LIG from polybenzoxazine and demonstrated its stability in acid/alkali environments, along with the polymer substrate[434]. Other polymers, such as polysulfone, poly (ether sulfone),

and polyphenylsulfone[435], and photoresist[436] have also been transformed into LIG. Yieu et al. reported a versatile method to produce graphene by DLW of diverse materials such as cross-linked polystyrene, epoxy, and cellulose [158]. The first laser irradiation converted the substrates into amorphous carbon, and the following lasering transformed the amorphous carbon into graphene. They also proposed an alternative way to realize LIG in a single scribing step with a defocused laser. Cellulose-dominated materials such as wood, cloth, and coconut shell, which easily decay into volatile compounds with DLW, were converted to LIG, with or without pretreatment with a fire-retardant under room atmosphere. The resulting LIG displayed a low sheet resistance of around 5 Ω/sq and was demonstrated as supercapacitors on a coconut. Moreover, the work investigated lists of polymers that could be converted to LIG under room atmosphere and those that cannot. The method indicated that any precursor convertible into amorphous carbon can be transformed into graphene with multiple laser-exposing steps.

1.4.5.3 Selectively transfer of direct-laser-written graphene

In most cases, direct-laser-written graphene (DLWG) remains in the same plane as its precursor, which may not be suitable for various substrate requirements of graphene-based electronic devices for different applications. This is even more crucial for GO-based DLWG since unreduced GO dissolves in aqueous solutions and changes the solution composition, thereby destroying the device. Therefore, either the unreduced GO should be removed or the DLWG should be transferred to a different substrate.

A strategy was reported for simultaneously patterning and transferring graphene or GO onto flexible plastic sheets with micrometer features [437].Laser irradiation (continuous wave laser diode, 976 nm) heated the graphene or GO film, resulting in the photothermal reduction of GO and localized melting of the PET film in contact with the graphene or GO. Upon cooling, strong welding occurred at the graphene-PET interface, resulting in partial transfer of graphene or rGO to the PET sheet (Figure 1.24a-c).

The Merkoçi group has recently reported a novel and simple stamping transfer method to obtain DLWG electrodes on a wide variety of substrates (Figure 1.24d and e) [156]. In this method, a GO film was formed on a PVDF filter membrane by vacuum filtration, before being patterned and reduced by a Light-Scribe DVD driver. The DLWG was then selectively transferred to various substrates, including PET, paper, nitrocellulose, glass, fabric, and silicon, with a mechanical press, leaving the GO on the host filter membrane. Meanwhile, the resulting electrodes were reinforced by the press. The DLWG consisted of a few-nanometer-thick

graphene flakes with considerable conductivity. 3D circuits, proximity sensors, nitrocellulose-based electrochemical sensors, and electroluminescent lamps were fabricated to demonstrate the versatile utilities of the method.

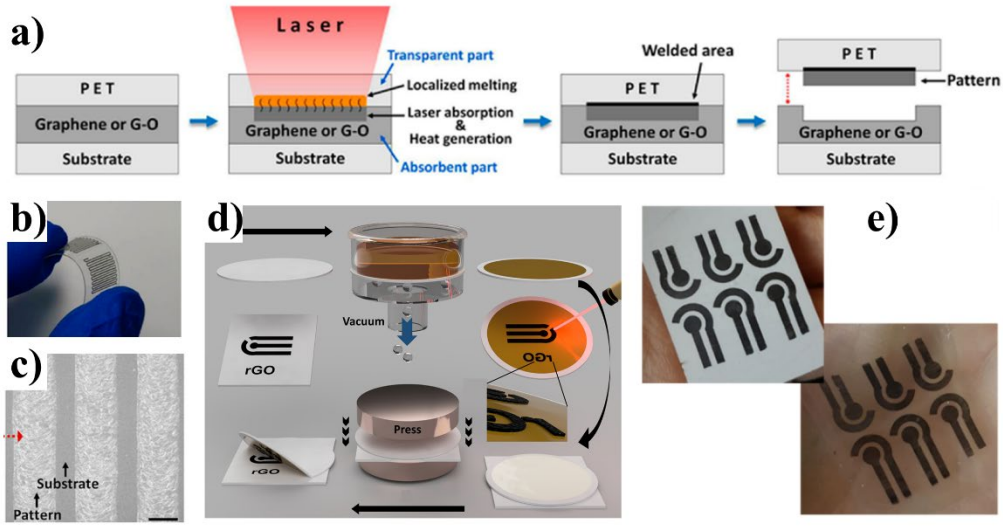

Figure 1.24 (a) Schematic of the laser-assisted selective transfer patterning of graphene and GO film (b) Photo and (c) SEM image (scale bar, 200 μm) of the transferred graphene patterns on PET film. (d) Schematic of laser patterning process of the graphene nanofilm. (e) Photo of the transferred DLWG electrodes on nitrocellulose (upper panel) and PET (bottom panel). Reprinted (adapted) from ref: (a-c)[437], (d, e) [156].

Li et al. transferred layered LIG composites continuously with different patterns and functionalities to various thermoplastic films by a roll-to-roll process [438]. Patterned LIG composites were formed by DLW of PI and then laminated with polymer films of interest by passing through a modified commercial thermal laminator. The host PI can be removed by simply peeling off. Multilayer composites could be obtained by adding polymer films, followed by subsequent lamination. Devices, such as directly embedded electrodes, triboelectric nanogenerators, biomedically interesting surfaces, and puncture detectors, were produced, demonstrating the effectiveness of the strategy for rapid, large-area production of patterned, encapsulated LIG devices for real-life applications (Figure 1.25a).

Conformal transfer of LIG to adhesive tape has been reported for miniaturized electronics or sensors [440]. But PDMS-based lift-off is the most popular method to transfer LIG, especially in flexible electronics. For example, a highly stretchable and sensitive strain sensor was fabricated by transfer and embedment of LIG pattern in PDMS (Figure 1.25b) [439]..

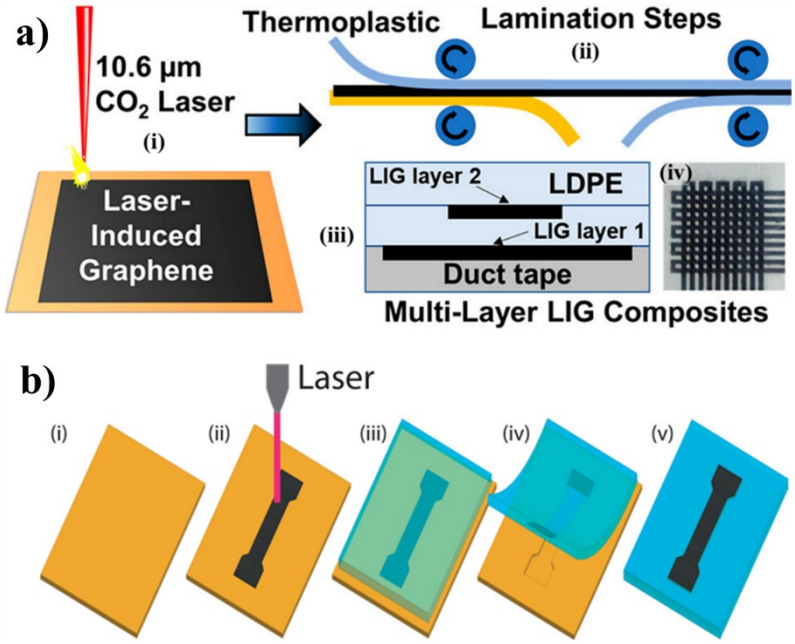

Figure 1.25 (a) Schematic of the lamination transfer process of LIG. (b) Schematic of the flexible strain sensor fabrication process :(i) attach PI tape to a PET sheet; (ii) pattern PI by DLW; (iii) pour and impregnate LIG with diluted uncured PDMS; (iv-v) peel off the PDMS sheet after solidification. Reprinted from ref: (a) [438], (b)[439].

1.4.6 Electrochemical (bio)sensing applications of DLW graphene electrodes

The large electrochemical potential window, fast electron transfer rate, and highly porous structure make direct-laser-written graphene (DLWG) electrodes powerful platforms for electrochemical (bio)sensors. The polymerization, heteroatom doping, and transitional metal nanoparticle decoration can form nanocomposites with DLWG, further improving the sensing performance. DLWG has demonstrated some of the best sensing performance so far as an electrode and transducer, opening the door toward real-world on-site applications, such as human health monitoring, food safety analysis, and environmental pollution detection.

A flexible and highly sensitive non-enzymatic glucose sensor was fabricated by DLW of GO with a DVD-laser scriber [441].. Electrodeposited copper nanoparticles (Cu-NPs) were used as the catalyst for glucose oxidation, and silicone rubber was used to avoid the re-dispersion of unreduced GO into the electrolyte solution and to define the sensing area of the rGO electrode. The sensor exhibited a wide linear detection range (1 μM-4.54 mM) with a low LOD (0.35 μM). Similarly, Eider et al. demonstrated a H_2O_2 sensor using silver nanoparticle decorated

LIG as electrodes (DVD-laser reduced GO), and the sensor showed a linear range from 0.1 to 10 mM, and a low LOD of 7.9 µM [442].

Another non-enzymatic glucose sensor was developed based on surface engineering of laser-scribed graphene (LSG from PI) by immobilization of copper oxide nanoparticles (CuO NPs). The size of the nanoparticles was optimized under focused sunlight to enhance the catalytic efficiency. The sensor displayed a LOD of 0.1 µM, linearity of 1 µM-5 mM in buffer, and high stability and reproducibility in various biofluids, including whole blood, serum, sweat, and urine. Furthermore, conformal transfer of the LSG to Scotch tape (LSGST) endowed wearable sensors for direct monitoring of glucose in sweat (Figure 1.26a) [440].

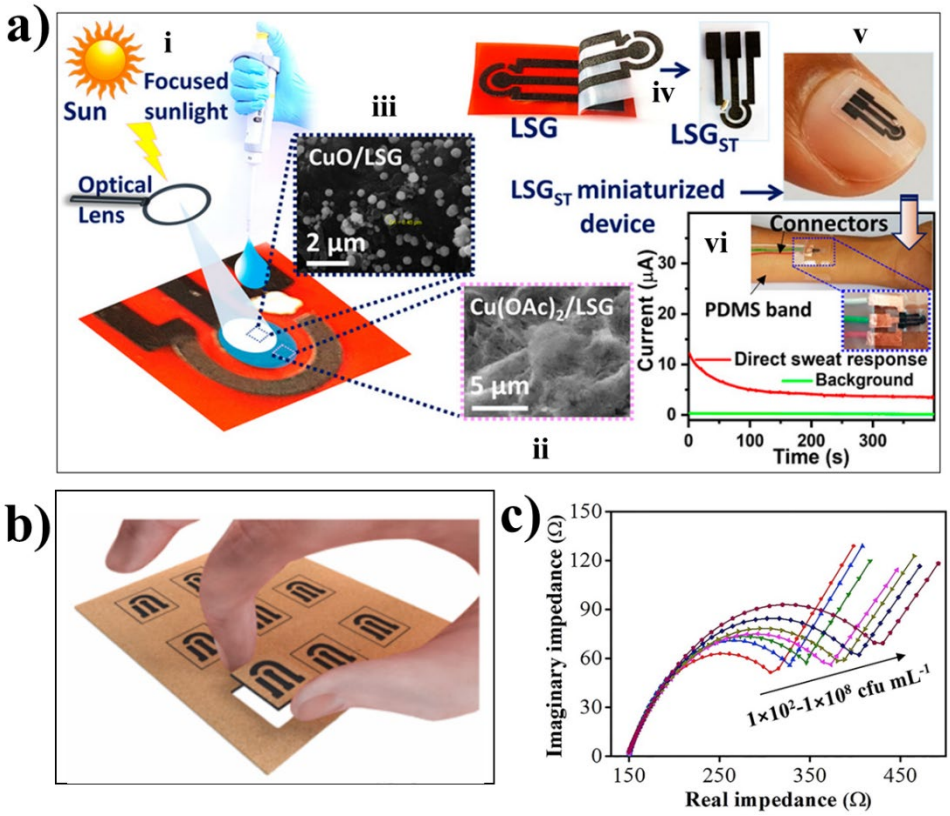

Figure 1.26 (i) Illustration of the electrode modification with CuO under sunlight. SEM image of the LSG before (ii) and after (iii) CuO formation. (iv) Conformal transfer of the LSG electrode to Scotch tape. (v) Photograph of the miniaturized device on a human nail. (vi) Photograph of wearable CuO/LSGST miniaturized sensor and the amperometry response for direct sweat measurement compared with baseline. (b) Illustration of LIG electrode array from paperboard. (c)The impedance response with various concentrations of E. coli O157:H7 (1×10^2 to 1×10^8 cfu/mL). Reprinted (adapted) from ref: (a) [440], (b) [445], (c) [388].

LSG from PI was demonstrated for thrombin detection in blood serum with a LOD of 1 pM in buffer and 5 pM in serum [443]. Nanostructured gold-modified LSG (LSG-AuNS) was demonstrated for electrochemical sensing of human epidermal growth factor receptor 2 (Her-2). The aptasensor exhibited a LOD of 0. 008 ng/mL and a linear range of 0.1-200 ng/mL with square wave voltammetry measurements. The sensor was also verified in undiluted human serum. Besides, the potential for POC detection of the sensor was displayed by a hand-held electrochemical system controlled by a home-developed phone application[444].

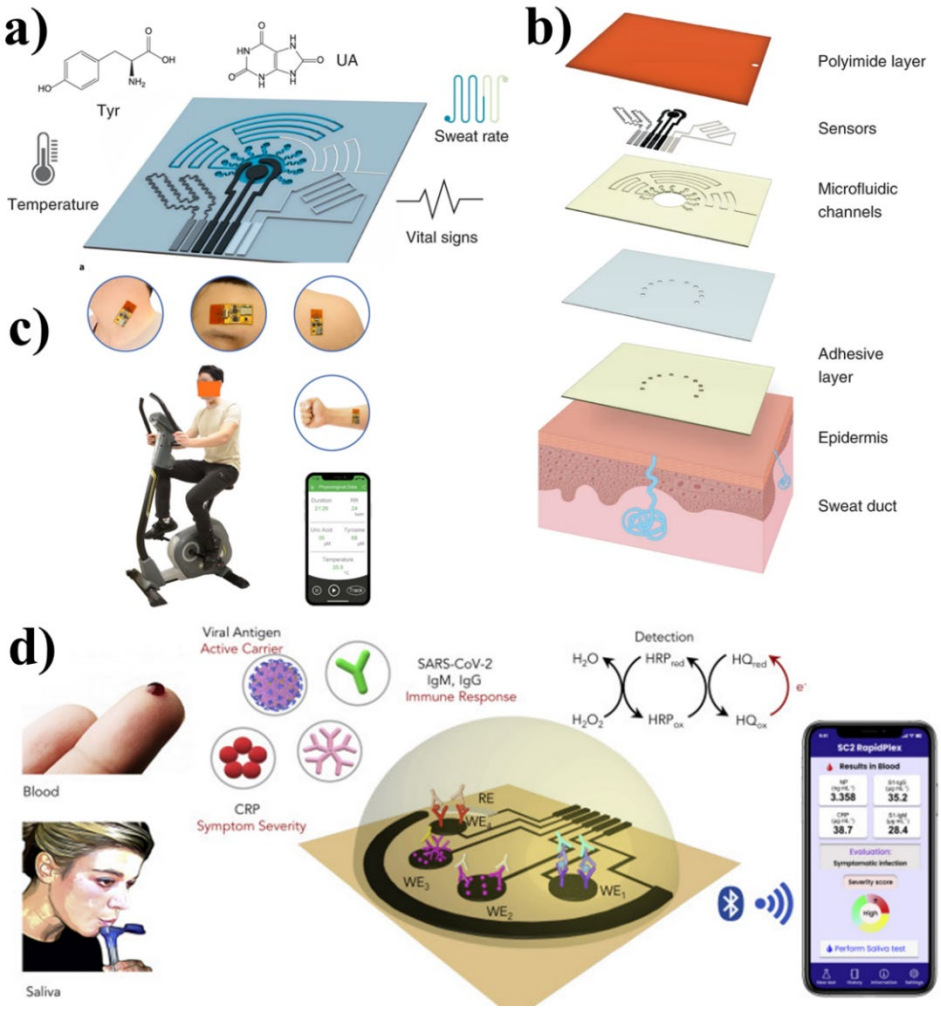

Figure 1.27 (a) An entirely laser-engraved multifunctional sensor for sweat UA and Tyr detection, sweat rate estimation, temperature sensing and vital-sign monitoring. (b) Structural illustration of the sensor. (c) Photographs of a healthy subject wearing the sensor patch at different body parts. (d) Working mechanism of the SARS-CoV-2 RapidPlex platform. Adapted from ref: (a-c) [446], (d) [447].

William et al. produced a graphene @ aluminosilicate particle nanocomposite electrode (Figure 1.26b) for the detection of ascorbic acid, caffeic acid, and picric acid using CV and DPV techniques [445]. The nanocomposite electrode was fabricated via one-step DLW of paperboard, demonstrating a scalable and environmentally-friendly fabrication method with promising potential for portable electrochemical devices. Noble metal nanoparticle-3D graphene hybrid nanocomposites were also utilized for the detection of bacterial (*E. coli O157:H7*) via EIS[388]. These hybrid nanocomposites were fabricated by one-step DLW of PI film coated with gold, silver or platinum salt-chitosan hydrogel ink (Figure 1.26c).

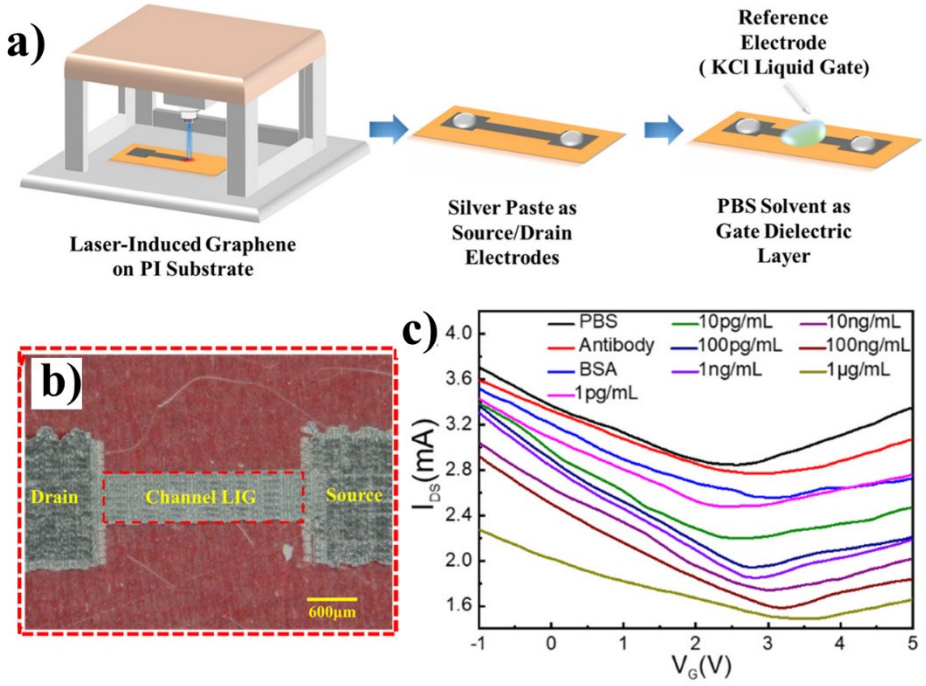

Figure 1.28 (a) Schematic of the fabrication process of the LIG-FET. (b) Optical image of the LIG-FET. (c) Transfer characteristics of the LIG-FET biosensor responding to gate solutions with different molecules and different concentrations of the target spike protein. Adapted from ref [448]

Wei's group reported an entirely laser-engraved sensor for simultaneous sweat sampling, chemical sensing, and vital sign monitoring (Figure 1.27a) [446]. The sensor contains five layers, including multiplexed LIG-based sensors on a PI sheet, microfluidic channels on a double-sided medical tape, a PET sheet, and another layer of medical tape (Figure 1.27b). The sensor can continuously detect human body temperature, respiration rate, uric acid (UA), and tyrosine (Tyr) in sweat using DPV. The sensor showed excellent performance when worn by

human subjects, including patients and healthy controls (Figure 1.27c). The same group also made significant efforts to address the COVID-19 situation. They proposed an ultrasensitive, low-cost, multiplexed electrochemical sensing system based on laser scribing of PI, named SARS-CoV-2 RapidPlex (Figure 1.27d) [447]. The system can detect SARS-CoV-2 viral proteins, antibodies, and an inflammatory biomarker through specific immuno-recognition. Rapid (1-minute incubation with the targets) and remote (wireless data transfer by mobile) assessment of COVID-19 was successfully achieved using serum and saliva samples from COVID-19-positive and negative subjects. The platform facilitated personalized, multiplexed detection of biomarkers, showing great potential for possible future pandemics.

Tianrui et al. demonstrated the first use of a LIG-based field effect transistor (LIG-FET) for virus detection without sample pretreatment or labelling [448]. Different reduction degrees in the channel region and the source/drain electrode region were achieved by scribing with different laser powers. Highly specific antibodies facilitated quick and sensitive detection of the SARS-CoV-2 spike protein in 15 minutes (1 pg/mL in PBS, 1 ng/mL in human serum) (see Figure 1.28).

1.5 Directly written graphene-based electrodes towards POC test: conclusions, challenges and perspectives

Graphene-based electrodes have shown significant potential for developing sensitive electrochemical sensors, due to their tunable electrical conductivity, high surface area, versatile functionality, and biocompatibility. Various methods for graphene production have been reported, including bottom-up growth, top-down reduction/oxidation and exfoliation, each can profoundly affect graphene's properties.

Direct writing, such as inkjet printing and laser writing, is a highly useful tool for rapid prototyping of graphene electrodes/devices, offering advantageous features such as conformal and on-demand writing, high design freedom, and low-cost, high-throughput production. Inkjet printing of graphene has mainly focused on flexible thin film electronics/sensors, and direct laser writing of graphene patterns has demonstrated considerable potential as a platform for electrochemical biosensing, given its highly porous structure and fast mass transportation and electron transfer rates.

Directly written graphene electrodes as biosensors are transforming healthcare, food safety, and environmental monitoring. However, for practical point-of-care tests in real-life situations,

graphene-based devices are still in the prototype stage and face many challenges in the fabrication, operation, and data analysis processes. Addressing these challenges will require extensive efforts from research communities. Nonetheless, these challenges also present countless opportunities for innovation and advancement.

1.5.1 Electrode production

1.5.1.1 Inkjet printing

Despite the various methods available for producing graphene-based materials, the large-scale, low-cost, and eco-friendly production of high-quality, uniformly structured graphene inks remains a significant challenge. Furthermore, the low ink loading rate, typically within the range of 0.002-1 wt.%, leads to low conductivity of the pattern or requires extensive layer printing. In addition, neat graphene or highly reduced graphene oxide inks tend to aggregate due to π-π stacking and van der Waals interactions, making printing difficult. Additives such as ethyl cellulose and surfactants are helpful, but they require removal through an annealing process (usually≥300 °C), which limits the choice of substrates to heat-resistant materials. Achieving a balance between excellent rheological properties of the ink and uniform/strong graphene adhesion to the substrate is also challenging, as it depends on various elements such as surface tension and viscosity of the ink, substrate surface energy, coffee ring effect, and the application scenario of the electrode. These issues can potentially be overcome by novel preparation, functionalization, and hybridization of the inks, pre-functionalization of substrates, and adjustment of the sintering process. Furthermore, the further development of inks that are compatible with consumer-grade inkjet printers could hold great promise for achieving low-cost, high-throughput sensor production. This is of commercial interest and utmost importance for researchers with limited resources.

1.5.1.2 Direct laser writing

Despite abundant promising results, the underlying mechanism for precisely tuning the properties of graphene materials via laser irradiation is not yet fully understood. Meanwhile, a significant challenge of using direct-laser-written graphene (DLWG) is the effective transfer of DLWG to various substrates, to meet the needs of various application scenarios. Another challenge is the reproducibility of DLWG, which is influenced by anisotropic conductivity and a high dependence on the laser parameters. Moreover, renewable carbon resources such as wood and paper have variable components that may affect the reproducibility of DLWG.

Stability is also a concern, as the delicate porous structure of DLWG may degrade over long-term exposure to the atmosphere, and solution evaporation-induced capillary forces can change the hierarchical structure during the drying process. Additionally, commonly used polymers such as PI and PEI are susceptible to alkaline conditions that can damage the hosted DLWG.

1.5.1.3 Resolution

Smaller sizes, diverse functionalities, and optimized architectures are favored for electrochemical sensors, especially multiplexed POC sensors. This requires high-resolution patterning of graphene. However, it is still difficult to achieve patterns with direct writing in micrometer resolution (1-10 μm). For instance, research-grade inkjet printers have a resolution of ~10s μm; consumer-grade ones have a resolution of ~50s μm; DLW graphene has a resolution of ~50 μm under ultraviolet laser and 60–100 μm under infrared laser. In this case, a spatially shaped femtosecond laser may be useful since it can achieve precise patterning of graphene in sub-micrometer scale, but the costly laser machine (tens of thousands of dollars) is not accessible for everyone.

1.5.2 Sensor fabrication and disposal

The stability of the bio-elements needs to be further improved since they play a vital role in the stability of electrochemical sensors and thus the precise detection. Moreover, despite the achievements made in electrochemical multiplexed detection, such as the application of microelectrode arrays, it still presents high risks of cross-interference and high cost in materials and fabrication processes led by miniaturization. Graphene-based materials show excellent biocompatibility toward different bioreceptors with antibacterial activity, while the bio-toxicity towards diverse living organisms and the environmental influences are still not fully investigated. Moreover, the widely used plastic substrates, heavy metals from the electric circuits, and other residues after the usage of the sensors need to be properly addressed for environmental sustainability.

1.5.3 Practical detection in real sample

Until now, only glucose meters have entered the market among electrochemical biosensors. One of the main reasons is the fouling of sensors due to the complexity of the biomatrix. Particularly, most biomolecules can adsorb on graphene, resulting in unfavorable performance of graphene-based biosensors in real samples. Nanoengineered structures and coatings can be a promising avenue for antifouling[449, 450]. Multiple washing steps are necessary for most

biosensing processes, which are time-consuming and require trained personnel, making them not user-friendly for POC testing. Label-free based sensing strategies display great potential for this aim, while stable specific bioreceptors with strong affinity towards the targets need to be carefully chosen to obtain enough sensitivity. The smartphone-based platform is a promising strategy to bring electrochemical sensors out of the lab for self-testing at the POC level. However, the possible low signal-to-noise ratio coming from device miniaturization also presents a challenge. Integrating microfluidics and/or lab-on-a-chip devices with smartphones could be highly beneficial for robust, portable, wireless, and rapid detection in different fields from healthcare, disease diagnostics to environmental monitoring.

1.6 References

1. Nasir, M.Z.M., et al., 3d-Printed Electrodes for the Detection of Mycotoxins in Food. *Electrochem. Commun.*, 2020. **115**. DOI: 10.1016/j.elecom.2020.106735.
2. Ma, X., et al., Carbon-Based Nanocomposite Smart Sensors for the Rapid Detection of Mycotoxins. *Nanomaterials*, 2021. **11**(11). DOI: 10.3390/nano11112851.
3. Jiang, Z., et al., Graphene Biosensors for Bacterial and Viral Pathogens. *Biosens. Bioelectron.*, 2020. **166**: p. 112471. DOI: 10.1016/j.bios.2020.112471.
4. Cesewski, E. and B.N. Johnson, Electrochemical Biosensors for Pathogen Detection. *Biosens. Bioelectron.*, 2020. **159**: p. 112214. DOI: 10.1016/j.bios.2020.112214.
5. Wanjari, V.P., et al., Laser-Induced Graphene-Based Electrochemical Biosensors for Environmental Applications: A Perspective. *Environ. Sci. Pollut. Res. Int.*, 2022. DOI: 10.1007/s11356-022-21035-x.
6. Jun, H.Y., S.J. Kim, and C.H. Choi, Ink Formulation and Printing Parameters for Inkjet Printing of Two Dimensional Materials: A Mini Review. *Nanomaterials (Basel)*, 2021. **11**(12). DOI: 10.3390/nano11123441.
7. Kathirvelan, J., Recent Developments of Inkjet-Printed Flexible Sensing Electronics for Wearable Device Applications: A Review. *Sensor Review*, 2020. **41**(1): p. 46. DOI: 10.1108/sr-08-2020-0190.
8. IUPAC, Compendium of Chemical Terminology, 2nd Ed. (the "Gold Book"). Compiled by A. D. Mcnaught and A. Wilkinson. Blackwell Scientific Publications, Oxford (1997). DOI: 10.1351/pac199264010143).
9. *Biosensors Market by Type, Product, Technology, Application and Region (2012-2026)*. 2021 [cited 2022 14th October]; Available from: https://www.marketsandmarkets.com/Market-Reports/biosensors-market-798.html.
10. Aydin, E.B., M. Aydin, and M.K. Sezginturk, Biosensors and the Evaluation of Food Contaminant Biosensors in Terms of Their Performance Criteria. *Int. J. Environ. Anal. Chem.*, 2020. **100**(5): p. 602. DOI: 10.1080/03067319.2019.1672675.
11. Bhalla, N., et al., *Introduction to Biosensors*, in *Biosensor Technologies for Detection of Biomolecules*, P. Estrela, Editor. 2016. p. 1.
12. Gauglitz, G., Analytical Evaluation of Sensor Measurements. *Anal Bioanal Chem*, 2018. **410**(1): p. 5. DOI: 10.1007/s00216-017-0624-z.
13. Proll, G. and M. Ehni, *Immunoassays*, in *Handbook of Spectroscopy*. 2014. p. 1313.
14. Thevenot, D.R., et al., Electrochemical Biosensors: Recommended Definitions and Classification. *Pure Appl. Chem.*, 1999. **71**(12): p. 2333. DOI: 10.1351/pac199971122333.
15. Burcu Aydın, E., M. Aydın, and M. Kemal Sezgintürk, Biosensors and the Evaluation of Food Contaminant Biosensors in Terms of Their Performance Criteria. *Int. J. Environ. Anal. Chem.*, 2019. **100**(5): p. 602. DOI: 10.1080/03067319.2019.1672675.
16. Thevenot, D.R., et al., Electrochemical Biosensors: Recommended Definitions and Classification. *Biosens. Bioelectron.*, 2001. **16**(1-2): p. 121. DOI: 10.1016/s0956-

5663(01)00115-4.

17. Farrow, B., et al., A Chemically Synthesized Capture Agent Enables the Selective, Sensitive, and Robust Electrochemical Detection of Anthrax Protective Antigen. *ACS Nano*, 2013. **7**(10): p. 9452. DOI: 10.1021/nn404296k.

18. Bhimji, A., et al., An Electrochemical Elisa Featuring Proximal Reagent Generation: Detection of Hiv Antibodies in Clinical Samples. *Anal. Chem.*, 2013. **85**(14): p. 6813. DOI: 10.1021/ac4009429.

19. Johnson, K. *Curve Fitting for Immunoassays: Elisa and Multiplex Bead Based Assays (Legendplex™)*. Available from: https://www.biolegend.com/en-us/blog/curve-fitting-for-immunoassays-legendplex.

20. Azadeh, M., et al., Calibration Curves in Quantitative Ligand Binding Assays: Recommendations and Best Practices for Preparation, Design, and Editing of Calibration Curves. *AAPS J*, 2017. **20**(1): p. 22. DOI: 10.1208/s12248-017-0159-4.

21. Parolo, C., et al., Tutorial: Design and Fabrication of Nanoparticle-Based Lateral-Flow Immunoassays. *Nat. Protoc.*, 2020. **15**(12): p. 3788. DOI: 10.1038/s41596-020-0357-x.

22. Lerchi, M., et al., Lead-Selective Bulk Optodes Based on Neutral Ionophores with Subnanomolar Detection Limits. *Anal. Chem.*, 2002. **64**(14): p. 1534. DOI: 10.1021/ac00038a007.

23. Armbruster, D.A. and T. Pry, Limit of Blank, Limit of Detection and Limit of Quantitation. *Clinical Biochemist Reviews*, 2008. **29 Suppl 1**(Suppl 1): p. S49.

24. Shrivastava, A. and V. Gupta, Methods for the Determination of Limit of Detection and Limit of Quantitation of the Analytical Methods. *Chronicles of Young Scientists*, 2011. **2**: p. 21.

25. Fernandez-Ramos, M.D., et al., An Iupac-Based Approach to Estimate the Detection Limit in Co-Extraction-Based Optical Sensors for Anions with Sigmoidal Response Calibration Curves. *Anal Bioanal Chem*, 2011. **401**(9): p. 2881. DOI: 10.1007/s00216-011-5366-8.

26. Wang, J., *Analytical Electrochemistry*. 2006.

27. Robinson, P.K., Enzymes: Principles and Biotechnological Applications. *Essays Biochem*, 2015. **59**: p. 1. DOI: 10.1042/bse0590001.

28. plc., A. *Antibody Structure and Isotypes*. [cited 2022 11/03]; Available from: https://www.abcam.com/protocols/antibody-structure-and-isotypes.

29. Bartlett, P.N., *Bioelectrochemistry : Fundamentals, Experimental Techniques and Applications*. Chromatographia 2008: John Wiley & Sons.

30. Justino, C.I.L., et al., Recent Developments in Recognition Elements for Chemical Sensors and Biosensors. *TrAC, Trends Anal. Chem.*, 2015. **68**: p. 2. DOI: 10.1016/j.trac.2015.03.006.

31. Nelson, A.L., Antibody Fragments: Hope and Hype. *MAbs*, 2010. **2**(1): p. 77. DOI: 10.4161/mabs.2.1.10786.

32. Immunology, P. *Polyclonal Vs Monoclonal Antibodies*. [cited 2022 11/03]; Available from: https://www.pacificimmunology.com/resources/antibody-introduction/polyclonal-vs-monoclonal-%20antibodies/.

33. Birch, J.R. and A.J. Racher, Antibody Production. *Adv Drug Deliv Rev*, 2006. **58**(5-6): p. 671. DOI: 10.1016/j.addr.2005.12.006.

34. Kim, J., et al., Recent Advances in Aptasensor for Cytokine Detection: A Review. *Sensors (Basel)*, 2021. **21**(24). DOI: 10.3390/s21248491.

35. Vasilescu, A. and J.-L. Marty, Electrochemical Aptasensors for the Assessment of Food Quality and Safety. *TrAC, Trends Anal. Chem.*, 2016. **79**: p. 60. DOI: 10.1016/j.trac.2015.11.024.

36. Tuerk, C. and L. Gold, Systematic Evolution of Ligands by Exponential Enrichment: Rna Ligands to Bacteriophage T4 DNA Polymerase. *Science*, 1990. **249**(4968): p. 505. DOI: 10.1126/science.2200121.

37. Samad Hosseini, S., et al., Perspectives and Trends in Advanced DNA Biosensors for the Recognition of Single Nucleotide Polymorphisms. *Chem. Eng. J.*, 2022. **441**. DOI: 10.1016/j.cej.2022.135988.

38. Ozsoylu, D., T. Wagner, and M.J. Schoning, Electrochemical Cell-Based Biosensors for Biomedical Applications. *Curr. Top. Med. Chem.*, 2022. **22**(9): p. 713. DOI: 10.2174/1568026622666220304213617.

39. Ron, E.Z. and J. Rishpon, *Electrochemical Cell-Based Sensors*, in *Whole Cell Sensing Systems I : Reporter Cells and Devices*, S. Belkin and M.B. Gu, Editors. 2010. p. 77.

40. Gui, Q., et al., The Application of Whole Cell-Based Biosensors for Use in Environmental Analysis and in Medical Diagnostics. *Sensors (Basel)*, 2017. **17**(7). DOI: 10.3390/s17071623.

41. Naresh, V. and N. Lee, A Review on Biosensors and Recent Development of Nanostructured Materials-Enabled Biosensors. *Sensors (Basel)*, 2021. **21**(4). DOI: 10.3390/s21041109.

42. Setlem, S.K., B. Mondal, and S. Ramlal, A Fluorescent Aptasensor for the Detection of Aflatoxin B1 by Graphene Oxide Mediated Quenching and Release of Fluorescence. *J Microbiol Methods*, 2022. **193**: p. 106414. DOI: 10.1016/j.mimet.2022.106414.

43. Adhikari, J., et al., Current Progresses and Trends in Carbon Nanomaterials-Based Electrochemical and Electrochemiluminescence Biosensors. *J. Chin. Chem. Soc.*, 2020. **67**(6): p. 937. DOI: 10.1002/jccs.201900417.

44. Cao, J., T. Sun, and K.T.V. Grattan, Gold Nanorod-Based Localized Surface Plasmon Resonance Biosensors: A Review. *Sensors Actuators B: Chem.*, 2014. **195**: p. 332. DOI: 10.1016/j.snb.2014.01.056.

45. Aydin, S., A Short History, Principles, and Types of Elisa, and Our Laboratory Experience with Peptide/Protein Analyses Using Elisa. *Peptides*, 2015. **72**: p. 4. DOI: 10.1016/j.peptides.2015.04.012.

46. Ahirwar, R., A. Bhattacharya, and S. Kumar, Unveiling the Underpinnings of Various Non-Conventional Elisa Variants: A Review Article. *Expert Rev. Mol. Diagn.*, 2022. **22**(7): p. 761. DOI: 10.1080/14737159.2022.2117615.

47. Hosseini, S., et al., *Advantages, Disadvantages and Modifications of Conventional Elisa*, in *Enzyme-Linked Immunosorbent Assay (Elisa)*, S. Hosseini, et al., Editors. 2018, Springer Singapore: Singapore. p. 67.

48. Clark, L.C., Jr. and C. Lyons, Electrode Systems for Continuous Monitoring in Cardiovascular Surgery. *Ann N Y Acad Sci*, 1962. **102**: p. 29. DOI: 10.1111/j.1749-6632.1962.tb13623.x.

49. Ronkainen, N.J., H.B. Halsall, and W.R. Heineman, Electrochemical Biosensors. *Chem. Soc. Rev.*, 2010. **39**(5): p. 1747. DOI: 10.1039/b714449k.

50. Allen J. Bard, L.R.F., *Electrochemical Methods: Fundamentals and Applications*. 2nd ed. 2000.

51. Xiong, Y., et al., A Flexible, Ultra-Highly Sensitive and Stable Capacitive Pressure Sensor with Convex Microarrays for Motion and Health Monitoring. *Nano Energy*, 2020. **70**: p. 104436. DOI: 10.1016/j.nanoen.2019.104436.

52. Tsouti, V., et al., Capacitive Microsystems for Biological Sensing. *Biosens. Bioelectron.*, 2011. **27**(1): p. 1. DOI: 10.1016/j.bios.2011.05.047.

53. Heller, A. and B. Feldman, Electrochemical Glucose Sensors and Their Applications in Diabetes Management. *Chem Rev*, 2008. **108**(7): p. 2482. DOI: 10.1021/cr068069y.

54. Benck, J.D., et al., Substrate Selection for Fundamental Studies of Electrocatalysts and Photoelectrodes: Inert Potential Windows in Acidic, Neutral, and Basic Electrolyte. *PLoS One*, 2014. **9**(10): p. e107942. DOI: 10.1371/journal.pone.0107942.

55. Hayyan, M., et al., Investigating the Electrochemical Windows of Ionic Liquids. *J. Ind. Eng. Chem.*, 2013. **19**(1): p. 106. DOI: 10.1016/j.jiec.2012.07.011.

56. Lai, B.-C., J.-G. Wu, and S.-C. Luo, Revisiting Background Signals and the Electrochemical Windows of Au, Pt, and Gc Electrodes in Biological Buffers. *ACS Appl. Energy Mater.*, 2019. **2**(9): p. 6808. DOI: 10.1021/acsaem.9b01249.

57. Song, H., et al., Carbon-Based Electrochemical Sensors for in Vivo and in Vitro Neurotransmitter Detection. *Crit. Rev. Anal. Chem.*, 2021: p. 1. DOI: 10.1080/10408347.2021.1997571.

58. Kampouris, D.K. and C.E. Banks, Exploring the Physicoelectrochemical Properties of Graphene. *Chem. Commun. (Camb.)*, 2010. **46**(47): p. 8986. DOI: 10.1039/c0cc02860f.

59. Chen, Y., et al., Nanomaterials-Based Sensitive Electrochemiluminescence Biosensing. *Nano Today*, 2017. **12**: p. 98. DOI: 10.1016/j.nantod.2016.12.013.

60. Dakshayini, B.S., et al., Role of Conducting Polymer and Metal Oxide-Based Hybrids for Applications in Ampereometric Sensors and Biosensors. *Microchem. J.*, 2019. **147**: p. 7. DOI: 10.1016/j.microc.2019.02.061.

61. Huang, J., et al., Editors' Choice—Review—Impedance Response of Porous Electrodes: Theoretical Framework, Physical Models and Applications. *J. Electrochem. Soc.*, 2020. **167**(16): p. 166503. DOI: 10.1149/1945-7111/abc655.

62. Nemiwal, M., T.C. Zhang, and D. Kumar, Enzyme Immobilized Nanomaterials as Electrochemical Biosensors for Detection of Biomolecules. *Enzyme Microb Technol*, 2022. **156**: p. 110006. DOI: 10.1016/j.enzmictec.2022.110006.

63. Punckt, C., M.A. Pope, and I.A. Aksay, On the Electrochemical Response of Porous Functionalized Graphene Electrodes. *J. Phys. Chem. C*, 2013. **117**(31): p. 16076.

DOI: 10.1021/jp405142k.

64. Menshykau, D. and R.G. Compton, The Influence of Electrode Porosity on Diffusional Cyclic Voltammetry. *Electroanalysis*, 2008. **20**(22): p. 2387. DOI: 10.1002/elan.200804334.

65. Punckt, C., et al., Electrochemical Performance of Graphene as Effected by Electrode Porosity and Graphene Functionalization. *Electroanalysis*, 2010. **22**(23): p. 2834. DOI: 10.1002/elan.201000367.

66. Veerakumar, P., et al., Research Progress on Porous Carbon Supported Metal/Metal Oxide Nanomaterials for Supercapacitor Electrode Applications. *Ind. Eng. Chem. Res.*, 2020. **59**(14): p. 6347. DOI: 10.1021/acs.iecr.9b06010.

67. Burke, M., et al., Fabrication and Electrochemical Properties of Three-Dimensional (3d) Porous Graphitic and Graphenelike Electrodes Obtained by Low-Cost Direct Laser Writing Methods. *ACS Omega*, 2020. **5**(3): p. 1540. DOI: 10.1021/acsomega.9b03418.

68. Mariani, F., et al., Micro- and Nano-Devices for Electrochemical Sensing. *Mikrochim. Acta*, 2022. **189**(12): p. 459. DOI: 10.1007/s00604-022-05548-3.

69. Mendelson, Y., *Biomedical Sensors*, in *Introduction to Biomedical Engineering*, J.D. Enderle and J.D. Bronzino, Editors. 2012, Academic Press: Boston. p. 609.

70. Cesewski, E. and B.N. Johnson, Electrochemical Biosensors for Pathogen Detection. *Biosens. Bioelectron.*, 2020. **159**. DOI: 10.1016/j.bios.2020.112214.

71. Laczka, O., et al., Detection of Escherichia Coli and Salmonella Typhimurium Using Interdigitated Microelectrode Capacitive Immunosensors: The Importance of Transducer Geometry. *Anal. Chem.*, 2008. **80**(19): p. 7239. DOI: 10.1021/ac800643k.

72. Lingenfelter, P., et al., Reference Electrodes with Polymer-Based Membranes-Comprehensive Performance Characteristics. *Membranes (Basel)*, 2019. **9**(12): p. 161. DOI: 10.3390/membranes9120161.

73. IUPAC. Compendium of Chemical Terminology, n.e.t.G.B.O.v.-. Standard Hydrogen Electrode. DOI: 10.1351/goldbook.

74. Troudt, B.K., et al., Recent Progress in the Development of Improved Reference Electrodes for Electrochemistry. *Anal Sci*, 2022. **38**(1): p. 71. DOI: 10.2116/analsci.21SAR11.

75. da Silva, E.T., et al., Simple on-Plastic/Paper Inkjet-Printed Solid-State Ag/Agcl Pseudoreference Electrode. *Anal. Chem.*, 2014. **86**(21): p. 10531. DOI: 10.1021/ac503029q.

76. Kudr, J., et al., Inkjet-Printed Electrochemically Reduced Graphene Oxide Microelectrode as a Platform for Ht-2 Mycotoxin Immunoenzymatic Biosensing. *Biosens. Bioelectron.*, 2020. **156**: p. 112109. DOI: 10.1016/j.bios.2020.112109.

77. Seguí Femenias, Y., et al., Ag/Agcl Ion-Selective Electrodes in Neutral and Alkaline Environments Containing Interfering Ions. *Mater. Struct.*, 2015. **49**(7): p. 2637. DOI: 10.1617/s11527-015-0673-8.

78. Granholm, K., et al., Analytical Quality Solid-State Composite Reference Electrode Manufactured by Injection Moulding. *J. Solid State Electrochem.*, 2013. **18**(3): p. 607. DOI: 10.1007/s10008-013-2294-x.

79. Tymecki, Ł., E. Zwierkowska, and R. Koncki, Screen-Printed Reference Electrodes for Potentiometric Measurements. *Anal. Chim. Acta*, 2004. **526**(1): p. 3. DOI: 10.1016/j.aca.2004.08.056.

80. Moya, A., et al., Stable Full-Inkjet-Printed Solid-State Ag/Agcl Reference Electrode. *Anal. Chem.*, 2019. **91**(24): p. 15539. DOI: 10.1021/acs.analchem.9b03441.

81. Walker, N.L. and J.E. Dick, Leakless, Bipolar Reference Electrodes: Fabrication, Performance, and Miniaturization. *Anal. Chem.*, 2021. **93**(29): p. 10065. DOI: 10.1021/acs.analchem.1c00675.

82. Lewenstam, A., T. Blaz, and J. Migdalski, All-Solid-State Reference Electrode with Heterogeneous Membrane. *Anal. Chem.*, 2017. **89**(2): p. 1068. DOI: 10.1021/acs.analchem.6b02762.

83. Tintelott, M., et al., Realization of a Pedot:Pss/Graphene Oxide on-Chip Pseudo-Reference Electrode for Integrated Isfets. *Sensors (Basel)*, 2022. **22**(8). DOI: 10.3390/s22082999.

84. Majidi, M.R., et al., Reusable Potentiometric Screen-Printed Sensor and Label-Free Aptasensor with Pseudo-Reference Electrode for Determination of Tryptophan in the Presence of Tyrosine. *Talanta*, 2016. **150**: p. 425. DOI: 10.1016/j.talanta.2015.12.064.

85. Miura, N., et al., Novel Solid-State Manganese Oxide-Based Reference Electrode for Ysz-Based Oxygen Sensors. *Sensors Actuators B: Chem.*, 2011. **152**(2): p. 261. DOI: 10.1016/j.snb.2010.12.018.

86. Rius-Ruiz, F.X., et al., Disposable Planar Reference Electrode Based on Carbon Nanotubes and Polyacrylate Membrane. *Anal. Chem.*, 2011. **83**(14): p. 5783. DOI: 10.1021/ac200627h.

87. Lee, J., et al., Porous Carbon as a Quasi-Reference Electrode in Aqueous Electrolytes. *Electrochim. Acta*, 2016. **222**: p. 1800. DOI: 10.1016/j.electacta.2016.11.148.

88. Maloy, J.T., Factors Affecting the Shape of Current-Potential Curves. *J. Chem. Educ.*, 1983. **60**(4): p. 285. DOI: 10.1021/ed060p285.

89. Behrent, A., et al., Process-Property Correlations in Laser-Induced Graphene Electrodes for Electrochemical Sensing. *Mikrochim. Acta*, 2021. **188**(5): p. 159. DOI: 10.1007/s00604-021-04792-3.

90. Griffiths, K., et al., Laser-Scribed Graphene Presents an Opportunity to Print a New Generation of Disposable Electrochemical Sensors. *Nanoscale*, 2014. **6**(22): p. 13613. DOI: 10.1039/c4nr04221b.

91. Vaughan, E., et al., Visible Laser Scribing Fabrication of Porous Graphitic Carbon Electrodes: Morphologies, Electrochemical Properties, and Applications as Disposable Sensor Platforms. *ACS Appl. Electron. Mater.*, 2020. **2**(10): p. 3279. DOI: 10.1021/acsaelm.0c00612.

92. Konopka, S.J. and B. McDuffie, Diffusion Coefficients of Ferri- and Ferrocyanide Ions in Aqueous Media, Using Twin-Electrode Thin-Layer Electrochemistry. *Anal. Chem.*, 2002. **42**(14): p. 1741. DOI: 10.1021/ac50160a042.

93. Voiry, D., et al., Best Practices for Reporting Electrocatalytic Performance of Nanomaterials. *ACS Nano*, 2018. **12**(10): p. 9635. DOI: 10.1021/acsnano.8b07700.

94. Zankowski, S.P. and P.M. Vereecken, Electrochemical Determination of Porosity and Surface Area of Thin Films of Interconnected Nickel Nanowires. *J. Electrochem. Soc.*, 2019. **166**(6): p. D227. DOI: 10.1149/2.0311906jes.

95. Furst, A.L. and M.B. Francis, Impedance-Based Detection of Bacteria. *Chem Rev*, 2019. **119**(1): p. 700. DOI: 10.1021/acs.chemrev.8b00381.

96. Wei, M., et al., How to Choose a Proper Theoretical Analysis Model Based on Cell Adhesion and Nonadhesion Impedance Measurement. *ACS Sens*, 2021. **6**(3): p. 673. DOI: 10.1021/acssensors.0c02710.

97. Brosel-Oliu, S., et al., Impedimetric Transducers Based on Interdigitated Electrode Arrays for Bacterial Detection - a Review. *Anal. Chim. Acta*, 2019. **1088**: p. 1. DOI: 10.1016/j.aca.2019.09.026.

98. *Point of Care & Rapid Diagnostics Market by Product* 2022 25th Spt]; Available from: https://www.marketsandmarkets.com/Market-Reports/point-of-care-diagnostic-market-106829185.html?gclid=CjwKCAjw-L-ZBhB4EiwA76YzOeh67ZTyKolUds78uH9VeOoTeZ7d9w5avGjBEw_0aK8rZi5lSOyjXRoC-20QAvD_BwE.

99. Kost, G.J., N.K. Tran, and R.F. Louie, *Point-of-Care Testing: Principles, Practice, and Critical-Emergency-Disaster Medicine*, in *Encyclopedia of Analytical Chemistry*. 2008.

100. Quesada-Gonzalez, D. and A. Merkoci, Nanomaterial-Based Devices for Point-of-Care Diagnostic Applications. *Chem. Soc. Rev.*, 2018. **47**(13): p. 4697. DOI: 10.1039/c7cs00837f.

101. Kratz, A. and K.B. Lewandrowski, Principles & Practice of Point-of-Care Testing. *Arch. Pathol. Lab. Med.*, 2003. **127**(4): p. 511. DOI: 10.5858/2003-127-0511b-PPOPT.

102. Kettler, H., et al., *Mapping the Landscape of Diagnostics for Sexually Transmitted Infections : Key Findings and Recommendations / Hannah Kettler, Karen White, Sarah Hawkes*. 2004, World Health Organization: Geneva.

103. Land, K.J., et al., Reassured Diagnostics to Inform Disease Control Strategies, Strengthen Health Systems and Improve Patient Outcomes. *Nat Microbiol*, 2019. **4**(1): p. 46. DOI: 10.1038/s41564-018-0295-3.

104. Ning, Q., et al., Point-of-Care Biochemical Assays Using Electrochemical Technologies: Approaches, Applications, and Opportunities. *Mikrochim. Acta*, 2022. **189**(8): p. 310. DOI: 10.1007/s00604-022-05425-z.

105. Zhang, M., X. Cui, and N. Li, Smartphone-Based Mobile Biosensors for the Point-of-Care Testing of Human Metabolites. *Mater Today Bio*, 2022. **14**: p. 100254. DOI: 10.1016/j.mtbio.2022.100254.

106. Kulkarni, M.B., N.H. Ayachit, and T.M. Aminabhavi, Biosensors and Microfluidic Biosensors: From Fabrication to Application. *Biosensors (Basel)*, 2022. **12**(7): p. 543. DOI: 10.3390/bios12070543.

107. Zhang, D., et al., Detection of Pathogenic Microorganisms by Microfluidics Based Analytical Methods. *Anal. Chem.*, 2018. **90**(9): p. 5512. DOI: 10.1021/acs.analchem.8b00399.

108. Morgan, A.E. and G.A. Somorjai, Low Energy Electron Diffraction Studies of Gas

Adsorption on the Platinum (100) Single Crystal Surface. *Surface Science*, 1968. **12**(3): p. 405. DOI: 10.1016/0039-6028(68)90089-7.

109. Fitzer, E., et al., Recommended Terminology for the Description of Carbon as a Solid (Iupac Recommendations 1995). *Pure Appl. Chem.*, 1995. **67**(3): p. 473. DOI: 10.1351/pac199567030473.

110. Novoselov, K.S., et al., Electric Field Effect in Atomically Thin Carbon Films. *Science*, 2004. **306**(5696): p. 666. DOI: 10.1126/science.1102896.

111. Novoselov, K.S., et al., Two-Dimensional Gas of Massless Dirac Fermions in Graphene. *Nature*, 2005. **438**(7065): p. 197. DOI: 10.1038/nature04233.

112. O'Brien, R.C.C. *Graphene Market & 2d Materials Assessment 2023-2033*. 2022; Available from: https://www.idtechex.com/en/research-report/graphene-market-and-2d-materials-assessment-2023-2033/878.

113. Catania, F., et al., A Review on Recent Advancements of Graphene and Graphene-Related Materials in Biological Applications. *Applied Sciences*, 2021. **11**(2). DOI: 10.3390/app11020614.

114. Verma, M.L., et al., Synthesis and Application of Graphene-Based Sensors in Biology: A Review. *Environ. Chem. Lett.*, 2022. **20**(3): p. 2189. DOI: 10.1007/s10311-022-01404-1.

115. Ma, Y. and L. Zhi, Functionalized Graphene Materials: Definition, Classification, and Preparation Strategies. *Acta Physico-Chimica Sinica*, 2021: p. 2101004.

116. Ambrosi, A., et al., Electrochemistry of Graphene and Related Materials. *Chem. Rev.*, 2014. **114**(14): p. 7150. DOI: 10.1021/cr500023c.

117. Morozov, S.V., et al., Giant Intrinsic Carrier Mobilities in Graphene and Its Bilayer. *Phys. Rev. Lett.*, 2008. **100**(1): p. 016602. DOI: 10.1103/PhysRevLett.100.016602.

118. Stoller, M.D., et al., Graphene-Based Ultracapacitors. *Nano Lett.*, 2008. **8**(10): p. 3498. DOI: 10.1021/nl802558y.

119. Hernandez, Y., et al., High-Yield Production of Graphene by Liquid-Phase Exfoliation of Graphite. *Nat Nanotechnol*, 2008. **3**(9): p. 563. DOI: 10.1038/nnano.2008.215.

120. Compton, O.C. and S.T. Nguyen, Graphene Oxide, Highly Reduced Graphene Oxide, and Graphene: Versatile Building Blocks for Carbon-Based Materials. *Small*, 2010. **6**(6): p. 711. DOI: 10.1002/smll.200901934.

121. Brisebois, P.P. and M. Siaj, Harvesting Graphene Oxide – Years 1859 to 2019: A Review of Its Structure, Synthesis, Properties and Exfoliation. *J. Mater. Chem. C*, 2020. **8**(5): p. 1517. DOI: 10.1039/c9tc03251g.

122. Yu, W., et al., Progress in the Functional Modification of Graphene/Graphene Oxide: A Review. *RSC Advances*, 2020. **10**(26): p. 15328. DOI: 10.1039/d0ra01068e.

123. Lerf, A., 13c and 1h Mas Nmr Studies of Graphite Oxide and Its Chemically Modified Derivatives. *Solid State Ionics*, 1997. **101-103**: p. 857. DOI: 10.1016/s0167-2738(97)00319-6.

124. Chaudhary, K., et al., Protein Immobilization on Graphene Oxide or Reduced Graphene Oxide Surface and Their Applications: Influence over Activity, Structural and Thermal Stability of Protein. *Adv Colloid Interface Sci*, 2021. **289**: p. 102367.

DOI: 10.1016/j.cis.2021.102367.

125. Tarcan, R., et al., Reduced Graphene Oxide Today. *J. Mater. Chem. C*, 2020. **8**(4): p. 1198. DOI: 10.1039/c9tc04916a.

126. Bacon, M., S.J. Bradley, and T. Nann, Graphene Quantum Dots. *Particle & Particle Systems Characterization*, 2014. **31**(4): p. 415. DOI: 10.1002/ppsc.201300252.

127. Sun, Z., S. Fang, and Y.H. Hu, 3d Graphene Materials: From Understanding to Design and Synthesis Control. *Chem Rev*, 2020. **120**(18): p. 10336. DOI: 10.1021/acs.chemrev.0c00083.

128. Gosai, A., et al., Application of Functionalized Graphene Oxide Based Biosensors for Health Monitoring: Simple Graphene Derivatives to 3d Printed Platforms. *Biosensors (Basel)*, 2021. **11**(10). DOI: 10.3390/bios11100384.

129. Arshad, F., et al., Applications of Graphene-Based Electrochemical and Optical Biosensors in Early Detection of Cancer Biomarkers. *Colloids Surf. B. Biointerfaces*, 2022. **212**: p. 112356. DOI: 10.1016/j.colsurfb.2022.112356.

130. Lee, J., et al., Biosensors Based on Graphene Oxide and Its Biomedical Application. *Adv Drug Deliv Rev*, 2016. **105**(Pt B): p. 275. DOI: 10.1016/j.addr.2016.06.001.

131. Malhotra, N., et al., Toxicity Studies on Graphene-Based Nanomaterials in Aquatic Organisms: Current Understanding. *Molecules*, 2020. **25**(16). DOI: 10.3390/molecules25163618.

132. Ema, M., M. Gamo, and K. Honda, A Review of Toxicity Studies on Graphene-Based Nanomaterials in Laboratory Animals. *Regul Toxicol Pharmacol*, 2017. **85**: p. 7. DOI: 10.1016/j.yrtph.2017.01.011.

133. Tonelli, F.M., et al., Graphene-Based Nanomaterials: Biological and Medical Applications and Toxicity. *Nanomedicine (Lond)*, 2015. **10**(15): p. 2423. DOI: 10.2217/nnm.15.65.

134. Akhavan, O. and E. Ghaderi, Toxicity of Graphene and Graphene Oxide Nanowalls against Bacteria. *ACS Nano*, 2010. **4**(10): p. 5731. DOI: 10.1021/nn101390x.

135. Devasena, T., A.P. Francis, and S. Ramaprabhu, *Toxicity of Graphene: An Update*, in *Reviews of Environmental Contamination and Toxicology Book Series (Rect,Volume 259)*, P. DeVoogt, Editor. 2021. p. 51.

136. Borandeh, S., et al., Graphene Family Nanomaterials in Ocular Applications: Physicochemical Properties and Toxicity. *Chem. Res. Toxicol.*, 2021. **34**(6): p. 1386. DOI: 10.1021/acs.chemrestox.0c00340.

137. Asok, et al., Graphene-Based Nanomaterials Toxicity in Fish. *Rev. Environ. Contam. Toxicol.*, 2018. DOI: 10.1007/398201815

138. Novoselov, K.S., et al., Electric Field Effect in Atomically Thin Carbon Films. *Science*, 2004. **306**(5696): p. 666. DOI: 10.1126/science.1102896.

139. Hernandez, Y., et al., High-Yield Production of Graphene by Liquid-Phase Exfoliation of Graphite. *Nature Nanotechnology*, 2008. **3**(9): p. 563. DOI: 10.1038/nnano.2008.215.

140. Blake, P., et al., Graphene-Based Liquid Crystal Device. *Nano Lett.*, 2008. **8**(6): p. 1704. DOI: 10.1021/nl080649i.

141. Li, X., et al., Highly Conducting Graphene Sheets and Langmuir-Blodgett Films. *Nat Nanotechnol*, 2008. **3**(9): p. 538. DOI: 10.1038/nnano.2008.210.

142. Lotya, M., et al., Liquid Phase Production of Graphene by Exfoliation of Graphite in Surfactant/Water Solutions. *J Am Chem Soc*, 2009. **131**(10): p. 3611. DOI: 10.1021/ja807449u.

143. Lotya, M., et al., High-Concentration, Surfactant-Stabilized Graphene Dispersions. *ACS Nano*, 2010. **4**(6): p. 3155. DOI: 10.1021/nn1005304.

144. Englert, J.M., et al., Soluble Graphene: Generation of Aqueous Graphene Solutions Aided by a Perylenebisimide-Based Bolaamphiphile. *Adv. Mater.*, 2009. **21**(42): p. 4265. DOI: 10.1002/adma.200901578.

145. Mohan, V.B., et al., Graphene-Based Materials and Their Composites: A Review on Production, Applications and Product Limitations. *Composites Part B: Engineering*, 2018. **142**: p. 200. DOI: 10.1016/j.compositesb.2018.01.013.

146. Brodie, B.C., On the Atomic Weight of Graphite. *Philos. Trans. R. Soc. London*, 1859. **149**(1): p. 249.

147. Staudenmaier, L., Method for the Preparation of Graphitic Acid *Ber. Dtsch. Chem. Ges.*, 1898. **31**: p. 1481. DOI: 10.1002/cber.18980310237

148. Hummers, W.S. and R.E. Offeman, Preparation of Graphitic Oxide. *J. Am. Chem. Soc.*, 2002. **80**(6): p. 1339. DOI: 10.1021/ja01539a017.

149. Dreyer, D.R., R.S. Ruoff, and C.W. Bielawski, From Conception to Realization: An Historial Account of Graphene and Some Perspectives for Its Future. *Angew Chem Int Ed Engl*, 2010. **49**(49): p. 9336. DOI: 10.1002/anie.201003024.

150. Marcano, D.C., et al., Improved Synthesis of Graphene Oxide. *ACS Nano*, 2010. **4**(8): p. 4806. DOI: 10.1021/nn1006368.

151. Keramat, A., et al., The Potential of Graphene Oxide and Reduced Graphene Oxide in Diagnosis and Treatment of Cancer. *Curr. Med. Chem.*, 2022. **29**(26): p. 4529. DOI: 10.2174/0929867329666220208092157.

152. Gutiérrez-Cruz, A., et al., A Review of Top-Down and Bottom-up Synthesis Methods for the Production of Graphene, Graphene Oxide and Reduced Graphene Oxide. *J. Mater. Sci.*, 2022. **57**(31): p. 14543. DOI: 10.1007/s10853-022-07514-z.

153. Toh, S.Y., et al., Graphene Production Via Electrochemical Reduction of Graphene Oxide: Synthesis and Characterisation. *Chem. Eng. J.*, 2014. **251**: p. 422. DOI: 10.1016/j.cej.2014.04.004.

154. Kumar, R., et al., Laser-Assisted Synthesis, Reduction and Micro-Patterning of Graphene: Recent Progress and Applications. *Coordination Chemistry Reviews*, 2017. **342**: p. 34. DOI: 10.1016/j.ccr.2017.03.021.

155. Lu, Z., et al., Novel Flexible Bifunctional Amperometric Biosensor Based on Laser Engraved Porous Graphene Array Electrodes: Highly Sensitive Electrochemical Determination of Hydrogen Peroxide and Glucose. *J. Hazard. Mater.*, 2021. **402**: p. 123774. DOI: 10.1016/j.jhazmat.2020.123774.

156. Giacomelli, C., et al., Selective Stamping of Laser Scribed Rgo Nanofilms: From Sensing to Multiple Applications. *2D Materials*, 2020. **7**(2). DOI: 10.1088/2053-1583/ab68a7.

157. Kurra, N., et al., Laser-Derived Graphene: A Three-Dimensional Printed Graphene Electrode and Its Emerging Applications. *Nano Today*, 2019. **24**: p. 81. DOI: 10.1016/j.nantod.2018.12.003.

158. Chyan, Y., et al., Laser-Induced Graphene by Multiple Lasing: Toward Electronics on Cloth, Paper, and Food. *ACS Nano*, 2018. **12**(3): p. 2176. DOI: 10.1021/acsnano.7b08539.

159. El-Kady, M.F., et al., Laser Scribing of High-Performance and Flexible Graphene-Based Electrochemical Capacitors. *Science*, 2012. **335**(6074): p. 1326. DOI: 10.1126/science.1216744.

160. Fei, Y., S. Fang, and Y.H. Hu, Synthesis, Properties and Potential Applications of Hydrogenated Graphene. *Chem. Eng. J.*, 2020. **397**. DOI: 10.1016/j.cej.2020.125408.

161. Whitener, K.E., Review Article: Hydrogenated Graphene: A User's Guide. *J. Vac. Sci. Technol*, 2018. **36**(5). DOI: 10.1116/1.5034433.

162. Malek Hosseini, S.M.B., et al., Excimer Laser Assisted Very Fast Exfoliation and Reduction of Graphite Oxide at Room Temperature under Air Ambient for Supercapacitors Electrode. *Appl. Surf. Sci.*, 2018. **427**: p. 507. DOI: 10.1016/j.apsusc.2017.08.029.

163. Zhu, Y., et al., Highly Sensitive and Skin-Like Pressure Sensor Based on Asymmetric Double-Layered Structures of Reduced Graphite Oxide. *Sensors Actuators B: Chem.*, 2018. **255**: p. 1262. DOI: 10.1016/j.snb.2017.08.116.

164. Shelton, J.C., H.R. Patil, and J.M. Blakely, Equilibrium Segregation of Carbon to a Nickel (111) Surface: A Surface Phase Transition. *Surface Science*, 1974. **43**(2): p. 493. DOI: 10.1016/0039-6028(74)90272-6.

165. Song, X., et al., Seed-Assisted Growth of Single-Crystalline Patterned Graphene Domains on Hexagonal Boron Nitride by Chemical Vapor Deposition. *Nano Lett.*, 2016. **16**(10): p. 6109. DOI: 10.1021/acs.nanolett.6b02279.

166. Bao, J., et al., Synthesis of Freestanding Graphene on Sic by a Rapid-Cooling Technique. *Phys. Rev. Lett.*, 2016. **117**(20): p. 205501. DOI: 10.1103/PhysRevLett.117.205501.

167. Hwang, W.S., et al., Graphene Nanoribbon Field-Effect Transistors on Wafer-Scale Epitaxial Graphene on Sic Substrates. *APL Materials*, 2015. **3**(1). DOI: 10.1063/1.4905155.

168. Lee, H.C., et al., *Synthesis of Single-Layer Graphene: A Review of Recent Development, in 5th International Conference on Recent Advances in Materials, Minerals and Environment (RAMM) & 2nd International Postgraduate Conference on Materials, Mineral and Polymer (MAMIP)*. 2016. p. 916.

169. Lee, X.J., et al., Review on Graphene and Its Derivatives: Synthesis Methods and Potential Industrial Implementation. *J. Taiwan Inst. Chem. Eng.*, 2019. **98**: p. 163. DOI: 10.1016/j.jtice.2018.10.028.

170. Park, J.B., et al., Fast Growth of Graphene Patterns by Laser Direct Writing. *Appl. Phys. Lett.*, 2011. **98**(12). DOI: 10.1063/1.3569720.

171. Liu, Z., et al., Laser Cvd Growth of Graphene/Sic/Si Nano-Matrix Heterostructure with Improved Electrochemical Capacitance and Cycle Stability. *Carbon*, 2021. **175**: p. 377. DOI: 10.1016/j.carbon.2021.01.004.

172. Wang, J., et al., Pulsed Laser Deposition of Monolayer and Bilayer Graphene. *Appl. Surf. Sci.*, 2019. **494**: p. 651. DOI: 10.1016/j.apsusc.2019.07.176.

173. Kaushik, V., et al., Sharp Folded Graphene Ribbons Formed by Co2 Laser Ablation for Electron Field Emission Studies. *Vacuum*, 2014. **110**: p. 1. DOI: 10.1016/j.vacuum.2014.07.032.

174. Juvaid, M.M., D. Kumar, and M.S. Ramachandra Rao, Realization of Good Quality Bilayer Graphene by Single Step Laser Ablation Process. *Mater. Res. Bull.*, 2020. **126**. DOI: 10.1016/j.materresbull.2020.110840.

175. An, M., et al., Double-Emission Mechanism of Laser-Induced Hopg-Exfoliated Graphene Quantum Dots (Gqds). *Appl. Phys. Lett.*, 2019. **114**(2). DOI: 10.1063/1.5081018.

176. Ismail, Z., Laser Writing of Graphene on Cellulose Paper and Analogous Material for Green and Sustainable Electronic: A Concise Review. *Carbon Letters*, 2022. **32**(5): p. 1227. DOI: 10.1007/s42823-022-00365-3.

177. Luong, D.X., et al., Gram-Scale Bottom-up Flash Graphene Synthesis. *Nature*, 2020. **577**(7792): p. 647. DOI: 10.1038/s41586-020-1938-0.

178. Stanford, M.G., et al., Flash Graphene Morphologies. *ACS Nano*, 2020. **14**(10): p. 13691. DOI: 10.1021/acsnano.0c05900.

179. Algozeeb, W.A., et al., Flash Graphene from Plastic Waste. *ACS Nano*, 2020. **14**(11): p. 15595. DOI: 10.1021/acsnano.0c06328.

180. Akhtar, K., et al., *Scanning Electron Microscopy: Principle and Applications in Nanomaterials Characterization*, in *Handbook of Materials Characterization*, S.K. Sharma, Editor. 2018, Springer International Publishing: Cham. p. 113.

181. Li, D., et al., Processable Aqueous Dispersions of Graphene Nanosheets. *Nat Nanotechnol*, 2008. **3**(2): p. 101. DOI: 10.1038/nnano.2007.451.

182. Zhang, H.-B., et al., Electrically Conductive Polyethylene Terephthalate/Graphene Nanocomposites Prepared by Melt Compounding. *Polymer*, 2010. **51**(5): p. 1191. DOI: 10.1016/j.polymer.2010.01.027.

183. Chen, X., X. Wang, and D. Fang, A Review on C1s Xps-Spectra for Some Kinds of Carbon Materials. *Fullerenes, Nanotubes and Carbon Nanostructures*, 2020. **28**(12): p. 1048. DOI: 10.1080/1536383x.2020.1794851.

184. Zhang, Y., et al., Molecular Surface Functionalization of Carbon Materials Via Radical-Induced Grafting of Terminal Alkenes. *J Am Chem Soc*, 2019. **141**(20): p. 8277. DOI: 10.1021/jacs.9b02369.

185. Parvez, K., et al., Water-Based and Inkjet Printable Inks Made by Electrochemically Exfoliated Graphene. *Carbon*, 2019. **149**: p. 213. DOI: 10.1016/j.carbon.2019.04.047.

186. Youn, H.C., et al., High-Surface-Area Nitrogen-Doped Reduced Graphene Oxide for Electric Double-Layer Capacitors. *ChemSusChem*, 2015. **8**(11): p. 1875. DOI: 10.1002/cssc.201500122.

187. Lesiak, B., et al., C Sp2/Sp3 Hybridisations in Carbon Nanomaterials – Xps and (X)Aes Study. *Appl. Surf. Sci.*, 2018. **452**: p. 223. DOI: 10.1016/j.apsusc.2018.04.269.

188. Sokolov, D.A., et al., Excimer Laser Reduction and Patterning of Graphite Oxide. *Carbon*, 2013. **53**: p. 81. DOI: 10.1016/j.carbon.2012.10.034.

189. Ferrari, A.C., et al., Raman Spectrum of Graphene and Graphene Layers. *Phys. Rev. Lett.*, 2006. **97**(18): p. 187401. DOI: 10.1103/PhysRevLett.97.187401.

190. Malard, L.M., et al., Raman Spectroscopy in Graphene. *Phys. Rep.*, 2009. **473**(5-6): p. 51. DOI: 10.1016/j.physrep.2009.02.003.

191. Piperno, A., et al., Casting Light on Intracellular Tracking of a New Functional Graphene-Based Microrna Delivery System by Flim and Raman Imaging. *ACS Appl. Mater. Interfaces*, 2019. **11**(49): p. 46101. DOI: 10.1021/acsami.9b15826.

192. Milani, A., et al., Raman Spectroscopy as a Tool to Investigate the Structure and Electronic Properties of Carbon-Atom Wires. *Beilstein J Nanotechnol*, 2015. **6**: p. 480. DOI: 10.3762/bjnano.6.49.

193. Wu, J.B., et al., Raman Spectroscopy of Graphene-Based Materials and Its Applications in Related Devices. *Chem. Soc. Rev.*, 2018. **47**(5): p. 1822. DOI: 10.1039/c6cs00915h.

194. Xu, L. and L. Cheng, Graphite Oxide under High Pressure: A Raman Spectroscopic Study. *J. Nanomater.*, 2013. **2013**: p. 731875. DOI: 10.1155/2013/731875.

195. Xu, L. and L. Cheng, Graphite Oxide under High Pressure: A Raman Spectroscopic Study. *J. Nanomater.*, 2013. **2013**: p. 1. DOI: 10.1155/2013/731875.

196. Das, A., et al., Monitoring Dopants by Raman Scattering in an Electrochemically Top-Gated Graphene Transistor. *Nat Nanotechnol*, 2008. **3**(4): p. 210. DOI: 10.1038/nnano.2008.67.

197. Nair, R.R., et al., Fluorographene: A Two-Dimensional Counterpart of Teflon. *Small*, 2010. **6**(24): p. 2877. DOI: 10.1002/smll.201001555.

198. Muzyka, K. and G. Xu, Laser-Induced Graphene in Facts, Numbers, and Notes in View of Electroanalytical Applications: A Review. *Electroanalysis*, 2021. **34**(4): p. 574. DOI: 10.1002/elan.202100425.

199. Ferrari, A.C., Raman Spectroscopy of Graphene and Graphite: Disorder, Electron–Phonon Coupling, Doping and Nonadiabatic Effects. *Solid State Commun.*, 2007. **143**(1-2): p. 47. DOI: 10.1016/j.ssc.2007.03.052.

200. Cançado, L., et al., General Equation for the Determination of the Crystallite Size L a of Nanographite by Raman Spectroscopy. *Appl. Phys. Lett.*, 2006. **88**(16): p. 163106.

201. Huet, B. and J.P. Raskin, Role of Cu Foil in-Situ Annealing in Controlling the Size and Thickness of Cvd Graphene Domains. *Carbon*, 2018. **129**: p. 270.

202. Chrisey, D.B. and A. Piqué, *Chapter 1 - Introduction to Direct-Write Technologies for Rapid Prototyping*, in *Direct-Write Technologies for Rapid Prototyping*, A. Piqué, Editor. 2002, Academic Press: San Diego. p. 1.

203. Chrisey, D.B. and A. Piqué, *Introduction to Direct-Write Technologies for Rapid Prototyping*, in *Direct-Write Technologies for Rapid Prototyping*, A. Piqué, Editor. 2002, Academic Press: San Diego. p. 1.

204. Lai, X., et al., Inkjet Pattern-Guided Liquid Templates on Superhydrophobic Substrates for Rapid Prototyping of Microfluidic Devices. *ACS Appl. Mater.*

Interfaces, 2020. **12**(1): p. 1817. DOI: 10.1021/acsami.9b17071.

205. Gabardo, C.M. and L. Soleymani, Deposition, Patterning, and Utility of Conductive Materials for the Rapid Prototyping of Chemical and Bioanalytical Devices. *Analyst*, 2016. **141**(12): p. 3511. DOI: 10.1039/c6an00210b.

206. Hon, K.K.B., L. Li, and I.M. Hutchings, Direct Writing Technology—Advances and Developments. *CIRP Annals*, 2008. **57**(2): p. 601. DOI: 10.1016/j.cirp.2008.09.006.

207. Lahcen, A.A., et al., Electrochemical Sensors and Biosensors Using Laser-Derived Graphene: A Comprehensive Review. *Biosens. Bioelectron.*, 2020. **168**: p. 112565. DOI: 10.1016/j.bios.2020.112565.

208. Muzyka, K. and G. Xu, Laser-Induced Graphene in Facts, Numbers, and Notes in View of Electroanalytical Applications: A Review. *Electroanalysis*, 2022. **34**(4): p. 574. DOI: 10.1002/elan.202100425.

209. Cho, K., T. Lee, and S. Chung, Inkjet Printing of Two-Dimensional Van Der Waals Materials: A New Route Towards Emerging Electronic Device Applications. *Nanoscale Horiz*, 2022. **7**(10): p. 1161. DOI: 10.1039/d2nh00162d.

210. Mensing, J.P., T. Lomas, and A. Tuantranont, 2d and 3d Printing for Graphene Based Supercapacitors and Batteries: A Review. *Sustainable Mater.Technol.*, 2020. **25**: p. e00190. DOI: 10.1016/j.susmat.2020.e00190.

211. Sukeshini A, M., et al., Aerosol Jet® Printing of Functionally Graded Sofc Anode Interlayer and Microstructural Investigation by Low Voltage Scanning Electron Microscopy. *J. Power Sources*, 2013. **224**: p. 295. DOI: 10.1016/j.jpowsour.2012.09.094.

212. Xia, Y., et al., 3d Architectured Graphene/Metal Oxide Hybrids for Gas Sensors: A Review. *Sensors (Basel)*, 2018. **18**(5). DOI: 10.3390/s18051456.

213. Griffiths, K., et al., Laser-Scribed Graphene Presents an Opportunity to Print a New Generation of Disposable Electrochemical Sensors. *NANOSCALE*, 2014. **6**(22): p. 13613. DOI: 10.1039/c4nr04221b.

214. Vozzi, G., et al., Microsyringe-Based Deposition of Two-Dimensional and Three-Dimensional Polymer Scaffolds with a Well-Defined Geometry for Application to Tissue Engineering. *Tissue Eng.*, 2002. **8**(6): p. 1089. DOI: 10.1089/107632702320934182.

215. Salaita, K., et al., Massively Parallel Dip-Pen Nanolithography with 55 000-Pen Two-Dimensional Arrays. *Angew Chem Int Ed Engl*, 2006. **45**(43): p. 7220. DOI: 10.1002/anie.200603142.

216. Jang, J., et al., Self-Assembly of Ink Molecules in Dip-Pen Nanolithography: A Diffusion Model. *J. Phys. Chem. C*, 2001. **115**(6): p. 2721. DOI: 10.1063/1.1384550.

217. Li, Z., et al., Covalent Patterning of Graphene for Controllable Functionalization from Microscale to Nanoscale: A Mini-Review. *Front Chem*, 2022. **10**: p. 829614. DOI: 10.3389/fchem.2022.829614.

218. Shukla, S., S.-Y. Kang, and S. Saxena, Synthesis and Patterning of Graphene: Strategies and Prospects. *Applied Physics Reviews*, 2019. **6**(2). DOI: 10.1063/1.5055624.

219. Jiang, H., et al., Review of Photoreduction and Synchronous Patterning of Graphene

Oxide toward Advanced Applications. *J. Mater. Sci.*, 2019. **55**(2): p. 480. DOI: 10.1007/s10853-019-03981-z.

220. Hu, G., et al., Functional Inks and Printing of Two-Dimensional Materials. *Chem. Soc. Rev.*, 2018. **47**(9): p. 3265. DOI: 10.1039/c8cs00084k.

221. Jang, D., D. Kim, and J. Moon, Influence of Fluid Physical Properties on Ink-Jet Printability. *Langmuir*, 2009. **25**(5): p. 2629. DOI: 10.1021/la900059m.

222. Alaman, J., et al., Inkjet Printing of Functional Materials for Optical and Photonic Applications. *Materials (Basel)*, 2016. **9**(11). DOI: 10.3390/ma9110910.

223. Chung, S., K. Cho, and T. Lee, Recent Progress in Inkjet-Printed Thin-Film Transistors. *Adv Sci (Weinh)*, 2019. **6**(6): p. 1801445. DOI: 10.1002/advs.201801445.

224. Du, Z., X. Yu, and Y. Han, Inkjet Printing of Viscoelastic Polymer Inks. *Chin. Chem. Lett.*, 2018. **29**(3): p. 399. DOI: 10.1016/j.cclet.2017.09.031.

225. Gao, M., L. Li, and Y. Song, Inkjet Printing Wearable Electronic Devices. *J. Mater. Chem. C*, 2017. **5**(12): p. 2971. DOI: 10.1039/c7tc00038c.

226. Farooqui, M.F. and A. Shamim, Low Cost Inkjet Printed Smart Bandage for Wireless Monitoring of Chronic Wounds. *Sci. Rep.*, 2016. **6**: p. 28949. DOI: 10.1038/srep28949.

227. Raut, N.C. and K. Al-Shamery, Inkjet Printing Metals on Flexible Materials for Plastic and Paper Electronics. *J. Mater. Chem. C*, 2018. **6**(7): p. 1618. DOI: 10.1039/c7tc04804a.

228. Remuinan-Pose, P., et al., Preparation of Vancomycin-Loaded Aerogels Implementing Inkjet Printing and Superhydrophobic Surfaces. *Gels*, 2022. **8**(7): p. 417. DOI: 10.3390/gels8070417.

229. Pz, A., et al., Thermally Stable, Adhesively Strong Graphene/Polyimide Films for Inkjet Printing Ultrasound Sensors. *Carbon*, 2021.

230. Perello-Roig, R., et al., Cmos-Mems Voc Sensors Functionalized Via Inkjet Polymer Deposition for High-Sensitivity Acetone Detection. *Lab Chip*, 2021. **21**(17): p. 3307. DOI: 10.1039/d1lc00484k.

231. Huang, T.T. and W. Wu, Inkjet-Printed Wearable Nanosystems for Self-Powered Technologies. *Advanced Materials Interfaces*, 2020. **7**(12): p. 2000015. DOI: 10.1002/admi.202000015.

232. Prabhakaran, P., et al., Prospect and Retrospect of 3d Bio-Printing. *Acta Histochem*, 2022. **124**(7): p. 151932. DOI: 10.1016/j.acthis.2022.151932.

233. Persaud, A., et al., 3d Bioprinting with Live Cells. *Engineered Regeneration*, 2022. **3**(3): p. 292. DOI: 10.1016/j.engreg.2022.07.002.

234. Xu, J., et al., Chitosan-Based High-Strength Supramolecular Hydrogels for 3d Bioprinting. *Int J Biol Macromol*, 2022. **219**: p. 545. DOI: 10.1016/j.ijbiomac.2022.07.206.

235. Rayleigh, L., On the Instability of Jets. *Proceedings of the London Mathematical Society*, 1878. **s1-10**(1): p. 4. DOI: 10.1112/plms/s1-10.1.4.

236. Rayleigh, L., Some Applications of Photography1. *Nature*, 1891. **44**(1133): p. 249. DOI: 10.1038/044249e0.

237. Sweet, R.G., Cumming, Raymond C., *Fluid Droplet Recorder with a Plurality of Jets*. 1968, RICHARD G. SWEET,RAYMOND C. CUMMING: United States.

238. Sweet, R.G., High Frequency Recording with Electrostatically Deflected Ink Jets. *Rev. Sci. Instrum.*, 1965. **36**(2): p. 131. DOI: 10.1063/1.1719502.

239. Schneider, J.M. and C.D. Hendricks, Source of Uniform-Sized Liquid Droplets. *Rev. Sci. Instrum.*, 1964. **35**(10): p. 1349. DOI: 10.1063/1.1718742.

240. I, Z.S., *Pulsed Droplet Ejecting System*. 1972, CLEVITE CORP.: United States.

241. Winston, C.R., *Method of and Apparatus for Transferring Ink*. 1962: United States.

242. *The Future of Inkjet Printing to 2027*. [cited 2022 09-16]; Available from: https://www.smithers.com/services/market-reports/printing/the-future-of-inkjet-printing-to-2027.

243. Derby, B., *Inkjet Printing of Functional and Structural Materials: Fluid Property Requirements, Feature Stability, and Resolution*, in *Annual Review of Materials Research, Vol 40*, D.R. Clarke, M. Ruhle, and F. Zok, Editors. 2010. p. 395.

244. Chung, S., et al., Inkjet-Printed Stretchable Silver Electrode on Wave Structured Elastomeric Substrate. *Appl. Phys. Lett.*, 2011. **98**(15). DOI: 10.1063/1.3578398.

245. Sui, Y. and C.A. Zorman, Review—Inkjet Printing of Metal Structures for Electrochemical Sensor Applications. *J. Electrochem. Soc.*, 2020. **167**(3): p. 037571. DOI: 10.1149/1945-7111/ab721f.

246. de Gans, B.J., P.C. Duineveld, and U.S. Schubert, Inkjet Printing of Polymers: State of the Art and Future Developments. *Adv. Mater.*, 2004. **16**(3): p. 203. DOI: 10.1002/adma.200300385.

247. Kudr, J., et al., Inkjet-Printed Electrochemically Reduced Graphene Oxide Microelectrode as a Platform for Ht-2 Mycotoxin Immunoenzymatic Biosensing. *Biosens. Bioelectron.*, 2020. **156**(January): p. 112109. DOI: 10.1016/j.bios.2020.112109.

248. Martínez-Domingo, C., et al., Organic-Based Field Effect Transistors for Protein Detection Fabricated by Inkjet-Printing. *Org. Electron.*, 2020. **84**: p. 105794. DOI: 10.1016/j.orgel.2020.105794.

249. Medina-Sánchez, M., et al., An Inkjet-Printed Field-Effect Transistor for Label-Free Biosensing. *Adv. Funct. Mater.*, 2014. **24**(40): p. 6291. DOI: 10.1002/adfm.201401180.

250. Bialas, K., et al., Electrochemical Sensors Based on Metal Nanoparticles with Biocatalytic Activity. *Mikrochim. Acta*, 2022. **189**(4): p. 172. DOI: 10.1007/s00604-022-05252-2.

251. Kang, D.J., L. Gonzaléz-García, and T. Kraus, Soft Electronics by Inkjet Printing Metal Inks on Porous Substrates. *Flexible and Printed Electronics*, 2022. **7**(3): p. 033001. DOI: 10.1088/2058-8585/ac8360.

252. Kamyshny, A. and S. Magdassi, Conductive Nanomaterials for 2d and 3d Printed Flexible Electronics. *Chem. Soc. Rev.*, 2019. **48**(6): p. 1712. DOI: 10.1039/c8cs00738a.

253. Kwon, K.-S., et al., Review of Digital Printing Technologies for Electronic Materials. *Flexible and Printed Electronics*, 2020. **5**(4): p. 043003. DOI: 10.1088/2058-

8585/abc8ca.

254. Abdolmaleki, H., P. Kidmose, and S. Agarwala, Droplet-Based Techniques for Printing of Functional Inks for Flexible Physical Sensors. *Adv. Mater.*, 2021. **33**(20): p. e2006792. DOI: 10.1002/adma.202006792.

255. Hussin, H., et al., Review—Recent Progress in the Diversity of Inkjet-Printed Flexible Sensor Structures in Biomedical Engineering Applications. *J. Electrochem. Soc.*, 2021. **168**(7): p. 077508. DOI: 10.1149/1945-7111/ac0e4b.

256. Tran, T.S., N.K. Dutta, and N.R. Choudhury, Graphene Inks for Printed Flexible Electronics: Graphene Dispersions, Ink Formulations, Printing Techniques and Applications. *Adv Colloid Interface Sci*, 2018. **261**: p. 41. DOI: 10.1016/j.cis.2018.09.003.

257. Sundriyal, P. and S. Bhattacharya, Inkjet-Printed Electrodes on A4 Paper Substrates for Low-Cost, Disposable, and Flexible Asymmetric Supercapacitors. *ACS Appl Mater Interfaces*, 2017. **9**(44): p. 38507. DOI: 10.1021/acsami.7b11262.

258. Htwe, Y.Z.N. and M. Mariatti, Printed Graphene and Hybrid Conductive Inks for Flexible, Stretchable, and Wearable Electronics: Progress, Opportunities, and Challenges. *J Sci-Adv Mater Dev*, 2022. **7**(2): p. 20. DOI: 10.1016/j.jsamd.2022.100435.

259. Fromm, J.E., Numerical Calculation of the Fluid Dynamics of Drop-on-Demand Jets. *IBM J. Res. Dev.*, 1984. **28**(3): p. 322. DOI: 10.1147/rd.283.0322.

260. Derby, B., et al., Freeform Fabrication of Ceramics by Hot-Melt Ink-Jet Printing. *MRS Proceedings*, 2011. **625**: p. 195. DOI: 10.1557/proc-625-195.

261. You, M., et al., Inkjet Printing of Upconversion Nanoparticles for Anti-Counterfeit Applications. *Nanoscale*, 2015. **7**(10): p. 4423. DOI: 10.1039/c4nr06944g.

262. Yoo, H. and C. Kim, Experimental Studies on Formation, Spreading and Drying of Inkjet Drop of Colloidal Suspensions. *Colloids Surf. Physicochem. Eng. Aspects*, 2015. **468**: p. 234. DOI: 10.1016/j.colsurfa.2014.12.032.

263. Li, X., et al., Inkjet Bioprinting of Biomaterials. *Chem Rev*, 2020. **120**(19): p. 10793. DOI: 10.1021/acs.chemrev.0c00008.

264. Nayak, L., et al., A Review on Inkjet Printing of Nanoparticle Inks for Flexible Electronics. *J. Mater. Chem. C*, 2019. **7**(29): p. 8771. DOI: 10.1039/c9tc01630a.

265. Lemarchand, J., et al., Challenges, Prospects, and Emerging Applications of Inkjet-Printed Electronics: A Chemist's Point of View. *Angew Chem Int Ed Engl*, 2022. **61**(20): p. e202200166. DOI: 10.1002/anie.202200166.

266. Zub, K., S. Hoeppener, and U.S. Schubert, Inkjet Printing and 3d Printing Strategies for Biosensing, Analytical, and Diagnostic Applications. *Adv. Mater.*, 2022. **34**(31): p. e2105015. DOI: 10.1002/adma.202105015.

267. Komuro, N., et al., Inkjet Printed (Bio)Chemical Sensing Devices. *Anal Bioanal Chem*, 2013. **405**(17): p. 5785. DOI: 10.1007/s00216-013-7013-z.

268. Mandsberg, N.K., et al., Consumer-Grade Inkjet Printer for Versatile and Precise Chemical Deposition. *ACS Omega*, 2021. **6**(11): p. 7786. DOI: 10.1021/acsomega.1c00282.

269. Yang, Q., et al., Wearable and Fully Printed Microfluidic Nanosensor for Sweat Rate,

Conductivity, and Copper Detection with Healthcare Applications. *Biosens. Bioelectron.*, 2022. **202**: p. 114005. DOI: 10.1016/j.bios.2022.114005.

270. Blom, H., et al., Data-Enriched Edible Pharmaceuticals (Deep) of Medical Cannabis by Inkjet Printing. *Int. J. Pharm.*, 2020. **589**: p. 119866.

271. Sartori, A.F., et al., Inkjet-Printed High-Q Nanocrystalline Diamond Resonators. *Small*, 2019. **15**(4): p. e1803774. DOI: 10.1002/smll.201803774.

272. Lai, X., et al., Inkjet Pattern-Guided Liquid Templates on Superhydrophobic Substrates for Rapid Prototyping of Microfluidic Devices. *ACS Appl. Mater. Interfaces*, 2020. **12**(1): p. 1817. DOI: 10.1021/acsami.9b17071.

273. Yoshioka, Y. and G.E. Jabbour, Desktop Inkjet Printer as a Tool to Print Conducting Polymers. *Synth. Met.*, 2006. **156**(11-13): p. 779.

274. Htwe, Y.Z.N., et al., Properties Enhancement of Graphene and Chemical Reduction Silver Nanoparticles Conductive Inks Printed on Polyvinyl Alcohol (Pva) Substrate. *Synth. Met.*, 2019. **256**. DOI: 10.1016/j.synthmet.2019.116120.

275. Li, N., et al., A Fully Inkjet-Printed Transparent Humidity Sensor Based on a Ti(3)C(2)/Ag Hybrid for Touchless Sensing of Finger Motion. *Nanoscale*, 2019. **11**(44): p. 21522. DOI: 10.1039/c9nr06751e.

276. Torrisi, F., et al., Inkjet-Printed Graphene Electronics. *ACS Nano*, 2012. **6**(4): p. 2992. DOI: 10.1021/nn2044609.

277. Huang, L., et al., Graphene-Based Conducting Inks for Direct Inkjet Printing of Flexible Conductive Patterns and Their Applications in Electric Circuits and Chemical Sensors. *Nano Research*, 2011. **4**(7): p. 675. DOI: 10.1007/s12274-011-0123-z.

278. Kordas, K., et al., Inkjet Printing of Electrically Conductive Patterns of Carbon Nanotubes. *Small*, 2006. **2**(8-9): p. 1021. DOI: 10.1002/smll.200600061.

279. Lee, J., B. Purushothaman, and J.M. Song, Inkjet Bioprinting on Parchment Paper for Hit Identification from Small Molecule Libraries. *ACS Omega*, 2020. **5**(1): p. 588. DOI: 10.1021/acsomega.9b03169.

280. Rivadeneyra, A., et al. *Cost-Effective Pedot:Pss Temperature Sensors Inkjetted on a Bendable Substrate by a Consumer Printer*. Polymers, 2019. **11**, DOI: 10.3390/polym11050824.

281. da Costa, T.H. and J.-W. Choi, Low-Cost and Customizable Inkjet Printing for Microelectrodes Fabrication. *Micro and Nano Systems Letters*, 2020. **8**(1). DOI: 10.1186/s40486-020-0104-7.

282. Waasdorp, R., et al., Accessing Individual 75-Micron Diameter Nozzles of a Desktop Inkjet Printer to Dispense Picoliter Droplets on Demand. *RSC Advances*, 2018. **8**(27): p. 14765. DOI: 10.1039/c8ra00756j.

283. Deegan, R.D., et al., Capillary Flow as the Cause of Ring Stains from Dried Liquid Drops. *Nature*, 1997. **389**(6653): p. 827. DOI: 10.1038/39827.

284. Hu, G., et al., A General Ink Formulation of 2d Crystals for Wafer-Scale Inkjet Printing. *Science Advances*, 2020. **6**(33): p. eaba5029. DOI: 10.1126/sciadv.aba5029.

285. Hu, H. and R.G. Larson, Marangoni Effect Reverses Coffee-Ring Depositions. *J Phys Chem B*, 2006. **110**(14): p. 7090. DOI: 10.1021/jp0609232.

286. Seo, C., et al., Altering the Coffee-Ring Effect by Adding a Surfactant-Like Viscous Polymer Solution. *Sci. Rep.*, 2017. **7**(1): p. 500. DOI: 10.1038/s41598-017-00497-x.

287. Savino, R., D. Paterna, and N. Favaloro, Buoyancy and Marangoni Effects in an Evaporating Drop. *J. Thermophys Heat Transfer*, 2002. **16**(4): p. 562. DOI: 10.2514/2.6716.

288. J, M., D. D, and A.R. R, Review—Current Trends in Disposable Graphene-Based Printed Electrode for Electrochemical Biosensors. *J. Electrochem. Soc.*, 2020. **167**(6). DOI: 10.1149/1945-7111/ab818b.

289. Soltman, D. and V. Subramanian, Inkjet-Printed Line Morphologies and Temperature Control of the Coffee Ring Effect. *Langmuir*, 2008. **24**(5): p. 2224. DOI: 10.1021/la7026847.

290. He, P. and B. Derby, Controlling Coffee Ring Formation During Drying of Inkjet Printed 2d Inks. *Advanced Materials Interfaces*, 2017. **4**(22). DOI: 10.1002/admi.201700944.

291. Park, H.Y., et al., Control of Surface Wettability for Inkjet Printing by Combining Hydrophobic Coating and Plasma Treatment. *Thin Solid Films*, 2013. **546**: p. 162. DOI: 10.1016/j.tsf.2013.03.067.

292. Zhu, D., Z. Wang, and D. Zhu, Highly Conductive Graphene Electronics by Inkjet Printing. *J. Electron. Mater.*, 2020. **49**(3): p. 1765. DOI: 10.1007/s11664-019-07920-1.

293. Hassan, K., et al., Functional Inks and Extrusion-Based 3d Printing of 2d Materials: A Review of Current Research and Applications. *Nanoscale*, 2020. **12**(37): p. 19007. DOI: 10.1039/d0nr04933f.

294. Howe, R.C.T., et al., Surfactant-Aided Exfoliation of Molybdenum Disulfide for Ultrafast Pulse Generation through Edge-State Saturable Absorption. *physica status solidi (b)*, 2016. **253**(5): p. 911. DOI: 10.1002/pssb.201552304.

295. Maddipatla, D., B.B. Narakathu, and M. Atashbar, Recent Progress in Manufacturing Techniques of Printed and Flexible Sensors: A Review. *Biosensors (Basel)*, 2020. **10**(12). DOI: 10.3390/bios10120199.

296. Inagaki, M., et al., Carbonization and Graphitization of Polyimide Film "Novax". *Carbon*, 1991. **29**(8): p. 1239. DOI: 10.1016/0008-6223(91)90042-h.

297. Kamarudin, S.F., M. Mustapha, and J.-K. Kim, Green Strategies to Printed Sensors for Healthcare Applications. *Polymer Reviews*, 2020. **61**(1): p. 116. DOI: 10.1080/15583724.2020.1729180.

298. Öhlund, T., et al., Paper Surfaces for Metal Nanoparticle Inkjet Printing. *Appl. Surf. Sci.*, 2012. **259**: p. 731. DOI: 10.1016/j.apsusc.2012.07.112.

299. Xiang, H., et al., Green Flexible Electronics Based on Starch. *npj Flexible Electronics*, 2022. **6**(1): p. 15. DOI: 10.1038/s41528-022-00147-x.

300. Kant, T., et al., Inkjet-Printed Paper-Based Electrochemical Sensor with Gold Nano-Ink for Detection of Glucose in Blood Serum. *New J. Chem.*, 2021. **45**(18): p. 8297. DOI: 10.1039/d1nj00771h.

301. Li, L., et al., Transparent Ag@Au–Graphene Patterns with Conductive Stability Via Inkjet Printing. *J. Mater. Chem. C*, 2017. **5**(11): p. 2800. DOI: 10.1039/c6tc05227d.

302. Perelaer, J., B.J. de Gans, and U.S. Schubert, Ink-Jet Printing and Microwave Sintering of Conductive Silver Tracks. *Adv. Mater.*, 2006. **18**(16): p. 2101. DOI: 10.1002/adma.200502422.

303. Wolf, F.M., et al., Rapid Low-Pressure Plasma Sintering of Inkjet-Printed Silver Nanoparticles for Rfid Antennas. *J. Mater. Res.*, 2013. **28**(9): p. 1254.

304. Allen, M.L., et al., Electrical Sintering of Nanoparticle Structures. *Nanotechnology*, 2008. **19**(17): p. 175201. DOI: 10.1088/0957-4484/19/17/175201.

305. Beitollahi, H., M. Safaei, and S. Tajik, Application of Graphene and Graphene Oxide for Modification of Electrochemical Sensors and Biosensors: A Review. *Int J Nano Dimens*, 2019. **10**(2): p. 125.

306. Taniselass, S., M.K.M. Arshad, and S.C.B. Gopinath, Graphene-Based Electrochemical Biosensors for Monitoring Noncommunicable Disease Biomarkers. *Biosens. Bioelectron.*, 2019. **130**: p. 276. DOI: 10.1016/j.bios.2019.01.047.

307. Wang, J., et al., Ink-Based 3d Printing Technologies for Graphene-Based Materials: A Review. *Advanced Composites and Hybrid Materials*, 2019. **2**(1): p. 1. DOI: 10.1007/s42114-018-0067-9.

308. Hartwig, M., R. Zichner, and Y. Joseph, Inkjet-Printed Wireless Chemiresistive Sensors—a Review. *Chemosensors*, 2018. **6**(4): p. 66. DOI: 10.3390/chemosensors6040066.

309. Evans, S.E., et al., 2d and 3d Inkjet Printing of Biopharmaceuticals - a Review of Trends and Future Perspectives in Research and Manufacturing. *Int J Pharm*, 2021. **599**: p. 120443. DOI: 10.1016/j.ijpharm.2021.120443.

310. Pandhi, T., et al., A Review of Inkjet Printed Graphene and Carbon Nanotubes Based Gas Sensors. *Sensors (Basel)*, 2020. **20**(19). DOI: 10.3390/s20195642.

311. Htwe, Y.Z.N., M.K. Abdullah, and M. Mariatti, Optimization of Graphene Conductive Ink Using Solvent Exchange Techniques for Flexible Electronics Applications. *Synth. Met.*, 2021. **274**. DOI: 10.1016/j.synthmet.2021.116719.

312. Majee, S., et al., Scalable Inkjet Printing of Shear-Exfoliated Graphene Transparent Conductive Films. *Carbon*, 2016. **102**: p. 51. DOI: 10.1016/j.carbon.2016.02.013.

313. Htwe, Y.Z.N. and M. Mariatti, Printed Graphene and Hybrid Conductive Inks for Flexible, Stretchable, and Wearable Electronics: Progress, Opportunities, and Challenges. *J Sci-Adv Mater Dev*, 2022. **7**(2). DOI: 10.1016/j.jsamd.2022.100435.

314. Li, J., et al., Scalable Fabrication and Integration of Graphene Microsupercapacitors through Full Inkjet Printing. *ACS Nano*, 2017. **11**(8): p. 8249. DOI: 10.1021/acsnano.7b03354.

315. McManus, D., et al., Water-Based and Biocompatible 2d Crystal Inks for All-Inkjet-Printed Heterostructures. *Nat Nanotechnol*, 2017. **12**(4): p. 343. DOI: 10.1038/nnano.2016.281.

316. Li, J., et al., Efficient Inkjet Printing of Graphene. *Adv. Mater.*, 2013. **25**(29): p. 3985. DOI: 10.1002/adma.201300361.

317. Secor, E.B., et al., Inkjet Printing of High Conductivity, Flexible Graphene Patterns. *J. Phys. Chem. Lett.*, 2013. **4**(8): p. 1347. DOI: 10.1021/jz400644c.

318. Zeng, M., et al., Colloidal Nanosurfactants for 3d Conformal Printing of 2d Van Der

Waals Materials. *Adv. Mater.*, 2020. **32**(39): p. e2003081. DOI: 10.1002/adma.202003081.

319. Arapov, K., et al., Conductive Screen Printing Inks by Gelation of Graphene Dispersions. *Adv. Funct. Mater.*, 2016. **26**(4): p. 586. DOI: 10.1002/adfm.201504030.

320. Secor, E.B., et al., Rapid and Versatile Photonic Annealing of Graphene Inks for Flexible Printed Electronics. *Adv. Mater.*, 2015. **27**(42): p. 6683. DOI: 10.1002/adma.201502866.

321. Juntunen, T., et al., Inkjet Printed Large-Area Flexible Few-Layer Graphene Thermoelectrics. *Adv. Funct. Mater.*, 2018. **28**(22). DOI: 10.1002/adfm.201800480.

322. Pei, L. and Y.-F. Li, Rapid and Efficient Intense Pulsed Light Reduction of Graphene Oxide Inks for Flexible Printed Electronics. *RSC Advances*, 2017. **7**(81): p. 51711. DOI: 10.1039/c7ra10416b.

323. Vlăsceanu, G.M., H. Iovu, and M. Ioniţă, Graphene Inks for the 3d Printing of Cell Culture Scaffolds and Related Molecular Arrays. *Composites Part B: Engineering*, 2019. **162**: p. 712. DOI: 10.1016/j.compositesb.2019.01.010.

324. Song, D., et al., High-Resolution Transfer Printing of Graphene Lines for Fully Printed, Flexible Electronics. *ACS Nano*, 2017. **11**(7): p. 7431. DOI: 10.1021/acsnano.7b03795.

325. Htwe, Y.Z.N., M.K. Abdullah, and M. Mariatti, *Effect of Sodium Dodecyl Concentration on the Properties of Graphene Conductive Inks, in Materials Today: Proceedings*. 2022. p. 2836.

326. Khan, J. and M. Mariatti, Effect of Natural Surfactant on the Performance of Reduced Graphene Oxide Conductive Ink. *J. Cleaner Prod.*, 2022. **376**: p. 134254. DOI: 10.1016/j.jclepro.2022.134254.

327. Niaraki Asli, A.E., et al., High-Yield Production of Aqueous Graphene for Electrohydrodynamic Drop-on-Demand Printing of Biocompatible Conductive Patterns. *Biosensors (Basel)*, 2020. **10**(1): p. 6. DOI: 10.3390/bios10010006.

328. Capasso, A., et al., Ink-Jet Printing of Graphene for Flexible Electronics: An Environmentally-Friendly Approach. *Solid State Commun.*, 2015. **224**: p. 53. DOI: 10.1016/j.ssc.2015.08.011.

329. Khan, J., S.A. Momin, and M. Mariatti, A Review on Advanced Carbon-Based Thermal Interface Materials for Electronic Devices. *Carbon*, 2020. **168**: p. 65. DOI: 10.1016/j.carbon.2020.06.012.

330. Htwe, Y.Z.N., M.K. Abdullah, and M. Mariatti, Water-Based Graphene/Agnps Hybrid Conductive Inks for Flexible Electronic Applications. *J. Mater. Res. Technol.*, 2022. **16**: p. 59. DOI: 10.1016/j.jmrt.2021.11.159.

331. Deng, D., et al., In Situ Preparation of Silver Nanoparticles Decorated Graphene Conductive Ink for Inkjet Printing. *J. Mater. Sci.: Materials in Electronics*, 2017. **28**(20): p. 15411. DOI: 10.1007/s10854-017-7427-z.

332. Zhu, D. and M. Wu, Highly Conductive Nano-Silver Circuits by Inkjet Printing. *J. Electron. Mater.*, 2018. **47**(9): p. 5133. DOI: 10.1007/s11664-018-6418-z.

333. Hoon Seo, T., et al., Graphene-Silver Nanowire Hybrid Structure as a Transparent and Current Spreading Electrode in Ultraviolet Light Emitting Diodes. *Appl. Phys.*

Lett., 2013. **103**(5). DOI: 10.1063/1.4817256.

334. Wang, G., et al., Annealed Graphene Sheets Decorated with Silver Nanoparticles for Inkjet Printing. *Chem. Eng. J.*, 2015. **260**: p. 582. DOI: 10.1016/j.cej.2014.09.037.

335. Pan, D., et al., Functional Graphene-Gold Nano-Composite Fabricated Electrochemical Biosensor for Direct and Rapid Detection of Bisphenol A. *Anal. Chim. Acta*, 2015. **853**: p. 297. DOI: 10.1016/j.aca.2014.11.004.

336. Saidina, D.S., et al., Performance of Graphene Hybrid-Based Ink for Flexible Electronics. *J. Mater. Sci.: Materials in Electronics*, 2019. **30**(22): p. 19906. DOI: 10.1007/s10854-019-02357-y.

337. Xu, Y., et al., Inkjet-Printed Energy Storage Device Using Graphene/Polyaniline Inks. *J. Power Sources*, 2014. **248**: p. 483. DOI: 10.1016/j.jpowsour.2013.09.096.

338. Gong, Q., Y. Wang, and H. Yang, A Sensitive Impedimetric DNA Biosensor for the Determination of the Hiv Gene Based on Graphene-Nafion Composite Film. *Biosens. Bioelectron.*, 2017. **89**(Pt 1): p. 565. DOI: 10.1016/j.bios.2016.02.045.

339. Ghanbari, K. and S. Bonyadi, An Electrochemical Sensor Based on Pt Nanoparticles Decorated over-Oxidized Polypyrrole/Reduced Graphene Oxide Nanocomposite for Simultaneous Determination of Two Neurotransmitters Dopamine and 5-Hydroxy Tryptamine in the Presence of Ascorbic Acid. *Int. J. Polym. Anal. Charact.*, 2020. **25**(3): p. 1. DOI: 10.1080/1023666x.2020.1766785.

340. Wang, W., et al., A Label-Free Fiber Optic Spr Biosensor for Specific Detection of C-Reactive Protein. *Sci. Rep.*, 2017. **7**(1): p. 16904. DOI: 10.1038/s41598-017-17276-3.

341. Pollock, A.J., S.A. Zaver, and J.J. Woodward, A Sting-Based Biosensor Affords Broad Cyclic Dinucleotide Detection within Single Living Eukaryotic Cells. *Nat Commun*, 2020. **11**(1): p. 3533. DOI: 10.1038/s41467-020-17228-y.

342. Ryoo, S.R., et al., High-Throughput Chemical Screening to Discover New Modulators of Microrna Expression in Living Cells by Using Graphene-Based Biosensor. *Sci. Rep.*, 2018. **8**(1): p. 11413. DOI: 10.1038/s41598-018-29633-x.

343. El Barghouti, M., et al., *Enhancement of Localized Surface Plasmon Resonances of Silver Nanoparticles Array Upon the Presence of Graphene Coatings: Lspr Biosensor, in International Conference on Advanced Materials, Microscopy and Energy (ICAMME 2019)*. 2020.

344. Fan, S.Y., et al., Erratum: Simultaneous Real-Time Detection of Pregnancy-Associated Plasma Protein-a and -A2 Using a Graphene Oxide-Based Surface Plasmon Resonance Biosensor [Erratum]. *Int J Nanomedicine*, 2020. **15**: p. 2437. DOI: 10.2147/IJN.S256766.

345. Ge, Z., et al., A Novel Solution-Gated Graphene Transistor Biosensor for Ultrasensitive Detection of Trinucleotide Repeats. *Analyst*, 2020. **145**(14): p. 4795. DOI: 10.1039/d0an00205d.

346. He, X., et al., A Label-Free Electrochemical DNA Biosensor for Kanamycin Detection Based on Diblock DNA with Poly-Cytosine as a High Affinity Anchor on Graphene Oxide. *Anal Methods*, 2020. **12**(27): p. 3462. DOI: 10.1039/d0ay00025f.

347. Jalil, O., C.M. Pandey, and D. Kumar, Electrochemical Biosensor for the Epithelial Cancer Biomarker Epcam Based on Reduced Graphene Oxide Modified with

Nanostructured Titanium Dioxide. *Mikrochim. Acta*, 2020. **187**(5): p. 275. DOI: 10.1007/s00604-020-04233-7.

348. Kalkal, A., et al., Biofunctionalized Graphene Quantum Dots Based Fluorescent Biosensor toward Efficient Detection of Small Cell Lung Cancer. *ACS Appl. Bio Mater.*, 2020. **3**(8): p. 4922. DOI: 10.1021/acsabm.0c00427.

349. Wan, Z., et al., Laser Induced Graphene for Biosensors. *Sustainable Mater.Technol.*, 2020. **25**: p. e00205. DOI: 10.1016/j.susmat.2020.e00205.

350. Kralj, M., et al. *Conductive Inks Based on Melamine Intercalated Graphene Nanosheets for Inkjet Printed Flexible Electronics*. Nanomaterials, 2022. **12**, DOI: 10.3390/nano12172936.

351. Pandhi, T., et al., Fully Inkjet-Printed Multilayered Graphene-Based Flexible Electrodes for Repeatable Electrochemical Response. *RSC Advances*, 2020. **10**(63): p. 38205. DOI: 10.1039/d0ra04786d.

352. Hondred, J.A., I.L. Medintz, and J.C. Claussen, Enhanced Electrochemical Biosensor and Supercapacitor with 3d Porous Architectured Graphene Via Salt Impregnated Inkjet Maskless Lithography. *Nanoscale Horizons*, 2019. **4**(3): p. 735. DOI: 10.1039/c8nh00377g.

353. Nagar, B., et al., Highly Loaded Mildly Edge-Oxidized Graphene Nanosheet Dispersions for Large-Scale Inkjet Printing of Electrochemical Sensors. *ChemElectroChem*, 2020. **7**(2): p. 460. DOI: 10.1002/celc.201901697.

354. Zheng, J., et al., An Inkjet Printed Ti3c2-Go Electrode for the Electrochemical Sensing of Hydrogen Peroxide. *J. Electrochem. Soc.*, 2018. **165**(5): p. B227. DOI: 10.1149/2.0051807jes.

355. Bardpho, C., et al., Ultra-High Performance Liquid Chromatographic Determination of Antioxidants in Teas Using Inkjet-Printed Graphene-Polyaniline Electrode. *Talanta*, 2016. **148**: p. 673. DOI: 10.1016/j.talanta.2015.05.020.

356. Niaraki, A., et al., Minute-Sensitive Real-Time Monitoring of Neural Cells through Printed Graphene Microelectrodes. *Biosens. Bioelectron.*, 2022. **210**: p. 114284. DOI: 10.1016/j.bios.2022.114284.

357. Demuru, S., et al., All-Inkjet-Printed Graphene-Gated Organic Electrochemical Transistors on Polymeric Foil as Highly Sensitive Enzymatic Biosensors. *ACS Appl. Nano Mater.*, 2022. **5**(1): p. 1664. DOI: 10.1021/acsanm.1c04434.

358. Das, S.R., et al., 3d Nanostructured Inkjet Printed Graphene Via Uv-Pulsed Laser Irradiation Enables Paper-Based Electronics and Electrochemical Devices. *Nanoscale*, 2016. **8**(35): p. 15870. DOI: 10.1039/c6nr04310k.

359. Xiang, L., et al., Inkjet Printed Flexible Biosensor Based on Graphene Field Effect Transistor. *IEEE Sens. J.*, 2016. **16**(23): p. 1. DOI: 10.1109/jsen.2016.2608719.

360. Chen, Y., et al., Graphene-Based in-Planar Supercapacitors by a Novel Laser-Scribing, in-Situ Reduction and Transfer-Printed Method on Flexible Substrates. *J. Power Sources*, 2019. **420**: p. 82. DOI: 10.1016/j.jpowsour.2019.02.096.

361. Peng, Z., et al., A Multi-Functional No2 Gas Monitor and Self-Alarm Based on Laser-Induced Graphene. *Chem. Eng. J.*, 2022. **428**. DOI: 10.1016/j.cej.2021.131079.

362. Wang, H., et al., Laser-Induced Graphene Based Flexible Electronic Devices.

Biosensors (Basel), 2022. **12**(2). DOI: 10.3390/bios12020055.

363. Hoffman, J., et al., The Effect of Laser Wavelength on the Ablation Rate of Carbon. *Appl. Phys. A*, 2014. **117**(1): p. 395. DOI: 10.1007/s00339-014-8506-0.

364. Solati, E., M. Mashayekh, and D. Dorranian, Effects of Laser Pulse Wavelength and Laser Fluence on the Characteristics of Silver Nanoparticle Generated by Laser Ablation. *Appl. Phys. A*, 2013. **112**(3): p. 689. DOI: 10.1007/s00339-013-7812-2.

365. Gaumet, J.J., et al., Energetics for Carbon Clusters Produced Directly by Laser Vaporization of Graphite: Dependence on Laser Power and Wavelength. *J. Chem. Soc., Faraday Trans.*, 1993. **89**(11): p. 1667. DOI: 10.1039/ft9938901667.

366. Luo, S., P.T. Hoang, and T. Liu, Direct Laser Writing for Creating Porous Graphitic Structures and Their Use for Flexible and Highly Sensitive Sensor and Sensor Arrays. *Carbon*, 2016. **96**: p. 522. DOI: 10.1016/j.carbon.2015.09.076.

367. Stanford, M.G., et al., High-Resolution Laser-Induced Graphene. Flexible Electronics Beyond the Visible Limit. *ACS Appl. Mater. Interfaces* , 2020. **12**(9): p. 10902. DOI: 10.1021/acsami.0c01377.

368. Farson, D.F., et al., Femtosecond Laser Micromachining of Dielectric Materials for Biomedical Applications. *J. Micromech. Microeng.*, 2008. **18**(3): p. 035020. DOI: 10.1088/0960-1317/18/3/035020.

369. Loh, L.E., et al. *Effect of Laser Beam Profile on Melt Track in Selective Laser Melting*. in *6th International Conference on Advanced Research in Virtual and Physical Prototyping (VRatP)*. 2013. Leiria, PORTUGAL.

370. Jeong, Y.S., et al., Effect of Laser Beam Profile on the Ablated Hts Target Surface. *Physica C: Superconductivity*, 1997. **282-287**: p. 663. DOI: 10.1016/s0921-4534(97)00480-2.

371. Giacomelli, C., et al., Selective Stamping of Laser Scribed Rgo Nanofilms: From Sensing to Multiple Applications. *2D Materials*, 2020. **7**(2): p. 024006. DOI: 10.1088/2053-1583/ab68a7.

372. Joy Sarkar, M.R. *Laser Fading Technology: Facts and Opportunities*. 2019 [cited 2023 Feb 17]; Available from: https://www.textiletoday.com.bd/laser-fading-technology-facts-and-opportunities/.

373. *Laser Cutting Vs. Engraving Machinnes*. [cited 2023 Feb 17].

374. Qiu, H.J., et al., Recent Advance in Fabricating Monolithic 3d Porous Graphene and Their Applications in Biosensing and Biofuel Cells. *Biosens. Bioelectron.*, 2017. **89**(Pt 1): p. 85. DOI: 10.1016/j.bios.2015.12.029.

375. Chen, Z., et al., Three-Dimensional Flexible and Conductive Interconnected Graphene Networks Grown by Chemical Vapour Deposition. *Nat Mater*, 2011. **10**(6): p. 424. DOI: 10.1038/nmat3001.

376. Chen, K., et al., Scalable Chemical-Vapour-Deposition Growth of Three-Dimensional Graphene Materials Towards Energy-Related Applications. *Chem. Soc. Rev.*, 2018. **47**(9): p. 3018. DOI: 10.1039/c7cs00852j.

377. Sha, J., et al., Three-Dimensional Printed Graphene Foams. *ACS Nano*, 2017. **11**(7): p. 6860. DOI: 10.1021/acsnano.7b01987.

378. Xu, Y., et al., Self-Assembled Graphene Hydrogel Via a One-Step Hydrothermal

Process. *ACS Nano*, 2010. **4**(7): p. 4324. DOI: 10.1021/nn101187z.

379. Yang, X., et al., Liquid-Mediated Dense Integration of Graphene Materials for Compact Capacitive Energy Storage. *Science*, 2013. **341**(6145): p. 534. DOI: 10.1126/science.1239089.

380. Wu, Z.S., et al., Three-Dimensional Nitrogen and Boron Co-Doped Graphene for High-Performance All-Solid-State Supercapacitors. *Adv. Mater.*, 2012. **24**(37): p. 5130. DOI: 10.1002/adma.201201948.

381. Pei, S. and H.-M. Cheng, The Reduction of Graphene Oxide. *Carbon*, 2012. **50**(9): p. 3210. DOI: 10.1016/j.carbon.2011.11.010.

382. Strong, V., et al., Patterning and Electronic Tuning of Laser Scribed Graphene for Flexible All-Carbon Devices. *ACS Nano*, 2012. **6**(2): p. 1395. DOI: 10.1021/nn204200w.

383. Yang, L., et al., Intrinsically Breathable and Flexible No(2) Gas Sensors Produced by Laser Direct Writing of Self-Assembled Block Copolymers. *ACS Appl Mater Interfaces*, 2022. **14**(15): p. 17818. DOI: 10.1021/acsami.2c02061.

384. Gao, W., et al., Direct Laser Writing of Micro-Supercapacitors on Hydrated Graphite Oxide Films. *Nat Nanotechnol*, 2011. **6**(8): p. 496. DOI: 10.1038/nnano.2011.110.

385. Kumar, R., et al., Fabrication and Electrochemical Evaluation of Micro-Supercapacitors Prepared by Direct Laser Writing on Free-Standing Graphite Oxide Paper. *Energy*, 2019. **179**: p. 676. DOI: 10.1016/j.energy.2019.05.032.

386. Yagati, A.K., et al., Laser-Induced Graphene Interdigitated Electrodes for Label-Free or Nanolabel-Enhanced Highly Sensitive Capacitive Aptamer-Based Biosensors. *Biosens. Bioelectron.*, 2020. **164**: p. 112272. DOI: 10.1016/j.bios.2020.112272.

387. Yoon, H., et al., A Chemically Modified Laser-Induced Porous Graphene Based Flexible and Ultrasensitive Electrochemical Biosensor for Sweat Glucose Detection. *Sensors Actuators B: Chem.*, 2020. **311**. DOI: 10.1016/j.snb.2020.127866.

388. You, Z., et al., Laser-Induced Noble Metal Nanoparticle-Graphene Composites Enabled Flexible Biosensor for Pathogen Detection. *Biosens. Bioelectron.*, 2020. **150**: p. 111896. DOI: 10.1016/j.bios.2019.111896.

389. Peng, Z., et al., Flexible Boron-Doped Laser-Induced Graphene Microsupercapacitors. *ACS Nano*, 2015. **9**(6): p. 5868. DOI: 10.1021/acsnano.5b00436.

390. Ye, R., et al., In Situ Formation of Metal Oxide Nanocrystals Embedded in Laser-Induced Graphene. *ACS Nano*, 2015. **9**(9): p. 9244. DOI: 10.1021/acsnano.5b04138.

391. Ye, R., D.K. James, and J.M. Tour, Laser-Induced Graphene: From Discovery to Translation. *Adv. Mater.*, 2019. **31**(1): p. e1803621. DOI: 10.1002/adma.201803621.

392. Guo, L., et al., Bandgap Tailoring and Synchronous Microdevices Patterning of Graphene Oxides. *J. Phys. Chem. C*, 2012. **116**(5): p. 3594. DOI: 10.1021/jp209843m.

393. Viskadouros, G., et al., Direct Laser Writing of Flexible Graphene Field Emitters. *Appl. Phys. Lett.*, 2014. **105**(20). DOI: 10.1063/1.4902130.

394. Yung, K.C., et al., Laser Direct Patterning of a Reduced-Graphene Oxide Transparent Circuit on a Graphene Oxide Thin Film. *J. Appl. Phys.*, 2013. **113**(24).

DOI: 10.1063/1.4812233.

395. Sokolov, D.A., K.R. Shepperd, and T.M. Orlando, Formation of Graphene Features from Direct Laser-Induced Reduction of Graphite Oxide. *J. Phys. Chem. Lett.* , 2010. **1**(18): p. 2633. DOI: 10.1021/jz100790y.

396. Zhang, Y., et al., Direct Imprinting of Microcircuits on Graphene Oxides Film by Femtosecond Laser Reduction. *Nano Today*, 2010. **5**(1): p. 15.

397. Trusovas, R., et al., Reduction of Graphite Oxide to Graphene with Laser Irradiation. *Carbon*, 2013. **52**: p. 574. DOI: 10.1016/j.carbon.2012.10.017.

398. Zhang, P., et al., Three-Dimensional Water Evaporation on a Macroporous Vertically Aligned Graphene Pillar Array under One Sun. *J. Mater. Chem. A*, 2018. **6**(31): p. 15303. DOI: 10.1039/c8ta05412f.

399. Yuan, Y., et al., Laser Photonic-Reduction Stamping for Graphene-Based Micro-Supercapacitors Ultrafast Fabrication. *Nat Commun*, 2020. **11**(1): p. 6185. DOI: 10.1038/s41467-020-19985-2.

400. Li, R.Z., et al., High-Rate in-Plane Micro-Supercapacitors Scribed onto Photo Paper Using in Situ Femtolaser-Reduced Graphene Oxide/Au Nanoparticle Microelectrodes. *Energy Environ. Sci.*, 2016. **9**(4): p. 1458. DOI: 10.1039/c5ee03637b.

401. Inagaki, M., et al., Carbonization of Polyimide Film "Kapton". *Carbon*, 1989. **27**(2): p. 253. DOI: 10.1016/0008-6223(89)90131-0.

402. Lin, J., et al., Laser-Induced Porous Graphene Films from Commercial Polymers. *Nat Commun*, 2014. **5**(1): p. 5714. DOI: 10.1038/ncomms6714.

403. Li, G., Direct Laser Writing of Graphene Electrodes. *J. Appl. Phys.*, 2020. **127**(1). DOI: 10.1063/1.5120056.

404. Wyss, K.M., D.X. Luong, and J.M. Tour, Large-Scale Syntheses of 2d Materials: Flash Joule Heating and Other Methods. *Adv. Mater.*, 2022. **34**(8): p. e2106970. DOI: 10.1002/adma.202106970.

405. Ren, M., J. Zhang, and J.M. Tour, Laser-Induced Graphene Hybrid Catalysts for Rechargeable Zn-Air Batteries. *ACS Appl. Energy Mater.*, 2019. **2**(2): p. 1460. DOI: 10.1021/acsaem.8b02011.

406. Zhang, J., et al., Oxidized Laser-Induced Graphene for Efficient Oxygen Electrocatalysis. *Adv. Mater.*, 2018. **30**(21): p. e1707319. DOI: 10.1002/adma.201707319.

407. Stanford, M.G., et al., Laser-Induced Graphene Triboelectric Nanogenerators. *ACS Nano*, 2019. **13**(6): p. 7166. DOI: 10.1021/acsnano.9b02596.

408. Ren, M., et al., Co(2) to Formic Acid Using Cu-Sn on Laser-Induced Graphene. *ACS Appl. Mater. Interfaces*, 2020. **12**(37): p. 41223. DOI: 10.1021/acsami.0c08964.

409. Stanford, M.G., et al., Laser-Induced Graphene for Flexible and Embeddable Gas Sensors. *ACS Nano*, 2019. **13**(3): p. 3474. DOI: 10.1021/acsnano.8b09622.

410. Rathinam, K., et al., Polyimide Derived Laser-Induced Graphene as Adsorbent for Cationic and Anionic Dyes. *Carbon*, 2017. **124**: p. 515. DOI: 10.1016/j.carbon.2017.08.079.

411. Stanford, M.G., et al., Self-Sterilizing Laser-Induced Graphene Bacterial Air Filter. *ACS Nano*, 2019. **13**(10): p. 11912. DOI: 10.1021/acsnano.9b05983.

412. Getachew, B.A., D.S. Bergsman, and J.C. Grossman, Laser-Induced Graphene from Polyimide and Polyethersulfone Precursors as a Sensing Electrode in Anodic Stripping Voltammetry. *ACS Appl. Mater. Interfaces*, 2020. **12**(43): p. 48511. DOI: 10.1021/acsami.0c11725.

413. Vivaldi, F.M., et al., Three-Dimensional (3d) Laser-Induced Graphene: Structure, Properties, and Application to Chemical Sensing. *ACS Appl Mater Interfaces*, 2021. **13**(26): p. 30245. DOI: 10.1021/acsami.1c05614.

414. Duy, L.X., et al., Laser-Induced Graphene Fibers. *Carbon*, 2018. **126**: p. 472. DOI: 10.1016/j.carbon.2017.10.036.

415. Luong, D.X., et al., Laminated Object Manufacturing of 3d-Printed Laser-Induced Graphene Foams. *Adv. Mater.*, 2018. **30**(28): p. e1707416. DOI: 10.1002/adma.201707416.

416. Cheng, L., et al., Laser-Induced Graphene for Environmental Applications: Progress and Opportunities. *Materials Chemistry Frontiers*, 2021. **5**(13): p. 4874. DOI: 10.1039/d1qm00437a.

417. Zheng, H.Y., T.T. Tan, and W. Zhou, Studies of Krf Laser-Induced Long Periodic Structures on Polyimide. *Optics and Lasers in Engineering*, 2009. **47**(1): p. 180. DOI: 10.1016/j.optlaseng.2008.06.015.

418. Yung, W.K.C., et al., 355nm Nd:Yag Laser Ablation of Polyimide and Its Thermal Effect. *J. Mater. Process. Technol.*, 2000. **101**(1-3): p. 306. DOI: 10.1016/s0924-0136(00)00467-2.

419. Shin, B.S., J.Y. Oh, and H. Sohn, Theoretical and Experimental Investigations into Laser Ablation of Polyimide and Copper Films with 355-Nm Nd:Yvo4 Laser. *J. Mater. Process. Technol.*, 2007. **187-188**: p. 260. DOI: 10.1016/j.jmatprotec.2006.11.106.

420. Du, Q., et al., Surface Microstructure and Chemistry of Polyimide by Single Pulse Ablation of Picosecond Laser. *Appl. Surf. Sci.*, 2018. **434**: p. 588. DOI: 10.1016/j.apsusc.2017.10.200.

421. Wang, L., et al., A Comparative Study of Laser-Induced Graphene by Co(2) Infrared Laser and 355 Nm Ultraviolet (Uv) Laser. *Micromachines (Basel)*, 2020. **11**(12). DOI: 10.3390/mi11121094.

422. Li, Y., et al., Laser-Induced Graphene in Controlled Atmospheres: From Superhydrophilic to Superhydrophobic Surfaces. *Adv. Mater.*, 2017. **29**(27). DOI: 10.1002/adma.201700496.

423. Ye, R., et al., Laser-Induced Graphene Formation on Wood. *Adv. Mater.*, 2017. **29**(37). DOI: 10.1002/adma.201702211.

424. Han, X., et al., Laser-Induced Graphene from Wood Impregnated with Metal Salts and Use in Electrocatalysis. *ACS Appl. Nano Mater.*, 2018. **1**(9): p. 5053. DOI: 10.1021/acsanm.8b01163.

425. Trusovas, R., et al., Graphene Layer Formation in Pinewood by Nanosecond and Picosecond Laser Irradiation. *Appl. Surf. Sci.*, 2019. **471**: p. 154. DOI: 10.1016/j.apsusc.2018.12.005.

426. Le, T.S.D., et al., Ultrafast Laser Pulses Enable One-Step Graphene Patterning on Woods and Leaves for Green Electronics. *Adv. Funct. Mater.*, 2019. **29**(33). DOI: 10.1002/adfm.201902771.

427. Law, K.L. and R. Annual, *Plastics in the Marine Environment*, in *Annual Review of Marine Science*. 2017. p. 205.

428. Park, H., et al., Electronic Functionality Encoded Laser-Induced Graphene for Paper Electronics. *ACS Appl. Nano Mater.*, 2020. **3**(7): p. 6899. DOI: 10.1021/acsanm.0c01255.

429. Chyan, Y., et al., Graphene Art. *ACS Appl. Nano Mater.*, 2019. **2**(5): p. 3007. DOI: 10.1021/acsanm.9b00391.

430. Kulyk, B., et al., Laser-Induced Graphene from Paper for Mechanical Sensing. *ACS Appl. Mater. Interfaces*, 2021. **13**(8): p. 10210. DOI: 10.1021/acsami.0c20270.

431. Long, Y., et al., Molybdenum-Carbide-Graphene Composites for Paper-Based Strain and Acoustic Pressure Sensors. *Carbon*, 2020. **157**: p. 594. DOI: 10.1016/j.carbon.2019.10.083.

432. Zang, X., et al., Laser-Induced Molybdenum Carbide-Graphene Composites for 3d Foldable Paper Electronics. *Adv. Mater.*, 2018. **30**(26): p. e1800062. DOI: 10.1002/adma.201800062.

433. Cammarano, A., G. Luca, and E. Amendola, Surface Modification and Adhesion Improvement of Polyester Films. *Open Chemistry*, 2013. **11**(1): p. 35. DOI: 10.2478/s11532-012-0135-x.

434. Cao, L., et al., Stable and Durable Laser-Induced Graphene Patterns Embedded in Polymer Substrates. *Carbon*, 2020. **163**: p. 85. DOI: 10.1016/j.carbon.2020.03.015.

435. Singh, S.P., et al., Sulfur-Doped Laser-Induced Porous Graphene Derived from Polysulfone-Class Polymers and Membranes. *ACS Nano*, 2018. **12**(1): p. 289. DOI: 10.1021/acsnano.7b06263.

436. Beckham, J.L., et al., High-Resolution Laser-Induced Graphene from Photoresist. *ACS Nano*, 2021. **15**(5): p. 8976. DOI: 10.1021/acsnano.1c01843.

437. Oh, J.-S., et al., Laser-Assisted Simultaneous Patterning and Transferring of Graphene. *J. Phys. Chem. C*, 2012. **117**(1): p. 663. DOI: 10.1021/jp309382w.

438. Li, J.T., et al., Laminated Laser-Induced Graphene Composites. *ACS Nano*, 2020. **14**(7): p. 7911. DOI: 10.1021/acsnano.0c02835.

439. Rahimi, R., et al., Highly Stretchable and Sensitive Unidirectional Strain Sensor Via Laser Carbonization. *ACS Appl. Mater. Interfaces*, 2015. **7**(8): p. 4463. DOI: 10.1021/am509087u.

440. Prabhakaran, A. and P. Nayak, Surface Engineering of Laser-Scribed Graphene Sensor Enables Non-Enzymatic Glucose Detection in Human Body Fluids. *ACS Appl. Nano Mater.*, 2019. **3**(1): p. 391. DOI: 10.1021/acsanm.9b02025.

441. Lin, S., et al., A Flexible and Highly Sensitive Nonenzymatic Glucose Sensor Based on Dvd-Laser Scribed Graphene Substrate. *Biosens. Bioelectron.*, 2018. **110**: p. 89. DOI: 10.1016/j.bios.2018.03.019.

442. Aparicio-Martínez, E., et al., Flexible Electrochemical Sensor Based on Laser Scribed Graphene/Ag Nanoparticles for Non-Enzymatic Hydrogen Peroxide

Detection. *Sensors Actuators B: Chem.*, 2019. **301**: p. 127101. DOI: 10.1016/j.snb.2019.127101.

443. Fenzl, C., et al., Laser-Scribed Graphene Electrodes for Aptamer-Based Biosensing. *ACS Sens*, 2017. **2**(5): p. 616. DOI: 10.1021/acssensors.7b00066.

444. Rauf, S., et al., Gold Nanostructured Laser-Scribed Graphene: A New Electrochemical Biosensing Platform for Potential Point-of-Care Testing of Disease Biomarkers. *Biosens. Bioelectron.*, 2021. **180**: p. 113116. DOI: 10.1016/j.bios.2021.113116.

445. de Araujo, W.R., et al., Single-Step Reagentless Laser Scribing Fabrication of Electrochemical Paper-Based Analytical Devices. *Angew Chem Int Ed Engl*, 2017. **56**(47): p. 15113. DOI: 10.1002/anie.201708527.

446. Yang, Y., et al., A Laser-Engraved Wearable Sensor for Sensitive Detection of Uric Acid and Tyrosine in Sweat. *Nat. Biotechnol.*, 2020. **38**(2): p. 217. DOI: 10.1038/s41587-019-0321-x.

447. Torrente-Rodriguez, R.M., et al., Sars-Cov-2 Rapidplex: A Graphene-Based Multiplexed Telemedicine Platform for Rapid and Low-Cost Covid-19 Diagnosis and Monitoring. *Matter*, 2020. **3**(6): p. 1981. DOI: 10.1016/j.matt.2020.09.027.

448. Cui, T.R., et al., Ultrasensitive Detection of Covid-19 Causative Virus (Sars-Cov-2) Spike Protein Using Laser Induced Graphene Field-Effect Transistor. *Molecules*, 2021. **26**(22). DOI: 10.3390/molecules26226947.

449. Russo, M.J., et al., Antifouling Strategies for Electrochemical Biosensing: Mechanisms and Performance toward Point of Care Based Diagnostic Applications. *ACS Sens*, 2021. **6**(4): p. 1482. DOI: 10.1021/acssensors.1c00390.

450. Miodek, A., et al., Optimisation and Characterisation of Anti-Fouling Ternary Sam Layers for Impedance-Based Aptasensors. *Sensors (Basel)*, 2015. **15**(10): p. 25015. DOI: 10.3390/s151025015.

2 Inkjet-printed electrochemically reduced graphene oxide microelectrode for HT-2 detection

2.1 Introduction

The need for point-of-care and portable/wearable electrochemical sensors has led to a demand for miniaturized analytical platforms. Microelectrodes are an exciting avenue for electrochemical sensor construction due to their small size, fast and sensitive response [1-3]. However, traditional fabrication methods such as photolithography suffer from disadvantages such as complicated assembly processes, expensive instrumentation, and the use of harmful chemicals[4, 5]..

Inkjet printing (IP) has emerged as a promising alternative technique for the production of advanced electronic devices. IP allows for direct and non-contact printing of patterns sized from micrometer to centimeter onto various substrates such as plastics, cellulose, and wearable e-textiles[6-8].. Furthermore, IP has the advantage of mass production of small, disposable, low-cost electrochemical biosensors. However, inkjet printers can vary significantly in cost, performance, and versatility, so it is important to have comprehensive information for users to choose the proper printer based on their budget and application scenarios.

Recently, graphene has been considered as an alternative to metallic-nanoparticles-based inks, which are expensive, tend to oxidize, and require high-temperature post-printing sintering [9-11]. Graphene consists of a single layer of carbon atoms arranged in a honeycomb lattice structure, presenting high surface-to-volume ratios[12], remarkable conductivity[13], and excellent biocompatibility[14]. These properties endow graphene wide application in electrochemical sensing [15-18]. Although the characteristics of IP graphene-based platforms cannot compete with the high conductivity, deposition control, and optical transparency of chemically deposited graphene, it has nonetheless attracted the attention of researchers worldwide [9, 10].

One of the primary challenges of printing with pristine graphene is the tendency of the material to aggregate, leading to low ink stability and printhead nozzle clogging [19]. To overcome this, exfoliated graphene oxide (GO) has been used as a source material. The oxygen content of GO, including hydroxyl, carbonyl, carboxyl and epoxy groups, increases the hydrophilicity and enables its dispersion in water-based inks; while these functionalities change some carbon atoms from sp^2 to sp^3 hybridization, destroying the π conjugated graphene lattice, making GO electrical resistive [20, 21]. GO inks can create continuous films over desired substrates, and reduced graphene oxide (rGO) film can be obtained using post-printing treatment [22].. rGO,

in which the oxygen-containing groups are partially reduced, possesses a good heterogeneous electron transfer rate but enough oxygen groups to facilitate functionalization [23]. Electrochemical reduction of GO is a fast, simple, and economic alternative approach to the commonly used chemical [24] and thermal reduction [25] methods. Chemical reduction either involves the use of toxic reducing agents or can lead to contamination of the resulting material. While thermal reduction is only applicable for heat-resistant materials, not for commonly used substrates, e.g., plastic and paper [26].

Regarding global agriculture, HT-2 toxin ($C_{22}H_{32}O_8$, CAS No.26934-87-2), produced by different Fusarium species, is one of the most relevant mycotoxin groups [27]. HT-2 can contaminate small grain cereals and maize in the field, as well as during wet storage and inappropriate transport. Studies have shown that HT-2 toxin is only partially degraded during thermal food processing [28]. The harmful effects of HT-2 are not limited to inhibiting protein synthesis and cell proliferation in plants; it can also cause acute or chronic intoxication in humans and animals [29]. According to the Recommendation of the European Commission, the limit of detection for the sum of HT-2 and T-2 toxins should not exceed 25 μg/kg [30], while common levels of toxins in contaminated grains for human consumption and breakfast cereals range from the 10s to 100s of μg/kg [31] Therefore, a rapid and low-cost detection platform would be beneficial for the health and food safety industry.

This chapter described the development of a water-based GO ink to fabricate rGO microelectrodes and demonstrate their biosensing ability, following the evaluation of consumer and research-grade printers' performance. A three-electrode system was built with inkjet-printed GO micropattern on plastic as the working electrode, screen-printed carbon, and Ag/AgCl as the counter and reference electrodes, respectively. After optimizing the GO reduction parameters, electrochemically reduced graphene oxide (ERGO) microelectrodes were obtained. An enzymatic immunosensor was constructed based on the as-prepared electrode for detecting HT-2 mycotoxin, with detailed optimization, indicating its potential for real-life applications.

2.2 Materials and methods

2.2.1 Materials

Silver nanoparticle ink MU01 and FD01, named Ag-1 and Ag-2 in the following contents respectfully, and a porous substrate (NB-TP-3GU100) were obtained from Mitsubishi paper

mill ltd. Ethylene glycol (EG), sodium dodecyl sulfate (SDS), 1-naphthyl phosphate monosodium salt (1-NP), 1-naphthol (1-N), diethanolamine (DEA), n-hydroxy succinimide (NHS), n-(3-dimethylaminopropyl)-n-ethyl carbodiimide hydrochloride (EDC), 2-(N-Morpholino) ethane sulfonic acid (MES) were purchased from Sigma-Aldrich (St. Louis, MO, USA) in ACS purity and were used as received. All water-based solutions were prepared using milli-Q water (resistivity higher than 18.2 MΩ/cm at 25 °C) from Millipore (Burlington, MA, USA).

2.2.2 Printer comparisons

All patterns were designed with AutoCAD 2018 (Autodesk, USA). Silver nanoparticle inks were used since they are among the most developed and commonly used materials in the inkjet printing field due to their simple synthesis, low cost, and easy access [32-34]. Ag-2 was deposited with Dimatix 2831 (dubbed Dimatix, FUJIFILM Dimatix, USA) with a DMC-11610 printhead dispensing 10 pL nominal drop volume (nozzle diameter of 21.5 μm). A waveform from the ink supplier was used, with a printing temperature of 35 °C, plate temperature of 35 °C, drop spacing of 15 μm, and jetting frequency of 2 kHz. The distance between the printhead and substrate was set to 500 μm. Ag-1 was deposited with Epson XP 15000 (dubbed Epson, Seiko Epson Corporation). It has 6 ink channels with gray, red, cyan, magenta, yellow, and black ink cartridges, and for each channel, there are 180 nozzles sized of ~26 μm with a distance of ~141 μm, and the nozzle-line distance is ~2.2 mm. Ag-1 was filled in the yellow cartridge while keeping other cartridges with the original inks. The parameters used were the same as our previously reported work [35], in brief: use the best print quality, without any color correction, and turn off all the other functions of the printer (such as quiet printing mode, and reducing or enlarging documents).

The pattern dimensions were calculated from relative optical pictures with a custom MATLAB function [36]. It is based on a defined constant value against which all other measured distances were determined. Briefly, after inspecting an SEM copper grid under SEM and optical microscope, the sizes (X μm) of the squares inside the grid were obtained from SEM, and the pixel number of X μm in the optical image was counted (Y); thus, giving the pixel size of the optical image (X/Y μm). Taking a picture of the target object under the optical microscope with the same setting as above, with the pixel number (Z), the dimension of the object could be determined as D=ZX/Y μm. All the pixels were identified and counted by MATLAB (Figure 2.1).

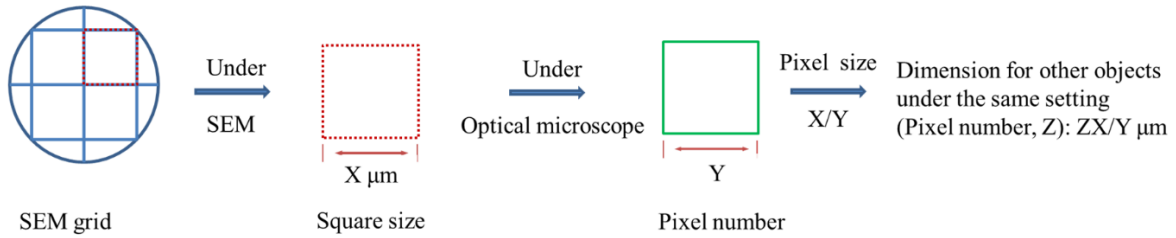

Figure 2.1 Pattern dimension calculating process.

2.2.3 Fabrication of electrode

Poly (ethylene 2,6-naphthalate) (PEN, 0.075 mm thickness, Goodfellow, Huntingdon, UK) substrate was cleaned using atmospheric-pressure oxygen plasma for 30 min (Harrick Plasma, Ithaca, NY, USA), followed by soaking in 1 M NaOH bath for 30 min at 25 °C, then washed with water and dried with compressed air flow. The counter electrodes and graphite tracks of working electrodes were screen-printed using carbon sensor paste (C2030519P4, Gwent Group, Pontypool, UK). Pseudo-reference electrodes were printed using Ag/AgCl paste (C61003P7, Gwent Group, Pontypool, UK). The electrodes were cured at 120 °C for 30 min in an oven (JP Selecta, Barcelona, Spain).

40 mL of single layer GO water solution (N002-PS-1.0, Angstron Materials, Dayton, OH, USA) of concentration 1 wt.% was sonicated for 2 h (80 % amplitude, 1 s pulse, 1 s pause, cooling temperature 15 °C, protecting temperature 40 °C) using an ultra-sonicator equipped with a 1000 W sonic head and a water-cooling system (Col-Int TECH, Irmo, SC, USA). To create the ink, 600 mg of the sonicated GO solution, 6 mg of SDS, and 1.8 mL of EG were added to 3.6 mL of milli-Q water, and mixed using a Q125 probe sonicator (Qsonica, Melville, NY, USA) with the following settings: time 300 s, amplitude 100 %, pulse 2 s, pause 1 s. The solution was cooled using an ice bath during sonication. The ink was obtained by filtering with a cellulose acetate syringe filter (0.45 μm cut-off, VWR, Radnor, PA, USA).

The GO working electrodes were printed using the same parameters as before, but with modifications to the jetting voltage (11 V) and frequency (5 kHz) on a Dimatix printer. A single nozzle was used to print 10 mm-long working electrodes, with 30 printing cycles, 30 s pauses between layers, and a drop-spacing of 30 μm. A custom waveform profile was employed, as shown in Figure 2.2a. For piezo-based drop-on-demand inkjet printers, the jetting process is controlled by piezoelectric ceramics (PZT, in the case of Dimatix) which encounters shape deformation when applied an electric signal (waveform). As depicted in Figure 2.2b, the PZT bimorph is slightly bent towards the flow chamber at standby state under a voltage level of 25%

(100% corresponds to 11 V in this case). In segment one, the voltage is lowered to 7%, and the PZT moves towards a neutral straight position, causing ink to be drawn into the chamber from the ink cartridge. In segment two, the voltage is increased to 100%, and the PZT squeezes the chamber, forcing ink out of the nozzle. In segment three, the voltage is lowered back to the standby state (level 25%), and the PZT waits for the next ejection.

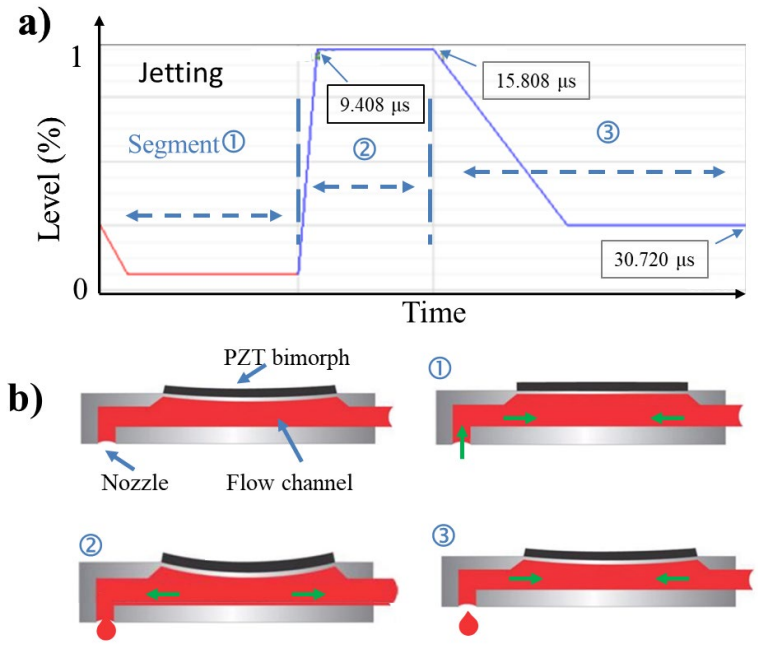

Figure 2.2 (a)Waveform for GO electrode printing. (b) Illustration of the ink flow within the printhead at different waveform segments; adapted from ref[37].

Before the reduction of the GO, the electrodes were treated at 120°C for 2 hours to evaporate the ink solvents. Then, 50 µL of KCl solution in milli-Q water was pipetted onto the electrode to cover the pseudo-reference electrode, counter electrode, and the entire GO strip, including the undefined part of the graphite carbon working electrode track. Chronopotentiometry (CA) was used to reduce the electrodes at -1.5 V vs the onboard Ag/AgCl reference. After reduction, the electrodes were washed with milli-Q water and dried using compressed air. To prevent solutions from contacting the graphite part of the working electrode, an insulating line (Dielectric ink D2070423P5, Gwent Group, Pontypool, UK) was hand-pasted and cured at 200°C for 5 min.

2.2.4 Biosensor fabrication

Anti-HT2 Fab and anti-IC-HT2 ScFv-ALP fusion antibodies were provided by VTT (Espoo, Finland) [38]. HT-2 toxin ($C_{22}H_{32}O_8$, CAS No. 26934-87-2) was bought from Sigma-Aldrich

(St. Louis, MO, USA). The content of a whole vial of the mycotoxin was dissolved in dimethyl sulfoxide (1 mg/mL) to create the stock solution. Individual HT-2 concentrations were obtained by dilution. Gibco One Shot Fetal bovine serum (Thermo Fisher Scientific, Waltham, MA, USA) was used as a matrix for real sample analysis.

Anti-HT2 Fab was attached to the ERGO microelectrode via EDC/NHS linker chemistry. In detail, after the electrodes were washed with MES buffer (pH 6), a 30 µL drop of EDC/NHS solution (0.1 M, in MES buffer) was added to the printed area and left to incubate at room temperature for 30 min. The electrodes were then thoroughly washed with MES buffer to remove any excess EDC/NHS and 10 µL of Anti-HT2 Fab (10 µg/mL, in phosphate-buffered saline (PBS) pH 6.5) was added onto the electrode and incubated for another 30 min. The drop was then removed and 30 µL of Tris buffer (pH 8) was added to the electrode for 30 min to block the unreacted -COOH group on rGO. Subsequently, 30 µL of blocking buffer (2 % bovine serum albumin in PBS pH 7.4 with 0.05 % tween-20) was pipetted onto the electrode and incubated for 30 min to avoid unspecific fouling. The electrodes were washed twice with washing buffer (PBS pH 7.4 with 0.05 % tween-20) and samples containing the mycotoxin (30 µL total volume, diluted in blocking buffer in 1:1 ratio, 30 min incubation) were added. The electrodes were then washed thoroughly with washing buffer and dried at 25 °C. Anti-IC-HT2 scFv-ALP was then added for 30 min and then removed with washing buffer. Analysis was performed by the addition of 5 mM 1-NP dissolved in 0.1 M DEA buffer (pH 9.8 containing 1 mM $MgCl_2$). After 5 min of incubation with 1-NP, DPV electrochemical analysis was performed vs the onboard Ag/AgCl reference electrode using the following settings: initial potential −0.8 V, end potential 0.7 V, scan rate 5 mV/s, modulation amplitude +175 mV, modulation time 10 ms, interval time 1 s, no deposition or conditioning potential was set.

2.2.5 Electrochemical active surface area calculation

To determine the mass transport limited electroactive area of the ERGO microelectrode, cyclic voltammograms (CV) were obtained using 1 mM $[Fe(CN)_6]^{3-}/[Fe(CN)_6]^{4-}$ redox probe in 0.1 M KCl. The electroactive surface was calculated according to the Randles-Sevcik equation for the (quasi) reversible electrode process:

$$Ip = 2.69 \cdot 10^5 \cdot A \cdot D^{1/2} \cdot n^{3/2} \cdot v^{1/2} \cdot C$$

where I_p is the anodic current peak (in amps), A is the electroactive area (cm^2), D is the diffusion coefficient of $[Fe(CN)_6]^{4-}$ in solution and is 6.1×10^{-6} cm^2/s [39], n is the number of

electrons transferred in half-reaction (1 in case of $[Fe(CN)_6]^{4-}$), ν is scan rate (0.1 V/s was chosen) and C is $[Fe(CN)_6]^{4-}$ concentration (mol/cm^3).

2.2.6 Instrumentation

SEM was taken with Magellan 400 L field emission scanning electron microscope (SEM, FEI, Hillsboro, OR, USA) at a working distance of 10 mm and voltage of 10 kV; the samples were mounted on aluminum stubs and then sputtered with Au. Microscope pictures were taken either by the inbuild fiducial camera of Dimatix or an optical microscope (Eclipse LV100DA, Nikon Corporation, Tokyo, Japan). X-ray photoelectron spectroscopy (XPS) measurements were performed at room temperature with a SPECS PHOIBOS 150 hemispherical analyzer (SPECS GmbH, Berlin, Germany) in a base pressure of 5 $\times 10^{-10}$ mbar using monochromatic Al K-alpha radiation (1486.74 eV) as an excitation source. XPS spectra were then fitted with convolution of Gaussian and Lorentzian peak shapes after Shirley background subtraction. Raman spectra were obtained using a confocal Raman microscope alpha300r equipped with a 488 nm laser (WITec, Ulm, Germany) and parameters of 1.5 mW laser power, grating of 600 g / nm, objective 50x, exposure of 10 s and 3 accumulations for every single spectrum. For electrochemical measurements, an Autolab PGSTAT 302 (Metrohm, Herissau, Switzerland) equipped with a frequency response analyzer PGST30 was used. EIS was conducted at DC + 0.185 vs Ag/AgCl, AC amplitude ± 10 mV, 0.01-1000 Hz with 1 mM $[Fe(CN)_6]^{3-}$/$[Fe(CN)_6]^{4-}$ in 0.1 M KCl. The spectra including equivalent circuit elements calculations, were evaluated using NOVA (both Metrohm, Herissau, Switzerland).

2.3 Results and discussion

2.3.1 Printer comparisons

The fineness and complexity of printed devices depend highly on the material depositing accuracy of the equipment used. Single droplets, which are the smallest elements an inkjet printer can deposit, were printed to compare printing accuracy. A porous substrate (NB-TP-3GU100) was used because it can absorb the solvents inside the inks quickly and then pin the drops in situ, keeping the drop size and location on the substrate as printed, and eliminating the possible coffee ring effect. In other words, the droplet size is defined by the volume of ink deposited on the substrate instead of the solvent spreading area during drying.

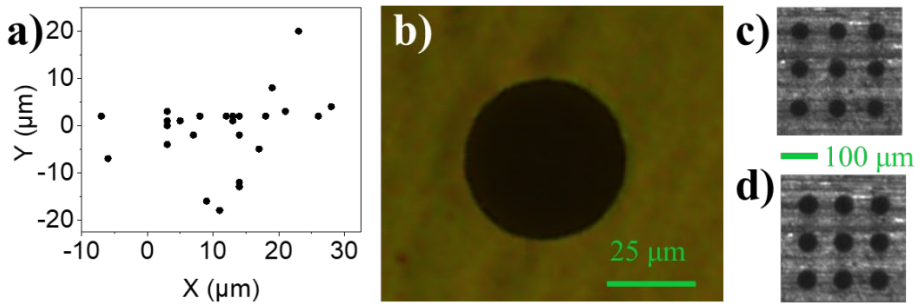

Figure 2.3 (a) Obtained coordinates of 25 drops intended to print at (0, 0). (b) Microscope image of a droplet, and (c, d) optical images (by the fiducial camera) of droplet arrays with drop spacing of 100 µm. The arrays were printed for one (c) and two layers (d); the substrate was taken out of the printer after printing the first layer, and the second layer was deposited after position calibration with the inbuilt alignment system.

Dimatix's printing accuracy was tested with ink Ag-2 by repeatedly printing a single droplet at a specific place (in this case, with coordinates X = 0, Y = 0). Figure 2.3a displays the obtained coordinates of 25 drops, and further analysis gives a statistical coordinate of 11.4 ± 8.9, -0.96 ± 7.9 µm. These results indicate that Dimatix has a depositing accuracy of approximately 20 µm in the X-axis and 10 µm in the Y-axis, which is reasonable considering its motor moving steps (cartridge movement in the X direction is 11.502 µm/step, and plate/substrate movement in the Y direction is 1.875 µm/step).

The optical picture in Figure 2.3b shows a smooth-edged, circle-shaped droplet with a diameter of approximately 46 µm. The droplet arrays with a drop spacing of 100 µm (Figure 2.3c) illustrate almost identical droplets (diameter 47.2 ± 2.5 µm). The actual drop distance (distance between droplet centers) measured is 99.4 ± 3.2 µm, which shows the printer has an intra-layer depositing error of 3.2 µm. Remarkably, the drops showed great overlapping after replacing the substrate and printing one more layer (Figure 2.3d), proving a high alignment accuracy of Dimatix.

To obtain single droplet arrays by the Epson printer, we designed square-array patterns in which each of the squares (one pixel) results in one ejected droplet theoretically, with the maximum resolution of the PDF files that AutoCAD could export (4800×4800 DPI, 5.3 µm/pixel). The square diameter and distance were defined with the integer multiple of 5.3 µm, as 5.3, 10.6, 15.9, 31.8, and 63.5 µm, with a distance of 211.7 µm for the first four arrays and 317.5 µm for the last one. The printing was defined as inline if printed along the printhead movement direction and outline if perpendicular to it. The results show that there were no patterns printed

with pixels sized 5.3 and 10.6 µm (Figure 2.4a and b), while there were when the pixels were larger (Figure 2.4c-e), demonstrating the minimum printable pixel as 15.9 µm. The obtained drop diameter ranged from 16.5 to 28.6 µm. This variation is accrued from the print spool process, which rasterizes the image data and converts it to printer-understandable command sequences. Then, the printer adjusts the jetting volume and numbers to ensure good visualization of the obtained pattern, leading to inconsistencies between the design and final pattern [40]. Some droplets displayed elliptical shapes with the major radius inline, which may be led by the high-speed movement of the printhead.

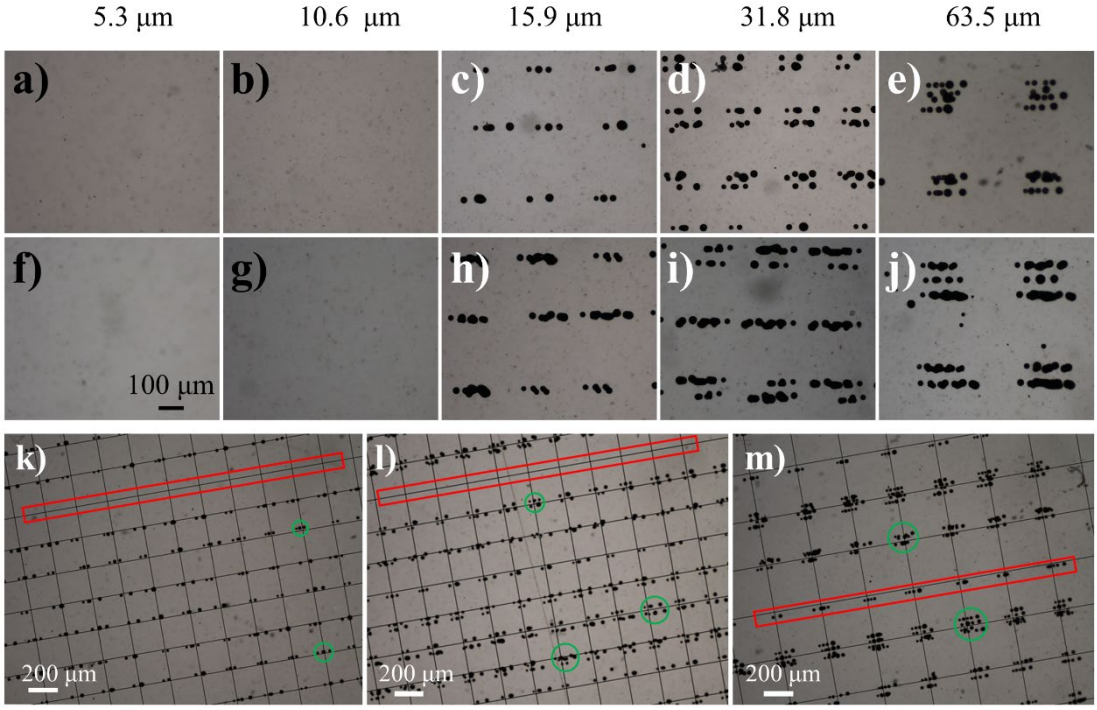

Figure 2.4 Optical pictures of printed droplet arrays by Epson, from designed patterns with different pixel sizes and distances. (a-d) pixel size 5.3, 10.6, 15.9 and 31.8 µm, respectively, with a distance of 211.7 µm; (e) pixel size 63.5 µm with a distance of 317.5 µm. (k, l, m) are pictures of the same printed traces as (c, d, e) at a lower magnitude, respectively. The black grids are virtual patterns with line crosses as the intended printing spots. The green circles indicate the printed "domains". The red squares indicate areas with missing dots. (f-j) Optical pictures of 3-layer printed droplet arrays with the same setting as that of the corresponding above (a-e) pictures. (a-j) have the same scale bar.

Ideally, all the printed patterns should include droplets with the same diameter and distance. However, for the designed arrays with 15.9 µm pixels, the resulting pattern consisted of small

"domains" with a diameter of 79 ± 22 µm, containing 2 or 3 drops in one line (Figure 2.4 c and k), and the domain distance gives 223.3 ± 19.5 µm (211.7 µm in the design); that for 31.8 µm pixels are domain diameter 121 ± 25 µm, with 2 to 9 drops in one or two lines (Figure 2.4 d and l) and domain distance 221.8 ± 16.6 (211.7 µm in the design); that for 63.5 µm pixels are domain diameter 248 ± 35 µm, with 2 to 20 drops in one to four lines (Figure 2.4 e and m) and domain distance 335.7 ± 26.7 µm (317.5 µm in the design). These data indicate that the drops were randomly distributed around the intended printing places with considerable errors. Figures 2.4k-m also indicate that the drops were well-oriented inline but much more irregular outline. Additionally, some dots were missing inline, which may have been caused by blocked nozzles (it is difficult to have 180 nozzles unblocked at the same time) or the outline moving step not matching with the drop distance in the designed patterns. Three-layer overlap printing (with substrate replacement) showed a similar trend and larger variations compared to one-layer printing (Figure 2.4f-j).

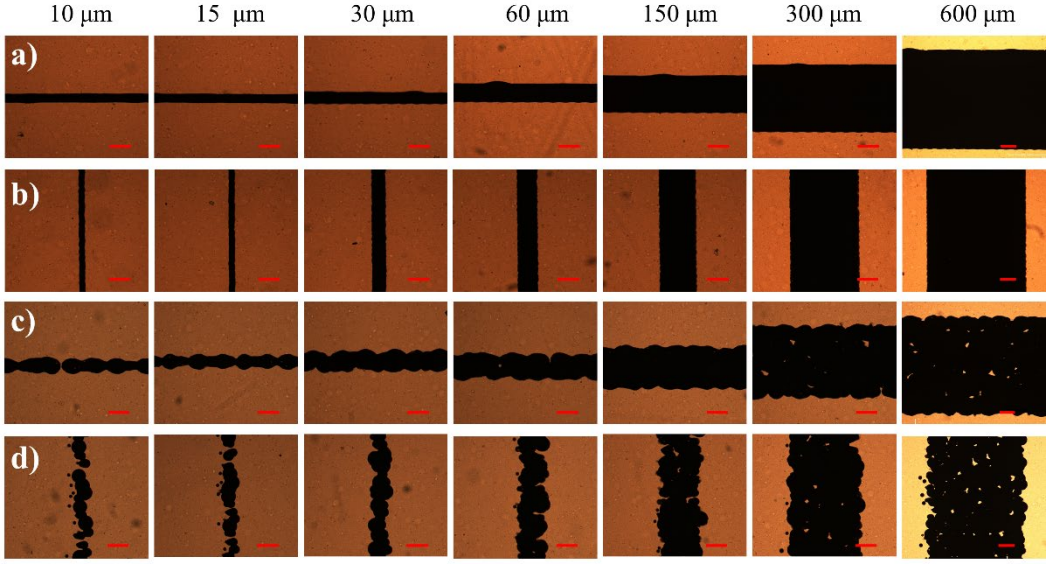

Figure 2.5 Representative optical pictures (transmission mode) of the lines printed with Dimatix (row a and b) and Epson (row c and d). The (a) and (c) rows are inlines (parallel to the printhead moving direction); (b) and (d) rows are outlines (perpendicular to the printhead moving direction); the printed lines are indicated by black color; the scale bars are 100 µm in all the cases.

To further compare the two printers, a series of lines were designed and printed. Since the exact minimum recognizable pixel size of Epson is unknown and the minimum printable pixel size is approximately 15 µm, the patterns were defined as integer multiples of 5 µm, based on the

printing resolution of Dimatix. (The maximum resolution of the pattern that Dimatix is capable of processing is 5080 DPI I[41],which corresponds to 5 μm per pixel.) The designs consisted of 2 cm long lines with widths ranging from 15 to 600 μm. As the line width increased, the printed traces could be considered as gradually changing from lines to squares. The lines printed with Dimatix appeared uniform, with high edge sharpness (Figure 2.5a and b). On the other hand, the lines printed with Epson presented defects such as uncovered areas among the intended printing places, disconnected lines, wave-like edges, and satellite drops (Figure 2.5c and d).

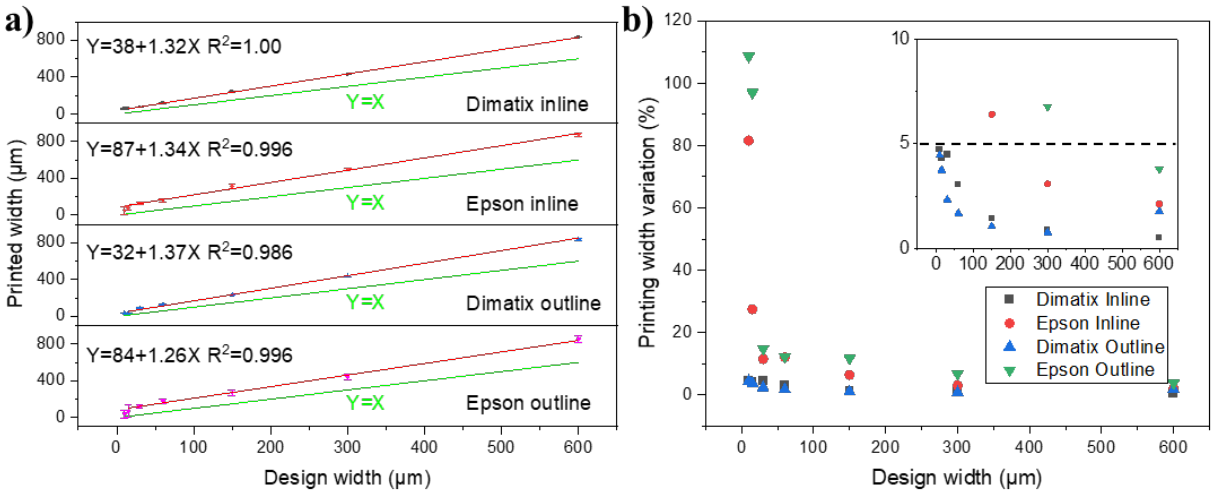

Figure 2.6 (a) Width dependence of the printed lines on the designed ones; the dots are raw data, the red solid lines are fitted plots, and the green lines are plots of Y=X; the fittings were done on X range from 15 to 600 μm, since designed 10 and 15-μm lines give the same printing line width. (b) Width variations of the obtained lines.

The actual width of the printed lines was determined using optical images. In Figure 2.6a, it can be observed that all the printed traces were wider than the designed lines, with an offset of approximately 85 μm for Epson and 35 μm for Dimatix. Epson showed greater variations in line width compared to Dimatix. Interestingly, the 10 and 15-μm lines had the same resulting width for Epson, indicating that Epson's minimum distinguishable pattern dimension is 15 μm, consistent with the results obtained with single droplet printing. Dimatix had a drop spacing of 15 μm, meaning that any dimension less than 15 μm was considered as 15 μm, resulting in the same value for 10 and 15-μm lines designed. The minimum printable pattern size for Dimatix was 5 μm according to the data sheet and our test. From Figure 2.6b, it can be observed that variations in line width obtained from Dimatix were less than 5% in the whole range of 10-600

μm, both inline and outline, whereas Epson required a wider design width of over 150 μm inline and 300 μm outline.

Epson is a readily available office consumer printer that costs approximately €400, while a Dimatix costs around €30,000. Epson has six ink channels that allow for multi-ink printing simultaneously. However, consumer printers are customized for the inks that manufacturers supply, and it is challenging to fabricate inks that work for consumer inkjet printers because how the parameter settings affect the behaviors of ink deposition is unknown. Dimatix offers the choice of printheads with different jetting volumes, adjustable printing parameters (e.g., applied electrical signal and temperature), and visualization of ink droplet formation and drying process through inbuilt cameras, making it more suitable for custom material deposition. However, the large nozzle number (180/channel) of Epson makes it much faster than Dimatix, which only has one channel with 16 nozzles.

2.3.2 ERGO microelectrode fabrication

Based on the findings discussed earlier, it is suggested that a research-grade inkjet printer (Dimatix) would be a suitable choice for microelectrode production. It is recommended that the size of the materials being used should be less than 1/100th the size of the nozzle to avoid nozzle obstruction and ensure successful printing [42]. To ensure that the GO sheets were of appropriate dimensions, they were first treated with continuous sonication, followed by filtration to remove undesired sizes. The lateral diameter of the treated GO significantly decreased after sonication, with a lateral range of 226-875 nm (Figure 2.7a), compared to the source GO with a lateral range of 3.0-4.5 μm (Figure 2.7b). It is well-known that sonication can induce fragmentation of the GO sheets, leading to crystal structure defects, which are important for heterogeneous electron transfer in electrochemistry [43, 44]. As the viscosity of water is too low and the surface tension is too high for inkjet printing, rheology modifier EG was added, along with SDS to adjust the ink's surface tension [45, 46].

The resolution and uniformity of printed designs depend on droplet spread and the ink's ability to wet the substrate [47]. Surface chemistry and roughness both contribute to substrate wetting. Here transparent and flexible PEN was chosen as substrate, which is commonly used for wearable electrode sensors [48]. Prior to printing, the substrate underwent atmospheric-pressure oxygen plasma treatment and subsequent chemical hydrolysis with NaOH. Plasma treatment can oxidize the polymer chain's aromatic rings [49], and NaOH treatment can increase the roughness of PEN [50]. Figure 2.7c and d demonstrate that droplet contact angle

decreased after plasma and NaOH treatment, indicating improved substrate wettability.

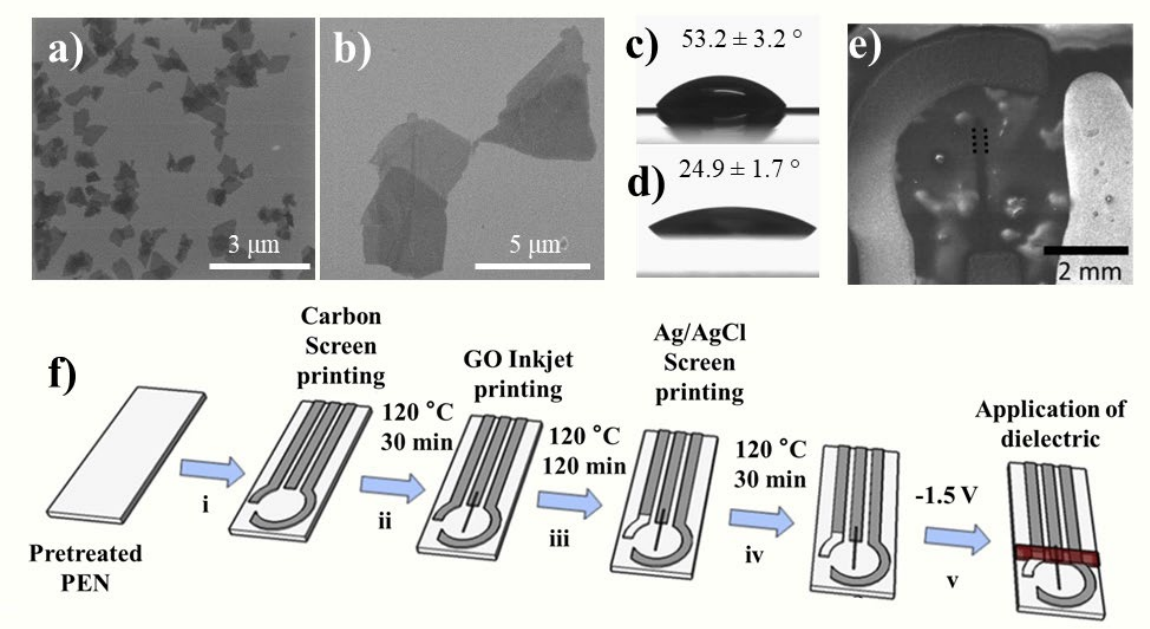

Figure 2.7 SEM micrograph of GO flakes contained in ink (a) and as obtained from manufacturer (b). Contact angle for a droplet of the ink on non-treated (c) and (d) treated PEN substrates. (e) SEM micrograph of the reported electrode, consists of inkjet printed GO strip (narrow black line, indicated by the dashed line), screen printed counter (dark arc) and reference electrodes (white arc). (f) Scheme of ERGO microelectrode fabrication. (i) carbon counter electrode and contacts were screen printed on plasma/NaOH treated PEN, and then oven-cured at 120 °C for 30 min; (ii) The GO working electrodes were inkjet-printed and then oven-cured at 120 °C for 2h; (iii) The Ag/AgCl reference electrodes were screen printed and oven-cured at 120 °C for 30 min; (iv) GO strip was electrochemically reduced at −1.5 V vs the onboard Ag/AgCl reference; (v) dielectric ink was handy-pasted as insulating line to prevent solutions from having contact with the connecting tracks.

A typical three-electrode configuration was built using various printing techniques. The working electrode was inkjet-printed using the developed GO ink, while the counter electrode and connections were screen-printed with carbon paste to avoid extra-long electrochemical reduction of GO. Ag/AgCl reference was screen-printed as well. Figure 2.7e shows an SEM micrograph of the entire electrode (the strip is invisible in the optical image of the electrode). After the reduction step, an insulating layer was added to cover the carbon connection of the working electrode and define the electrodes' active surface. The fabrication process is illustrated in Figure 2.7f.

2.3.3 ERGO microelectrode characterization

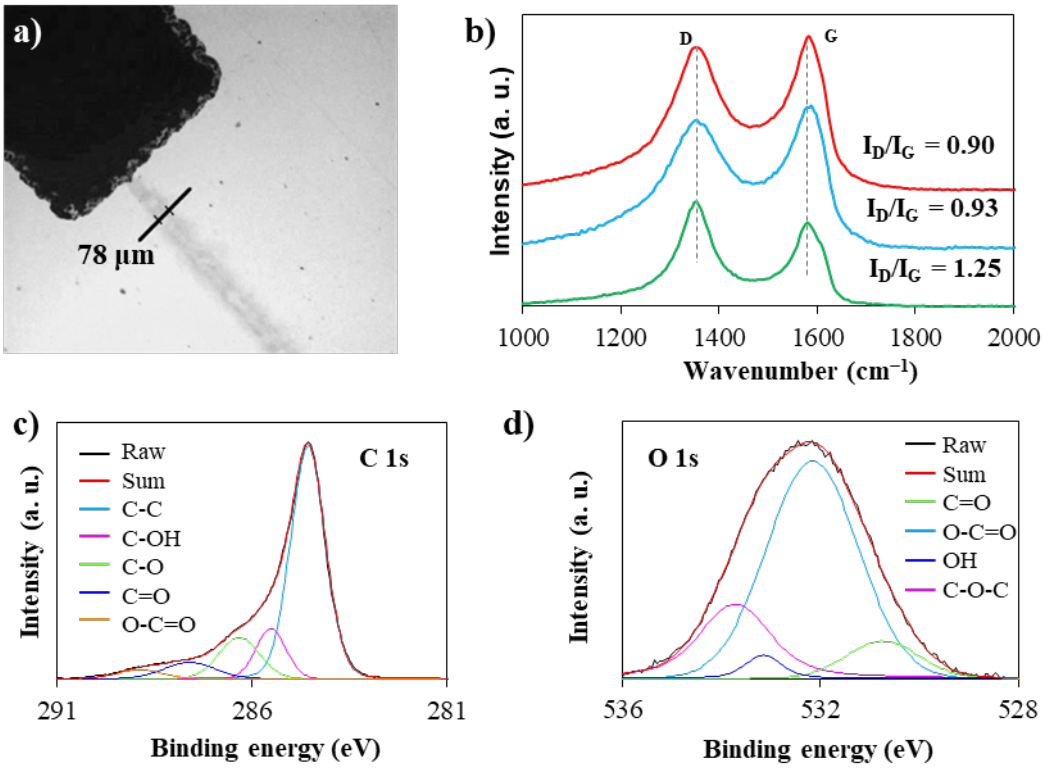

Figure 2.8 (a) Optical microscope image of IP GO strip electrode before reduction. The black feature is the end of the screen-printed connecting track, and the narrow grey line represents the inkjet-printed GO microelectrode. (b) Representative Raman spectra of GO electrode before reduction (red line), after thermal treatment (2 h at 120 °C and 5 min at 200 °C; blue line) and after electrochemical reduction with the same thermal treatment (green line). Deconvoluted XPS C 1s (c) and O 1s (d) spectra of ERGO.

An optical microscope image shows the GO microelectrode with a width of 78 µm (Figure 2.8a), which was then electrochemically reduced to gain ERGO, performed in 3 mM KCl solution at a potential of −1.5 V vs Ag/AgCl. The reduction was characterized using Raman spectroscopy by observation of the two characteristic D and G bands of graphene-based materials. It has been reported that the D band is related to the degree of defects and disorder within the hexagonal lattice and should not be observed in the case of pristine graphene, like that grown by chemical vapor deposition [51]. While the G band corresponds to the in-plane vibrations of sp^2 carbon atoms of graphene lattice and thus increases with the reduction of C-O/C=O. As such, the ratio of these peak intensities (I_D/I_G) is often used to survey the level of oxidation of graphene-based materials [52]. In both GO and ERGO samples, the D and G bands were observed at 1354 cm^{-1} and 1578 cm^{-1}, respectively (Figure 2.8b) and without any shifts

upon a comparison of the spectra before and after the reduction. However, the intensities of these peaks show obvious variations and suggest the successful electrochemical reduction of the GO to ERGO as the I_D/I_G ratio increased from 0.90 to 1.25. The observation also suggests an increase in lattice defects during the reduction process and is in good agreement with a previous study [53]. Raman spectra of a thermally treated working electrode were obtained as a control, which is similar to that of GO and shows distinguished differences to that of ERGO, indicating the thermal treatment during the fabrication process has negligible influence on the electrode. The ERGO electrodes were also characterized using XPS to determine the chemical states of carbon and oxygen (Figure 2.8c and d). Upon evaluation of the C 1s spectrum, the carbon peak was deconvoluted to 5 individual peaks, C-C sp2 (284.5 eV), C-OH (285.5 eV), C-O (286.4 eV), C=O (287.6 eV) and O-C=O (289.9 eV); Four distinguishable oxygen-containing peaks were observed in the O 1s spectrum (C=O at 530.7 eV, O-C=O at 532.2 eV, OH at 533.1 eV and C-O-C at 533.7 eV) [54-56]. It demonstrates that even after electrochemical reduction, carboxyl functional groups which will facilitate covalent attachment of antibodies were still presented within ERGO electrodes

2.3.4 ERGO microelectrode optimization with 1-N

The ERGO microelectrodes were characterized by cyclic voltammetry at varying speeds of polarization. As shown in Figure 2.9a, the ferri/ferrocyanide redox reaction exhibited clear oxidation and reduction peaks, with current increasing as scan rate increased. Plotting the anion oxidation current of ferrocyanide against the square root of scan rate revealed a linear correlation (Figure 2.9b), indicating a diffusion-controlled mechanism for the redox probe on the electrode. However, significant shifts in the faradaic peaks were observed, indicating slow electrode kinetics towards oxidation/reduction of the probe. This behavior was similar to that reported for highly ordered pyrolytic graphite electrodes [57]. The presence of oxygen in ERGO could also contribute to these shifts, as the ferri/ferrocyanide redox probe is highly sensitive to the oxygen content in the electrode material [58]. Using the Randles-Sevcik equation for (quasi) reversible electrode processes, the mass transport limited electroactive surface of the electrode was determined to be 5.2 mm^2, 0.2 mm^2 larger than the geometrical surface. The reduction condition of the electrode was optimized using DPV based on the detection of 1-naphthol (1-N, a reporting label for the subsequent enzymatic immunosensor). The experiments were conducted with electrodes fabricated using the same procedure as the microelectrodes, but with a larger geometric surface (1.0 mm × 5.0 mm) to observe greater

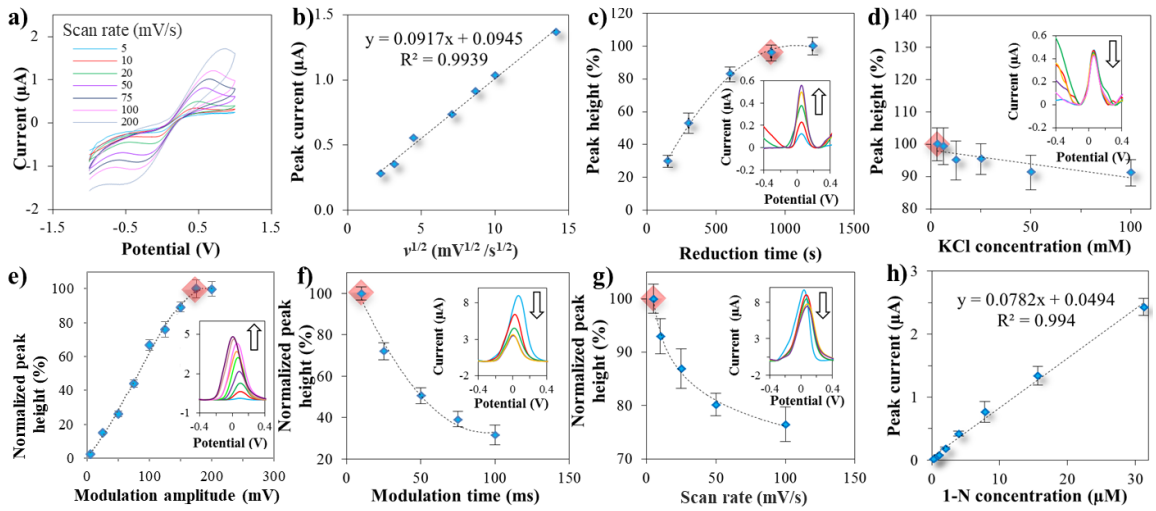

Figure 2.9 (a) CVs of 1 mM $[Fe(CN)_6]^{3-}/[Fe(CN)_6]^{4-}$ in 0.1 M KCl recorded on 1200 s-reduced ERGO electrode and (b) the dependence of anodic peak heights on the square root of scan rate. (c-g) Optimization for GO reduction based on the DPV oxidative detection of 1-N with the obtained ERGO electrode; (c) reduction time, (d) concentration of KCl, (e) modulation amplitude, (f) modulation time and (g) scan rate; red diamond indicates condition selected as optimal; typical DPV curves are shown within insets (at modulation amplitude 50 mV, modulation time 50 ms and scan rate 10 mV/s before optimization, with 1 mM of 1-N in DEA); the arrow is showing trend corresponding to x-axis parameter increase. (h) Signal response (DPV peak current at + 0.05 V) of 1-N on the optimized ERGO electrode.

differences. As shown in Figure 2.9c, a distinct oxidation peak of 1-N (+0.05 V vs the onboard Ag/AgCl reference, inset plots) was present and increased with the reduction time of the GO electrodes, indicating improved electrode sensing performance. It is worth noting that after 300 s of reduction at a constant potential of −1.5 V vs Ag/AgCl, the entire printed GO layer changed color from brown to black. However, a reduction time of 900 s increased the electrochemical signal by 45 ± 5% (n = 3). This increase may be attributed to the further reduction and denser packing of the graphene flakes, as indicated by Feng et al., who described the electrochemical reduction of GO as a multi-step process, with the reduction time determining the reduction degree [59]. Increasing the reduction time to 1200 s only negligibly enhanced electrode performance, thus 1000 s was typically used to ensure sufficient reduction. No significant changes in 1-N signals were observed with varying concentrations of KCl (Figure 2.9d). This suggests that the electrolyte solution had minimal effect on the performance of the ERGO microelectrode, and a concentration of 3 mM KCl was selected for the reduction.

The dependence of the 1-N DPV signal on the modulation amplitude, modulation time, and scan rate was evaluated. The red diamond in Figure 2.9e, f, and g indicates the optimal results, which had the highest oxidation current of 1-N. Therefore, for the DPV measurements, a modulation amplitude of +175 mV, modulation time of 10 ms, and a scan rate of 5 mV/s were used. Finally, the dependence of the 1-N oxidation signal at +0.05 V versus its concentration in DEA buffer was examined. The linear range of the calibration curve was observed to be between 31.25 and 0.24 μM, with an R^2 value of 0.994. These results showed that an electrode with the above-mentioned settings provided reliable and sensitive detection of 1-N, as demonstrated in Figure 2.9h.

2.3.5 ERGO strip microelectrode biosensor

To demonstrate the capabilities of the electrodes for possible real-world applications, HT-2 mycotoxin (chemical structure, Figure 2.10 inset) was detected with a typical electrochemical enzyme-linked immunosorbent assay (ELISA). Initially, anti-HT2 Fab was attached to the electrode through carbodiimide chemistry, using EDC/NHS, crosslinking the residual carboxylic groups found on the surface of ERGO to the primary amines of the Fab fragment. After the recognition of Anti-HT2 Fab with HT-2, anti-IC-HT2 scFv-ALP was applied, which is a single-chain variable antibody fragment (scFv) genetically fused with alkaline phosphatase (ALP) and can recognize the immunocomplex of HT-2 toxin & Anti-HT2 Fab. ALP cleaves non-electroactive 1-NP, producing electroactive 1-N, which can be oxidized with DPV, and thus, the oxidation peak current reports the concentration of the HT-2 in solution (Figure 2.10a). Noncompetitive ELISA is known to have better performance than indirect competitive ones[60], but competitive assays are commonly used for mycotoxin detection, since two antibodies cannot bind a mycotoxin simultaneously due to the small size of mycotoxins. Moreover, the anti-HT2 Fab is not able to specifically recognize HT-2 from T-2 toxin[61], due to their similar structures and T-2 is rapidly metabolized to HT-2 when consumed[62]. Thus, the specificity of the sensor was provided by anti-IC-HT2 scFv, which only binds with the immunocomplex of Anti-HT2 Fab & HT-2, instead of HT-2, T-2, and related molecules (T-2-triol, T-2-tetraol, diacetoxyscirpenol, 15-acetyldeoxynivalenol, 3-acetyl deoxynivalenol, deoxynivalenol, deoxynivalenol-3-glucoside, nivalenol, and neosolaniol) [61]. It is worth noting that the ALP was genetically attached to the anti-IC-HT2 scFv opposite to the antigen-binding site, without disturbing the antibody's performance. This was accomplished through molecular cloning techniques, in contrast to chemical conjugation, which results in random

fusing locations and number [63].

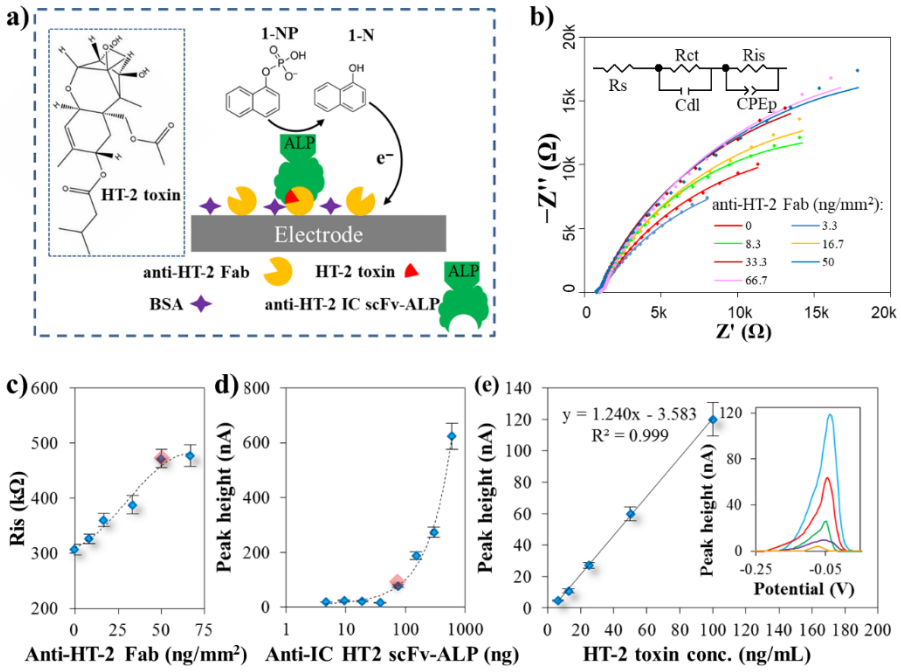

Figure 2.10 (a) Scheme of the HT-2 toxin biosensor based on ERGO microelectrode; the inset shows the chemical structure of HT-2. (b) EIS Nyquist plot of the electrode modified with anti-HT-2 Fab in 1 mM $[Fe(CN)_6]^{3-}/[Fe(CN)_6]^{4-}$ in 0.1 M KCl and the equivalent circuit used for data evaluation in the inset; the amount of applied Anti-HT2 Fab was measured in nanograms per square millimeter on the working electrode (ng/mm^2). (c) Dependence of Ris (interspace solution resistance within the antibody layer, obtained from the data in b) on applied anti-HT-2 Fab. (d) DPV 1-N oxidation signal without applying of HT-2 toxin, indicating the dependence of the biosensor's background signal on applied anti-HT-2 IC scFv-ALP. (e) Dependence of 1-N oxidation signal on concentrations of applied HT-2 toxin, the inset shows corresponding baseline-corrected DPV responses.

The successful attachment of Anti-HT2 Fab onto the ERGO working electrode was monitored using electrochemical impedance spectroscopy (EIS, 1 mM $[Fe(CN)_6]^{3-}/[Fe(CN)_6]^{4-}$ in 0.1 M KCl, DC + 0.185 vs Ag/AgCl, AC amplitude ± 10 mV, at frequency range 0.01-1000 Hz). Figure 2.10b shows that an increasing concentration of attached Anti-HT2 Fab resulted in an incremental change of the depressed semi-circles at low frequencies in the Nyquist diagram. The strong affinity between the electrode and the antibody resulted in the formation of a porous protein layer, and the high density of protein led to considerable solution resistance within the layer interface [64]. The charges either charged the capacitive protein layer and the electric double layer at the electrode surface or travelled through the interspace of the protein layer and

the electrode surface, resulting in the modulation of an equivalent circuit as shown in the inset of Figure 2.10b. The circuit included solution resistance Rs, the capacitance of the protein layer CPEp (with a constant phase element used to compensate for structure inhomogeneity), electric double layer capacitance of the electrode Cdl, interspace solution resistance within the protein layer Ris, and charge transfer resistance Rct. Ris increased with the increasing amount of applied Anti-HT2 Fab and reached a plateau at 50 ng/mm^2 (red diamond in Figure 2.10c), indicating the maximum immobilization of the antibody.

To optimize the amount of applied anti-IC-HT2 scFv-ALP, the DPV oxidative signal of 1-N (in the presence of 5 mM 1-NP) was used to obtain minimal background response. Higher concentrations of anti-IC-HT2 scFv-ALP could result in a substantial increase in the background signal, which is undesirable. Various concentrations of anti-IC-HT2 scFv-ALP were incubated with the Anti-HT2 Fab modified electrodes without the introduction of the HT-2 toxin. A concentration of 75 ng anti-IC-HT2 scFv-ALP (30 μL, 2.5 μg/mL) was selected as optimal (red diamond in Figure 2.10d). It should be noted that the current intensity in Figure 2.10d are in nA scale, whereas but previous ones in μg (Figure 2.9). This difference is due to the fact that the tests in Figure 2.10 were performed on as-prepared microelectrodes, while those in Figure 2.9 were performed on enlarged electrodes (1.0 mm × 5.0 mm).

Under the optimized conditions, the biosensor exhibited an increasing DPV 1-N signal in response to increasing concentrations of HT-2 toxin, with good linear dependence (Figure 2.10e), a dynamic range of 6.3-100.0 ng/mL and a limit of detection (LOD) of 1.6 ng/mL. The low LOD observed is comparable to other methods such as ELISA, surface plasmon resonance biosensors, or high-performance liquid chromatography with fluorescence detection [65-67]. Khan et al. reported a fluorescence resonance energy transfer amplified aptasensor to detect T-2 toxin (which is rapidly hydrolyzed to HT-2 toxin in vivo) with a LOD of 0.93 pg/mL[68]. A LOD of 0.38 ng/mL was reported for a non-competitive immunoassay based on the utilization of time-resolved fluorescence resonance energy transfer [61]. However, in our case, the sensitivity, as well as other detection parameters, can be further tuned by prolonging the incubation times of the substrate 1-NP with the immobilized ALP. During longer incubation times (longer incubation time, anti-IC-HT2 scFv-ALP will produce more 1-N). Notably, the peak of 1-N shifted from +0.05 V (in the case of 1-N sensing of the bare ERGO microelectrode) to -0.08 V (inset, Figure 2.10e). This shift can be attributed to a change in the quasi-reference electrode potential due to multiple incubation and washing steps.

As matrix effects can significantly influence the sensitivity of analysis, an assessment of the detection of HT-2 was performed using spiked fetal bovine serum (FBS). A HT-2 standard solution (1 μg/mL) was diluted with FBS solution (HT-2:FBS = 1:9 in volume) and then mixed with blocking buffer in a ratio of 1:1. The recovery of the standard ranged from 87.8% to 108.5% (n=5).

2.4 Conclusions

In this study, we focused on the fabrication of reduced graphene oxide microelectrodes, where reduced graphene was not only the modifier of highly conductive electrode material but also the electrode material itself. A comparison showed that the consumer printer was not as accurate and reliable as the research-grade printer under optimal conditions, and the latter is qualified for ink patterning on a 10s μm scale. A water-based commercial GO ink was formulated for microelectrode printing with the research-grade inkjet printer onto plasma-treated and chemically etched PEN sheets. The electrode was 78 μm in width, and reduced in KCl solution, where the reduction parameters and electrolyte concentrations were optimized. The increase in peak ratio (I_D/I_G) observed from Raman spectra confirmed the successful reduction of the GO. Based on the electrode, an enzymatic electrochemical immunosensor was optimized for HT-2 mycotoxin detection, showing a dynamic range of 6.3 -100.0 ng/mL and a LOD of 1.6 ng/mL. The proposed biosensor reached biologically relevant analytical parameters and satisfactory recovery in the biological matrix.

Nowadays, with miniaturized commercial potentiostats, ordinary smartphones can be used as electrochemical workstations. Consequently, the reported microelectrode can be used as a part of affordable and portable point-of-care analytical devices beneficial for food quality control [69, 70]. The reported fabrication procedure enables the manufacture of working electrode arrays which is attractive for analysis multiplexing. Moreover, the fabrication of such sensors on transparent plastic materials can be beneficial for the integration of additional sensing devices with optical readout.

2.5 References

1. Liu, R., et al., Recent Trends in Carbon-Based Microelectrodes as Electrochemical Sensors for Neurotransmitter Detection: A Review. *TrAC, Trends Anal. Chem.*, 2022. **148**. DOI: 10.1016/j.trac.2022.116541.
2. Laczka, O., et al., Detection of Escherichia Coli and Salmonella Typhimurium Using Interdigitated Microelectrode Capacitive Immunosensors: The Importance of Transducer Geometry. *Anal. Chem.*, 2008. **80**(19): p. 7239. DOI: 10.1021/ac800643k.
3. Wang, J., *Analytical Electrochemistry*. 2006.
4. Bachmann, B., et al., All-Inkjet-Printed Gold Microelectrode Arrays for Extracellular Recording of Action Potentials. *Flexible and Printed Electronics*, 2017. **2**(3). DOI: 10.1088/2058-8585/aa7928.
5. Niaraki, A., et al., Minute-Sensitive Real-Time Monitoring of Neural Cells through Printed Graphene Microelectrodes. *Biosens. Bioelectron.*, 2022. **210**: p. 114284. DOI: 10.1016/j.bios.2022.114284.
6. Hermerschmidt, F., et al., Truly Low Temperature Sintering of Printed Copper Ink Using Formic Acid. *Advanced Materials Technologies*, 2018. **3**(12). DOI: 10.1002/admt.201800146.
7. Karim, N., et al., All Inkjet-Printed Graphene-Based Conductive Patterns for Wearable E-Textile Applications. *J. Mater. Chem. C*, 2017. **5**(44): p. 11640. DOI: 10.1039/c7tc03669h.
8. Hoeng, F., et al., Inkjet Printing of Nanocellulose–Silver Ink onto Nanocellulose Coated Cardboard. *RSC Advances*, 2017. **7**(25): p. 15372. DOI: 10.1039/c6ra23667g.
9. Bonaccorso, F., et al., 2d-Crystal-Based Functional Inks. *Adv. Mater.*, 2016. **28**(29): p. 6136. DOI: 10.1002/adma.201506410.
10. Singh, M., et al., Inkjet Printing-Process and Its Applications. *Adv. Mater.*, 2010. **22**(6): p. 673. DOI: 10.1002/adma.200901141.
11. Park, B.K., et al., Direct Writing of Copper Conductive Patterns by Ink-Jet Printing. *Thin Solid Films*, 2007. **515**(19): p. 7706. DOI: 10.1016/j.tsf.2006.11.142.
12. Lei, Y.-M., et al., Detection of Heart Failure-Related Biomarker in Whole Blood with Graphene Field Effect Transistor Biosensor. *Biosens. Bioelectron.*, 2017. **91**: p. 1. DOI: 10.1016/j.bios.2016.12.018.
13. Mbayachi, V.B., et al., Graphene Synthesis, Characterization and Its Applications: A Review. *Results in Chemistry*, 2021. **3**: p. 100163. DOI: 10.1016/j.rechem.2021.100163.
14. Nguyen, E.P., C. de Carvalho Castro Silva, and A. Merkoci, Recent Advancement in Biomedical Applications on the Surface of Two-Dimensional Materials: From Biosensing to Tissue Engineering. *Nanoscale*, 2020. **12**(37): p. 19043. DOI: 10.1039/d0nr05287f.
15. Catania, F., et al., A Review on Recent Advancements of Graphene and Graphene-Related Materials in Biological Applications. *Applied Sciences*, 2021. **11**(2). DOI: 10.3390/app11020614.

16. Verma, M.L., et al., Synthesis and Application of Graphene-Based Sensors in Biology: A Review. *Environ. Chem. Lett.*, 2022. **20**(3): p. 2189. DOI: 10.1007/s10311-022-01404-1.

17. Ma, Y. and L. Zhi, Functionalized Graphene Materials: Definition, Classification, and Preparation Strategies. *Acta Physico-Chimica Sinica*, 2021: p. 2101004.

18. Ambrosi, A., et al., Electrochemistry of Graphene and Related Materials. *Chem. Rev.*, 2014. **114**(14): p. 7150. DOI: 10.1021/cr500023c.

19. Michel, M., C. Biswas, and A.B. Kaul, High-Performance Ink-Jet Printed Graphene Resistors Formed with Environmentally-Friendly Surfactant-Free Inks for Extreme Thermal Environments. *Applied Materials Today*, 2017. **6**: p. 16. DOI: 10.1016/j.apmt.2016.12.001.

20. Chen, Y., et al., High Performance Supercapacitors Based on Reduced Graphene Oxide in Aqueous and Ionic Liquid Electrolytes. *Carbon*, 2011. **49**(2): p. 573. DOI: 10.1016/j.carbon.2010.09.060.

21. Benchirouf, A., C. Muller, and O. Kanoun, Electromechanical Behavior of Chemically Reduced Graphene Oxide and Multi-Walled Carbon Nanotube Hybrid Material. *Nanoscale Res Lett*, 2016. **11**(1): p. 4. DOI: 10.1186/s11671-015-1216-5.

22. Pei, L. and Y.-F. Li, Rapid and Efficient Intense Pulsed Light Reduction of Graphene Oxide Inks for Flexible Printed Electronics. *RSC Advances*, 2017. **7**(81): p. 51711. DOI: 10.1039/c7ra10416b.

23. Ren, X., et al., Sulfur-Doped Graphene-Based Immunological Biosensing Platform for Multianalysis of Cancer Biomarkers. *ACS Appl. Mater. Interfaces*, 2017. **9**(43): p. 37637. DOI: 10.1021/acsami.7b13416.

24. Keramat, A., et al., The Potential of Graphene Oxide and Reduced Graphene Oxide in Diagnosis and Treatment of Cancer. *Curr. Med. Chem.*, 2022. **29**(26): p. 4529. DOI: 10.2174/0929867329666220208092157.

25. Gutiérrez-Cruz, A., et al., A Review of Top-Down and Bottom-up Synthesis Methods for the Production of Graphene, Graphene Oxide and Reduced Graphene Oxide. *J. Mater. Sci.*, 2022. **57**(31): p. 14543. DOI: 10.1007/s10853-022-07514-z.

26. Toh, S.Y., et al., Graphene Production Via Electrochemical Reduction of Graphene Oxide: Synthesis and Characterisation. *Chem. Eng. J.*, 2014. **251**: p. 422. DOI: 10.1016/j.cej.2014.04.004.

27. Hussein, H.S. and J.M. Brasel, Toxicity, Metabolism, and Impact of Mycotoxins on Humans and Animals. *Toxicology*, 2001. **167**(2): p. 101. DOI: 10.1016/s0300-483x(01)00471-1.

28. Kuchenbuch, H.S., et al., Thermal Stability of T-2 and Ht-2 Toxins During Biscuit- and Crunchy Muesli-Making and Roasting. *Food Addit. Contam. Part A Chem. Anal. Control Expo. Risk Assess.*, 2018. **35**(11): p. 2158. DOI: 10.1080/19440049.2018.1530456.

29. Rocha, O., K. Ansari, and F.M. Doohan, Effects of Trichothecene Mycotoxins on Eukaryotic Cells: A Review. *Food Addit Contam*, 2005. **22**(4): p. 369. DOI: 10.1080/02652030500058403.

30. EC, Commission Recommendation 2013/165/Eu of 27 March 2013 on the Presence of T-2 and Ht-2 Toxin in Cereals and Cereal Products. *Off. j. Eur. Communities*,

2013(91): p. 12.

31. Kaukoranta, T., et al., Contrasting Responses of T-2, Ht-2 and Don Mycotoxins and Fusarium Species in Oat to Climate, Weather, Tillage and Cereal Intensity. *Eur. J. Plant Pathol.* , 2019. **155**(1): p. 93. DOI: 10.1007/s10658-019-01752-9.

32. Yoo, M., et al., Silver Nanoparticle-Based Inkjet-Printed Metamaterial Absorber on Flexible Paper. *IEEE Antennas Wirel. Propag. Lett.*, 2015. **14**: p. 1718.

33. Raut, N.C. and K. Al-Shamery, Inkjet Printing Metals on Flexible Materials for Plastic and Paper Electronics. *J. Mater. Chem. C*, 2018. **6**(7): p. 1618. DOI: 10.1039/c7tc04804a.

34. Sui, Y. and C.A. Zorman, Review—Inkjet Printing of Metal Structures for Electrochemical Sensor Applications. *J. Electrochem. Soc.*, 2020. **167**(3): p. 037571. DOI: 10.1149/1945-7111/ab721f.

35. Rosati, G., et al., A Plug, Print & Play Inkjet Printing and Impedance-Based Biosensing Technology Operating through a Smartphone for Clinical Diagnostics. *Biosens. Bioelectron.*, 2022. **196**: p. 113737. DOI: 10.1016/j.bios.2021.113737.

36. Rosati, G., et al., Silver Nanoparticles Inkjet-Printed Flexible Biosensor for Rapid Label-Free Antibiotic Detection in Milk. *Sensors Actuators B: Chem.*, 2019. **280**: p. 280. DOI: 10.1016/j.snb.2018.09.084.

37. Haque, R.I., et al., Inkjet Printing of High Molecular Weight Pvdf-Trfe for Flexible Electronics. *Flexible and Printed Electronics*, 2016. **1**(1): p. 015001. DOI: 10.1088/2058-8585/1/1/015001.

38. Arola, H.O., et al., A Simple and Specific Noncompetitive Elisa Method for Ht-2 Toxin Detection. *Toxins (Basel)*, 2017. **9**(4). DOI: 10.3390/toxins9040145.

39. Prathish, K.P., et al., Chemically Modified Graphene and Nitrogen-Doped Graphene: Electrochemical Characterisation and Sensing Applications. *Electrochim. Acta*, 2013. **114**: p. 533. DOI: 10.1016/j.electacta.2013.10.080.

40. Waasdorp, R., et al., Accessing Individual 75-Micron Diameter Nozzles of a Desktop Inkjet Printer to Dispense Picoliter Droplets on Demand. *RSC Advances*, 2018. **8**(27): p. 14765. DOI: 10.1039/c8ra00756j.

41. *Dimatix*. Available from: https://www.fujifilm.com/us/en.

42. Tran, T.S., N.K. Dutta, and N.R. Choudhury, Graphene Inks for Printed Flexible Electronics: Graphene Dispersions, Ink Formulations, Printing Techniques and Applications. *Advances in Colloid and Interface Science*, 2018. **261**: p. 41. DOI: 10.1016/j.cis.2018.09.003.

43. Zhong, J.H., et al., Quantitative Correlation between Defect Density and Heterogeneous Electron Transfer Rate of Single Layer Graphene. *J Am Chem Soc*, 2014. **136**(47): p. 16609. DOI: 10.1021/ja508965w.

44. Ye, S. and J. Feng, The Effect of Sonication Treatment of Graphene Oxide on the Mechanical Properties of the Assembled Films. *RSC Advances*, 2016. **6**(46): p. 39681. DOI: 10.1039/c6ra03996k.

45. Li, P., et al., Preparation of Graphene Oxide-Based Ink for Inkjet Printing. *J Nanosci Nanotechnol*, 2018. **18**(1): p. 713. DOI: 10.1166/jnn.2018.13942.

46. Vaseem, M., et al., Inkjet Printed Fractal-Connected Electrodes with Silver

Nanoparticle Ink. *ACS Appl Mater Interfaces*, 2012. **4**(6): p. 3300. DOI: 10.1021/am300689d.

47. Stringer, J. and B. Derby, Limits to Feature Size and Resolution in Ink Jet Printing. *J. Eur. Ceram. Soc.*, 2009. **29**(5): p. 913. DOI: 10.1016/j.jeurceramsoc.2008.07.016.

48. Shiwaku, R., et al., A Printed Organic Circuit System for Wearable Amperometric Electrochemical Sensors. *Sci. Rep.*, 2018. **8**(1): p. 6368. DOI: 10.1038/s41598-018-24744-x.

49. Gonzalez, E., 2nd, et al., Remote Atmospheric-Pressure Plasma Activation of the Surfaces of Polyethylene Terephthalate and Polyethylene Naphthalate. *Langmuir*, 2008. **24**(21): p. 12636. DOI: 10.1021/la802296c.

50. Cammarano, A., G. Luca, and E. Amendola, Surface Modification and Adhesion Improvement of Polyester Films. *Open Chemistry*, 2013. **11**(1): p. 35. DOI: 10.2478/s11532-012-0135-x.

51. Juang, Z.-Y., et al., Graphene Synthesis by Chemical Vapor Deposition and Transfer by a Roll-to-Roll Process. *Carbon*, 2010. **48**(11): p. 3169. DOI: 10.1016/j.carbon.2010.05.001.

52. Ramesha, G.K. and S. Sampath, Electrochemical Reduction of Oriented Graphene Oxide Films: An in Situ Raman Spectroelectrochemical Study. *J. Phys. Chem. C*, 2009. **113**(19): p. 7985. DOI: 10.1021/jp811377n.

53. Kuang, B., et al., Chemical Reduction Dependent Dielectric Properties and Dielectric Loss Mechanism of Reduced Graphene Oxide. *Carbon*, 2018. **127**: p. 209. DOI: 10.1016/j.carbon.2017.10.092.

54. Casero, E., et al., Lactate Biosensor Based on a Bionanocomposite Composed of Titanium Oxide Nanoparticles, Photocatalytically Reduced Graphene, and Lactate Oxidase. *Microchimica Acta*, 2013. **181**(1-2): p. 79. DOI: 10.1007/s00604-013-1070-z.

55. Casero, E., et al., Comparative Response of Biosensing Platforms Based on Synthesized Graphene Oxide and Electrochemically Reduced Graphene. *Electroanalysis*, 2013. **25**(1): p. 154. DOI: 10.1002/elan.201200480.

56. Raj, M.A. and S.A. John, Fabrication of Electrochemically Reduced Graphene Oxide Films on Glassy Carbon Electrode by Self-Assembly Method and Their Electrocatalytic Application. *J. Phys. Chem. C*, 2013. **117**(8): p. 4326. DOI: 10.1021/jp400066z.

57. Brownson, D.A.C., et al., Electrochemistry of Graphene: Not Such a Beneficial Electrode Material? *RSC Advances*, 2011. **1**(6): p. 978. DOI: 10.1039/c1ra00393c.

58. Tan, S.M., et al., Electron Transfer Properties of Chemically Reduced Graphene Materials with Different Oxygen Contents. *J. Mater. Chem. A*, 2014. **2**(27): p. 10668. DOI: 10.1039/c4ta01034e.

59. Feng, X., W. Chen, and L. Yan, Electrochemical Reduction of Bulk Graphene Oxide Materials. *RSC Advances*, 2016. **6**(83): p. 80106. DOI: 10.1039/c6ra17469h.

60. Jackson, T.M. and R.P. Ekins, Theoretical Limitations on Immunoassay Sensitivity. Current Practice and Potential Advantages of Fluorescent Eu3+ Chelates as Non-Radioisotopic Tracers. *J. Immunol. Methods*, 1986. **87**(1): p. 13. DOI: 10.1016/0022-1759(86)90338-8.

61. Arola, H.O., et al., Specific Noncompetitive Immunoassay for Ht-2 Mycotoxin Detection. *Anal. Chem.*, 2016. **88**(4): p. 2446. DOI: 10.1021/acs.analchem.5b04591.

62. Dohnal, V., et al., Metabolic Pathways of T-2 Toxin. *Curr. Drug Metab.*, 2008. **9**(1): p. 77. DOI: 10.2174/138920008783331176.

63. Avrameas, S., *Enzyme Immunoassays and Related Techniques: Development and Limitations*, in *New Developments in Diagnostic Virology*, P.A. Bachmann, Editor. 1983, Springer Berlin Heidelberg: Berlin, Heidelberg. p. 93.

64. Huang, Y., et al., Protein Adsorption Behavior on Reduced Graphene Oxide and Boron-Doped Diamond Investigated by Electrochemical Impedance Spectroscopy. *Carbon*, 2019. **152**: p. 354. DOI: 10.1016/j.carbon.2019.06.023.

65. Yoshizawa, T., et al., A Practical Method for Measuring Deoxynivalenol, Nivalenol, and T-2 + Ht-2 Toxin in Foods by an Enzyme-Linked Immunosorbent Assay Using Monoclonal Antibodies. *Biosci Biotechnol Biochem*, 2004. **68**(10): p. 2076. DOI: 10.1271/bbb.68.2076.

66. Meneely, J.P., et al., A Rapid Optical Immunoassay for the Screening of T-2 and Ht-2 Toxin in Cereals and Maize-Based Baby Food. *Talanta*, 2010. **81**(1-2): p. 630. DOI: 10.1016/j.talanta.2009.12.055.

67. Lippolis, V., et al., Improvement of Detection Sensitivity of T-2 and Ht-2 Toxins Using Different Fluorescent Labeling Reagents by High-Performance Liquid Chromatography. *Talanta*, 2008. **74**(5): p. 1476. DOI: 10.1016/j.talanta.2007.09.024.

68. Khan, I.M., et al., Silver Nanoclusters Based Fret Aptasensor for Sensitive and Selective Fluorescent Detection of T-2 Toxin. *Sensors Actuators B: Chem.*, 2018. **277**: p. 328. DOI: 10.1016/j.snb.2018.09.021.

69. da Silva, E.T.S.G., et al., Electrochemical Biosensors in Point-of-Care Devices: Recent Advances and Future Trends. *ChemElectroChem*, 2017. **4**(4): p. 778. DOI: 10.1002/celc.201600758.

70. Vashist, S.K., et al., Emerging Technologies for Next-Generation Point-of-Care Testing. *Trends Biotechnol.*, 2015. **33**(11): p. 692. DOI: 10.1016/j.tibtech.2015.09.001.

2.6 Contributions

This work has been performed in collaboration with Dr. Jiri Kudr, Prof. Vojtech Adam, Prof. Ondrej Zitka, from the Department of Chemistry and Biochemistry, Mendel University in Brno (Brno, Czech Republic), and Dr. Henri Arola, Prof. Tarja K. Nevanen from VTT Technical Research Centre of Finland (Espoo, Finland). VTT validated and supplied the antibodies. Dr. Jiri Kudr worked on the development of the biosensor during his visiting to the nanobioelectronics and biosensors group (Barcelona, Spain).

3 Laser reduced graphene oxide electrode for *E. coli* detection

3.1 Introduction

Electrochemical sensors have been widely used in various fields, such as disease diagnostics, hazard monitoring and food quality control, due to their low cost, high sensitivity and ease of miniaturization [1-3]. The tunable conductivity, high surface area and biocompatibility make graphene a promising material for constructing electrochemical sensors[4-6]. Low-defect graphene is usually produced by physical exfoliation with expensive/toxic solvents (n-methyl-2-pyrrolidone, dimethyl sulfoxide, N, N-dimethylformamide); or chemical vapor deposition [7], which shows low throughput and involves high temperatures and complicated transfer process, limiting the practical use of graphene electrodes. In this regard, functionalized graphene[8] such as graphene oxide (GO) has emerged as an alternative, but the inherent dielectric property of GO confines its application in electronic devices [9]. In contrast, reduced graphene oxide (rGO) shows good electrical conductivity and a high electron transfer rate, and maintains oxygen-containing groups for further functionalization[10]. Chemical[11], thermal[12] and electrochemical[13] methods have been reported to reduce GO, resulting in rGO electrodes with different surface composites and defect densities, which affect the performance of the electrode significantly.

The patterning of graphene electrodes is of great importance for the fabrication of electrochemical sensors [4, 14, 15]. Often photolithographic techniques are used to pattern low-defect graphene [15, 16], however, these methods are not widely available due to the need for expensive equipment and clean room facilities. Templated-based strategies such as vacuum filtration[17], chemical covalent bonding[18] and contact-transfer printing[19] have also been demonstrated for graphene patterning, but they require physically or chemically patterned models, and may need hazardous chemicals, making the process unscalable. Printing methods could produce graphene electrodes on large scale and at low cost[20]. However, to obtain good printing, additives are usually necessary to adjust the rheological properties of the graphene inks, which may affect the electrochemical performance of the final electrodes. Meanwhile, pre-treatment of the substrate may be needed to achieve stable and uniform ink adhesion. In addition, high-temperature annealing is usually required after printing [21], which limits the choice of substrates to heat-resistant materials. Since printing is a solution-based manufacturing process, the van der Waals force and π-π stacking effect can lead to restacking of graphene sheets during sintering, resulting in a reduced surface area of the graphene [22].

Direct laser writing has been proven an easy, efficient, low-cost, chemical and mask-free

method for graphene electrode fabrication, by simultaneously patterning and reducing GO, or *in situ* creation of graphene from carbon-based materials [23-25]. The Kaner group reported a pioneer work in which laser induced graphene (LIG) was produced with a standard LightScribe DVD driver, with a total cost of less than 20 $, including the laser [26]. Lin et al [27] developed porous graphene by direct laser writing of a commercial polyimide sheet with a CO_2 laser in 2014 and explained the mechanism first. Ever since, polyimide substrates have dominated the field, despite the intensive efforts devoted to graphene production with alternative materials, including other polymers, carbon and natural materials [14, 28, 29]. Various works have illustrated biosensors based on the electrodes formed by laser-scribed polyimide films [14, 23, 25]. However, as far as we know, there is not any reported biosensor developed with electrodes made of the laser induced reduction of GO. The main issues behind this are: (1) The reduction happens *in situ*, meaning that GO and rGO are present in the same plane. It is not desirable since the highly soluble GO will dissolve in any biological media[22, 30]. (2) LIG is very fragile and can be damaged by gentle gas flows[31, 32]. To overcome these issues, the Nam group developed a method to transfer and pattern graphene simultaneously, but it is only applicable to the substrates that don't absorb the excitation laser[33]. Our group have recently reported a novel, stamp transfer method, capable of fabricating rGO electrodes on a wide variety of substrates[34]. In this work, a GO film formed by vacuum filtration was reduced and patterned with a LightScribe DVD driver, and then was transferred to various substrates with a mechanical press while the GO remained on the original host substrate. At the same time, the mechanical properties of the LIG were enhanced during the pressing. However, this work only verified that such electrodes were applicable for electrochemical sensing, instead of biosensing. In addition, the process required a vacuum pump and expensive filter membranes, thus could only produce small batch sizes and was relatively slow.

Herein we report a simple, efficient method for the large-scale production of laser reduced graphene oxide (LRGO) electrodes based on the above-mentioned work by our group and demonstrate its capability of biosensing. A typical three-electrode system was built, consisting of working and counter electrodes made of LRGO stamp-transferred onto polyester (PE) sheets, inkjet printed silver contacts and Ag/AgCl reference electrode (by a sequent chlorination process). As a proof of concept, a biosensor was demonstrated for the first time based on such electrodes to detect *Escherichia coli* (*E. coli*) by creating an electrochemical enzyme linked immunosorbent assay (ELISA). Its sensing ability was verified in phosphate buffered saline (PBS) buffer with a commercial potentiostat, showing a dynamic range of 917 -2.1×10^7

CFU/mL and a detection limit of 283 CFU/mL. The sensor was also tested in artificial urine, and on a portable, wireless system controlled by a mobile phone[35], demonstrating the potential of application towards the point of care.

3.2 Experiments

3.2.1 Materials

GO solution, (GO water dispersion, 10 mg/mL) was purchased from Graphenea (San Sebastian, Spain). Polyester (PE) sheets (AUTOSTAT HT1802168201) were obtained from MacDermid Autotype Ltd. (Wantage, UK). Phosphate buffered saline tables, Tween™ 20 and Tryptic Soy Agar were ordered from Merck Life Science S.L.U (Madrid, Spain). Phosphate buffered saline buffer (PBS, 10 mM, pH 7.4) was prepared by dissolving PBS tablets in ultrapure water. PBS with Tween 20 (PBST) buffer was prepared by adding Tween™ 20 (final concentration 0.05 wt.%) in PBS buffer (10 mM). Polyclonal anti-*E. coli* antibody (PA1-7213) was obtained from Fisher Scientific (Madrid, Spain). HRP-labelled antibodies (ab20425) and 3, 3', 5, 5'-Tetramethylbenzidine (TMB) substrate (ab171523) were purchased from Abcam plc (Cambridge, UK). *Escherichia coli* (*E. coli*, CECT 4972) and *Staphylococcus aureus subsp. Aureus* (SA, CECT 5190) were purchased from CECT (Valencia, Spain), and *Salmonella Typhimurium* (ST, ATCC 14028) from ATCC (Virginia, USA).

3.2.2 LRGO electrode production

PE substrates were washed with isopropanol (IPA) and dried with nitrogen or compressed air. Afterwards, 5 ml of GO solution was drop-casted on an 8 × 8 cm square defined on the PE sheet with paper tape (to prevent the solution from spreading), shaken gently by hand and then dried at 60 °C for 2 h. A CO_2 laser engraver (Rayjet 50 Laser Engraver, Trotec Laser GmbH, Marchtrenk, Austria) was used to scribe the GO film to produce laser reduced graphene oxide (LRGO), the laser settings were, power = 2.07 W and speed = 1.5 m/s. The LRGO was placed face down on the desired substrate, fixed tightly in place with scotch tape, sandwiched between four sheets of A4 paper (2 layers above and 2 layers below the sample) and placed in a hydraulic press (SPECAC manual hydraulic press 15 ton, UK). A 6-ton force was applied for 1 min to transfer the LRGO onto the hosting substrate, forming both the working electrode (WE) and counter electrode (CE). Silver contacts were inkjet printed with a Dimatix 2831 (FUJIFILM Dimatix, USA. Print temperature 30 °C, plate temperature 60 °C, drop space 25 μm, 3 layers),

using a silver ink (Sicrys I40DM-106, PV Nano Cell Ltd, Migdal Ha'Emek, Israel) and then oven-cured at 160 °C for 2 h. Poly dimethyl siloxane (PDMS, SYLGARD® 184 silicon elastomer kit, Dow corning, MI, USA) was used as an insulating layer; a schematic summary of the insulation process has been included in Figure 3.1. Ag/AgCl pseudo-reference electrodes (RE) were obtained by chlorinating the printed Ag trace with 0.4 % NaClO for 3 min[36].

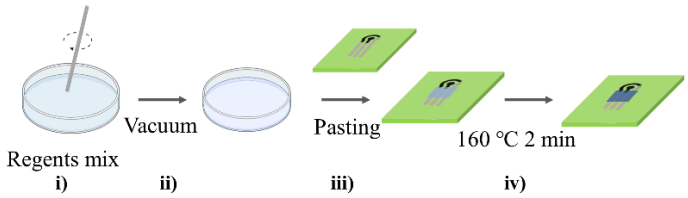

Figure 3.1 Schematic illustration of the insulation process using poly dimethyl siloxane (PDMS). (i) Mix the base solution and curing agent in a 10:1 weight ratio; (ii) place in a vacuum chamber for 5 min to remove the bubbles generated during mixing; (iii) paste the mixed liquid over the desired area (between the electrodes and connection points); (iv) Cure at 160 °C for 2 min.

3.2.3 Characterizations of LRGO

Cyclic voltammetry (CV) was done with a commercial potentiostat (PalmSens4, PalmSens BV, Houten, Netherlands), in an aqueous solution of 0.5 mM potassium ferrocyanide, 0.5 mM potassium ferricyanide and 0.1 M KCl at a scan rate of 50 mV/s. For defining the electrochemical active surface area (ECSA) with non-faradic mothed, CVs were performed in 0.1 M $NaClO_4$ (in ethanol) by using a 3 mm diameter LRGO disk as WE, four LRGO squares (Each 1 cm^2) as CEs and a commercial Ag/AgCl electrode (CHI111, CH Instruments, Inc.) as the RE. The height of the films was measured by an optical profilometer (Profilm 3D, Filmetrics Inc.) equipped with a 10 × objective and using a stage movement speed of 0.12 mm/s. Scanning electron microscopy (SEM) was performed with a Quanta 650 (UK) at a working distance of 10 mm and voltage of 10 kV; the samples were mounted on aluminum stubs and sputtered with Au before imaging. The sheet resistance was obtained by measuring square (1 cm×1 cm) samples with a Keithley 2400 using a four-point probe system (van der Pauw method). Raman spectra were obtained with a Raman microscope (Alpha300 R-Raman Imaging Microscope, Oxford Instruments) using a 488 nm laser with a spot size of approximately 3 μm. The parameters used were: laser power = 1 mW, grating = 600 gr/nm, objective = 50×, exposure time = 10 s, accumulations = 2, waveform range = 500~3500/cm.

XPS measurements were performed at room temperature with a SPECS PHOIBOS 150 hemispherical analyzer (SPECS GmbH, Berlin, Germany) at a base pressure of $5x10^{-10}$ mbar using monochromatic Al K alpha radiation (1486.74 eV) as the excitation source, operated at 300 W. The sampling area was 3.5 mm×1 mm and the energy resolution as measured by the full width at half maximum (FWHM) of the Ag 3d 5/2 peak for a sputtered silver foil and was found to be 0.62 eV. The fitting of the obtained spectra was done with XPSPEAK 41 with a Shirley background correction.

3.2.4 LRGO electrode functionalization

The LRGO working electrode was activated with 1-pyrenebutanoic acid succinimidyl ester solution (PBASE, 1 µL of 2 mg/mL in dimethylformamide) at room temperature for 4 h. The electrode was then cleaned twice with IPA and four times with ultrapure water. The capture antibody (cAb, 15 µg/mL in 10 mM PBS) was spontaneously immobilized by incubating 5 µL of the solution on the WE (4 °C, overnight). Ethylamine (4 µL, 0.1 M in PBS) was put on the WE for 30 min to block any unreacted PBASE, and then the electrode was further blocked with bovine serum albumin (BSA, 5µL, 5% in PBS) at 37°C for 1h to prevent non-specific fouling in complex media. Between each step, the electrode was washed twice with PBST and twice with PBS; all the steps above were performed in a humidity chamber.

3.2.5 Bacteria preparation

Bacteria were cultured overnight in Tryptic Soy Agar at 37 ºC. Afterwards, colonies were picked and suspended in PBS. Then the bacterial solutions were diluted to obtain an OD600 value as close to 10^9 CFU/mL as possible[37]. Finally, the bacteria were heat-killed at 65 ºC for 20 min [38].

3.2.6 Electrochemical Bacterial detection

To perform the bacteria detection, 5 µL of the bacteria-containing solution was pipetted onto the WE, left for 30 min, and then washed twice with PBST and twice with PBS. Directly after cleaning, 4 µL of the detection antibody solution (dAb, ab20425, 2 µg/mL) was pipetted onto the WE and left for 30 min and then washed twice with PBST and 4 times with PBS. Subsequently, 50 µL of the TMB ELISA solution was added, and the chronoamperometric sensing started. Chronoamperometry (CA) was performed at +0.125 V, vs the onboard Ag/AgCl RE, with both the PalmSens4 and a wireless smartphone-driven potentiostat

developed in-house and fabricated according to a previous publication[35].

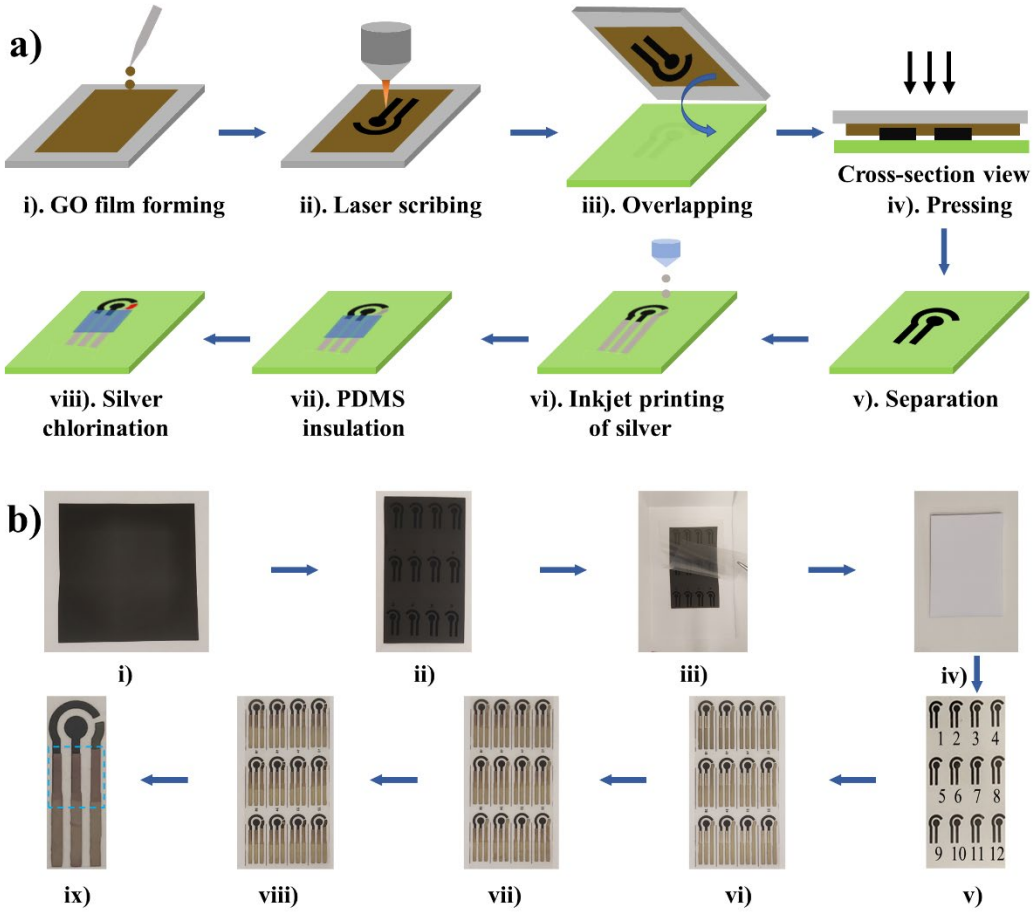

Figure 3.2 (a) Illustration of the fabrication process for laser reduced graphene oxide electrode (LRGO). (i) GO solution was drop cast on a defined area and dried at 60 °C, forming a GO film on a polyester (PE) sheet; (ii) laser scribing to reduce and pattern the GO film, resulting LRGO; (iii) place LRGO face-down onto the desired substrate; (iv) apply a pressure to transfer the LRGO; (v) a mirrored LRGO pattern was transferred after the separation; (vi) inkjet printing of the silver connections; (vii) poly dimethyl siloxane (PDMS) was casted as dielectric layer; (viii) By adding NaClO, Ag was transformed to AgCl, obtaining a reference electrode. (b) Optical pictures corresponding to each step shown in (a); (ix) is an enlarged picture of the final electrode, consisting of LRGO working electrode (black spot), LRGO counter electrode (black arc) and Ag/AgCl pseudo-reference and PDMS insulation layer inside the dashed square.

3.2.7 ELISA Bacterial detection

The ELISA test was performed according to a previously established protocol with minor modifications[39]. Firstly, 100 µL of capture antibody (PA1-7213, 2 µg/mL in Carbonate-

Bicarbonate Buffer, pH 9.6) was aliquoted into a 96-well ELISA plate (44-2404-21, MaxiSorp, Fisher Scientific, Spain) and incubated at 4 °C overnight. Secondly, 200 µL of BSA (3% in PBS) was added into the wells and incubated at 37 °C for 1 h, to prevent non-specific fouling of the wells. Thirdly, 100 µL of bacterial samples was added and kept at room temperature for 1h. The wells were washed three times with PBST between each step and then incubated with 100 µL of HRP-labeled detection antibodies (HRP-dAb, 0.33 µg/mL ab20425, in PBS) for 1 hour at room temperature. Finally, the ELISA wells were washed 5 times with PBST. Afterwards, 100 µL of the TMB substrate solution was added into each well and left for 10 min at room temperature. Finally, 50 µL of 2 M H_2SO_4 was added into the wells and then the absorbance of each well was detected at 450 nm using a SpectraMax iD3 Multi-Mode Microplate Reader (Molecular Devices, USA).

3.3 Results and discussions

3.3.1 LRGO electrode fabrication and characterization

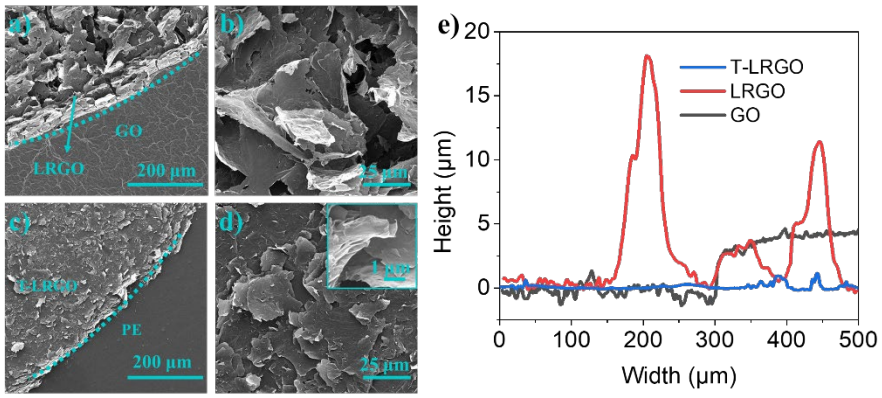

Figure 3.3 SEM image of, the border between LRGO and GO film (a), LRGO (b), LRGO after being transferred on PE sheet, named T-LRGO (c). (d) Magnified image of the T-LRGO on PE; inset is an enlarged Figure of the same area. (e) One-dimensional surface profiles of GO, LRGO and T-LRGO.

In this study, AutoCAD 2018 (Autodesk, USA) was used to design all patterns, which were then sent to the laser engraver and inkjet printer for fabrication of the LRGO electrodes. The combination of direct writing methods and stamp-transferring procedure enabled a simple, fast, maskless, and mass-scale production of the LRGO electrodes (Figure 3.2). The drop-casted GO film exhibited typical bumps and ravines of graphene-based materials[22, 30, 40], and was transformed into a porous structure with flakes of ~10 µm in length after laser scribing, as seen

in SEM images in Figure 3.3a and b. The color of the film also changed from dark brown to black, consistent with previous reports [34]. The film maintained a highly porous 3D framework, although it was flatter (Figure 3.3c and d) after transferring. The optical profilometer data (Figure 3.3e) indicated a thickness of 3-4.5 µm for the GO film, which became more heterogeneous and reached a height of 18.2 µm in some areas due to the violent expansion of the film caused by gases (H_2O, CO and CO_2) generated by the photothermal effect during the laser scribing process [14]. The thickness was then reduced to 0.4-1.3 µm due to the strong force applied during the transfer process.

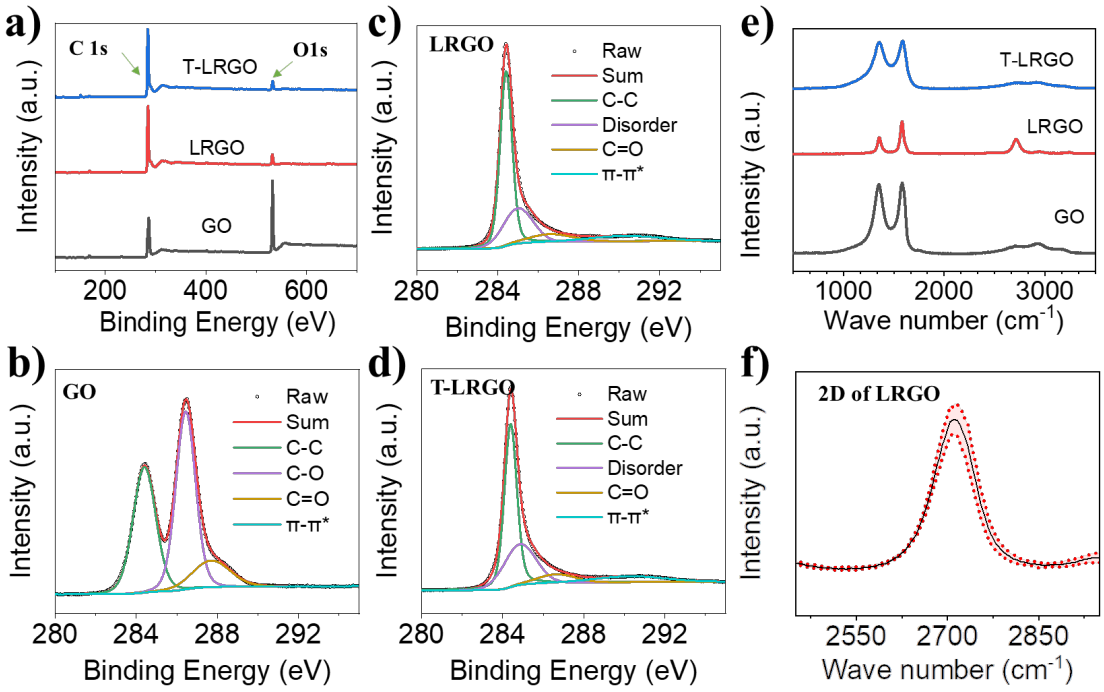

Figure 3.4 (a) XPS survey and high-resolution C 1s spectra of (b) GO, (c) LRGO and (d) T-LRGO. (e) Representative Raman spectra of GO, LRGO and T-LRGO on PE. (f) Average 2D band of LRGO from 5-time random Raman measurements (shaded area indicates the standard deviation).

GO, LRGO, and T-LRGO were characterized XPS characterization, where the dominant peaks of C and O were observed in all three samples (Figure 3.4a). The increase in the C/O ratio from GO (2.7) to LRGO (22.0) indicated a successful reduction. During the stamp-transferring process, the surface of LRGO was in contact with the new substrate, making the surface of T-LRGO the inner layer of LRGO. A similar C/O ratio of T-LRGO (23.4) and LRGO (22.0) demonstrates that the laser reduction was not limited to the surface but penetrated the bulk of GO. The high-resolution C1s spectrum of GO (Figure 3.4b) showed peaks at 284.4, 286.4, and

287.7 eV, corresponding to carbons with the bonds of C-C, C-O, C=O, respectively[27, 41-46]. Further analysis revealed that the relative peak areas were 39.0% (284.4eV), 46.8% (286.4eV), and 13.9% (287.7eV) (Table 3.1), and the high proportion of oxygen verified the high oxidation degree of GO. The C1s spectrum of LRGO (Figure 3.4c) presented an irregular carbon peak at 285.0 eV (25.6%) [45, 46], negligible C-O peak (8.8%), and disappeared C=O, further proving the effective reduction of GO by laser scribing. The increase of the sp^2 carbon component and the significant increase of π-π* satellite peak (at 291.2eV, 9.2%; 0.3% in the case of GO) specified the restoration of the graphene lattice. The data for LRGO and T-LRGO were the same within error, indicating that the reduction was homogenous through the whole depth of GO, and the transfer did not affect the chemical properties of the graphene. Together, these results suggest that the reduction degree was high, and this is further supported by the conductivity difference. The sheet resistance of GO is >20 MΩ/sq[26], while it decreased significantly to 90.6±3.9Ω/sq (considering the thickness as 1 μm).

Table 3.1 XPS C 1s elemental composition in GO, LRGO and T-LRGO; C/O means C/O ratio obtained by the relative peak areas of C 1s and O 1s peak for the survey spectra.*

GO			LRGO			T-LRGO		
C1s	Binding energy (eV)	Area percentage (%)	C1s	Binding energy (eV)	Area percentage (%)	C1s	Binding energy (eV)	Area percentage (%)
C-C	284.4	39.0	C-C	284.4	56.4	C-C	284.4	57.7
C-O	286.4	46.8	disorder	285.0	25.6	disorder	285.0	26.0
C=O	287.7	13.9	C-O	286.4	8.8	C-O	286.4	7.0
π-π*	291.2	0.3	π-π*	291.2	9.2	π-π*	291.2	9.4
C/O*	2.7		C/O *	22.0		C/O *	23.4	

The Raman spectra (shown in Figure 3.4e) reveal the presence of the characteristic D (~1345 cm^{-1}) and G (~1580 cm^{-1}) bands of graphene in all samples, with peak intensity ratios (I_D/I_G) of 1.00±0.02 for GO, 0.41±0.07 for LRGO, and 0.99±0.01 for T-LRGO (n=6). Additionally, the 2D band at ~2700 cm^{-1} is only present in LRGO. The G band corresponds to the in-plane vibration of carbon atoms in the graphene lattice, while the D band reflects defects and structural disorder that generate collective in-plane vibration of atoms towards and away from the center of the hexagonal lattice. The 2D band is the second order of the D band and can indicate the layer number and states of graphene [40, 47, 48]. The significant decrease in I_D/I_G

after laser scribing confirms the reduction of GO, which is consistent with the results of XPS and sheet resistance measurements. The normalized average of the spectra recorded at five random locations on a single electrode showed small standard deviations (Figure 3.4f), indicating the uniform reduction across the GO film. The full width of half maximum (FWHM) of the 2D band, obtained by the Lorentzian function, was 74.97±2.93 cm^{-1}, suggesting that the LRGO film consists of few-layered graphene. Interestingly, T-LRGO displayed Raman spectra that were the same as GO within error, in contrast to what was observed in XPS. This suggests that there may have been residues of unreduced GO on the surface of T-LRGO. It is worth noting that XPS samples a large area (spot size of 1 × 3.5 mm in this case), probing the sample to a certain depth and reflecting the average chemical components in a volume of the surface. In contrast, Raman is a surface characterization technique, meaning that the signals are dominated by what is present on the electrode surface. Therefore, it is assumed that a thin layer of GO remained on the surface of the electrode.

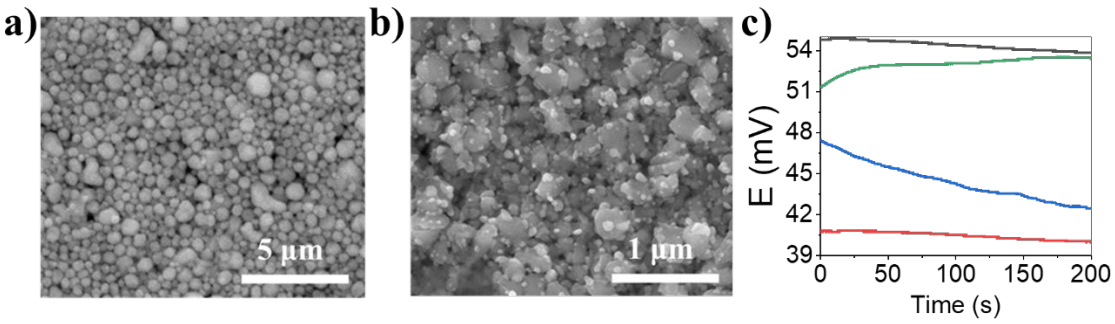

Figure 3.5 SEM pictures of inkjet printed silver trace before (a) and after (b) the treatment with NaClO. (c) Open circuit potential measurements of the as-prepared quasi-reference electrodes vs. a commercial Ag/AgCl reference electrode.

Figure 3.2b IX shows a photograph of the final electrodes, which consisted of LRGO working and counter electrodes, as well as Ag/AgCl quasi-reference electrodes. Inkjet-printed silver was used to create electrode connections and to fabricate the reference electrode with minor modifications from the reference[36]. From the SEM images (Figure 3.5a and b), the pristine Ag lines were composed of nanoparticles sized from approximately 30-120 nm, and after treatment with NaClO, flakes of around 300 nm with grains of approximately 30 nm appeared. Meanwhile, EDX data showed that the atomic ratio of Ag/Cl decreased from 96% to 1.8%, demonstrating the successful chlorination of Ag. Open circuit potential measurements of the printed quasi-reference electrodes (n=4) versus a commercial Ag/AgCl electrode (CHI111, CH Instruments, Inc.) showed a potential fluctuation of less than 4 mV and a potential difference

of less than 14 mV in 200 s (Figure 3.5c), indicating the functionality of the as-prepared reference.

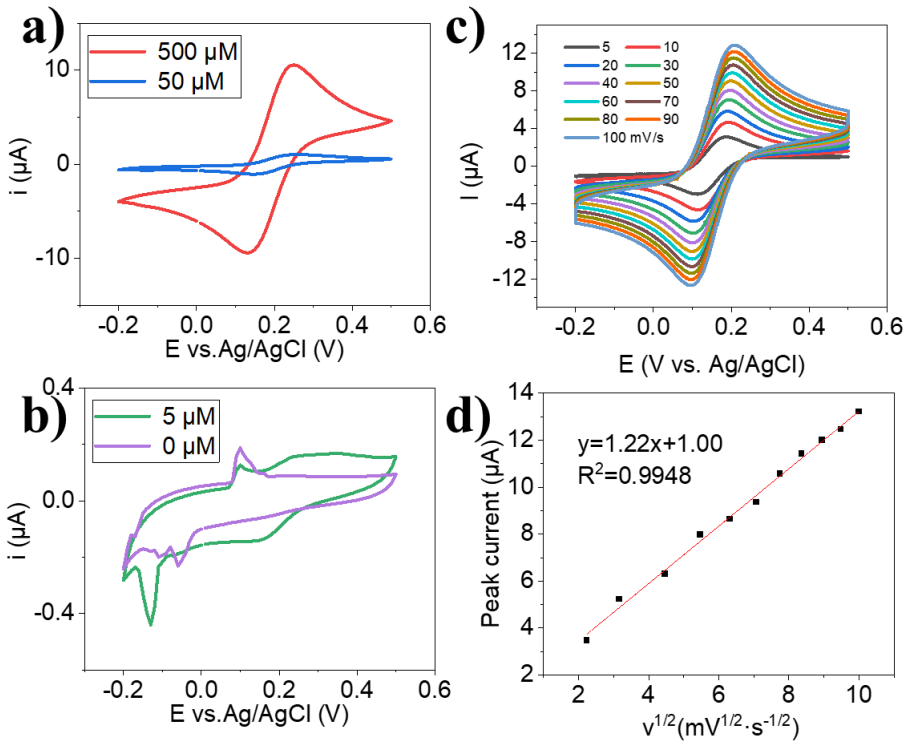

Figure 3.6 (a and b) Representative CVs obtained in different concentrations of $[Fe(CN)_6]^{3-}$ / $[Fe(CN)_6]^{4-}$ 0.1 M KCl (scan rate 50 mV/s, third scan shown). (c) CVs obtained in 500 µM $[Fe(CN)_6]^{3-}$ / $[Fe(CN)_6]^{4-}$ at different scan rates and (d) peak current plotted as a function of the square root of scan rate; the black dots represent raw data and the red line is a linear fit to the data. All the measurements were done vs the on-chip CE and RE.

CV was conducted with $[Fe(CN)_6]^{3-}$/$[Fe(CN)_6]^{4-}$ (redox probe), and the characteristic redox peaks (Figure 3.6a and b) were present in the concentration range of 5-500 µM, showing the high sensitivity of the electrode towards the redox probe. Further performing CV with 500 µM of the probe, the peak current increased with the increase of the scan rate (Figure 3.6c), and the dependence of the peak current on the square root of the scan rates revealed a linear relationship (Figure 3.6d). This suggests a diffusion-controlled mechanism for the oxidation/reduction of the redox couple. The small ΔE, 73 mV, at a scan rate of 30 mV/s, proves a redox process close to reversible (ΔE = 59/n mV, where n is the electron transfer number in the half reaction, and here is 1). According to the Randles-Sevcik equation[49]for the reversible electrode process, the mass transfer controlled ECSA was 0.124 ± 0.01 cm^2, which was 1.77 times bigger than the geometric area of the electrode (0.07 cm^2).

It is well known that highly reduced GO is hydrophobic [50], but the wetting property of T-LRGO was found to vary from hydrophilic to hydrophobic, as reflected by the irregular water contact angle. This could be due to the rough surface, as indicated in Figure 3.3, and the randomly distributed GO flakes mentioned above. The capillary force induced by water evaporation during the drying process may compact the porous structure of the electrode, resulting in a reduced surface area. To avoid this, the electrodes were always kept in a humidity chamber after functionalization. PBASE has commonly been used to functionalize graphene-based electrodes, which hinders the faradic charge transfer process on the electrodes [51]. Conversely, in our case, this was significantly enhanced after PBASE functionalization, as indicated by the improved peak current and reduced ΔE (from 116 to 75 mV, Figure 3.7a). This could be explained by the fact that PBASE turned the hydrophobic LRGO to hydrophilic. The reproducibility of the electrodes was evaluated by CV performed on 18 electrodes (6 electrodes selected randomly from each of three batches). The electrodes were modified with PBASE to make them hydrophilic, and then the measurements were conducted in 0.5 mM $[Fe(CN)_6]^{4-}$/$[Fe(CN)_6]^{3-}$ with 0.1 M KCl. The peak potentials were identical for all the electrodes tested (Figure 3.7b). Anodic peak currents display a relative standard deviation (RSD) of 4.2% intra-batch and 5.6% inter-batch, proving the reproducibility of the prepared electrodes.

The surface area, roughness, and porosity can significantly affect the performance of electrochemical sensors [1, 24]. To obtain ECSA of the LRGO electrodes, non-Faradic CVs at different scan rates were performed in 0.1 M $NaClO_4$ dissolved in ethanol (to avoid the issue of hydrophobicity), as shown in Figure 3.7c. Plotting the current density (j) against the scan rate (υ), as shown in Figure 3.7d, revealed a linear relationship in which the slope equals the area-specific double layer capacitance (C_S), and ECSA of the electrode could be calculated using the following equations [52]:

$$j = \frac{I}{S}$$

$$\mathrm{Cs} = j/v$$

$$\mathrm{ECSA} = S \cdot C_S/C_{Ref}$$

Where S is the geometric surface area of the electrode; υ is scan rate; I is current; j is current density; C_{Ref} is the area specific double layer capacitance of a flat reference surface.

Based on the reference capacitance (C_{Ref}) of graphite (~20 μF/cm^2) [53, 54], the ECSA of the electrode was calculated to be 0.781 ± 0.022 cm^2 from three replicates. This is 11 times larger

than the geometric area (0.07 cm^2), which is expected given the highly rough and porous nature of the electrodes. The standard deviation of the three replicates indicates the reproducibility of the LRGO working electrodes. It is important to note that the Randles-Sevcik equation is strictly applicable to smooth electrode surfaces with planar semi-infinite diffusion of the redox couple for a (quasi) reversible process and can calculate the mass-transfer controlled ECSA [55]. Therefore, the obtained ECSA value (0.124 ± 0.01 cm^2) is much smaller than that obtained above (0.781 ± 0.022 cm^2), which is based on the CV measurements that show negligible resistance contributed from the mass transfer and the hydrophobicity of the electrode (ethanol as a solvent for $NaClO_4$ vs water for ferro-ferricyanide).

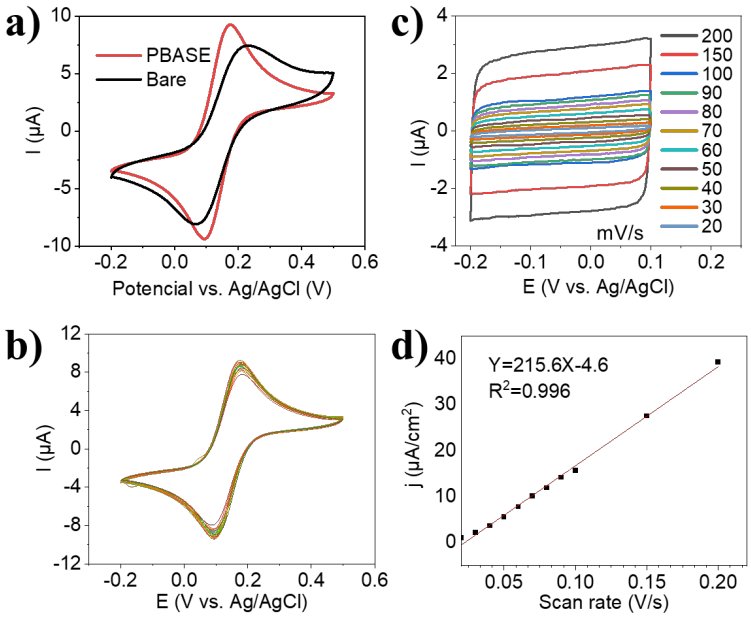

Figure 3.7 (a) Representative CVs of the bare electrode and that modified with PBASE; (b) CVs from 18 electrodes modified with PBASE; the CVs were obtained with 0.5 mM [Fe (CN) $_6]^{3-}$ / [Fe (CN) $_6]^{4-}$ in 0.1 M KCl vs the onboard CE and RE at a scan rate of 50 mV/s. (c) CVs obtained in a solution of 0.1 M $NaClO_4$ in ethanol vs a LRGO CE (4 cm^2) and a Ag wire pseudo reference electrode, at a series of scan rates. (d) Current density from (c) plotted as a function of the scan rate. The black dots represent raw data and the red line is a linear fit to the data.

3.3.2 LRGO-based electrochemical immunosensor for *E. coli* detection

To demonstrate the potential of the electrode for biosensing, an immunosensor was developed for the detection of pathogenic bacteria. *E. coli* was chosen as a representative since its detection is of great importance for healthcare, food safety, and environmental monitoring [38, 56]. Standard optical ELISA was performed to select the suitable capture and detection

antibodies and was used as a reference for the performance evaluation of the T-LRGO electrode based sensor. The optical ELISA was capable of detecting *E. coli* in the range of 9.35×10^4 - 9.06×10^6 CFU/mL with a limit of detection (LOD) of 1.30×10^4 CFU/mL (Figure 3.8a, Table 3.2).

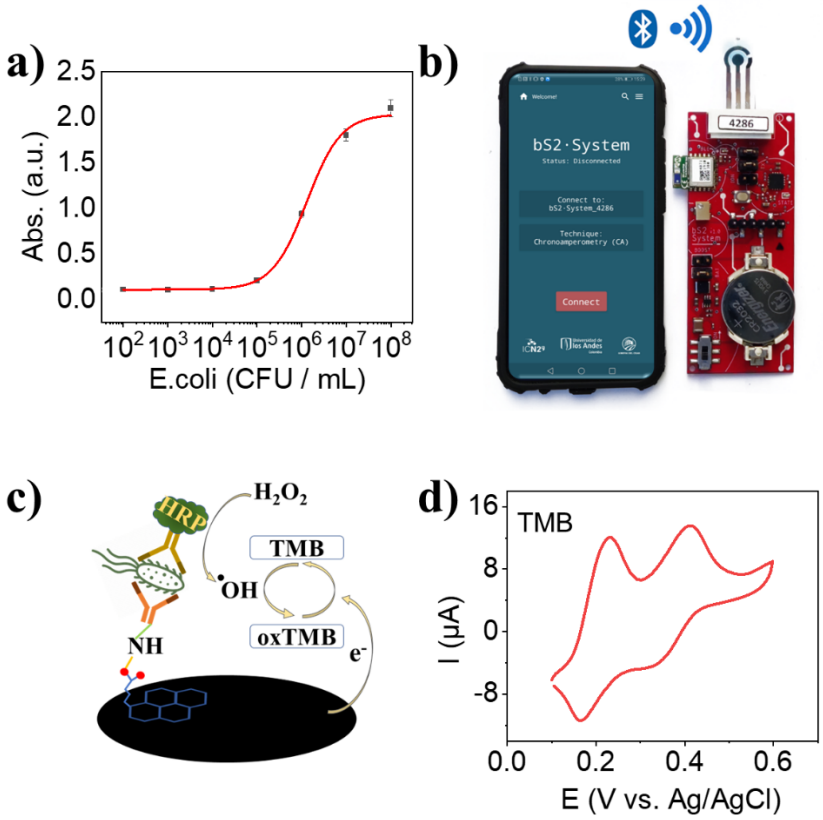

Figure 3.8 (a) Calibration curve of E. coli concentration vs normalized absorbance response from optical ELISA. (b) The portable wireless system used for the detection of E. coli (not to scale). (c) Scheme showing the mechanism of the electrochemical ELISA. (d) CV of TMB on functionalized T-LRGO (vs the onboard Ag/AgCl reference).

Table 3.2 4-Parameter Logistic model fitting parameters for the optical ELISA and electrochemical ELISA.

Standard optical ELISA		Electrochemical ELISA	
Model	Logistic	Model	Logistic
Equation	y = A2 + (A1-A2) / (1 + (x/x0) ^p)	Equation	y = A2 + (A1-A2) / (1 + (x/x0) ^p)
Plot	abs.	Plot	Normalized response
A1	0.11 ± 7.62E-4	A1	-0.045 ± 0.035
A2	2.03 ± 0.055	A2	1.04 ± 0.045
x0	1300903 ± 109381	x0	133550 ± 47258
p	1.13 ± 0.037	p	0.376 ± 0.055
Adj. R-Square	0.9977	Adj. R-Square	0.99267

The same antibodies were used to functionalize the T-LRGO and develop a point-of-care sensing platform, which was operated wirelessly by a smartphone, as shown in Figure 3.8b [35]. The electrochemical sensing mechanism is schematically represented in Figure 3.8c. Briefly, HRP catalyzes H_2O_2 and produces OH radicals, which can oxidize TMB. The oxidized TMB (oxTMB) can be detected electrochemically, where the generated reduction current is proportional to the amount of oxTMB present. The quantity of oxTMB is determined by the amount of HRP-labeled dAb, which is proportional to the number of bacteria captured on the electrode. Therefore, the reduction current evaluates *E. coli* quantitively.

Figure 3.8d displays the CV of TMB on the functionalized T-LRGO. The oxidation peaks at +0.231 V and +0.411 V, and the reduction peaks at +0.166 V and +0.367 V are clearly distinguishable. Figure 3.9a illustrates the current vs time transients of the functionalized electrode with *E. coli* concentrations ranging from 0 to 10^9 CFU/mL. The normalized dose-response curve in Figure 3.9b shows a sigmoidal response, which was fitted with a 4-Parameter Logistic model [64, 65]. The sensor achieved a LOD of 283 CFU/mL (Blank+3SD) with a detection range of 917-2.1×10^7 CFU/mL (the lowest and highest detectable concentrations calculated from 10% and 90% of the maximum signal response on the calibration curve). Compared to the conventional ELISA (Table 3.2), the T-LRGO electrode-based sensing platform showed enhanced performance, consistent with other reported electrochemical ELISA [64]. The sensor is applicable in the clinically relevant range of *E. coli* in urine (10^3 - 10^5

CFU/mL) [66-70], and it is advantageous that all the results were obtained with only 5 μL of sampling. Ultra-sensitive detection, even down to single cell, has been demonstrated [59, 61, 62], but typically require tedious material synthesis and complicated sensor construction (Table 3.3). Our platform showed comparable performance with other electrochemical sensors [57, 58, 60], and could be further improved with optimization of the antibody concentrations. (This work mainly focused on the fabrication and characterization of the electrodes, and the sensor construction was merely a proof of concept.)

Table 3.3. Representative nanomaterial-based biosensors for E. coli detection reported in literature. NPs = nanoparticles; N-GQDs = nitrogen-doped graphene quantum dots; MWCNTs = multiwall carbon nanotubes.

Platform	Technique	Detection range (CFU/mL)	LOD (CFU/mL)	Response time (min)	Sample volume (μL)	Ref
Metal NPs-LIG	EIS	1×10^2-1×10^8	10^2	30	-	[57]
Silica NPs	CV	8×10^4 - 8×10^6	2×10^3	30	10	[58]
Au NPs	LFA	10^4 - 10^6	10^4	10	150	[38]
Fe_3O_4@SiO_2/ polymer/ fluorescein	Fluorescent	4 - 4×10^8	3	75	1000	[59]
MWCNTs/ chitosan / thionine	CV	10^2-10^9	10^2	180	200	[60]
N-GQDs/MIP	ECL	10-10^7	5	140	-	[61]
rGO/Al_2O_3/Au NPs	FET	1-100	Single cell	50 s	1	[62]
MoS_2/Au/optical fiber	SPR	10^3 - 8×10^9	94	~15	-	[63]
LRGO	CA	917 - 2.1×10^7	283	60	5	This work

To verify the selectivity of the sensor, *Salmonella enterica serovar Typhimurium* (ST) and *Staphylococcus aureus subsp. Aureus* (SA) were tested in place of and alongside *E. coli*. The results shown in Figure 3.9c indicate that these bacteria did not produce signals higher than that of the blank. Likewise, when run alongside *E. coli*, the responses were the same as that when *E. coli* was present alone, and a similar trend was observed in the ELISA test (Figure

3.9d), proving that the sensor was specific towards *E. coli*. Other control tests (Figure 3.10a) confirmed that without *E. coli* and cAb, the signal response was negligible (-0.083±0.034 µA, N=4). When only *E. coli* was absent (blank control, N=4), it increased to -0.349±0.010 µA, demonstrating the cross-reactivity between the antibodies, which is common when using polyclonal antibodies [71, 72]. When only cAb was excluded, the current (-0.391±0.108 µA, N=4) was the same within error as that of the blank, indicating insignificant unspecific binding of *E. coli* towards the electrodes.

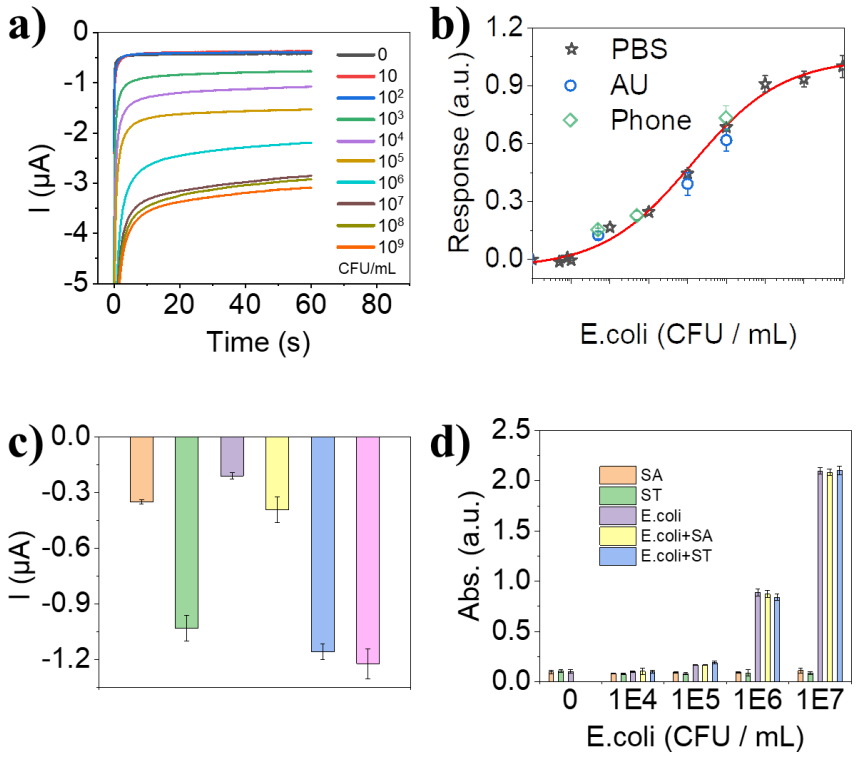

Figure 3.9 (a) Representative current vs time transients of various E. coli concentrations, recorded at +0.125 V vs Ag/AgCl. (b) Calibration curve of E. coli concentration vs normalized current response from the chronoamperometry at + 0.125 V; the black stars were recorded with a commercial potentiostat in PBS, the green diamonds were recorded with the smartphone-driven potentiostat developed in-house and the blue circles were performed with a commercial potentiostat in artificial urine. (c) Selectivity studies showing the current response without bacteria (orange), with Escherichia coli (green), Staphylococcus aureus (purple), Salmonella typhimurium (yellow), Escherichia coli and Staphylococcus aureus (blue), Escherichia coli and Salmonella typhimurium (pink); in all cases, each bacterial concentration was 10^4 CFU/mL, with a 1:1 mix of each in the last two conditions. (d) Selectivity test by ELISA with cAb 2 µg/ml and dAb 0.33 µg/ml, N=3. The stability of the sensors was tested in different storage conditions.

Batches of sensors were stored in humidity chambers at room temperature (20 °C), in the fridge (4 °C) and freezer (-20 °C), all under N_2. Detection of E.coli was conducted in 30 days at several time points (Figure 3.10b, N=4), showing similar signal variations in 10 days under 20°C and 4°C (RSD≤7.6%), comparable to the variations of the electrodes (5.6%) calculated previously. Even after being stored for 30 days, the sensors showed similar performance (RSD of the current response, 12.8% for 4°C, 13.0% for 20°C, and 14.0% for -20°C). Given all the above, the sensors were relatively stable, and the storage temperature did not significantly affect the sensor's stability. The slightly higher RSD of sensors stored under -20°C may be due to the freezing-thawing cycles when taking the sensor in and out of the freezer, which could damage the antibodies [73].

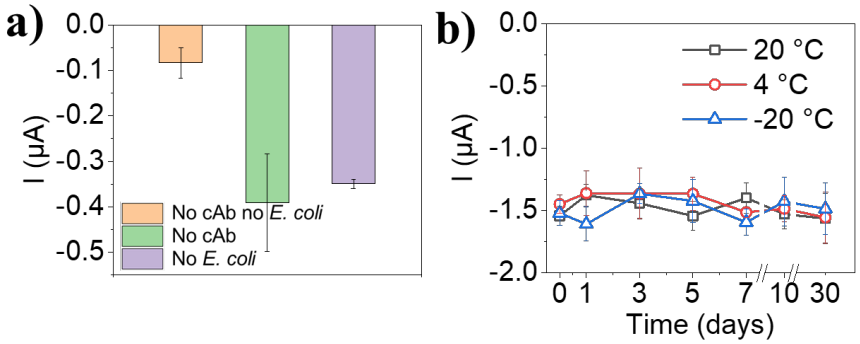

Figure 3.10 (a) Control experiments conducted either without the cAb, E. coli or without both. (b) Current response to 10^5 CFU/ mL of E. coli obtained from the sensors stored in different conditions for 1 month.

The functionality of the sensors was evaluated in spiked artificial urine, and the results were shown in Figure 3.9b (blue circles), which were in good agreement with those obtained in PBS. The recovery rates obtained were 119% for 500 CFU/mL, 88% for 10^5 CFU/mL, and 90% for 10^6 CFU/mL of *E. coli*, suggesting that this sensing platform is potentially applicable in real-world matrices.

The realization of point-of-care (POC) tests requires a sensitive, cheap, wireless, and portable sensing platform. To make the sensors more applicable for POC, a smartphone-based wireless system previously built [35] was used to detect three concentrations of *E. coli* and compared with a commercial potentiostat. The obtained current responses were the same within the error as those recorded with the commercial potentiostat (Figure 3.9b, green diamonds).

Table 3.4. Detailed timetable of electrode fabrication.

Steps	Time	Tools /	Pieces*
Substrate cleaning	1 min	Isopropanol	~1
GO drop casting	5 min	micro- pipette	4~6
GO film forming	2 h	oven	~250
Laser reduction	10 min	Rayjet 50	~50
Stamp-transferring	~1 min	mechanical press	1
Ag print	~10 min	Dimatix 2831	~20
Ag sinter	2 h	oven	~250
Doctor blading of PDMS	1 min	by hand	~4
PDMS solidification	2 min	oven	~250
Ag chlorination	3 min	micro- pipette	~3

Pieces, refers to the number of the substrate processable in each step; 12 electrodes can be made in one batch. The rate-limiting step was substrate treatment or stamp-transferring process, limited to 48 electrodes / 5 min. Under ideal conditions, considering working for 8 h a day and the batches could be made parallelly, a single user could produce 2016 electrodes per day.*

Table 3.5 detailed material cost for the device fabrication.

Materials	Quantity	Price (€)	Number*	Price/device (€)
GO solution	1 L	300	24/5 mL	0.063
Polyester	300 m^2	450	24/128 cm^2	0.001
Ag ink	50 mL	400	>500/mL	0.016
PDMS	1 kg	700	60/g	0.012
cAb	1 mL	435	50/μL	0.009
dAb	250 μL	490	125/μL	0.016
Total price 0.1154 €				

Number, refers to the electrode number per unit of materials. Polyimide substrate, IM301451, DuPont™ Kapton® FPC, thickness 0.125 mm, area 0.61×1 m=0.61 m^2, ~700 €, ~1147 €/m^2; GO solution, 5 mL liquid could cover a square area (8 × 8 cm), ~234 €/m^2.*

The production of ~ 500 electrodes in one day confirms the scalability of such electrode fabrication mothed, although the whole process for making 12 electrodes (one batch) took ~

4.5 hours. More than 2000 electrodes could be produced per day, according to the above calculation (Table 3.4). It is worth mentioning that, the cost for GO was 0.06 € per electrode, 4 times cheaper than polyimide; the total cost of the materials is 0.09 € per electrode, and the whole sensor costs less than 0.12 € (Table 3.5). Despite the CO_2 laser used here is not common lab equipment, other low-cost lasers with wavelengths ranging from 248 nm to 10.6 μm can be used for LRGO production [14, 24, 26, 34, 74]. Silver connections and the reference electrode can also be printed with many low-cost strategies, via consumer inkjet printers, screen printing or simple hand pasting. This means the sensing platforms based on T-LRGO electrodes could be developed in most research labs around the world.

3.4 Conclusions and future work

In this work, we reported a scalable method for LRGO electrode production on polyester substrate and verified the biosensing ability of the electrode by *E. coli* detection in PBS and artificial urine after the functionalization of the electrode. The proof-of-concept sensing platform is capable of detecting *E. coli* in the range of 917 - 2.1×10^7 CFU/mL, with a LOD of 283 CFU/mL, within the clinically relevant range of *E. coli* in human urine. We believe the platform could be applied for the detection of other bacteria or biomarkers, by changing the antibodies.

It is of interest to transfer such LRGO-based sensors to various substrates for other applications, such as wearable sensors[47, 75, 76]. Our primary study confirms that the LRGO film could be transferred to different substrates, as shown in Figure 3.11, demonstrating the potential applicability. Note that the maximum resolution and spot size of the laser defines the resolution of the obtained pattern, and with our device, it is down to tens of micrometer scale, thus making it possible to develop microelectrode.

Figure 3.11 T-LRGO on various substrates. The inset picture shows an interdigitated LRGO pattern before transferring. The scale bar is 1 cm unless labelled otherwise.

3.5 References

1. Lahcen, A.A., et al., Electrochemical Sensors and Biosensors Using Laser-Derived Graphene: A Comprehensive Review. *Biosens. Bioelectron.*, 2020. **168**: p. 112565. DOI: 10.1016/j.bios.2020.112565.
2. Tortorich, R., H. Shamkhalichenar, and J.-W. Choi, Inkjet-Printed and Paper-Based Electrochemical Sensors. *Applied Sciences*, 2018. **8**(2): p. 288. DOI: 10.3390/app8020288.
3. Hammond, J.L., et al., Electrochemical Biosensors and Nanobiosensors. *Essays Biochem*, 2016. **60**(1): p. 69. DOI: 10.1042/EBC20150008.
4. Krishnan, S.K., et al., A Review on Graphene-Based Nanocomposites for Electrochemical and Fluorescent Biosensors. *RSC Advances*, 2019. **9**(16): p. 8778. DOI: 10.1039/c8ra09577a.
5. Singh, E., M. Meyyappan, and H.S. Nalwa, Flexible Graphene-Based Wearable Gas and Chemical Sensors. *ACS Appl. Mater. Interfaces*, 2017. **9**(40): p. 34544. DOI: 10.1021/acsami.7b07063.
6. Htwe, Y.Z.N. and M. Mariatti, Printed Graphene and Hybrid Conductive Inks for Flexible, Stretchable, and Wearable Electronics: Progress, Opportunities, and Challenges. *J Sci-Adv Mater Dev*, 2022. **7**(2): p. 20. DOI: 10.1016/j.jsamd.2022.100435.
7. Novoselov, K.S., et al., A Roadmap for Graphene. *Nature*, 2012. **490**(7419): p. 192. DOI: 10.1038/nature11458.
8. Krishnan, S.K., et al., A Review on Graphene-Based Nanocomposites for Electrochemical and Fluorescent Biosensors. *RSC Adv*, 2019. **9**(16): p. 8778. DOI: 10.1039/c8ra09577a.
9. Mousavi, S.M., et al., Applications of Graphene Oxide in Case of Nanomedicines and Nanocarriers for Biomolecules: Review Study. *Drug Metab. Rev.*, 2019. **51**(1): p. 12. DOI: 10.1080/03602532.2018.1522328.
10. Ren, X., et al., Sulfur-Doped Graphene-Based Immunological Biosensing Platform for Multianalysis of Cancer Biomarkers. *ACS Appl. Mater. Interfaces*, 2017. **9**(43): p. 37637. DOI: 10.1021/acsami.7b13416.
11. Titelman, G.I., et al., Characteristics and Microstructure of Aqueous Colloidal Dispersions of Graphite Oxide. *Carbon*, 2005. **43**(3): p. 641. DOI: 10.1016/j.carbon.2004.10.035.
12. Wu, Z.-S., et al., Synthesis of High-Quality Graphene with a Pre-Determined Number of Layers. *Carbon* 2009. **47**(2): p. 493. DOI: 10.1016/j.carbon.2008.10.031.
13. Kudr, J., et al., Inkjet-Printed Electrochemically Reduced Graphene Oxide Microelectrode as a Platform for Ht-2 Mycotoxin Immunoenzymatic Biosensing. *Biosens. Bioelectron.*, 2020. **156**: p. 112109. DOI: 10.1016/j.bios.2020.112109.
14. Kurra, N., et al., Laser-Derived Graphene: A Three-Dimensional Printed Graphene Electrode and Its Emerging Applications. *Nano Today*, 2019. **24**: p. 81. DOI: 10.1016/j.nantod.2018.12.003.
15. Wei, T., et al., Recent Advances in Graphene Patterning. *Chempluschem*, 2020. **85**(8):

p. 1655. DOI: 10.1002/cplu.202000419.

16. Backes, C., et al., Production and Processing of Graphene and Related Materials. *2D Materials*, 2020. **7**(2): p. 022001. DOI: 10.1088/2053-1583/ab1e0a.
17. Nagar, B., et al., Fully Printed One-Step Biosensing Device Using Graphene/Aunps Composite. *Biosens. Bioelectron.*, 2019. **129**: p. 238. DOI: 10.1016/j.bios.2018.09.073.
18. Li, Z., et al., Covalent Patterning of Graphene for Controllable Functionalization from Microscale to Nanoscale: A Mini-Review. *Frontiers in Chemistry*, 2022. **10**. DOI: 10.3389/fchem.2022.829614.
19. Ruan, X.J., et al., Microcontact Printing with Laser Direct Writing Carbonization for Facile Fabrication of Carbon-Based Ultrathin Disk Arrays and Ordered Holey Films. *Small*, 2019. **15**(44): p. 1902819. DOI: 10.1002/smll.201902819.
20. Ambaye, A.D., et al., Recent Developments in Nanotechnology-Based Printing Electrode Systems for Electrochemical Sensors. *Talanta*, 2021. **225**: p. 121951. DOI: 10.1016/j.talanta.2020.121951.
21. Kathirvelan, J., Recent Developments of Inkjet-Printed Flexible Sensing Electronics for Wearable Device Applications: A Review. *Sensor Review*, 2020. **41**(1): p. 46. DOI: 10.1108/sr-08-2020-0190.
22. Georgakilas, V., et al., Noncovalent Functionalization of Graphene and Graphene Oxide for Energy Materials, Biosensing, Catalytic, and Biomedical Applications. *Chem Rev*, 2016. **116**(9): p. 5464. DOI: 10.1021/acs.chemrev.5b00620.
23. Mishra, N.K., et al., Highly Selective Laser-Induced Graphene (Lig)/Polysulfone Composite Membrane for Hydrogen Purification. *Applied Materials Today*, 2021. **22**: p. 100971. DOI: 10.1016/j.apmt.2021.100971.
24. Chyan, Y., et al., Laser-Induced Graphene by Multiple Lasing: Toward Electronics on Cloth, Paper, and Food. *ACS NANO*, 2018. **12**(3): p. 2176. DOI: 10.1021/acsnano.7b08539.
25. Jung, Y., et al., Smart Paper Electronics by Laser-Induced Graphene for Biodegradable Real-Time Food Spoilage Monitoring. *Applied Materials Today*, 2022. **29**: p. 101589. DOI: 10.1016/j.apmt.2022.101589.
26. El-Kady, M.F., et al., Laser Scribing of High-Performance and Flexible Graphene-Based Electrochemical Capacitors. *Science*, 2012. **335**(6074): p. 1326. DOI: 10.1126/science.1216744.
27. Lin, J., et al., Laser-Induced Porous Graphene Films from Commercial Polymers. *Nat Commun*, 2014. **5**(1): p. 5714. DOI: 10.1038/ncomms6714.
28. Kumar, R., et al., Laser-Assisted Synthesis, Reduction and Micro-Patterning of Graphene: Recent Progress and Applications. *Coord. Chem. Rev.*, 2017. **342**: p. 34. DOI: 10.1016/j.ccr.2017.03.021.
29. Wan, Z., et al., Laser Induced Graphene for Biosensors. *Sustainable Mater.Technol.*, 2020. **25**: p. e00205. DOI: 10.1016/j.susmat.2020.e00205.
30. Jiang, H., et al., Review of Photoreduction and Synchronous Patterning of Graphene Oxide toward Advanced Applications. *J. Mater. Sci.*, 2019. **55**(2): p. 480. DOI: 10.1007/s10853-019-03981-z.

31. Guan, Y.C., et al., Fabrication of Laser-Reduced Graphene Oxide in Liquid Nitrogen Environment. *Sci. Rep.*, 2016. **6**: p. 28913. DOI: 10.1038/srep28913.

32. Jin, Y. and W. Lee, Cross-Linking Stabilizes Electrical Resistance of Reduced Graphene Oxide in Humid Environments. *Langmuir*, 2019. **35**(16): p. 5427. DOI: 10.1021/acs.langmuir.8b03416.

33. Oh, J.-S., et al., Laser-Assisted Simultaneous Patterning and Transferring of Graphene. *J. Phys. Chem. C*, 2012. **117**(1): p. 663. DOI: 10.1021/jp309382w.

34. Giacomelli, C., et al., Selective Stamping of Laser Scribed Rgo Nanofilms: From Sensing to Multiple Applications. *2D Materials*, 2020. **7**(2): p. 024006. DOI: 10.1088/2053-1583/ab68a7.

35. Yang, Q., et al., Wearable and Fully Printed Microfluidic Nanosensor for Sweat Rate, Conductivity, and Copper Detection with Healthcare Applications. *Biosens. Bioelectron.*, 2022. **202**: p. 114005. DOI: 10.1016/j.bios.2022.114005.

36. da Silva, E.T., et al., Simple on-Plastic/Paper Inkjet-Printed Solid-State Ag/Agcl Pseudoreference Electrode. *Anal. Chem.*, 2014. **86**(21): p. 10531. DOI: 10.1021/ac503029q.

37. Bergua, J.F., et al., Improved Aliivibrio Fischeri Based-Toxicity Assay: Graphene-Oxide as a Sensitivity Booster with a Mobile-Phone Application. *J. Hazard. Mater.*, 2021. **406**: p. 124434. DOI: 10.1016/j.jhazmat.2020.124434.

38. Bergua, J.F., et al., Lateral Flow Device for Water Fecal Pollution Assessment: From Troubleshooting of Its Microfluidics Using Bioluminescence to Colorimetric Monitoring of Generic Escherichia Coli. *Lab Chip*, 2021. **21**(12): p. 2417. DOI: 10.1039/d1lc00090j.

39. Bergua, J.F., et al., Low-Cost, User-Friendly, All-Integrated Smartphone-Based Microplate Reader for Optical-Based Biological and Chemical Analyses. *Anal. Chem.*, 2022. **94**(2): p. 1271. DOI: 10.1021/acs.analchem.1c04491.

40. Mbayachi, V.B., et al., Graphene Synthesis, Characterization and Its Applications: A Review. *Results in Chemistry*, 2021. **3**: p. 100163. DOI: 10.1016/j.rechem.2021.100163.

41. Mukherjee, R., et al., Photothermally Reduced Graphene as High-Power Anodes for Lithium-Ion Batteries. *Acs Nano*, 2012. **6**(9): p. 7867.

42. Shiyanova, K.A., et al., Segregated Network Polymer Composites with High Electrical Conductivity and Well Mechanical Properties Based on Pvc, P(Vdf-Tfe), Uhmwpe, and Rgo. *ACS Omega*, 2020. **5**(39): p. 25148. DOI: 10.1021/acsomega.0c02859.

43. Li, G., Direct Laser Writing of Graphene Electrodes. *J. Appl. Phys.*, 2020. **127**(1). DOI: 10.1063/1.5120056.

44. Zhu, Y., et al., Graphene and Graphene Oxide: Synthesis, Properties, and Applications. *Adv. Mater.*, 2010. **22**(35): p. 3906. DOI: 10.1002/adma.201001068.

45. Sokolov, D.A., et al., Excimer Laser Reduction and Patterning of Graphite Oxide. *Carbon*, 2013. **53**: p. 81. DOI: 10.1016/j.carbon.2012.10.034.

46. Strong, V., et al., Patterning and Electronic Tuning of Laser Scribed Graphene for Flexible All-Carbon Devices. *ACS Nano*, 2012. **6**(2): p. 1395. DOI:

10.1021/nn204200w.

47. Chen, X.-D., et al., High-Quality and Efficient Transfer of Large-Area Graphene Films onto Different Substrates. *Carbon*, 2013. **56**: p. 271. DOI: 10.1016/j.carbon.2013.01.011.

48. Rocha, J.F., et al., Graphene Oxide Fibers by Microfluidics Assembly: A Strategy for Structural and Dimensional Control. *Nanoscale*, 2021. **13**(14): p. 6752. DOI: 10.1039/d0nr08380a.

49. Allen J. Bard, L.R.F., *Electrochemical Methods: Fundamentals and Applications*. 2nd ed. 2000.

50. Narayanam, P.K., et al., Transparent and Hydrophobic "Reduced Graphene Oxide–Titanium Dioxide" Nanocomposites for Nonwetting Device Applications. *ACS Appl. Nano Mater.*, 2018. **1**(10): p. 5691. DOI: 10.1021/acsanm.8b01302.

51. Torrente-Rodriguez, R.M., et al., Sars-Cov-2 Rapidplex: A Graphene-Based Multiplexed Telemedicine Platform for Rapid and Low-Cost Covid-19 Diagnosis and Monitoring. *Matter*, 2020. **3**(6): p. 1981. DOI: 10.1016/j.matt.2020.09.027.

52. Voiry, D., et al., Best Practices for Reporting Electrocatalytic Performance of Nanomaterials. *ACS Nano*, 2018. **12**(10): p. 9635. DOI: 10.1021/acsnano.8b07700.

53. Xia, J., et al., Measurement of the Quantum Capacitance of Graphene. *Nat Nanotechnol*, 2009. **4**(8): p. 505. DOI: 10.1038/nnano.2009.177.

54. Wang, Y., et al., Supercapacitor Devices Based on Graphene Materials. *J. Phys. Chem. C*, 2009. **113**(30): p. 13103. DOI: 10.1021/jp902214f.

55. Behrent, A., et al., Process-Property Correlations in Laser-Induced Graphene Electrodes for Electrochemical Sensing. *Mikrochim. Acta*, 2021. **188**(5): p. 159. DOI: 10.1007/s00604-021-04792-3.

56. Lazcka, O., F.X. Del Campo Fj Fau - Muñoz, and F.X. Muñoz, Pathogen Detection: A Perspective of Traditional Methods and Biosensors. *Biosens. Bioelectron.*, 2006. **22**(7): p. 1205. DOI: 10.1016/j.bios.2006.06.036.

57. You, Z., et al., Laser-Induced Noble Metal Nanoparticle-Graphene Composites Enabled Flexible Biosensor for Pathogen Detection. *Biosens. Bioelectron.*, 2020. **150**: p. 111896. DOI: 10.1016/j.bios.2019.111896.

58. Mathelié-Guinlet, M., et al., Silica Nanoparticles-Assisted Electrochemical Biosensor for the Rapid, Sensitive and Specific Detection of Escherichia Coli. *Sensors Actuators B: Chem.*, 2019. **292**: p. 314. DOI: 10.1016/j.snb.2019.03.144.

59. Hu, R.R., et al., A Novel Biosensor for Escherichia Coli O157:H7 Based on Fluorescein-Releasable Biolabels. *Biosens. Bioelectron.*, 2016. **78**: p. 31. DOI: 10.1016/j.bios.2015.11.018.

60. Gayathri, C.H., et al., An Electrochemical Immunosensor for Efficient Detection of Uropathogenic E. Coli Based on Thionine Dye Immobilized Chitosan/Functionalized-Mwcnt Modified Electrode. *Biosens. Bioelectron.*, 2016. **82**: p. 71. DOI: 10.1016/j.bios.2016.03.062.

61. Chen, S., et al., Electrochemiluminescence Detection of Escherichia Coli O157:H7 Based on a Novel Polydopamine Surface Imprinted Polymer Biosensor. *ACS Appl. Mater. Interfaces*, 2017. **9**(6): p. 5430. DOI: 10.1021/acsami.6b12455.

62. Thakur, B., et al., Rapid Detection of Single E. Coli Bacteria Using a Graphene-Based Field-Effect Transistor Device. *Biosens. Bioelectron.*, 2018. **110**: p. 16. DOI: 10.1016/j.bios.2018.03.014.

63. Kaushik, S., et al., Rapid Detection of Escherichia Coli Using Fiber Optic Surface Plasmon Resonance Immunosensor Based on Biofunctionalized Molybdenum Disulfide (Mos(2)) Nanosheets. *Biosens. Bioelectron.*, 2019. **126**: p. 501. DOI: 10.1016/j.bios.2018.11.006.

64. Farrow, B., et al., A Chemically Synthesized Capture Agent Enables the Selective, Sensitive, and Robust Electrochemical Detection of Anthrax Protective Antigen. *ACS Nano*, 2013. **7**(10): p. 9452. DOI: 10.1021/nn404296k.

65. Bhimji, A., et al., An Electrochemical Elisa Featuring Proximal Reagent Generation: Detection of Hiv Antibodies in Clinical Samples. *Anal. Chem.*, 2013. **85**(14): p. 6813. DOI: 10.1021/ac4009429.

66. Orenstein, R. and E.S. Wong, Urinary Tract Infections in Adults. *Am. Fam. Physician*, 1999. **59**(5): p. 1225.

67. Laupland, K.B., et al., Community-Onset Urinary Tract Infections: A Population-Based Assessment. *Infection*, 2007. **35**(3): p. 150. DOI: 10.1007/s15010-007-6180-2.

68. Moxley, R.A., et al., Correction: Intimate Attachment of Escherichia Coli O157: H7 to Urinary Bladder Epithelium in the Gnotobiotic Piglet Model *Microorganisms*, 2020. **8**(12): p. 1. DOI: 10.3390/microorganisms8122016.

69. Shi, L., et al., Rapid, Quantitative, High-Sensitive Detection of Escherichia Coli O157:H7 by Gold-Shell Silica-Core Nanospheres-Based Surface-Enhanced Raman Scattering Lateral Flow Immunoassay. *Front. Microbiol.*, 2020. **11**: p. 1. DOI: 10.3389/fmicb.2020.596005.

70. Huang, T., et al., Rapid Identification of Urinary Tract Infections Based on Ultrasensitive Bacteria Detection Using Volumetric Bar-Chart Chip. *Sensors and Actuators, B: Chemical*, 2019. **298**: p. 126885. DOI: 10.1016/j.snb.2019.126885.

71. Stathopoulou, E.A., et al., Cross-Reaction between Antibodies to the Major Epitope of Ro60 Kd Autoantigen and a Homologous Peptide of Coxsackie Virus 2b Protein. *Clin Exp Immunol*, 2005. **141**(1): p. 148. DOI: 10.1111/j.1365-2249.2005.02812.x.

72. Vaarala, O., et al., Crossreaction between Antibodies to Oxidised Low-Density Lipoprotein and to Cardiolipin in Systemic Lupus Erythematosus. *The Lancet*, 1993. **341**(8850): p. 923.

73. Bhatnagar, B.S., R.H. Bogner, and M.J. Pikal, Protein Stability During Freezing: Separation of Stresses and Mechanisms of Protein Stabilization. *Pharmaceutical Development and Technology*, 2007. **12**(5): p. 505. DOI: 10.1080/10837450701481157.

74. Lu, Z., et al., Novel Flexible Bifunctional Amperometric Biosensor Based on Laser Engraved Porous Graphene Array Electrodes: Highly Sensitive Electrochemical Determination of Hydrogen Peroxide and Glucose. *J. Hazard. Mater.*, 2021. **402**: p. 123774. DOI: 10.1016/j.jhazmat.2020.123774.

75. Tran, T.S., N.K. Dutta, and N.R. Choudhury, Graphene Inks for Printed Flexible Electronics: Graphene Dispersions, Ink Formulations, Printing Techniques and

Applications. *Adv Colloid Interface Sci*, 2018. **261**: p. 41. DOI: 10.1016/j.cis.2018.09.003.

76. Cinti, S. and F. Arduini, Graphene-Based Screen-Printed Electrochemical (Bio)Sensors and Their Applications: Efforts and Criticisms. *Biosens. Bioelectron.*, 2017. **89**(Pt 1): p. 107. DOI: 10.1016/j.bios.2016.07.005.

4 General conclusions and future perspectives

This thesis focuses on the design and fabrication of graphene-based electrodes with maskless, non-contact, low-cost direct writing methods for practical biosensing towards the point-of-care level. Considering the exposed objectives in Chapter 1 and the obtained results in Chapters 2, and 3 the following conclusion remarks are drawn:

A. Comparative studies were conducted on the performance of piezo-DOD-based, consumer-grade, and research-grade inkjet printers using Dimatix 2831 and Epson 15000 as representatives by printing Ag NP inks on a coated porous substrate.

1) Dimatix showed precise and high-resolution (5 μm) material deposition, and could print patterns with a depositing accuracy of ~20 μm inline, ~10 μm outline, and intra-layer depositing error of 3.2 μm.

2) Epson could distinguish input patterns with a minimum dimension of ~15 μm with considerable error, was featured for low printer cost, and superfast device production.

3) To obtain good patterns (the variations of the obtained line width less than 5%), the design needs to be wider than 10 μm for Dimatix, while for Epson, wider than 150 μm inline and 300 μm outline.

4) Perspectives: Obtaining the whole electrode system (e.g., working, counter, and reference electrodes), or more ambitiously, a whole sensor (with bio-inks) by a single printer with various inks in different cartridges, should be of great interest via further exploration of multichannel printing with consumer printers.

B. Graphene microelectrodes were fabricated on PEN by inkjet printing and a subsequent electrochemical reduction and were demonstrated for HT-2 mycotoxin sensing.

1) Graphene microelectrodes with a width of 78 μm were obtained by inkjet printing of a water-based graphene oxide ink and the following electrochemical reduction.

2) An immunoenzymatic electrochemical sensor was constructed for HT-2 mycotoxin sensitive detection based on the microelectrode platform.

3) The sensor displays a low LOD of 1.6 ng/mL and a linear dynamic range of 6.3-100 ng/mL in PBS buffer, with satisfactory recovery in a biological matrix.

4) The sensing platform should be applicable for the detection of other biomarkers, by changing the antibodies.

5) Perspectives: Considering the small dimension of the electrode, it is worthwhile to

integrate more than one electrode on the platform for multiplex sensing.

C. Graphene electrodes were fabricated with direct writing on polyester substrates and were used for *E. coli* detection towards the point-of-care.

1) A simple, fast, and maskless method for large-scale, low-cost laser reduced graphene oxide electrode fabrication was developed through direct laser writing and inkjet printing coupled with a stamp-transferring method.

2) The transferred electrodes were characterized by SEM, XPS, Raman, and electrochemical methods.

3) The biosensing potential of the electrodes was proven by the proof-of-concept detection of *E. coli* with a wide dynamic range (917-2.1×10^7 CFU/mL) and low LOD (283 CFU/mL) using just 5 µL of the sample.

4) The test was also verified in spiked artificial urine, and the sensor was integrated into a portable wireless system driven and measured by a smartphone.

5) This work demonstrates the potential to use these biosensors for real-world, point-of-care applications.

6) Perspectives: The development of microelectrode arrays by this method and the optimization of printing and stamping onto other substrates would be promising for different applications.

Overall, this thesis provides valuable insights into the design and fabrication of graphene-based electrodes for biosensing towards point-of-care applications, with promising avenues for future research.